

## **DOCTOR OF PHILOSOPHY**

### **Development and Application of Bragg Edge Neutron Transmission Imaging on the IMAT Beamline**

Ramadhan, Ranggi Sahmura

*Award date:*  
2019

*Awarding institution:*  
Coventry University

[Link to publication](#)

#### **General rights**

Copyright and moral rights for the publications made accessible in the public portal are retained by the authors and/or other copyright owners and it is a condition of accessing publications that users recognise and abide by the legal requirements associated with these rights.

- Users may download and print one copy of this thesis for personal non-commercial research or study
- This thesis cannot be reproduced or quoted extensively from without first obtaining permission from the copyright holder(s)
- You may not further distribute the material or use it for any profit-making activity or commercial gain
- You may freely distribute the URL identifying the publication in the public portal

#### **Take down policy**

If you believe that this document breaches copyright please contact us providing details, and we will remove access to the work immediately and investigate your claim.

# **Development and Application of Bragg Edge Neutron Transmission Imaging on the IMAT Beamline**

by

**Ranggi Sahmura Ramadhan**

June 2019



Faculty of Engineering, Environment and Computing

*A thesis submitted in partial fulfilment of the University's requirements for the Degree of  
Doctor of Philosophy*

This item has been removed due to third party copyright. The unabridged version of the thesis can be viewed at the  
Lanchester library, Coventry University



## Certificate of Ethical Approval

Applicant:

Ranggi Ramadhan

Project Title:

Development and application of neutron transmission imaging for strain mapping in aerospace application

This is to certify that the above named applicant has completed the Coventry University Ethical Approval process and their project has been confirmed and approved as Low Risk

Date of approval:

15 May 2019

Project Reference Number:

P90766



## **Acknowledgements**

I would like to express my gratitude to my Director of Studies Prof. Michael Fitzpatrick, and to my supervisory team Dr. Bo Chen and Dr. David Parfitt for their guidance, constructive suggestion and feedback throughout this PhD project. The support and the freedom that they have given me while running the project have made the experience really positive.

I would like to offer my special thanks to Dr. Winfried Kockelmann, for his patient guidance, encouragement and support in this project. His willingness to give his time so generously during the experiments and hours of discussions has been very much appreciated.

My special thanks are extended to the research colleagues at the Coventry University, Dr. Niall Smyth and Dr. Abdul K. Syed, also to the researchers at the ISIS neutron source, Dr. Triestino Minniti, Dr. Saurabh Kabra and Dr. Genoveva Burca. Also special thanks to Dr. Anton S. Tremsin of the University of California Berkeley for the support and advises in the experiment and data analysis.

I would like to thank Coventry University and Science and Technology Facilities Council for funding this PhD project through the Facility Development Studentship.

Finally, I wish to thank my parents, my sister and my wife for their support and encouragement throughout my study.



## Abstract

Bragg edge neutron transmission imaging has been developed on the new IMAT beamline at the ISIS pulsed neutron source, UK, and pilot studies have been performed on engineering materials. The purpose of this work is to establish Bragg edge imaging on the new beamline in terms of data collection methodology and data analysis, and to demonstrate its potential for engineering and material studies through a series of exemplar experiments.

The objectives of this thesis are to develop the data analysis of Bragg edge imaging, to characterise the IMAT beamline parameters which are relevant for Bragg edge imaging, to evaluate and to validate the Bragg edge strain mapping capability of the beamline, and to provide an extensive demonstration of Bragg edge imaging for engineering applications. These objectives are achieved by performing a series of trials and calibration experiments on the IMAT beamline, including measurements of different powders and calibration samples using a microchannel plate (MCP) detector and measurements of samples at high temperature, both of which were carried out for the first time on the beamline. Benchmarking experiments using more established methods were also performed to validate strain measurements performed on IMAT. Demonstrator experiments were carried out to emphasize the advantages of Bragg edge imaging, where residual strain measurements and crystallographic analysis were performed on engineering components which had been subjected to different manufacturing processes, e.g., laser shock peening.

Results from this work show that the IMAT beamline is highly suitable for carrying out Bragg edge strain mapping for engineering components. A typical measurement with the MCP detector can provide a 2D strain map with spatial resolution in the range of 100-600  $\mu\text{m}$  and uncertainties below 200  $\mu\epsilon$  in a single exposure with counting times below 10 hours. This work demonstrates, for the first time, a novel, cross-correlation-based data analysis approach to provide an alternative measure of Bragg edge shifts for both non-textured and textured samples. This work also shows that Bragg edge imaging can be used to map strains, texture distributions, to follow texture evolution, and to measure the temperature dependence of the Debye-Waller factor.

Based on the findings of this work, the IMAT beamline is capable of performing Bragg edge imaging, which is a powerful technique for engineering studies. This work serves

as an important step in establishing Bragg edge strain mapping, especially on the IMAT beamline. This thesis also provides guidance for future users to perform the calibration steps and material studies involving Bragg edge imaging on IMAT and other time-of-flight neutron imaging beamlines.

## Publications

Work included in this thesis has been presented in the following publications and conference proceedings:

### *Journal papers:*

1. Ramadhan, R. S., Kockelmann, W., Minniti, T., Chen, B., Parfitt, D., Fitzpatrick, M. E., & Tremsin, A. S. (2019). Characterization and application of Bragg-edge transmission imaging for strain measurement and crystallographic analysis on the IMAT beamline. *Journal of Applied Crystallography*, 52(2), 351–368.
2. Ramadhan, R. S., Syed, A. K., Tremsin, A. S., Kockelmann, W., Dalgliesh, R., Chen, B., ... Fitzpatrick, M. E. (2018). Mapping residual strain induced by cold working and by laser shock peening using neutron transmission spectroscopy. *Materials & Design*, 143, 56–64.
3. Kockelmann, W., Minniti, T., Pooley, D., Burca, G., Ramadhan, R., Akeroyd, F., ... Nightingale, J. (2018). Time-of-Flight Neutron Imaging on IMAT@ISIS: A New User Facility for Materials Science. *Journal of Imaging*, 4(3), 47.
4. Tremsin, A., Kockelmann, W., Kelleher, J., Paradowska, A., Ramadhan, R., & Fitzpatrick, M. (2018). Energy-Resolved Neutron Imaging for Reconstruction of Strain Introduced by Cold Working. *Journal of Imaging*, 4(3), 48.

### *Conference proceedings:*

1. Ramadhan, R. S., Kockelmann, W., Tremsin, A. S., & Fitzpatrick, M. E. (2018). Neutron Transmission Strain Measurements on IMAT: Residual Strain Mapping in an AlSiCp Metal Matrix Composite. *Materials Research Proceedings*, 4, 149–154.
2. Kockelmann, W., Minniti, T., Ramadhan, R.S., Ziesce, R., Pooley, D.E., Capelli, S., Glaser, D., & Tremsin, A.S. (2019). Wavelength resolved neutron imaging on IMAT. *Materials Research Forum*, in print.



# Table of contents

<b>List of figures</b>	<b>xvii</b>
<b>List of tables</b>	<b>xxiii</b>
<b>Nomenclature</b>	<b>xxv</b>
<b>1 Introduction</b>	<b>1</b>
1.1 Background . . . . .	1
1.2 Motivation . . . . .	2
<b>2 Introduction to Neutrons for Materials Analysis</b>	<b>5</b>
2.1 Neutron fundamentals . . . . .	5
2.1.1 Neutron properties . . . . .	5
2.1.2 Neutron generation . . . . .	7
2.1.3 Neutron moderation . . . . .	9
2.1.4 Neutron detection . . . . .	10
2.2 Interaction of neutrons with matter . . . . .	12
2.2.1 Neutron cross section and neutron attenuation . . . . .	12
2.2.2 Neutron scattering . . . . .	13
2.3 Neutron for materials analysis . . . . .	14
2.3.1 Radiography and tomography . . . . .	14
2.3.2 Scattering-based methods . . . . .	15
2.3.3 Diffraction in neutron transmission . . . . .	16
<b>3 Bragg Edge Neutron Transmission Imaging</b>	<b>19</b>
3.1 Time-of-flight method . . . . .	19
3.2 Neutron diffraction . . . . .	20
3.2.1 Bragg's law and the Bragg diffraction peak . . . . .	20
3.2.2 Neutron diffraction for stress analysis . . . . .	23

3.3	Bragg edge neutron transmission . . . . .	26
3.3.1	Neutron transmission setup . . . . .	26
3.3.2	Interpretation of transmission spectra and generation of Bragg edges	26
3.3.3	Bragg edge analysis for materials studies . . . . .	29
3.4	Principle of Bragg edge neutron transmission imaging . . . . .	30
3.4.1	Basic principles . . . . .	30
3.4.2	Components of the neutron transmission imaging setup . . . . .	31
3.5	Bragg edge imaging for residual strain measurement . . . . .	33
3.5.1	Residual stress . . . . .	33
3.5.2	Stress-strain analysis and measurement . . . . .	34
3.5.3	Bragg edge transmission imaging for residual strain measurement .	36
<b>4</b>	<b>Experimental Method and Data Analysis for Bragg edge Neutron Transmission Imaging</b>	<b>37</b>
4.1	Experimental design of neutron transmission imaging . . . . .	37
4.1.1	Gauge volume . . . . .	37
4.1.2	Geometry of a neutron transmission experiment . . . . .	38
4.1.3	Material selection . . . . .	40
4.1.4	Geometrical blurring . . . . .	43
4.1.5	Sample interface effect . . . . .	45
4.2	Data analysis of neutron transmission imaging . . . . .	47
4.2.1	Data structure of TOF neutron transmission imaging experiment .	47
4.2.2	Bragg edge fitting and parameters . . . . .	47
4.2.3	Bragg edge parameter map reconstruction . . . . .	50
4.2.4	Bragg edge parameter mapping software tool . . . . .	51
<b>5</b>	<b>Time-of-flight Neutron Imaging Beamline: IMAT at ISIS, UK</b>	<b>55</b>
5.1	Overview of the IMAT beamline . . . . .	55
5.2	IMAT instrumentation . . . . .	57
5.2.1	General schematics . . . . .	57
5.2.2	Source and moderator . . . . .	61
5.2.3	Beam transport system . . . . .	62
5.2.4	Beam defining components . . . . .	63
5.2.5	Sample area . . . . .	64
5.2.6	IMAT infrastructure . . . . .	66
5.3	IMAT imaging detectors . . . . .	66
5.3.1	MCP detector . . . . .	66

5.3.2	GP2 detector . . . . .	68
5.3.3	Messina camera boxes . . . . .	69
5.4	IMAT GUI and analysis tools . . . . .	70
5.4.1	IMAT GUI . . . . .	70
5.4.2	Image-J . . . . .	71
5.4.3	TPX_Edgefit . . . . .	72
5.4.4	BEATRIX . . . . .	73
<b>6</b>	<b>Characterisation of the IMAT Beamline</b>	<b>75</b>
6.1	IMAT flight path . . . . .	75
6.1.1	Theoretical background . . . . .	75
6.1.2	Experimental and data analysis . . . . .	76
6.1.3	Results . . . . .	77
6.2	IMAT wavelength resolution . . . . .	79
6.2.1	Background . . . . .	79
6.2.2	Experimental and data analysis . . . . .	80
6.2.3	Results . . . . .	80
6.3	Spatial resolution of IMAT with MCP camera . . . . .	81
6.3.1	Background . . . . .	81
6.3.2	Experimental and data analysis . . . . .	82
6.3.3	Results . . . . .	82
6.4	Discussion . . . . .	83
<b>7</b>	<b>Development of the Residual Strain Mapping on IMAT</b>	<b>89</b>
7.1	Overview . . . . .	89
7.2	Assessment of Bragg edge fitting functions . . . . .	92
7.3	Cross-correlation-based Bragg edge analysis . . . . .	94
7.4	Commissioning experiments for Bragg edge strain mapping . . . . .	98
7.4.1	High temperature measurement . . . . .	98
7.4.2	Spatial resolution measurement . . . . .	101
7.4.3	Strain validation measurement . . . . .	102
7.5	Results . . . . .	104
7.5.1	Transmission spectra at high temperature . . . . .	104
7.5.2	Uncertainty and strain resolution . . . . .	104
7.5.3	Accuracy of the lattice parameter & strain measurement . . . . .	108
7.5.4	Accuracy of the cross-correlation data analysis . . . . .	108
7.5.5	Spatial resolution of the reconstructed map . . . . .	111

7.5.6 Validation: Neutron transmission vs diffraction . . . . .	113
7.6 Discussion . . . . .	115
<b>8 Bragg Edge Imaging for Crystallography</b>	<b>119</b>
8.1 Overview . . . . .	119
8.2 Experiments . . . . .	121
8.3 Results . . . . .	122
8.3.1 Crystallographic texture mapping . . . . .	122
8.3.2 Recrystallisation imaging . . . . .	124
8.3.3 Debye-Waller factor analysis . . . . .	124
8.4 Discussion . . . . .	125
<b>9 Energy-resolved Bragg Edge Imaging of Engineering Materials</b>	<b>127</b>
9.1 Overview . . . . .	127
9.1.1 Laser shock peening . . . . .	127
9.1.2 Cold-expansion of fastener holes . . . . .	130
9.2 Experiments . . . . .	131
9.2.1 Materials, specimens and neutron transmission setup . . . . .	131
9.2.2 Benchmark experiments . . . . .	139
9.3 Results . . . . .	141
9.3.1 Residual strain profiles for different peening parameters . . . . .	141
9.3.2 Mapping the residual strain in the developing LSP area . . . . .	143
9.3.3 Characterisation of the LSP process with high intensity and high coverage . . . . .	145
9.3.4 Residual strain mapping of LSP sample with complex geometries .	147
9.3.5 Comparison between shot, laser shock, and cavitation shot-less peening	149
9.3.6 Residual strain mapping around cold-expanded holes . . . . .	151
9.4 Discussion . . . . .	155
<b>10 Conclusions</b>	<b>157</b>
10.1 Conclusions . . . . .	157
10.2 Future work . . . . .	159
<b>References</b>	<b>161</b>
<b>Appendix A TPX_EdgeFit Manual for Bragg Edge Strain Mapping</b>	<b>175</b>
A.1 Overview . . . . .	175
A.2 Data Analysis . . . . .	176

A.2.1	Overlap correction . . . . .	176
A.2.2	Data scaling . . . . .	176
A.2.3	Transmission spectra . . . . .	178
A.2.4	Parameter initialisation . . . . .	179
A.2.5	Prepare flat files for normalisation . . . . .	180
A.2.6	Prepare the 'ParamFile' . . . . .	181
A.2.7	Run the TPX_EdgeFit Software . . . . .	183
A.2.8	Output of the data analysis . . . . .	183
A.3	Post-processing . . . . .	184
A.3.1	Create and apply mask . . . . .	184
A.3.2	Calculate strain . . . . .	185
A.3.3	Scale, colour profile and calibration bar . . . . .	186
A.3.4	Plot line profile of strain . . . . .	187
<b>Appendix B</b>	<b>BEATRIX Manual for Bragg Edge Strain Mapping</b>	<b>189</b>
B.1	Overview . . . . .	189
B.2	Data Analysis . . . . .	189
B.2.1	Accessing BEATRIX software . . . . .	190
B.2.2	Preparing the 'Global_Settings' file . . . . .	190
B.2.3	Run the data analysis . . . . .	193
B.3	Post processing . . . . .	193
<b>Appendix C</b>	<b>Publications</b>	<b>195</b>



# List of figures

2.1	Neutron generation through fission process . . . . .	7
2.2	Neutron generation through spallation process . . . . .	8
2.3	Comparison of the neutron intensity and the time structure of the neutron beam between a steady-state source and a pulsed source . . . . .	9
2.4	Illustration of pulse shape after moderation using coupled and decoupled moderator . . . . .	10
2.5	Interaction of neutrons with matter . . . . .	12
2.6	Comparison between thermal neutrons and X-rays . . . . .	13
3.1	Illustration to describe the time-of-flight (TOF) method . . . . .	21
3.2	Illustration of the diffraction phenomenon from a set of lattice planes . . . . .	21
3.3	Schematic of a neutron diffraction measurement at a continuous neutron source	22
3.4	Schematic of a neutron diffraction measurement at a pulsed neutron source	22
3.5	Neutron diffraction experiment for strain measurement at a pulsed neutron source . . . . .	25
3.6	Setup of a neutron transmission experiment . . . . .	27
3.7	Example of absorption, different types of scattering, Bragg reflection and total neutron cross section . . . . .	28
3.8	Bragg edges of iron (Fe) calculated using cross section values produced by <i>nxs</i> software . . . . .	29
3.9	Illustration of Bragg edge neutron transmission imaging principle . . . . .	31
3.10	Main components of a neutron transmission imaging system . . . . .	32
3.11	Schematic diagram of residual stress found on the cross section toughened glass in the absence of external load. . . . .	33
3.12	Stress component on three-dimensional element. . . . .	35
4.1	Illustration of gauge volume in neutron diffraction and neutron transmission setup. . . . .	38

4.2	Consideration of the sample geometry for neutron transmission experiment	41
4.3	Sample alignment in a neutron transmission experimental setup . . . . .	42
4.4	Calculated transmission spectrum of titanium . . . . .	43
4.5	Illustration of geometrical image unsharpness or blurring due to the beam divergence . . . . .	44
4.6	The effect of the interface between sample and other materials on the Bragg edge spectra . . . . .	45
4.7	Data structure of the time-of-flight (TOF) neutron transmission imaging experiment . . . . .	47
4.8	Example of Bragg edge fitting . . . . .	49
4.9	Illustration of Bragg edge parameter map reconstruction. . . . .	51
4.10	Typical algorithm of Bragg edge parameter mapping. . . . .	53
5.1	Schematic of ISIS pulsed neutron source with the neutron and muon beamlines.	59
5.2	IMAT extension building to R80 experimental hall. . . . .	60
5.3	Overall overview schematic of the IMAT beamline. . . . .	60
5.4	Schematic of the neutron generation and moderation at ISIS. . . . .	62
5.5	Schematics of the beam transport system and the beam defining components.	63
5.6	Photograph of choppers in operation on IMAT beamline . . . . .	64
5.7	Photograph of the pinhole selector wheel and the retractable slits on IMAT beamline . . . . .	65
5.8	Photograph of the sample positioning system (SPS), camera positioning system (CPS) and the sample area of IMAT. . . . .	66
5.9	Exploded view of the main components and photograph of MCP detector on IMAT . . . . .	67
5.10	Schematic of the main components and photograph of the Messina camera box on IMAT . . . . .	70
5.11	IBEX Graphical User Interface to control IMAT instruments and cameras. .	71
5.12	The interface of the Neutron Imaging ISIS plugin on ImageJ. . . . .	72
6.1	Experimental setup of calibration experiment. . . . .	77
6.2	Example of transmission spectrum measured from a calibration sample and corresponding calibration points. . . . .	79
6.3	Pulse width and resolution function of IMAT instrument . . . . .	81
6.4	Experimental setup of spatial resolution measurement . . . . .	83
6.5	Radiographs of Siemens Star attached to an Fe rod, taken with different sample-to-detector distance $l$ (thus different geometrical blurring $d_b$ ) . . . . .	84

6.6 An example of the analysed sharp edge of the Siemens Star with the corresponding ESF and MTF . . . . .	84
6.7 The relation between geometrical blurring $d_b$ and the spatial resolution . . . . .	85
6.8 Flight path measurement of IMAT at different location across the detector. . . . .	86
7.1 Bragg edge and Bragg diffraction peaks of Al2024 . . . . .	90
7.2 Comparison between different Bragg edge fitting functions. . . . .	93
7.3 Changes in Bragg edge shape due to crystallographic texture. . . . .	95
7.4 Illustration of the steps of performing the cross-correlation-based Bragg edge analysis. . . . .	96
7.5 Cross correlation analysis on textured Bragg edge. . . . .	97
7.6 Photographs of high temperature experiment. . . . .	100
7.7 Setup of high temperature experiment on IMAT, with simultaneous measurement of CeO <sub>2</sub> and Fe powders. . . . .	101
7.8 Setup of neutron transmission (red lines and arrows) and neutron diffraction (blue dots and arrows) measurements on an AlSiC <sub>p</sub> metal matrix composite. . . . .	103
7.9 Transmission spectra of Fe powder at different temperature. . . . .	105
7.10 Transmission spectra of rolled Al plate at different temperature. . . . .	105
7.11 Statistical quality of Fe {111} Bragg edges, measured using different macro-pixel sizes. . . . .	106
7.12 Strain uncertainty analysed from the Fe {110} as a function of effective measurement time. . . . .	107
7.13 Lattice parameters of Fe, CeO <sub>2</sub> , and Al powders as a function of temperature. . . . .	109
7.14 Thermal lattice strains $\Delta a/a_0$ of Fe and CeO <sub>2</sub> analysed using cross-correlation and Bragg edge fitting methods. . . . .	110
7.15 Thermal lattice strain of the rolled aluminium plate, analysed from texture-affected Al {111} Bragg edge using the cross-correlation method and the Bragg edge function fitting method. . . . .	111
7.16 Example of the masking process of CeO <sub>2</sub> data. . . . .	112
7.17 Spatial resolution as a function of macro-pixel size. . . . .	112
7.18 Bragg edge height maps of Siemens Star edge behind the Fe rod with corresponding ESF and MTF. . . . .	114
7.19 Spatial resolution of a Bragg edge map as a function of macro-pixel size, reconstructed from data with different geometrical blurring values $d_b$ . . . . .	115
7.20 Residual strain map of AlSiC <sub>p</sub> metal matrix composite and comparison with neutron diffraction result. . . . .	116

8.1	Photograph, illustration, and result of Bragg edge texture mapping experiment	123
8.2	Neutron transmission imaging and EBSD results for validation, from Sun et al. (2018)	123
8.3	Transmission spectra and radiographs of a rolled Al plate at different temperature, showing recrystallisation.	125
8.4	Temperature parameter $Y$ of Fe at different temperatures through Bragg edge analysis, compared with literature values.	126
9.1	Schematic and illustration of residual stress generation of laser shock peening process.	128
9.2	Illustration of cold-expansion process.	131
9.3	Experimental setup of the neutron transmission for laser peened 2024-T351 aluminium alloy sheets with sample aligned to measure strain in x-axis direction.	133
9.4	Experimental setup of the neutron transmission for laser peened 2024 aluminium plates with sample aligned to measure strain in the x-axis direction.	134
9.5	Experimental setup of the neutron transmission for laser peened 7050 aluminium blocks with sample aligned to measure strain in x-axis direction.	135
9.6	Experimental setup of the neutron transmission for the complex-shaped laser shock peened steel coupons.	136
9.7	Experimental setup of the neutron transmission for the peened steel coupons.	137
9.8	Experimental setup of the neutron transmission for the cold expansion samples.	138
9.9	Experimental setup of the neutron diffraction for the cold expansion samples.	140
9.10	Residual strain maps of laser shock peened Al2024-T351 thin plates, peened with different peening parameters.	141
9.11	Line profiles of strains extracted from the 2D strain map.	142
9.12	Strain comparison between incremental hole drilling and neutron transmission results.	143
9.13	Residual strain and Bragg edge height map of the laser shock peened Al2024 plates.	144
9.14	Residual strain map and energy-resolved radiography of the laser peened Al7050 blocks.	146
9.15	Line profiles of strains taken from the strain map of sample SA1 - SA5 and the comparison between transmission spectra of sample SA3 and SA5.	147
9.16	Reconstructed strain maps and line profile of strains of the complex-shaped, laser peened steel samples.	148

9.17 Reconstructed strain maps and line profile of strains of the 12%Cr steel coupons peened with different technique. . . . .	150
9.18 Residual strain map of cold-expanded and conventionally drilled hole, and comparison between Bragg edge transmission results and other strain measurement technique. . . . .	152
9.19 Residual strain maps of the drilled and cold-expanded holes on Al2024-T351 and Al7075-T651 plate. . . . .	153
9.20 Line profiles of residual strain measured using neutron diffraction on ENGIN-X beamline, and the comparison of the results with neutron transmission strain measurement. . . . .	154
A.1 Open beam region on sample and flat data set. . . . .	177
A.2 Example of spreadsheet containing transmission spectrum. . . . .	179
A.3 Pre-prepared EdgeFit spreadsheet for Bragg edge parameter initialisation. .	180
A.4 Example of spreadsheet file containing $I_0$ spectrum for transmission spectra normalisation. . . . .	181
A.5 ParamFile, the input parameter file for the TPX_EdgeFit software. . . . .	182
A.6 Creating and applying mask to highlight the region of interest. . . . .	185
A.7 An example of reconstructed strain map and line profile of strain. . . . .	186
B.1 Global_settings file of the BEATRIX software. . . . .	192
B.2 Output of the BEATRIX software opened with GUI-based TBrowser. . . . .	192



# List of tables

2.1	Neutron characteristics at different energy range (Herwig, 2009) . . . . .	6
4.1	Optimum sample thickness of different materials for the analysis of the first Bragg edge in transmission imaging experiment, calculated using Eq. (4.1)	42
5.1	IMAT instrument parameters for time-of-flight imaging as listed in (Kockelmann et al., 2018). The parameters written in blue are the ones validated in this work, presented and discussed in the following chapters. . . . .	58
6.1	Lattice parameters $\lambda_{hkl}$ and structure factors $F$ of the calibration samples used in the experiment, with the most intense Bragg edges indexed. The values are calculated using the <i>nxsPlotter</i> software (Boin, 2012). The product of $j * (\lambda_{hkl}^2  F ^2)$ , where $j$ is multiplicity, represents the Bragg edge height, with the values normalised to the most intense Bragg edges. . . . .	78
6.2	Results of calibration measurement using CeO <sub>2</sub> , Be, Al and Fe powder . . .	79
9.1	Summary of different sample sets prepared in the current work. All samples were measured on IMAT unless stated otherwise. . . . .	132



# Nomenclature

## Roman Symbols

$a$	Lattice parameter of cubic material ( $\text{\AA}$ )
$A_{\text{act}}$	Actual measurement/ detection area ( $\text{mm}^2$ )
$a_0$	Fitted constant of Bragg edge model
$a_{hkl}$	Fitted constant of Bragg edge model
$b_0$	Fitted constant of Bragg edge model
$b_{hkl}$	Fitted constant of Bragg edge model
$D$	Pinhole diameter (mm)
$d$	Lattice spacing ( $\text{\AA}$ )
$d_0$	Unstressed lattice spacing ( $\text{\AA}$ )
$d_b$	Geometrical blurring (mm)
$d_{hkl}$	Lattice spacing of a corresponding $\{hkl\}$ ( $\text{\AA}$ )
$E$	Young's Modulus (Pa)
$E_n$	Neutron energy (meV)
$\varepsilon$	Elastic strain ( $\mu\varepsilon$ )
$F$	Structure factor
$f_{hkl}$	Material parameter related to structure factor ( $\text{\AA}^2/\text{cm}$ )
$h$	Planck's constant = $6.6261 \times 10^{-34}$ Js

$I_0$	Incident neutron intensity
$I$	Attenuated neutron intensity
$I_{\text{base}}$	Base attenuation without coherent scattering
$K_1$	Fitted constant of Bragg edge model
$K_2$	Fitted constant of Bragg edge model
$L$	Pinhole-to-detector distance (mm)
$l$	Sample-to-detector distance (mm)
$L_f$	Flight path (m)
$m_n$	Neutron mass = $1.67 \times 10^{-27}$ kg
$N$	Number of nuclei per unit volume
$n$	Number of unit cell per unit volume
$R(\beta)$	Ratio between the number of crystallites in the sample with plane normal making an angle $\beta$ with the incident beam, compared to that in material with random texture.
$T$	Temperature (K)
$t$	Neutron time-of-flight (s)
$\Delta t_0$	Time offset of the source trigger received by the data processing electronics
$t_{\text{act}}$	Actual measurement time (hour)
$t_{\text{eff}}$	Effective measurement time (hour)
$Tr$	Transmission
$\nu$	Poisson's ratio
$V_0$	Volume of unit cell ( $\text{m}^3$ )
$v_n$	Neutron velocity ( $\text{ms}^{-1}$ )
$W$	Debye-Waller exponent
$Y$	Temperature parameter of Debye-Waller factor

$y$  Correlation coefficient

$z$  sample thickness (mm)

### Greek Symbols

$\beta_{hkl}$  Angle between  $\{hkl\}$  normal to the incident beam

$\lambda$  Neutron wavelength ( $\text{\AA}$ )

$\lambda_{hkl}$  Bragg edge wavelength position of corresponding  $\{hkl\}$  ( $\text{\AA}$ )

$\mu$  Attenuation coefficient ( $\text{cm}^2$ )

$\rho$  Bragg edge height

$\sigma$  Instrument-Sample dependent edge broadening parameter of Bragg edge model

$\Sigma_m$  macroscopic cross section ( $\text{cm}^2$ )

$\sigma_0$  Attenuation contribution other than elastic coherent scattering at the Bragg edge wavelength position of the corresponding  $\{hkl\}$  planes

$\sigma_{ij}$  Stress tensor (Pa)

$\sigma_m$  microscopic cross section (barn)

$\sigma_{\text{abs}}$  absorption (microscopic) cross section (barn)

$\sigma_{\text{Bragg}}$  Bragg (microscopic) cross section (barn)

$\sigma_{\text{coh-inel}}$  coherent-inelastic (microscopic) cross section (barn)

$\sigma_{hkl}$  Elastic coherent cross section at the Bragg edge wavelength position of the corresponding  $\{hkl\}$  planes

$\sigma_{\text{inc-el}}$  coherent-inelastic (microscopic) cross section (barn)

$\sigma_{\text{inc-inel}}$  coherent-inelastic (microscopic) cross section (barn)

$\sigma_{\text{tot}}$  total (microscopic) cross section (barn)

$\tau$  Decay constant, moderator dependent edge broadening parameter of Bragg edge model

$\theta$  Diffraction angle (degree)



# Chapter 1

## Introduction

### 1.1 Background

Standard neutron transmission imaging using ‘white beam’ is a well-established non-destructive measurement technique which has been proven to be useful in a broad range of research areas from biology (Watkin et al., 2009; Nakanishi, 2009), archaeology (Deschler-Erb et al., 2004; Andreani et al., 2009; Lehmann et al., 2010; Van Langh et al., 2011; Schillinger et al., 2018), material science (Penumadu, 2009; Kardjilov et al., 2011), and engineering (Penumadu, 2009; Banhart et al., 2010). The technique mainly takes advantage of the high penetrability of the neutron beam and its unique absorption and scattering cross section which, unlike for X-rays, are non-proportional to the atomic numbers. While white-beam (energy-averaged) neutron imaging is a powerful tool for research, a lot more information can be extracted by performing measurement at a range of neutron energies. The technique is so-called energy-resolved neutron imaging, and it comprises all techniques requiring a measurement of a transmission spectrum as a function of energy.

One particular energy-resolved imaging methods which becomes of interest to researchers in engineering and material science is Bragg edge imaging. A Bragg edge is a distinct signal in the transmission spectrum of a neutron beam that traverses polycrystalline material. Bragg edges occur because of the back-scattering phenomena: for a given  $\{hkl\}$ , Bragg angle,  $\theta$ , increases as the neutron wavelength increases until  $2\theta$  is equal to  $180^\circ$ . Above this critical value, the  $\{hkl\}$  lattice spacings no longer contributes to the scattering, resulting in a sharp increase in the transmission. The position of these edges can be used to determine the lattice spacing of the corresponding  $\{hkl\}$ . Accurate determination of lattice spacing and its utilisation to measure applied and residual stress through Bragg edge analysis has been reported previously (Steuwer et al., 2001, 2003). Texture and phase information in a material can also be obtained through analysis of these Bragg edges (Vogel, 2000; Santisteban et al.,

2001; Steuwer et al., 2005; Woracek et al., 2015). These demonstrate the potential of the technique for engineering studies.

With the geometrical advantage of neutron transmission and by using a position sensitive detector, the material properties mentioned above can be mapped across a bulk sample. This provides location-specific microstructural information, averaged along the transmission direction. The proof-of-concept of this has been provided more than 15 years ago (Santisteban et al., 2002a,b; Iwase et al., 2009, 2012; Strobl et al., 2012). Despite its potential, so far there are only a few applications of Bragg edge strain mapping (Tremsin et al., 2016a,b; Sun et al., 2018). They have only emerged in recent years, encouraged by the development of a high-spatial-resolution neutron imaging detector (Tremsin et al., 2013). Therefore, Bragg edge strain mapping is relatively less developed, i.e., standardised data analysis routines for this technique in various imaging beamlines around the world have not been established, and the output from this method is not well-characterised. Additionally, there is scope for Bragg edge imaging analysis to be extended beyond strain mapping.

Nevertheless, the versatility of this technique encouraged the development of the new imaging and materials science (IMAT) beamline at the ISIS pulsed neutron source, UK (Kockelmann et al., 2018). Recently, this beamline has gone through commissioning and has started its user program in March 2018. The potential use of the IMAT beamline, ranging from engineering samples to archaeological objects, has been explored (Minniti et al., 2016), and a particular application of energy-selective neutron imaging to investigate biological samples on IMAT has been presented by Vitucci et al. (2018a). The instrument parameters such as beam flux, beam profile and spectral resolution have been characterised (Minniti et al., 2018) without, however, performing the evaluation of Bragg edge transmission and imaging analysis on the instrument.

## 1.2 Motivation

This thesis is prepared to bridge some of the knowledge gaps i) in the development of Bragg edge imaging, including improvement of data analysis, characterisation of the result, and demonstration of the capability of the method, and ii) in the development of the new IMAT imaging beamline, as mentioned above. The objectives of this work are as follows:

1. To develop the data analysis aspect of Bragg edge imaging. This includes assessment and evaluation of existing data analysis methods. There are currently different approaches available for analysing Bragg edge transmission spectra, i.e., single and multiple Bragg edge fitting. Different analytical functions are also available to describe a Bragg edge. This work describes each method, highlights the advantages of each,

and provides recommendations on the most reliable and efficient method to be used for Bragg edge strain mapping. This work also explores a new approach in Bragg edge analysis to solve problems currently faced by existing methods.

2. To characterise the IMAT instrument parameters, especially those which are fundamental for Bragg edge imaging. Accurate definition of instrument parameters such as flight path and wavelength and spatial resolution determines the quality of the measurement result. This work provides the values of those parameters at the current state of the IMAT instrument. The calibration experiments are described in some detail as a reference for the future users.
3. To evaluate and validate the Bragg edge strain mapping results of the IMAT instrument. IMAT is a newly-constructed beamline and therefore validation of the data produced from the instrument is essential. It is also important to evaluate the performance of the instrument in carrying out measurements, e.g., the level of accuracy and uncertainty.
4. To extensively demonstrate the application of Bragg edge strain mapping and crystallographic analysis for engineering applications. This work provides various examples of Bragg edge strain mapping applications and highlights the advantages offered by the technique. This is aimed to encourage more engineering application of Bragg edge imaging.

Many of the experiments performed in this work were done for the first time on the IMAT instrument, and were done as part of IMAT commissioning. Among them are the first time use of MCP detector on IMAT, the first time use of a high temperature equipment on IMAT, one of the first users to use the sample positioner system and other equipment, as well as running experiments without initially knowing the instrument parameter. This is noteworthy since it highlights the contribution of this work in establishing Bragg edge imaging on IMAT.

The structure of the thesis is as follows. Chapter 2 introduces the principle of the neutron probe, including their properties, generation, and modes of detection. More importantly, the chapter describes the interaction of neutron with matter, understanding of which is fundamental for using neutrons for material analysis. Different experimental methods utilising neutrons are then described. Chapter 3 describes the principle of Bragg edge neutron transmission imaging in some detail. The concept of the time-of-flight (TOF) method is introduced. Prior to the description of Bragg edge neutron transmission, neutron diffraction is mentioned owing to its direct contribution to transmission. The spatial mapping part of the neutron transmission is then described. Chapter 4 provides the description of experimental

design considerations and detailed description of each stage of the data analysis method for Bragg edge imaging. Researchers who wish to use the Bragg edge imaging technique for strain mapping for the first time will find Chapter 3 and 4 informative to understand the principles and conception of the experiment. Chapter 5 presents a description of the IMAT beamline, which serves as an example of instrumentation of a time-of-flight neutron imaging beamline. IMAT design considerations, instrument components, imaging detectors and analysis software are described. Chapter 6 provides a validation of the IMAT parameters which are important for Bragg edge imaging applications, namely flight path, wavelength resolution and spatial resolution. Chapter 7 specifically describes the development of Bragg edge strain mapping on IMAT, starting from the assessment of different analytical functions, introduction of a novel Bragg edge analysis method, description of the commissioning experiments, and definition of the performance of Bragg edge strain measurement and strain mapping on IMAT. Future IMAT users can refer to Chapter 6 and 7 for designing their experiments and preparing their proposal. Chapter 8 presents the extension of Bragg edge analysis beyond strain mapping, where it is used to produce crystallographic texture maps and to perform Debye-Waller factor analysis. The main work of Chapter 6 to 8 has been published by the author in a journal publication (Ramadhan et al., 2019). Finally, Chapter 9 presents the Engineering application of Bragg edge imaging, not only on IMAT instrument but also on other imaging beamlines. Examples of residual strain measurements on various engineering components are presented, and the advantages and the limitations for the technique, as well as comparison with other more established techniques, are provided. Some of the materials in Chapter 9 have been published by the author in a journal publication (Ramadhan et al., 2018). Engineers, scientists, and the general reader who are interested in neutron application may find Chapter 9 interesting. The main findings of this work are then summarised in Chapter 10.

This work is a collaboration between Coventry University and ISIS neutron source, with the support of the University of California at Berkeley in the MCP detector development and operation. The PhD project was funded by the ISIS Facility Development Studentship, and therefore justify the strong emphasis of the thesis towards the facility development aspect of the research.

# **Chapter 2**

## **Introduction to Neutrons for Materials Analysis**

This chapter provides the basic understanding of the neutron and how it is used for materials analysis. Firstly, the fundamentals of the neutron such as its properties, generation, moderation and detection are presented. Then the interaction between neutrons and matter, as the basis of using neutrons for material analysis, is described. Finally, different experimental methods that utilise neutrons for material characterisation are discussed.

### **2.1 Neutron fundamentals**

#### **2.1.1 Neutron properties**

The neutron is a subatomic particle which constitutes the nucleus of an atom, together with the proton. Since their discovery by English physicist James Chadwick in 1932, neutrons have played important roles in shaping many technological developments we know today. While the fission of heavy elements due to bombardment of neutrons led to the creation of the atomic bomb, the breakthrough also resulted in the generation of electric power through nuclear fission. Excess neutrons from a nuclear reactor are commonly used to produce radioactive isotopes, which are useful for a wide variety of fields ranging from medicine and pharmacology to industry and technology. Neutrons have also become a powerful tool for scientific research, especially for determination of structural details and atomic arrangements in materials.

One of the signature properties of neutrons that makes them very useful in scattering and imaging applications are their electrical neutrality (Herwig, 2009). Since neutrons have zero charge, they interact primarily with the nuclei of atoms. This neutrality gives neutrons

Table 2.1 Neutron characteristics at different energy range (Herwig, 2009)

This item has been removed due to third party copyright. The unabridged version of the thesis can be viewed at the Lanchester library, Coventry University

their high penetration ability: neutrons penetrate through the gaps between nuclei that are far greater (100,000 times greater) than the size of the nucleus itself (Pynn, 2009). As a result, neutrons can be used to probe into the interior of large components and assemblies, non-destructively.

Another fundamental property of the neutron is its mass of  $m_n = 1.67 \times 10^{-27}$  kg. This mass gives the thermal neutron (a neutron with energy comparable to the energy of particles at room temperature) a de Broglie wavelength on the order of the atomic distances of condensed matter. This allows Bragg scattering from crystal lattices and is especially important for studying polycrystalline materials. The de Broglie wavelength  $\lambda$  is given by Eq. (2.1) where  $h = 6.6261 \times 10^{-34}$  Js is Planck's constant and  $v_n$  is the neutron velocity:

$$\lambda = \frac{h}{m_n v} \quad (2.1)$$

The relation between neutron velocity and neutron energy  $E_n$ , is given by Eq. (2.2). Neutrons can be loosely classified according to their energy, starting with ultra-cold neutrons being the lowest and epithermal neutrons being the highest. Neutron characteristics, i.e., velocity and wavelength at different energy ranges are presented in Table 2.1.

$$E_n = \frac{1}{2} m_n v_n^2 \quad (2.2)$$

Other properties with less significance to the current work are the neutron's intrinsic spin of  $\frac{1}{2}$  and nuclear magnetic moment of  $-0.9662 \times 10^{-26}$  J T<sup>-1</sup>. These properties cause neutrons to respond to external magnetic fields and allow them to interact with the magnetic moments of atoms (Herwig, 2009).

### 2.1.2 Neutron generation

Neutrons for research purposes are generated in two types of neutron sources: nuclear fission reactors (steady-state) and neutron spallation (pulsed) sources. In reactor sources, the neutrons are produced through the fission process. Neutron generation through fission is illustrated in Fig. 2.1. Fission happens when the nucleus of a heavy metal such as uranium-235 is hit by a neutron with thermal energy, splits into two, and releases energy while also producing two or three additional neutrons. In a nuclear reactor, some of the released neutrons produce an additional fission, causing a sustainable chain reaction. Neutrons escaping from the system become the neutron source. They are then slowed down through a moderation process, described later in **Section 2.1.3**, and used for scattering experiments. Examples of nuclear research reactors that act as neutron sources are the High Flux Isotope Reactor (HFIR) in Oak Ridge, United States; the High Flux Reactor (HFR) at the Institut Laue-Langevin (ILL) in Grenoble, France; FRM-II in Munich, Germany; OPAL at the Australian Nuclear Science and Technology Organisation (ANSTO); and the High Flux Advanced Neutron Application Reactor (HANARO) at the Korea Atomic Energy Research Institute (KAERI).

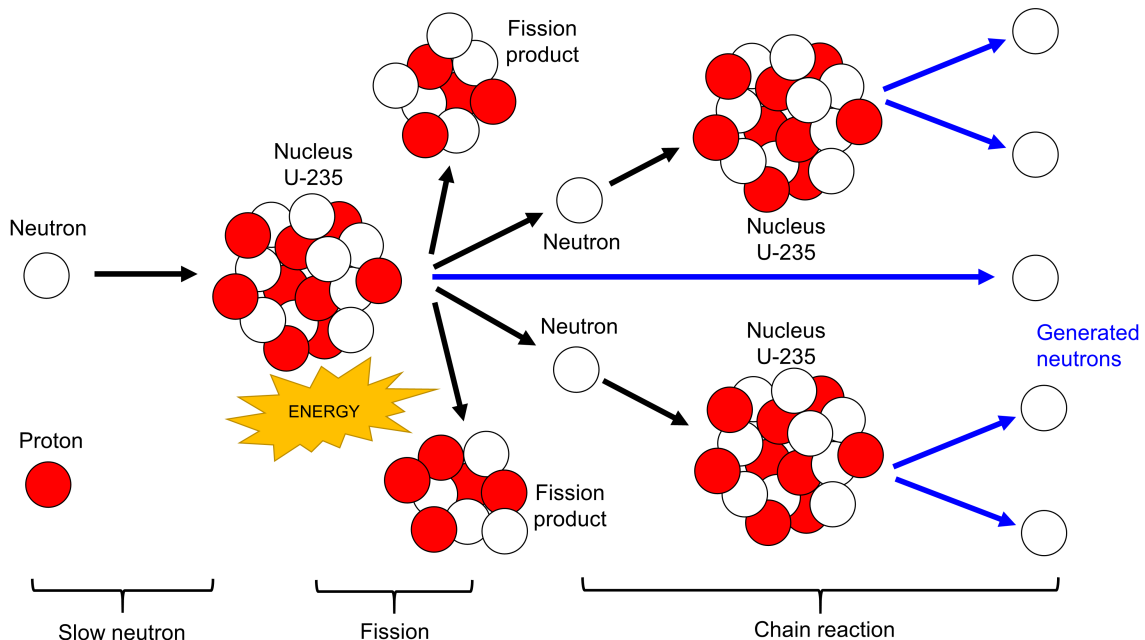


Fig. 2.1 Neutron generation through fission process, adapted from Filges and Goldenbaum (2010)

Neutrons can also be produced through a spallation process, illustrated in Fig. 2.2 where high energy particles (e.g., protons) bombard a heavy metal "target" (e.g., uranium, tungsten, tantalum). Spallation can be divided into two stages. In the first stage, the high-energy

primary particles hit the nucleons (neutrons and protons) of the target nucleus. This creates an intra-nuclear cascade, where secondary particles (neutrons, protons and pions) either escape and induce further spallation, or store their kinetic energy in the nucleus and leave the nucleus in an excited state. In the second stage, the excited nucleus "evaporates" and emits low-energy particles with the majority being neutrons (Russell, 1990). Spallation sources are generally built into four parts: (1) accelerator, (2) target, (3) neutron beamline, and (4) sample environment and detectors (Filges and Goldenbaum, 2010). In the accelerator, protons are pulled along the accelerator by switching the electric fields at a certain frequency. Accelerated protons in "bunches" hit the target and neutrons are produced. The high-energy neutrons are moderated before being directed to beamlines for scattering experiments. Example of spallation sources are ISIS at the Rutherford Appleton Laboratory, United Kingdom; SINQ at the Paul Scherrer Institut (PSI), Switzerland; Japan Proton Accelerator Research Complex (J-PARC); the Spallation Neutron Source (SNS) at Oak Ridge and the Los Alamos Neutron Science Centre (LANSCE), United States.

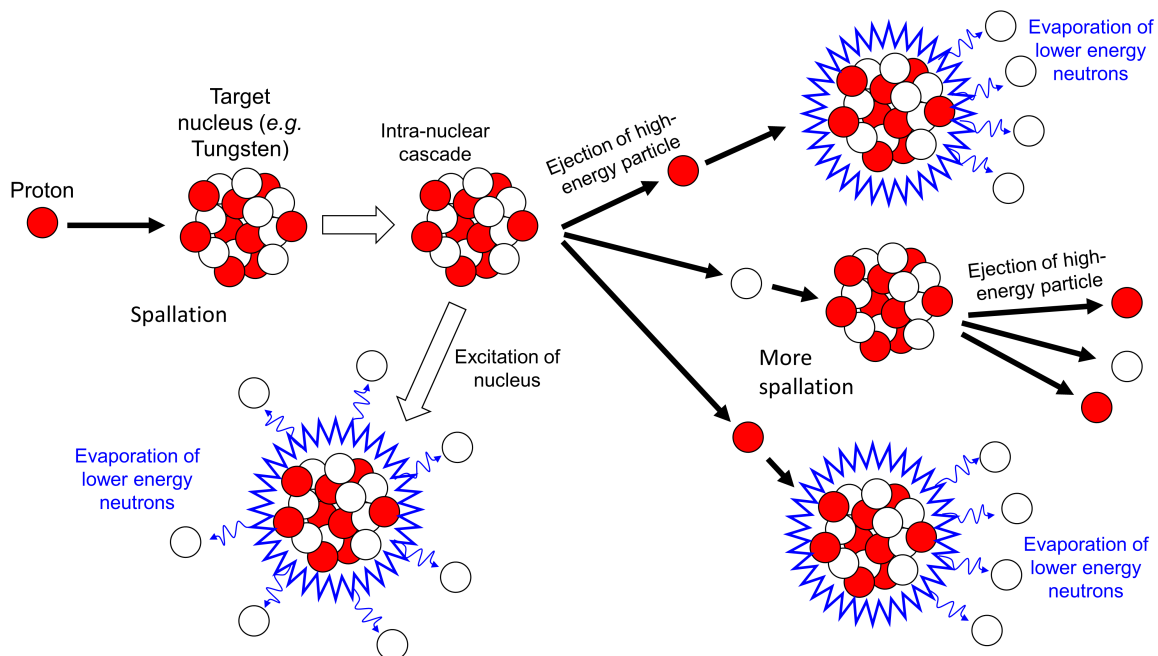


Fig. 2.2 Neutron generation through spallation process, adapted from Russell (1990)

The main differences between steady-state reactor sources and pulsed sources are in the neutron flux and the time structure of the neutron beam (Filges and Goldenbaum, 2010). While peak flux in the most intense spallation sources is comparable to the flux of steady state reactors, the average flux in reactor sources is much higher by approximately two orders of magnitude (de Novion, 2003), as illustrated in Fig. 2.3. However, since neutron scattering experiments need precise determination of neutron wavelengths, neutron monochromatisation

is required (by means of Bragg scattering using a monochromator crystal or by using mechanical choppers) at reactor sources. Monochromatization requires a trade-off between high resolution and high neutron intensity. On the other hand, at a pulsed source, the determination of kinetic energy (thus wavelength) of individual neutrons is possible using a "time-of-flight" (TOF) method (Filges and Goldenbaum, 2010). This makes pulsed neutron sources inherently suitable for energy-resolved and energy-dispersive neutron scattering experiments.

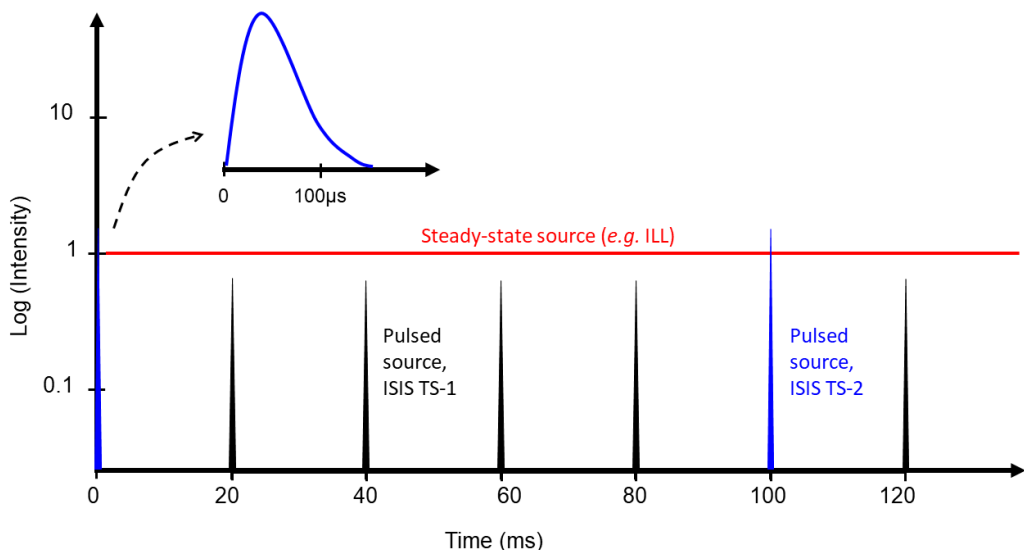


Fig. 2.3 Comparison of the neutron intensity and the time structure of the neutron beam between a steady-state source (e.g., ILL) and a pulsed source e.g., ISIS Target Station 1 (TS-1) and Target Station 2 (TS-2), adapted from Andersen (2013)

### 2.1.3 Neutron moderation

Neutrons that are produced from either fission or spallation have energies in the range of tens to hundreds of MeV, a range of energy that is too high to be used for neutron scattering experimentation. In order to reduce the energy to tens to hundreds of meV, neutrons from the source need to be slowed down. Since the neutron has no charge, its kinetic energy can only be decreased by the means of collision with other atoms (Vogel, 2000). This is performed by guiding the neutrons to a moderator material such as H<sub>2</sub>O, H<sub>2</sub>, D<sub>2</sub>O, or methane (usually in liquid or solid form). This process is called moderation.

There are a few factors that need to be considered in moderating neutrons, especially in a pulsed spallation source where the neutron pulse needs to be kept sharp. Since the time spent

by the neutron in the moderator broadens the pulse, factors such as moderator thickness and the presence of a decoupler (explained below) inside the moderator determine the sharpness of the pulse. A thin moderator reduces the time spent by the neutron in the moderator, and therefore sharpens the pulse, but at the expense of lower neutron flux and peak intensity (Burca, 2012). Reflectors are usually placed around the target and moderator to reflect the non-moderated, the partially-moderated, and the moderated neutrons leaving the moderator in directions other than the instrument port, back into the moderator to be further slowed down. This increases the time spent by the neutron in the moderator and thus broadens the pulse. An absorbing material (decoupler) can be placed to reduce the number of reflected neutrons, and prevent extra broadening (Arai and Crawford, 2009). The decoupling, however, also reduces the total intensity of the neutron pulse, Fig. 2.4.

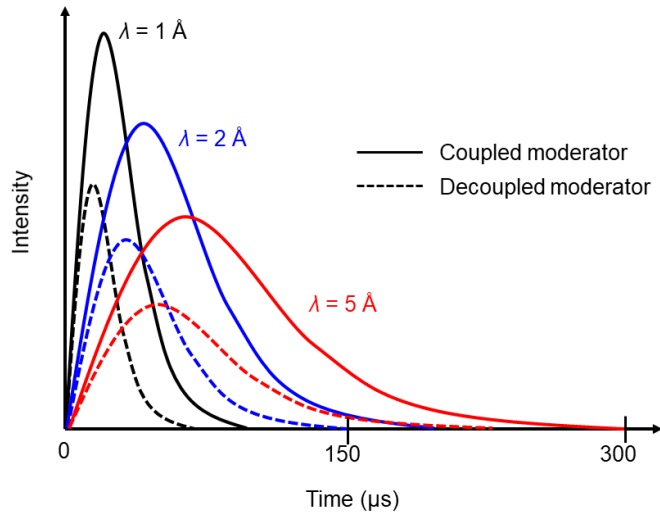


Fig. 2.4 Illustration of pulse shape after moderation using coupled and decoupled moderators. A decoupled moderator produces a relatively sharper pulse at the expense of lower neutron intensity. Adapted from (Andersen, 2013).

## 2.1.4 Neutron detection

For neutron scattering experiments, neutron detection holds as important a role as neutron generation itself. Recent developments in detector technologies have allowed new experimental techniques to be performed on neutron beamlines. Neutron detection is a whole research field in itself and therefore only the very basic points will be covered in this section,

including how neutrons can be detected, types of data acquisition, and examples of neutron detectors.

Neutrons, which have zero charge, cannot be directly detected electronically. While neutrons with high kinetic energy can ionise materials and produce electrical signals, thermal neutrons cannot. To produce a signal, thermal neutrons need to be converted to charged particles. This is normally done via a neutron capture reaction: the neutron is absorbed by materials such as  $^{10}\text{B}$ ,  $^3\text{He}$ ,  $^6\text{Li}$ , or  $\text{Gd}$ , which in turn produce charged particles and gamma rays (Crow, 2009). These charged particles can then be monitored in either integrating or counting mode. In integrating mode, individual neutron events are not distinguished, and rather accumulated in a single data/frame. In counting mode, meanwhile, each neutron event can be readout and registered, allowing the detected neutrons to be stored as a stack of data as a function of time-of-flight. The counting mode is used in the majority of neutron scattering experiments.

There are four main types of neutron detectors: 1) photographic film detectors, 2) scintillator detectors, 3) gas detectors, and 4) solid-state detectors:

1. Photographic film is an analogue detector which only works in signal integrating mode. It captures the trace of neutrons and records it onto X-ray film, either directly (particle emission from the neutron capture process directly illuminates the film) or indirectly (an irradiated screen with short-lived activation material is removed from the beam and placed in contact with the film).
2. Scintillator detectors use a material which absorbs ionising radiation and emits low-energy photons. A neutron scintillator requires a converter to generate the charged particles, via neutron capture reaction or internal conversion electrons (Crow, 2009). Materials such as cerium-activated  $^6\text{Li}$  glass are intrinsic scintillators where converter atom and phosphor are part of the same material, while binary scintillators (created by mixing converter and phosphor particles) such as  $^6\text{LiF}/\text{ZnS}$  have also been used. The emitted photons are subsequently readout using film or a charge-coupled device (CCD) camera, or fed into photo-multipliers (PMTs) to allow neutron counting detection.
3. Gas detectors consist of a metal cylinder with a thin wire anode filled with isotope-enriched gas. The neutron is absorbed, for example by  $^3\text{He}$  or  $^{10}\text{B}$ , and produces fast charged particles that are detected as an electric pulse at the anode.
4. In solid-state detectors, charged particles produced from neutron capture, enter a biased semiconductor device and produce a pulse which is then registered by readout counting electronics (Crow, 2009). Another example of a solid-state detector is a micro-channel

plate (MCP) detector, which is capable of neutron detection with high spatial and temporal resolution (Tremsin et al., 2011).

## 2.2 Interaction of neutrons with matter

### 2.2.1 Neutron cross section and neutron attenuation

Understanding the interaction of neutrons with matter is the key to using neutrons for materials analysis. As mentioned before, neutrons mainly interact with the nucleus of atoms. When an incident neutron beam passes through a material, one of the following situations can occur: 1) Absorption, where a neutron hits the atom nucleus and is absorbed. The nucleus is excited and  $\gamma$  particles are produced; 2) Scattering, where a neutron hits the atomic nucleus and is scattered with a given probability in any direction; 3) Transmission, where the neutron does not interact with the nuclei and traverses the material. These are illustrated in Fig. 2.5.

This item has been removed due to third party copyright. The unabridged version of the thesis can be viewed at the Lanchester library, Coventry University

Fig. 2.5 Interaction of neutrons with matter: a neutron can be absorbed by the atomic nucleus and emits  $\gamma$  particles, scattered by the atom nucleus to any direction, or transmitted through the sample without interacting with the nuclei in the material. Inset shows the cross section,  $\sigma$ , which is the effective area presented by the nucleus to the passing neutron (Pynn, 2009).

The statistical quantity of the neutrons' interaction with matter is described as the neutron cross section. An effective area that is presented by a single nucleus to a passing neutron is described as the microscopic cross section,  $\sigma_m$ , measured in barns ( $1 \text{ barn} = 10^{-28} \text{ m}^2$ ), and illustrated in the inset of Fig. 2.5. If neutron hits this area, it will be either absorbed or scattered. Therefore the total microscopic cross section is described as  $\sigma_{\text{tot}} = \sigma_{\text{scattering}} + \sigma_{\text{abs}}$ . Meanwhile, the macroscopic cross section,  $\Sigma_m$  is described as the probability of

interaction between a neutron and bulk material. It has the formula of  $\Sigma_m = N\sigma_m$ , where  $N$  is the number of nuclei per unit volume. The macroscopic cross section is also known as the attenuation coefficient,  $\mu$ . Neutrons and X-rays are attenuated differently, and may often produce a complementary result when they are used for imaging. X-rays, which primarily interact with the electron shells of atoms, are attenuated more by elements with larger atomic number. Meanwhile, the attenuation of neutrons has less dependency on the atomic number of elements, as light materials such as hydrogen and lithium have high neutron attenuation coefficients, while most metals and heavy elements have relatively low neutron attenuation coefficients. This is illustrated in Fig. 2.6(a). Due to this difference, neutron imaging is suitable to investigate light elements (liquids, plastics, etc) inside metal enclosures, while X-ray imaging is more suited to imaging metal inclusion in other materials, Fig. 2.6(b).

This item has been removed due to third party copyright. The unabridged version of the thesis can be viewed at the Lanchester library, Coventry University

Fig. 2.6 (a) Comparison between mass attenuation coefficient (attenuation coefficient divided by density) of thermal neutrons and 100 keV X-rays, adapted from (Kardjilov et al., 2011); (b) Comparison between radiography taken by neutrons and X-rays. Neutrons show plastic components inside the metal camera body, while X-rays highlight the metal parts of the camera. From Koerner et al., (2000).

### 2.2.2 Neutron scattering

In a neutron scattering experiment, a neutron travels with a certain kinetic energy, hits a nucleus, and is then scattered. Assuming the nucleus is fixed and the neutron energy is too

small to change the internal state of the nucleus, the scattering occurs without any transfer of energy ( $\Delta E = 0$ ). This is called elastic scattering (Pynn, 2009). In reality, the atoms vibrate about their equilibrium position in a solid, allowing some energy transfer ( $\Delta E \neq 0$ ). This is called inelastic scattering.

Scattered neutrons from different nuclei can create constructive interference, and this is called coherent scattering. Elastic coherent scattering provides information about the equilibrium state of the material, for example the measure of lattice spacing of a crystalline material. Meanwhile inelastic coherent scattering provides information about the collective motions of the atoms (Pynn, 2009), for example the measure of atomic vibration of materials at high temperature, which will be discussed later. Neutrons can also be scattered by different nuclei without interfering with each other, and this is termed incoherent scattering. While elastic incoherent scattering often appears as unwanted background in scattering experiments, inelastic incoherent scattering can provide information about atomic diffusion (Pynn, 2009).

## 2.3 Neutron for materials analysis

### 2.3.1 Radiography and tomography

Neutron radiography and neutron tomography are two imaging techniques which take advantage of the neutron's penetrating depth and the attenuation of neutrons in different materials. Neutron radiography is the generation of a 2-D projection of an object by traversing neutrons. Neutrons are attenuated differently by different components of the object and recorded by a neutron detector. The projected image is then analysed through the contrast difference between its components. The high-penetrability of neutrons has been used to investigate inclusions within a titanium casting of thickness over 6.25 cm (Richards et al., 2004), which is otherwise inaccessible by other radiographic techniques such as X-rays. Meanwhile, the sensitivity of neutrons to the presence of hydrogen and the ability of neutrons to easily penetrate metals allows examinations of water distribution and flow in an operating fuel cell (Kramer et al., 2005; Manke et al., 2007; Chen et al., 2007). Neutron radiography has also been used to study water uptake of plants (Oswald et al., 2008). The availability of high-flux neutron sources enables measurements to be performed in a stroboscopic mode: a series of very short neutron exposures is triggered at a certain stage of a cyclic process e.g., a running combustion engine), and accumulated over long period. This has been demonstrated by imaging a combustion chamber of a car engine rotating at 1000 rpm (Schillinger et al., 2006).

Tomography is an imaging technique which produces three-dimensional spatially resolved images obtained by taking a set of projections from an angular interval of either  $180^\circ$  or  $360^\circ$

as an input for mathematical reconstruction (Kardjilov et al., 2011). Different algorithms such as back-projection, iterative and analytical methods are available as techniques to reconstruct the 3D distribution of attenuation coefficient in the sample volume of interest (Abd El Bar et al., 2015). Neutron tomography has been used for engineering purposes to visualize sedimentation of fuel and oil in a combustion chamber (Strobl et al., 2009). Neutron tomography, together with neutron radiography, has also been used extensively to non-destructively examine historical and archaeological objects, where neutrons can reveal different layers of materials and features which will give an insight of the historical production process and technology of the artefacts (Lehmann et al., 2005; Festa et al., 2008).

The ability to resolve neutron energy enables energy-selective and energy-dispersive imaging. Neutron attenuation of materials can vary depending on neutron energy, allowing different materials or different phases of the same materials to be distinguished (Kardjilov et al., 2003; Kockelmann et al., 2007). The latest development in neutron imaging revolves around Bragg edge imaging, which will be discussed later in this section.

### 2.3.2 Scattering-based methods

Neutrons scattered by an array of atoms can provide structural information of the corresponding material. There are different methods that use the scattering of neutrons for materials analysis: among them are neutron diffraction, small-angle neutron scattering (SANS), neutron reflectometry and inelastic neutron scattering.

Diffraction or Bragg scattering is one of the simplest types of coherent scattering. In this case it is assumed that the atoms are arranged at fixed positions in a lattice. Depending on the material, the scattered neutrons will constructively interfere with each other only in particular directions and produce an intensity pattern (so-called Bragg peaks) from which the structure of the material is derived. Single-crystal diffraction measures the Bragg reflections from a single crystal across different wavelengths or diffraction angles in order to reveal the crystallographic structure of materials (Koetzle and McIntyre, 2012). Powder diffraction is also a powerful tool to refine crystallographic structures by detecting the positions and intensities of the diffracted neutrons from powders with a range of crystallographic orientations (Copley, 2001).

Measurement of the position of Bragg peaks from neutron diffraction allows the determination of lattice spacings, while the measurement of the relative shift in the positions provides information on lattice strains (Hutchings, 1992). Neutron diffraction has become a well-established strain measurement technique with an ISO standard available (ISO/TS 21432:2005, en) and specialised neutron diffraction instruments for stress measurement in engineering samples such as ENGIN-X (Santisteban et al., 2006a) are readily accessible.

Meanwhile, recording diffraction patterns as a function of the scattering angle by either rotating the sample or using a multi-detector setup around the sample enables determination of crystallographic texture (Kockelmann et al., 2006).

Investigation of larger structures (polymers, colloids or viruses) with dimension of tens to hundreds of Angstroms can be performed by decreasing the scattering angle. This technique is called small-angle neutron scattering (SANS) (Pynn, 2009; Hannon, 2010). Meanwhile, neutron reflectometry is another technique where neutrons are impinged on a smooth, flat surface at very small angles of incidence. The presence of layered material over the surfaces can be detected from the variation of the neutron reflectivity (Pynn, 2009). In inelastic neutron scattering, the atom is considered to move about its equilibrium position, causing an energy exchange between the atom and the neutron. By measuring the wave-vector of neutrons before and after the scattering event, the dynamic motion of the atoms (in terms of energy) can be determined (Pynn, 2009).

### 2.3.3 Diffraction in neutron transmission

It has been mentioned that as the neutrons pass through a material, some of them will be removed from the beam through absorption or scattering. The remaining neutrons traverse the sample and can be recorded by a detector, positioned directly in the incident beam propagating direction, as a neutron transmission signal (Priesmeyer, 2003). Since the scattering contributes to the attenuation, traces of the scattering persist in the transmission signal (Woracek et al., 2018). Therefore the analysis of this signal can provide similar information presented by conventional neutron diffraction such as lattice spacing and crystallographic texture. A neutron transmission signal with scattering signature is referred to as a Bragg edge spectrum (or Bragg-dip for the signal from single crystals). One of the advantages of the transmission geometry is that the spatial information is preserved. This allows neutron transmission, in conjunction with a suitable neutron detector (i.e., a position sensitive detector), to be used as an imaging technique where information such as lattice spacing and texture can be mapped in 2-D or even 3-D across the sample.

Bragg edge neutron transmission for strain measurement was proposed and demonstrated over 15 years ago (Vogel, 2000; Steuwer et al., 2001). However, the application of the technique for strain mapping was developed only recently due to advances in high spatial-resolution micro-channel-plate (MCP) detector technology. A small number of studies have been conducted in using Bragg edge transmission to produce 2-D strain maps in engineering components such as residual strain measurement in aerospace components (Ramadhan et al., 2018), self-locking threads (Tremsin et al., 2016a) and welded joints (Tremsin et al., 2016b; Sun et al., 2018), as well as applied strain measurement on steel under *in-situ* tensile loading

(Woracek et al., 2011). An effort to produce 3-D strain tomography has also been performed for special geometries (Hendriks et al., 2017; Sato et al., 2015; Abbey et al., 2012), although the ill-posed problem for strain tomography has been highlighted (Lionheart and Withers, 2015). Beside strain mapping, Bragg edge transmission has also been used to perform microstructure evaluation (Sato et al., 2015, 2011) as well as texture and phase analysis (Sato et al., 2017; Sun et al., 2018; Woracek et al., 2015; Makowska et al., 2016).

While there is a wide range of applications of neutrons for material science, the next chapters in this text will focus on Bragg edge neutron transmission imaging for strain mapping and crystallographic analysis, with emphasis given to evaluation of aerospace materials and aerospace components. In the next chapter, the principles of Bragg edge neutron transmission will be described in more detail.



# **Chapter 3**

## **Bragg Edge Neutron Transmission Imaging**

This section presents the principles of Bragg edge neutron transmission imaging, providing the basics of how the method can be used for materials analysis. The time-of-flight (TOF) method is important in understanding the transmission spectra and therefore is described in the first section. Next, neutron diffraction is described in detail due to its direct contribution to the Bragg edge transmission signal and its position as a complementary experimental technique to neutron transmission. Bragg edge neutron transmission is discussed, which covers the setup, interpretation of transmission spectra and generation of Bragg edges, as well as the principle of Bragg edge analysis and parameterisation. Finally, the imaging part of the Bragg edge neutron transmission is described.

### **3.1 Time-of-flight method**

Bragg edge transmission and energy-selective imaging studies require a sufficiently high resolution of energy (and thus wavelength) determination. As described by Kockelmann et al. (2007), the wavelength selection of neutrons for imaging can be achieved by one of the following possibilities:

1. Using a single crystal monochromator, where a polychromatic neutron beam is Bragg reflected to define a certain wavelength band. This practice is commonly found at continuous neutron sources.
2. Using turbine-type energy selectors or choppers. Choppers have one or more rotating disks made of neutron absorbing material with at least one aperture. Only neutrons

with a certain energy (thus certain velocity) can pass through the aperture, and therefore the energy band can be tuned.

3. Make use of the time structure of a pulsed source and determine the neutron energy via the time-of-flight (TOF) method. Since this text focuses on a pulsed source beamline, the TOF method will be discussed in more detail.

The time of flight method is illustrated in Fig. 3.1. Due to the method of accelerating the particles (i.e., protons), a pulsed source runs at a certain frequency. This means there is a certain time interval between subsequent proton pulse injections. For example, Target Station 2 (TS-2) at the ISIS pulsed source receives 10 Hz of pulses, hence proton injection every 100 milliseconds. A trigger signal is sent to the detector every time there is a proton pulse injection, Fig. 3.1. Neutrons with different energy arrive at the detector at different times, and by comparing the neutron arrival time against the trigger, neutron time-of-flight can be determined. If the distance between the neutron target and detector  $L_f$  is known, the TOF can be used to calculate the neutron wavelength and the neutron energy, by modifying Eq. (2.1) and Eq. (2.2), respectively, shown in Eq. (3.1).

$$\lambda = \frac{h \times \text{TOF}}{m_n \times L_f}; E = \left( \frac{m_n}{2} \right) \left( \frac{L_f}{\text{TOF}} \right)^2 \quad (3.1)$$

## 3.2 Neutron diffraction

### 3.2.1 Bragg's law and the Bragg diffraction peak

When atoms are arranged in a regular array, for example the atomic arrangements in a crystalline material, a specific condition needs to be fulfilled to achieve diffraction. This is stated in Bragg's Law, Eq. (3.2).

$$\lambda = 2d_{hkl} \sin \theta \quad (3.2)$$

Bragg's Law states that constructive interference will occur from a set of planes  $\{hkl\}$  with lattice spacing  $d_{hkl}$  only if the neutron wavelength  $\lambda$  and the scattering angle  $\theta$  meet the condition of Eq. (3.2). In other words, by knowing the neutron wavelength  $\lambda$  and the angle between the incident and the diffracted beam directions  $2\theta$ , the distance between planes (lattice spacing)  $d_{hkl}$  normal to the scattering vector  $q$  can be calculated. This is illustrated in Fig. 3.2.

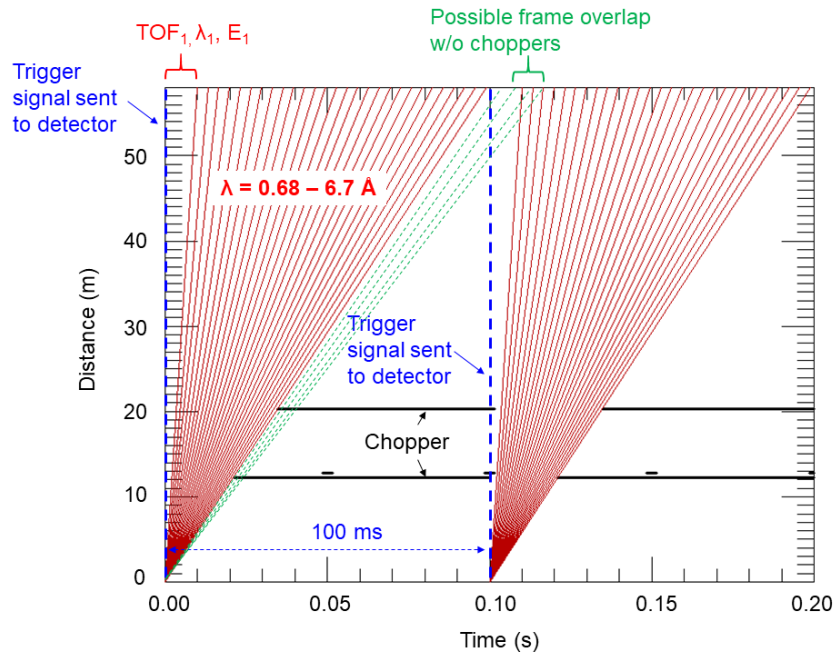


Fig. 3.1 Illustration to describe the time-of-flight (TOF) method for a 10 Hz source. A trigger signal is sent to the detector each time there is a pulse from the source. The neutron arrival time is compared against the trigger to determine the TOF. If the distance from target to detector is known, the neutron wavelength and neutron energy can be calculated. Higher energy neutrons (shorter wavelengths) have higher kinetic energy and therefore would be detected at earlier time. Neutron choppers, to define the wavelength band and to prevent overlap of neutrons from subsequent pulses (green dashed line), are shown.

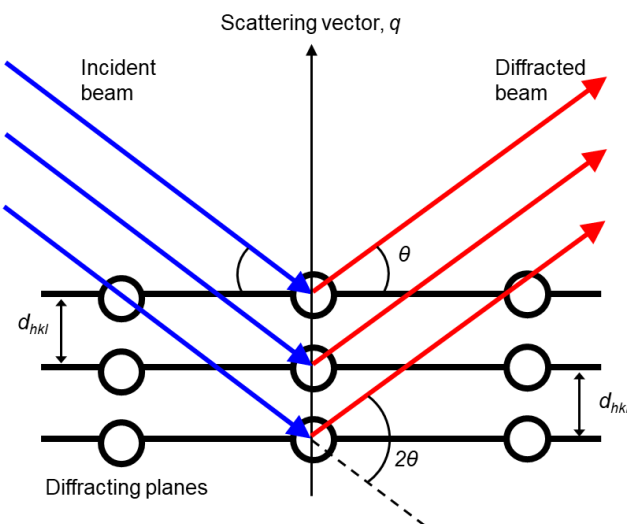


Fig. 3.2 Illustration of the diffraction phenomenon from a set of lattice planes  $\{hkl\}$ , which is governed by Bragg's Law, Eq. (3.2).

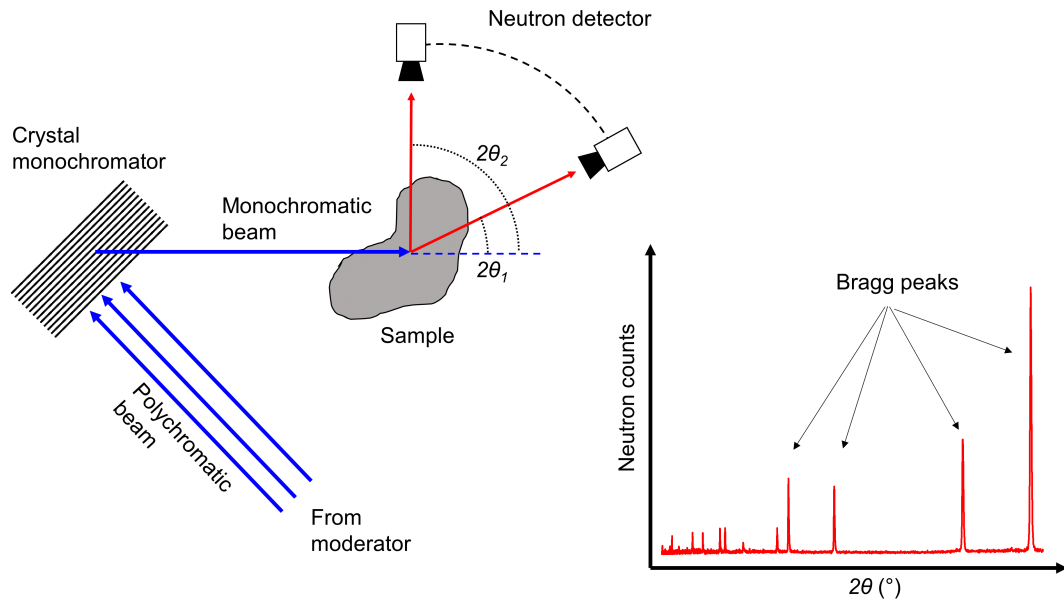


Fig. 3.3 Schematic of a neutron diffraction measurement at a continuous neutron source. A polychromatic neutron beam with a range of wavelengths is Bragg diffracted by a crystal monochromator, resulting in a monochromatic (single wavelength) beam. The diffracted neutrons from the sample are recorded by the detector as a function of diffraction angle, showing Bragg peaks at the  $2\theta$  position where the Bragg's law is fulfilled.

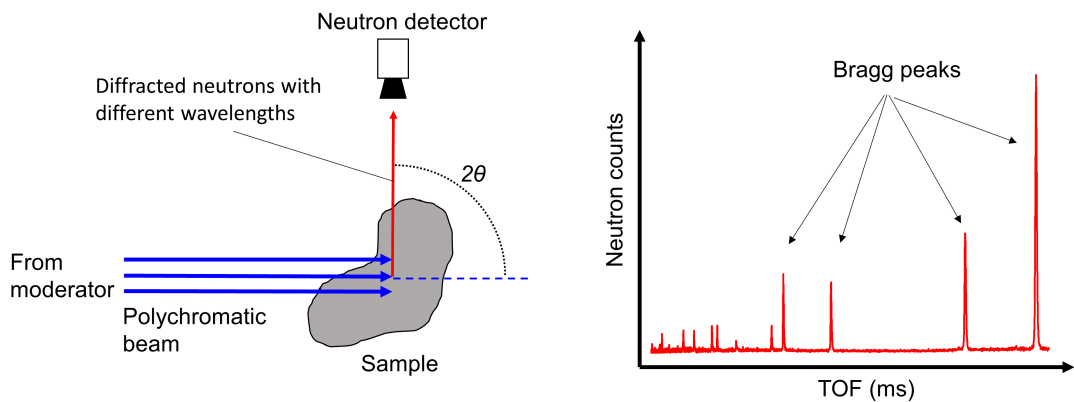


Fig. 3.4 Schematic of a neutron diffraction measurement at a pulsed neutron source. A polychromatic neutron beam is diffracted by the sample. Diffracted neutrons with different wavelengths arrive on the detector (located at fixed positions) at different times. The Bragg peaks are plotted as a function of time-of-flight (TOF)

At continuous neutron sources, diffraction from any set of planes of a polycrystalline material can be observed by selecting a single wavelength (monochromatic) neutron beam using a monochromator and measuring the diffracted signal as a function of diffraction angle. At angles where Bragg's Law is satisfied, high neutron counts will be observed and these are referred to as Bragg peaks. This is illustrated in Fig. 3.3. The position of these peaks will provide information on the lattice spacings of the corresponding planes. Meanwhile at pulsed sources, the sample is irradiated by a polychromatic neutron beam with a wide spectrum of neutron wavelengths. Neutrons with different wavelengths will be diffracted by the sample and arrive on the detector at different times. The Bragg peaks are recorded by one or more detectors, placed in a fixed position, as a function of the neutron's time-of-flight (TOF). This is illustrated in Fig 3.4.

### 3.2.2 Neutron diffraction for stress analysis

A Bragg peak, which is the result of scattering from a coherently diffracting volume of material, is characterised by three parameters:

1. The peak position, which provides information on the lattice spacing of the diffracting planes.
2. The peak intensity, which is related to the number of grains having planes that satisfy the Bragg condition and the arrangement of the atoms within the crystal unit cell.
3. The peak shape which is linked to the size of the grains, the presence of micro- or macro-strain, and the dislocation density in the gauge volume, see Sprauel (2003) for example.

These parameters can be translated into useful information for materials analysis. For example, the relative intensities of Bragg peaks can be used to carry out phase analysis and texture analysis (Brokmeier and Bunge, 1988). Furthermore, the broadening of Bragg peaks has been used to determine dislocation multiplication in stainless steel due to hydrogen charging (Liang et al., 2018).

The most prevalent application of neutron diffraction for engineering applications, however, is strain and stress measurement through the determination of Bragg peak positions. Fig. 3.5(a) illustrates the setup of a neutron diffraction experiment for stress measurement at a pulsed neutron source, e.g., the ENGIN-X instrument at the ISIS neutron source (Santisteban et al., 2006a). A fraction of the incident beam hitting the sample is diffracted to the detector. The volume of material which contributes to the diffraction, termed the gauge volume, is

defined by the intersection of the incident and diffracted beams, whose dimensions are determined by the neutron aperture (or slit) and collimators, respectively. The detector is positioned at 90° from the incident beam to define a near cubic gauge volume. The measured strain component is in the direction of the neutron scattering vector,  $q$ , which is the bisector of the incident and diffracted beams, Fig. 3.5(a). By using two detectors opposing each other, the strain components in the directions of  $q_1$  and  $q_2$ , corresponding to  $\varepsilon_{xx}$  and  $\varepsilon_{yy}$ , respectively, can be measured simultaneously, Fig. 3.5(a). In almost all neutron diffraction measurements which involve a three-dimensional state of stress, only strain in three mutually orthogonal directions are measured (Coules et al., 2013). With these strain values, and the knowledge of the material's Young's modulus,  $E$ , and Poisson's ratio,  $\nu$ , the corresponding direct stresses can be calculated using the three-dimensional Hooke's law for an elastically isotropic material as shown in Eq. (3.3), where  $i, j = x, y, z$ . In these cases, the assumption is made that either the stresses are principal stresses or finite shear stress components are ignored, therefore for both cases  $i = j$ . For the example given in Fig. 3.5(a), all of the strain values needed to calculate the stress  $\sigma_{xx}$ ,  $\sigma_{yy}$ , and  $\sigma_{zz}$  can be measured by simply rotating the sample 90° about the  $y$ -axis.

$$\sigma_{ij} = \frac{E}{(1+\nu)} \left[ \varepsilon_{ij} + \frac{\nu}{(1-2\nu)} (\varepsilon_{xx} + \varepsilon_{yy} + \varepsilon_{zz}) \right] \quad (3.3)$$

Using the definition of neutron wavelength in Eq. (3.1) and putting it into Eq. (3.2), neutron time-of-flight can be directly converted into lattice spacing, assuming the flight path  $L_f$  is known. Therefore, a diffraction spectrum can be plotted as a function of  $d$ -spacing. The presence of elastic strain in the material is indicated by the change in lattice spacing. This translates to a shift in the Bragg peak position  $\Delta d$ , with an example shown in Fig. 3.5(b). The strain  $\varepsilon$  is calculated using Eq. (3.4):

$$\varepsilon = \frac{d_0 - d}{d_0} = \frac{\Delta d}{d_0} \quad (3.4)$$

where  $d$  is the lattice spacing of the strained material and  $d_0$  is the strain-free lattice spacing. There are several methods for obtaining the  $d_0$  (Winholtz, 2003):

1. Measuring a stress-free powder. Although a powder will be completely stress-free, careful selection needs to be taken to make sure that the powder has the same composition and thermo-mechanical history as the stressed material.

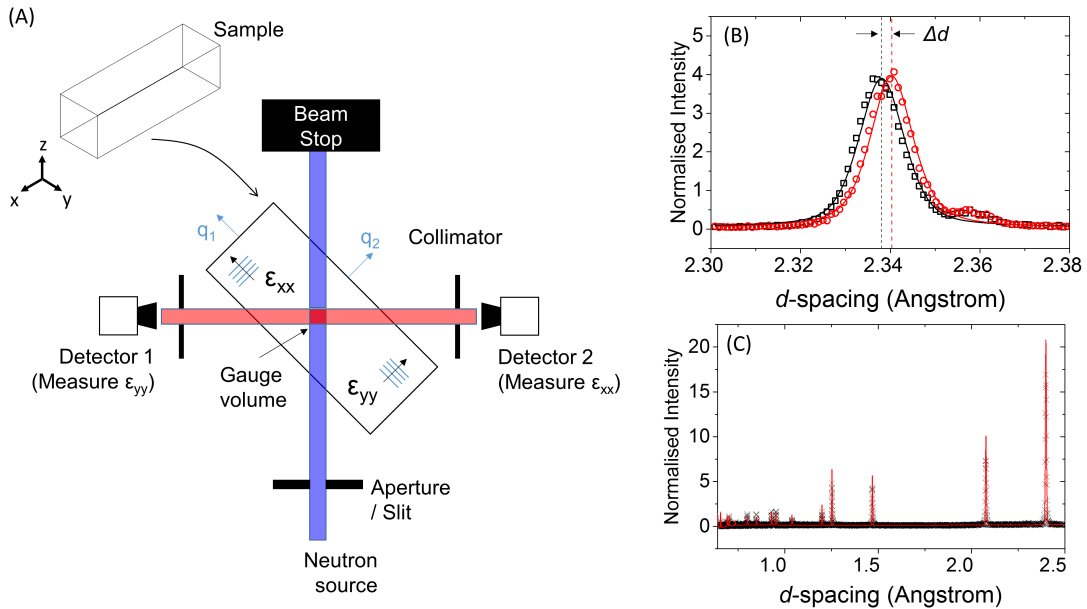


Fig. 3.5 (a) Schematics of a neutron diffraction experiment for strain measurement at a pulsed neutron source, e.g., ENGIN-X; (b) shift of Bragg peak position due to the change in lattice spacing, indicating the presence of strain. Solid lines are fitted peaks for accurate determination of Bragg peak position; (c) multiple-peak fitting on a neutron diffraction spectrum, shown by the red solid line

2. Measuring a stress-free region of the sample. Difficulties for this method are to demonstrate that the region is truly stress free and that the  $d_0$  is independent of the position within the sample.
3. Measuring a stress-free cut section of the sample. Cutting the sample into small coupons would relieve stresses within the material. Electrical discharge machining is usually used for metal components to avoid the introduction of new residual stresses to the stress-free coupons

Accurate determination of lattice spacing is, on a pulsed source instrument like ENGIN-X, usually performed by fitting a TOF profile function, comprising convolution of an exponential with a Voigt function to the individual peaks. This will result in plane-specific lattice spacing or  $d_{hkl}$ . Examples of this single-peak fitting are shown by the solid lines in Fig. 3.5(b). For plane-specific strain, Eq. (3.4) then becomes:

$$\varepsilon_{hkl} = \frac{d_{hkl0} - d_{hkl}}{d_{hkl0}} = \frac{\Delta d_{hkl}}{d_{hkl0}} \quad (3.5)$$

Strain and stress analysis produced from the single-peak analysis is not always directly comparable to the bulk behaviour of the material, i.e., needs to consider the elastic anisotropy of different lattice planes (Hutchings, 1992). The other way to analyse diffraction spectra is to perform a refinement to a full diffraction spectrum, which is usually done by using either Pawley or Rietveld refinement. This multi-peak refinement produces a lattice parameter or lattice constants of the unit cell, which represents the bulk behaviour of the material. The strain equation, for the simple case of a cubic material with lattice parameter  $a$ , then becomes:

$$\varepsilon_{\text{bulk}} = \frac{a_0 - a}{a_0} = \frac{\Delta a}{a_0} \quad (3.6)$$

An example of multi-peak refinement is shown by the red solid line in Fig. 3.5(C).

### 3.3 Bragg edge neutron transmission

#### 3.3.1 Neutron transmission setup

Fig. 3.6 illustrates the setup of a neutron transmission experiment where an incident neutron beam hits the sample, is transmitted, and then detected by a detector positioned behind the sample and in the direct path of the neutron beam. At a pulsed neutron source, the incident neutron intensity  $I_0$  is a function of wavelength as shown by the red curve in Fig. 3.6. An example of transmitted neutron intensity  $I$  attenuated by a material (in this case alpha-iron), which carries the trace of absorption and scattering, is illustrated by the blue curve in Fig. 3.6. Transmission is defined as  $I/I_0$  and illustrated by the black curve in Fig. 3.6, taking an example of a transmission spectrum of alpha-iron. As will be described later in the text, the  $d$ -spacing is equal to half of the wavelength in transmission geometry. Characteristic signals called Bragg edges can be observed in the transmission spectrum. The positions of the Bragg edges coincide with the positions of Bragg peaks of the diffraction spectrum, also from alpha-iron, shown by the green curve in Fig. 3.6.

#### 3.3.2 Interpretation of transmission spectra and generation of Bragg edges

All of the processes that remove neutrons from the incident beam, such as absorption and scattering, contribute to the neutron transmission spectrum. For an incident neutron beam of intensity  $I_0(\lambda)$  traversing a sample of thickness  $z$ , the attenuation  $I(\lambda)$  is expressed as

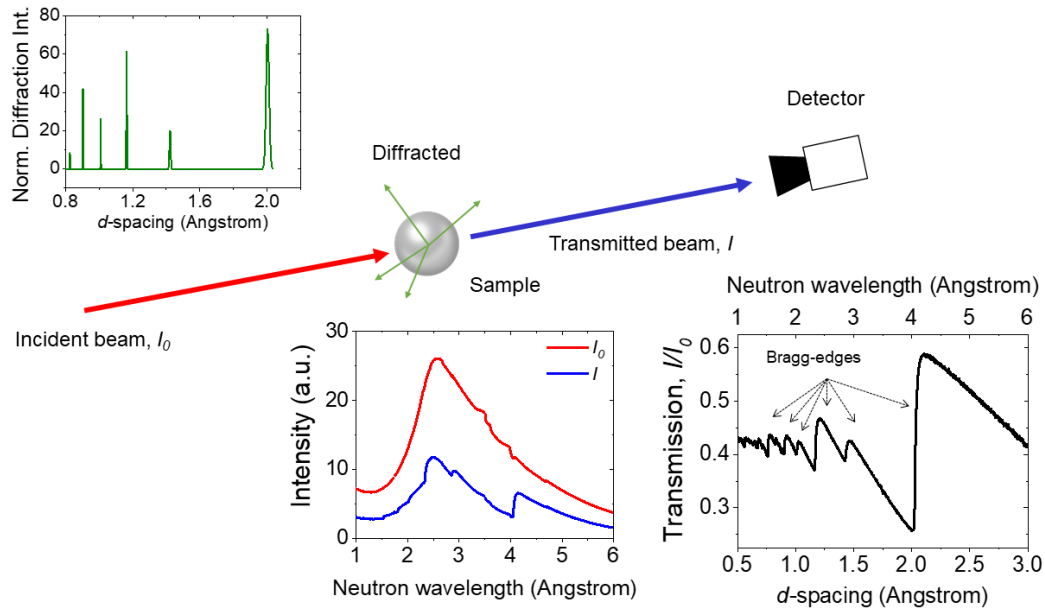


Fig. 3.6 Setup of neutron transmission experiment, where the incident beam, sample, and detector are arranged in a straight line. Normalising the attenuated neutron intensity  $I$  (blue curve) by the incident intensity  $I_0$  (red curve) yields the transmission spectrum (black curve). Bragg edges can be observed, having the same position as the Bragg peaks of the diffraction spectrum (green curve).

$$I(\lambda) = I_0(\lambda) \exp(-n\sigma_{\text{tot}}(\lambda)z) \quad (3.7)$$

where  $\sigma_{\text{tot}}(\lambda)$  is the total cross section of a unit cell of the material, and  $n$  is the number of unit cells per unit volume. The total cross section includes the contribution of different processes, e.g., absorption and different types of scattering: coherent-elastic/ Bragg, coherent-inelastic, incoherent-elastic, and incoherent-inelastic, Eq. (3.8):

$$\sigma_{\text{tot}} = \sigma_{\text{abs}} + \sigma_{\text{coh-inel}} + \sigma_{\text{inc-el}} + \sigma_{\text{inc-inel}} + \sigma_{\text{Bragg}} \quad (3.8)$$

An example of calculated absorption, different types of scattering, and total cross section is shown in Fig. 3.7, obtained using *nxs* software (Boin, 2012) for iron. The absorption cross section has a linear dependence on wavelength, while a theoretical function to calculate the wavelength dependence of the cross section of the scattering components other than Bragg scattering is available (Granada, 1984).

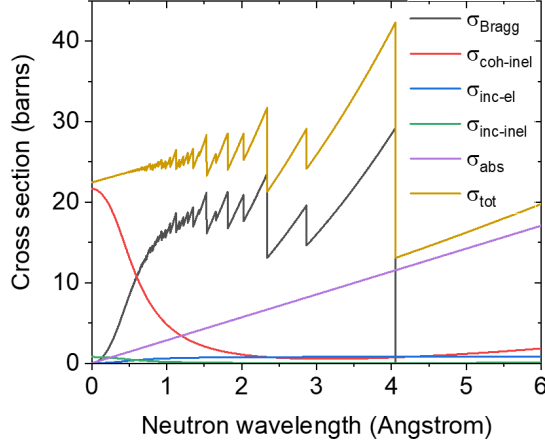


Fig. 3.7 Example of absorption, coherent-elastic/ Bragg, coherent-inelastic, incoherent-elastic, incoherent-inelastic scattering, and total neutron cross section of iron, calculated using *nxs* software (Boin, 2012)

Meanwhile, the Bragg scattering are governed by Bragg's Law, Eq. (3.2). Inferring from the equation, as the diffracting wavelength increases for a particular set of planes with lattice spacing  $d_{hkl}$ , the Bragg angle  $\theta$  increases until it reaches  $90^\circ$  where neutrons are scattered back towards the source. This is often referred to as Bragg reflection or back-scattering. Here the cross section reaches the maximum for the particular  $\{hkl\}$ . Above this critical wavelength, no scattering can occur from the particular lattice planes and this leads to a sharp decrease in cross-section, as shown in Fig. 3.7. The Bragg cross section for a random polycrystalline material can be expressed using the Fermi equation (Fermi et al., 1947):

$$\sigma_{\text{Bragg}}(\lambda) = \frac{\lambda^2}{4V_0} \sum_{hkl}^{2d_{hkl} < \lambda} |F_{hkl}|^2 d_{hkl} \quad (3.9)$$

where  $V_0$  is volume of the unit cell and  $F_{hkl}$  is the structure factor.

The neutron transmission  $Tr(\lambda)$  can be calculated as a ratio between the attenuated neutron intensity  $I(\lambda)$  and incident beam intensity  $I_0(\lambda)$ :

$$Tr(\lambda) = \frac{I(\lambda)}{I_0(\lambda)} = \exp(-n\sigma_{\text{tot}}(\lambda)z) \quad (3.10)$$

Inserting values to Eq. (3.10), the calculated transmission for a texture-free iron (Fe) with thickness of 10 mm ( $n = 4.25 \times 10^{22}$  unit cell/cm<sup>3</sup>) is shown in Fig. 3.8. The sudden drops in the Bragg cross section (Fig. 3.7) are translated into sudden jumps in transmission, Fig. 3.8A.

These are so-called Bragg edges. For wavelengths smaller than the critical value, diffraction occurs with diffraction angle  $\theta < 90^\circ$  while some neutrons are transmitted, Fig. 3.8B top. Increasing the wavelength to the critical value  $\lambda_c$ , back-scattering occurs where  $\theta = 90^\circ$ , and the transmitted neutrons reach a minimum value, Fig. 3.8B middle. No scattering occurs from the  $\{hkl\}$  above the critical wavelength value: most of the neutrons are transmitted while attenuation is only occurring through absorption. The critical wavelength for a particular  $\{hkl\}$  is also termed  $\lambda_{hkl}$ , and represents the Bragg edge position. Since  $\sin \theta = 1$  ( $2\theta = 180^\circ$ ) during back-scattering, the  $d_{hkl} = \lambda/2$ . As shown in Fig. 3.8B,  $d_{hkl}$  is measured for lattice planes normal to the scattering vector  $q$  and normal to the incident and transmitted beam direction.

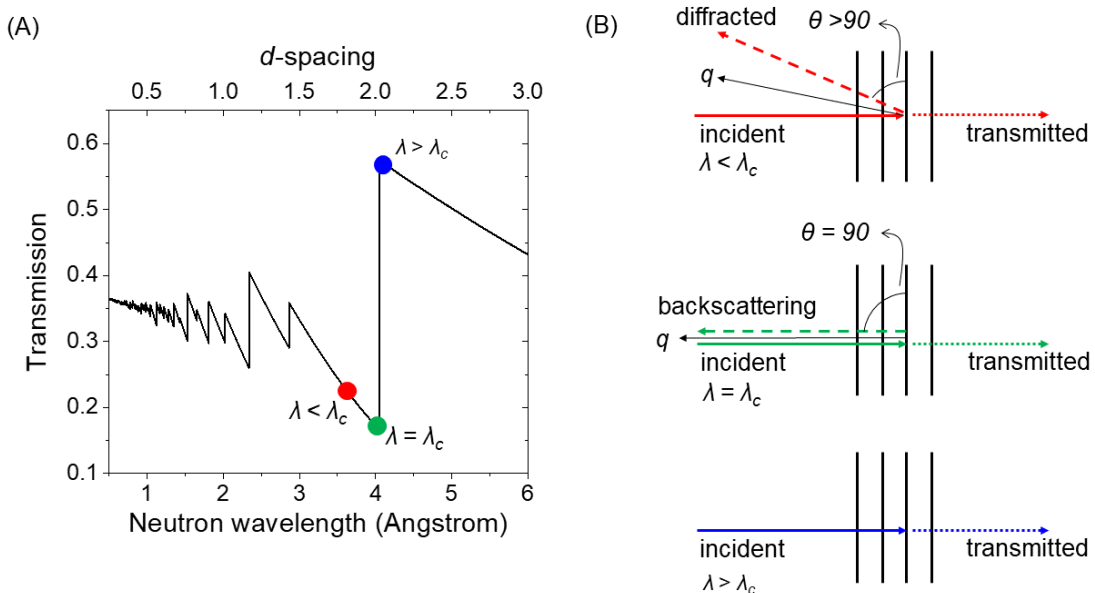


Fig. 3.8 Bragg edges of iron (Fe) with thickness of 10 mm, calculated using cross section values produced by *nxs* software.

### 3.3.3 Bragg edge analysis for materials studies

As a neutron transmission spectrum contains the trace of scattering, many of the materials parameters which are obtained from neutron diffraction can also be derived from neutron transmission. For a start, since the Bragg angle depends on the relative orientation between the neutron beam and the crystal, transmitted neutrons with a specific wavelength provide information of the number of crystallites having a selected orientation within the

sample (Kockelmann et al., 2007). A correct analysis of a transmission spectrum allows a crystallographic orientation mapping across the sample.

Meanwhile, Bragg edge features can be used to provide information of both crystallographic structure and dynamics within the sample as well as instrument parameters. Most notably, Bragg edge position can be directly converted to lattice spacing, and the shift in the Bragg edge from the reference position can reveal strain information. This is analogous to the Bragg peak shift analysis in diffraction measurements (Ramadhan et al., 2018). The Bragg edge width has been used to study plasticity on an overloaded component (Reid et al., 2018). Bragg edge height analysis can be used to determine phases present in samples (Vitucci et al., 2018a), and also the Debye-Waller factor changes as function of temperature, which will be described later in this thesis.

## 3.4 Principle of Bragg edge neutron transmission imaging

### 3.4.1 Basic principles

One of the main differences between neutron transmission and neutron diffraction is that neutron transmission preserves the information from the sample in real space. This is done by placing the transmission detector in line with the incident beam behind the sample position. Using a position sensitive detector, structural information across the sample can be spatially resolved as each individual pixel will theoretically contain a transmission spectrum with Bragg edges, Fig. 3.9. By analysing the Bragg edge pixel-by-pixel, a 2D map of different Bragg edge parameters can be reconstructed. This forms the basis of Bragg edge neutron transmission imaging.

There are several advantages of Bragg edge transmission imaging compared to neutron diffraction:

1. Bragg edge transmission imaging can produce a map of the material's structural information in a single exposure, while obtaining the equivalent information using neutron diffraction would require potentially hundreds of measurement points.
2. The setup for neutron transmission is relatively simple: a position-sensitive detector is placed directly behind and as close as possible to the sample and in line with the incident beam, unlike the neutron diffraction setup where the detectors are at an angle to the sample and the beam propagation direction.
3. The neutron transmission setup removes the uncertainty of the exact specimen or gauge location along the beam, which is present in neutron diffraction experiments.

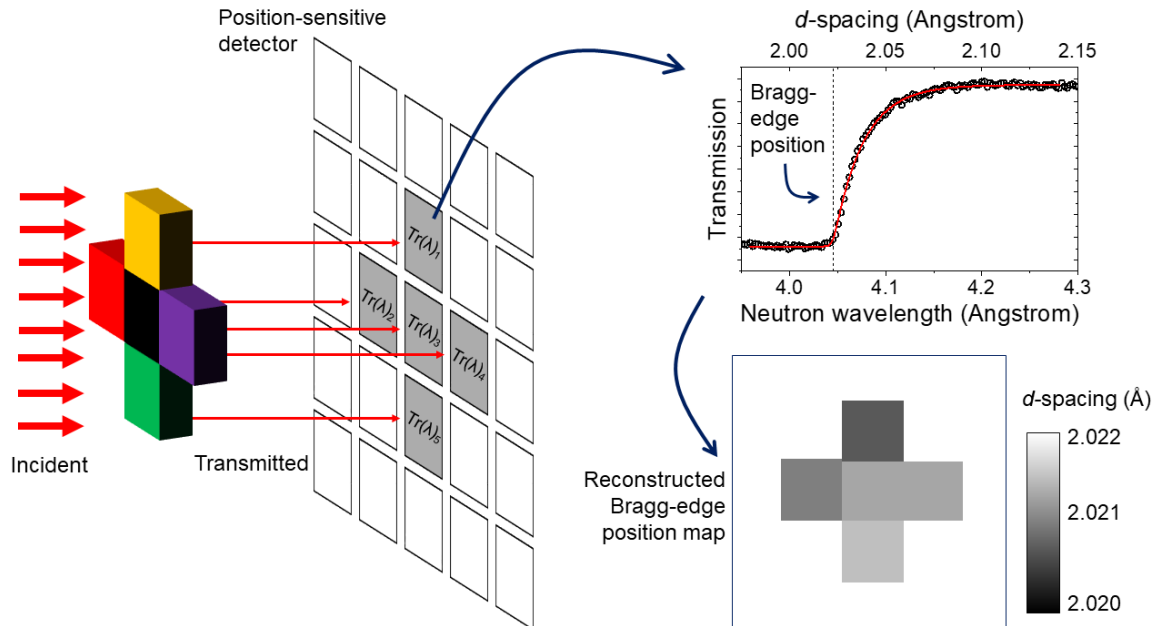


Fig. 3.9 Illustration of Bragg edge neutron transmission imaging principle. Transmitted neutrons are detected by a position-sensitive detector, where each pixel contains a Bragg edge signal from which the materials parameters (e.g.,  $d$ -spacings) can be derived. The parameter map can be then reconstructed.

However, as will be described later in the next chapter, the measured parameters are averaged through the thickness of the sample in the neutron propagation direction. Nevertheless, Bragg edge neutron transmission imaging is extremely useful for some applications, as will be demonstrated in this text.

### 3.4.2 Components of the neutron transmission imaging setup

A neutron imaging system mainly comprises four components: the neutron source, a beam collimator, the sample, and the detector, as shown in Fig. 3.10. These components will determine the quality of the image produced, i.e., the uncertainty of the reconstructed map and the spatial resolution.

1. The neutron source, which in this case is the moderator, determines the beam intensity and the sharpness of the pulse, both as a function of energy. Higher beam intensity would reduce the time required for the measurement to achieve statistically sufficient counts, while a sharper pulse means higher energy resolution, thus increasing the accuracy of the Bragg edge position determination. However, as described in Chapter 2, beam intensity and pulse sharpness often have a negative correlation.

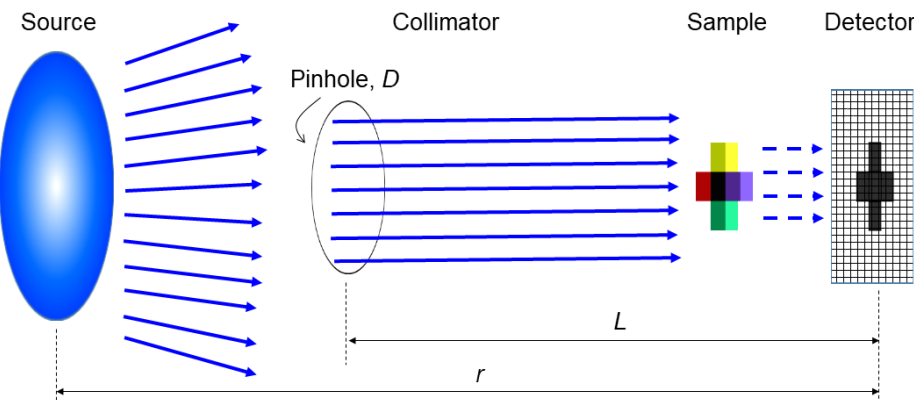


Fig. 3.10 Main components of a neutron transmission imaging system: neutron source, collimator to regulate the beam propagation direction, sample and neutron detector.

2. The beam collimator system usually comprises a pinhole (beam aperture) and a set of beam limiters. Collimation is required to make the beam parallel and therefore a well-defined image is produced. A collimated neutron beam, however, will still have some divergence. The beam divergence is determined by the diameter of the pinhole,  $D$  and pinhole-to-detector distance,  $L$ , Fig. 3.10, and is expressed as the collimation ratio  $L/D$ . The effect of geometrical blurring on the spatial resolution will be described later in the next chapter.
3. Since the Bragg edge pattern in the transmission signal is a consequence of scattering, samples which work well in other neutron scattering experiments (e.g., diffraction) will also work in neutron transmission. However, the gauge volume of a transmission measurement is partly defined by the neutron transmission path through the sample and therefore the thickness of the sample holds an important role in designing the experiment.
4. The neutron detector also contributes to the determination of spatial resolution. Detectors have a physical resolution which is governed by the size of an individual pixel. For example, the micro-channel plate (MCP) neutron detector at IMAT uses a Timepix readout chip with  $55 \times 55 \mu\text{m}^2$  pixel size. While this limits the resolution to  $55 \mu\text{m}$ , it has been shown that the spatial resolution can be improved by event centroiding (Tremsin et al., 2012). Spatial resolution of an image reconstructed from neutron transmission signal is also affected by the pixel-averaging or the macro-pixel method.

The considerations for designing the experiments, especially on the pulsed neutron source, and the data analysis are presented in the next chapter.

## 3.5 Bragg edge imaging for residual strain measurement

### 3.5.1 Residual stress

Residual stress is defined as stress that exists within a stationary solid body, in absence of any applied or external loads. Because the body is stationary and there is no applied load, the sum of any locked-in stress in the body must be zero. Therefore, residual stress would exist as local areas of compressive and tensile stresses with self-equilibrating manner. The schematic diagram of residual stress in the toughened glass from Schajer and Ruud (2013) is given as an example in Fig. 3.11. It can be seen that the compressive stress that exist on the surface of the glass is balanced by tensile stress in the middle.

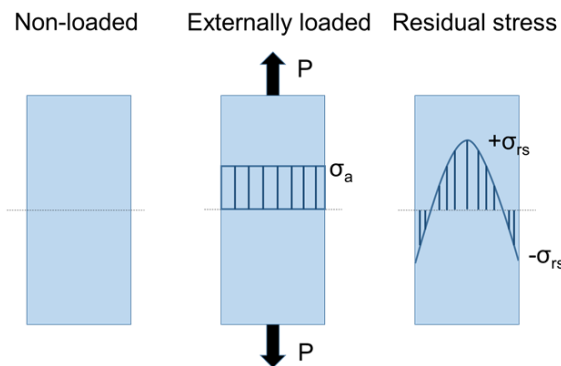


Fig. 3.11 Schematic diagram of residual stress found on the cross section toughened glass in the absence of external load.

Residual stress is generated from shape misfits within the component. Certain part of component deforms to the different extent with the rest. To preserve dimensional continuity, the area in the surrounding region deforms elastically and generate residual stress. As describe by Schajer and Ruud (2013), the cause of this misfits are:

1. Non-uniform plastic deformation. Manufacturing process such as rolling, bending, drawing and extrusion change the shape of component and can induce residual stress.
2. Surface modification. Manufacturing process such as machining, grinding, and peening could induce residual stress. Laser-shock peening, for example, induce residual stress by plastically deform surface of a component.
3. Large thermal gradient. Process such as welding expose component to high thermal gradient. As the weld cools and solidifies, it contracts to the greater extent compare

to the surrounding metal which was in much lower temperature. To preserve the geometrical continuity, the surrounding metal will ‘pull’ the weld, giving tensile residual stress in the weld, while generating compressive residual stress within itself.

In engineering, residual stress has become problems as well as potential solution. Detrimental effect of residual stress in engineering components has been investigated. For example, unfavourable residual stresses due to welding play role in the reduction of failure pressure of pressure vessel (Jeyakumar and Christopher, 2013). Tensile residual stress become a major concern in applying bonded crack retarder for aerospace structure (Syed et al., 2015). Residual stress is also an issue in additive manufacturing – a process that recently become an interest for aircraft parts, where tensile residual stress can lead to part warping (Hrabe et al., 2015).

Beneficial residual stress can also be induced to improve the life of aerospace components. Surface modification processes such as shot peening (Nam et al., 2015) and laser shock peening (Dorman et al., 2012; Maawad et al., 2012) have been applied for aerospace materials application such as titanium alloys and aluminium alloys. The studies show that the process induce compressive residual stress on the surface of components, improving fatigue life. Cold expansion of holes for aluminium alloys (Gopalakrishna et al., 2010) is another example of introducing compressive residual stress to enhance fatigue life.

### 3.5.2 Stress-strain analysis and measurement

Stress can be defined as a force applied to a surface area. Stresses, both applied and residual, are usually measured indirectly. Instead, strain is measured and corresponding stresses are calculated. Therefore, it is important to review the basics of strain-strain analysis, and strain measurement using neutrons.

General 3 dimensional stress state on a material can be described by considering an infinitesimally small cubic element with its faces aligned parallel to the axes of our chosen  $xyz$ -coordinate systems, as shown in Fig. 3.12. Each cube face will experience one normal stress (stress normal to the face) component and two shear stress (stress parallel to the face) components, which makes nine stress components in total, and can be arranged into an array:

$$\sigma = \begin{bmatrix} \sigma_{xx} & \tau_{xy} & \tau_{xz} \\ \tau_{yx} & \sigma_{yy} & \tau_{yz} \\ \tau_{zx} & \tau_{zy} & \sigma_{zz} \end{bmatrix} \quad (3.11)$$

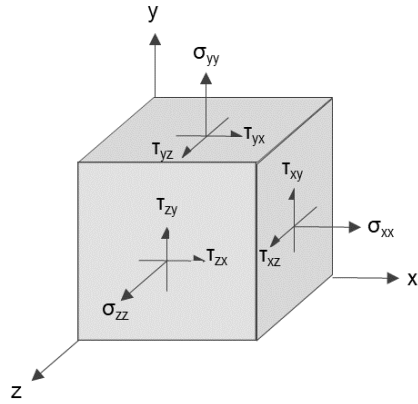


Fig. 3.12 Stress component on three-dimensional element.

Meanwhile, strain is a measure of deformation of a material with respect to its original geometry. Comparable with stress, in general condition on a material, the strain components can also be described as:

$$\boldsymbol{\varepsilon} = \begin{bmatrix} \varepsilon_{xx} & \varepsilon_{xy} & \varepsilon_{xz} \\ \varepsilon_{yx} & \varepsilon_{yy} & \varepsilon_{yz} \\ \varepsilon_{zx} & \varepsilon_{zy} & \varepsilon_{zz} \end{bmatrix} \quad (3.12)$$

where the diagonal elements represents strain along the direction of the coordinate system and the other elements are the shear strains between axes.

For basic structural analysis, the assumption is that the material response is linear and elastic, meaning stress is directly proportional to strain with a constant known as elastic or Young's modulus,  $E$ . There is also a Poission effect that is need to be considered, which a body deforming under load experiences a normal strain component parallel to the direction of loading and lateral strains at right angle to this. This means, under uniaxial tensile stress  $\tau_{xx}$ , the material will undergone strain  $\varepsilon_{xx} = \sigma_{xx}/E$  in the  $x$ -direction, and the lateral strains  $\varepsilon_{yy}$  and  $\varepsilon_{zz}$  are proportional to  $\varepsilon_{xx}$ :

$$\varepsilon_{yy} = \varepsilon_{zz} = -\nu\varepsilon_{xx} \quad (3.13)$$

where  $\nu$  is the Poission's ration.

The stress matrix is symmetrical, i.e.,  $\sigma_{xy} = \sigma_{yx}$  and can be diagonalised, which means for any point there is a system of particular axes called principal axes so that only elements of the diagonal are not equal to zero. These components are called the principal stresses. Strain matrix is also symmetrical, i.e.,  $\epsilon_{xy} = \epsilon_{yx}$ . Therefore, to determine the six independent components of the stress tensor at a point, at least six strain measurement must be made. However, by knowing the principal stress direction, or assuming one, three orthogonal strain measurement is sufficient to calculate the principal stresses.

$$\sigma_{xx} = \frac{E_{hkl}}{(1 - v_{hkl})(1 - 2v_{hkl})} \times [(1 - v_{hkl})\epsilon_{xx} + v_{hkl}(\epsilon_{yy} + \epsilon_{zz})] \quad \text{etc...} \quad (3.14)$$

In certain cases, for example biaxial plane stress ( $\sigma_{xx} = \sigma_{yy}, \sigma_{zz} = 0$ ), only the in-plane strain or the out-of-plane strain is required.

$$\sigma_{xx} = \frac{E_{hkl}\epsilon_{xx}}{1 - v_{hkl}} \quad \text{or} \quad \sigma_{xx} = \frac{E_{hkl}\epsilon_{zz}}{2v_{hkl}} \quad (3.15)$$

### 3.5.3 Bragg edge transmission imaging for residual strain measurement

As mentioned before, and will be described in detail in **Section 4.1.1**, the measured strain in neutron transmission geometry is averaged along the gauge volume. Therefore, it is suited best for investigating uniaxial system. Special cases of biaxial stress systems, as mentioned in **Section 3.5.2**, is also suitable for neutron transmission measurement since it only requires one strain direction to calculate the principal stresses. A system with more complicated stress state, e.g., for a partially biaxial stress system ( $\sigma_{xx} \neq \sigma_{yy}, \sigma_{zz} = 0$ ), or triaxial system, the principal stresses cannot be extracted without prior knowledge of the stresses in other direction (obtained either using FEA or complementary measurement, e.g., diffraction). Neutron transmission measurements of multiple orientations are not sufficient because, at different orientation, the neutron transmission gauge volume averages different voxel. Strain tomography is only possible for sample with special geometry (Abbey et al., 2012).

However, in many cases, the measurement of the strain variation of one component is still very useful in providing insight of the overall residual stress profile. The example of these are presented in Chapter 9, where neutron transmission is used to assess the effectiveness of residual-stress-inducing manufacturing processes such as laser peening and cold expansion by measuring the residual strain profiles.

# **Chapter 4**

## **Experimental Method and Data Analysis for Bragg edge Neutron Transmission Imaging**

Bragg edge neutron transmission imaging is a relatively new technique, and therefore part of this thesis aims to describe its setup and data analysis. This chapter provides a comprehensive explanation on the experimental design of neutron transmission imaging, which includes the geometry of the experimental setup, material selection, and other factors that need to be considered while designing Bragg edge transmission imaging experiments. This chapter also describes the process of analysing neutron transmission data, starting with the description of the data structure obtained from TOF neutron transmission, fitting the Bragg edge and reconstructing the Bragg edge map, and presenting the available software to perform the Bragg edge analysis. This chapter serves as a guidance for future users in designing and performing Bragg edge transmission imaging experiments, especially at a pulsed neutron source.

### **4.1 Experimental design of neutron transmission imaging**

#### **4.1.1 Gauge volume**

Especially in the field of residual stress measurement, gauge volume is defined as a specific volume of the sample from where the information is probed and averaged. Depending on the residual stress measurement method, the shape and size of the gauge volume is varied. For neutron diffraction, gauge volume is the intersect between the incident beam, which size is usually defined by a set of slits, and the diffracted neutrons which size is usually

defined by collimators limiting the view of the detector, Fig. 4.1(a). The direction of the strain component being measured is the bisector,  $Q$  of the incident and the diffracted beam, which is the  $x$ -axis direction in Fig. 4.1(a). To have a close to cubic-shaped gauge volume, diffraction detector is usually placed 90-degree from the incident beam.

For neutron transmission, the physical gauge volume is defined by the volume of material traversed by neutron with a cross section of a single pixel of the detector, Fig. 4.1(b). Since the Bragg edge features of the transmission profile is the result of back-scattering phenomena, the bisector  $Q$  is parallel with the incident and the diffracted beam, also the  $x$ -axis direction in Fig. 4.1(b). Despite the cross section of neutron transmission setup is elongated in the beam direction, the physical size of the pixel of transmission detector is really small and many gauge volumes are measured in a single exposure, and therefore 2D map of strain in high resolution can be produced conveniently by neutron transmisison.

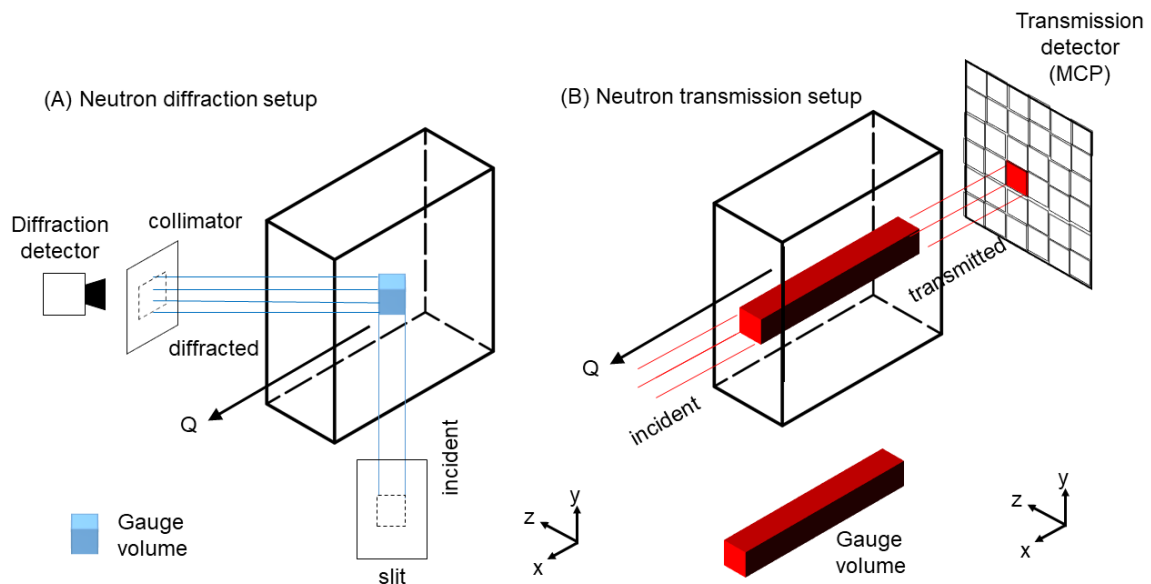


Fig. 4.1 Illustration of gauge volume in (a) neutron diffraction and (b) neutron transmission setup.

### 4.1.2 Geometry of a neutron transmission experiment

As mentioned previously, an individual gauge volume of a neutron transmission experiment is defined by the volume of material traversed by the neutrons with a cross section of a single pixel of the detector. Therefore, information in the incident beam propagation direction is

averaged through the sample thickness. The final imaging result is a 2-D projection of the sample with through-thickness average information.

Due to the geometry of the neutron transmission experiment, some aspects need to be considered for imaging:

1. Bragg edge transmission imaging works best for samples with homogeneous features along the beam propagation direction, examples shown in Fig. 4.2(a)-(c). In these cases, the variation of sample parameter, e.g., geometry, material, or residual strain is clearly mapped across the 2D plane either in a radiograph or a strain map.
2. The variation of sample features along the beam propagation direction, as shown by the examples in Fig. 4.2(d)-(f) might cause important information to be lost in the averaging.
3. The variation in geometrical features along the transmission direction, Fig. 4.2(d), will not only result in the variation of transmission (due to different amount of material which attenuate the incident neutrons) but also the variation of Bragg edge height (due to different amount of material contributing to scattering).
4. Fig. 4.2(e) provides an example of an experimental setup with two different materials along the transmission direction. The corresponding radiograph shows the area in the middle of the sample where the transmission from iron (Fe) and copper (Cu) are convoluted. This results in the Bragg edges from the two materials to be integrated in one spectrum. For certain material combinations, there is a risk of convolution between two closely-positioned Bragg edges, which will complicate the data analysis.
5. Fig. 4.2(f) shows an example of an experimental setup with variation of material's parameter, e.g., variation in lattice spacing due to residual strain, along the transmission direction. In the corresponding strain map, compressive residual strain under the treated surface is averaged with the more tensile strain under the non-treated surface. Therefore, unlike the strain map in Fig. 4.2(c), this result does not accurately represent the residual strain generated from the surface treatment process. Another example is the variation of strain component along the transmission direction, e.g., hoop and radial strain around a cold-expanded fastener hole, which being averaged by performing neutron transmission measurement with the neutron beam normal to the hole axis, example given in **Section 9.2.1**.
6. In many cases, one of the sample axes which becomes the measurement direction needs to be aligned parallel with the neutron propagation direction, Fig. 4.3(a). Proper

sample alignment will allow easier interpretation of the result, and the image output will accurately represent the 2-D cross-section of the sample containing structural information, i.e., lattice spacing, crystallographic texture, etc. Samples are usually aligned by getting an image where the sample edge is the sharpest, Fig. 4.3 (c). Sample misalignment and the resulting image are shown in Fig. 4.3 (b) and (d), respectively.

### 4.1.3 Material selection

Crystalline materials, which include metals and ceramics, are required to produce Bragg-scattering. Most of the materials that can be studied using neutron diffraction can be measured with Bragg edge transmission imaging. However, since the transmission spectrum carries the contributions of all phenomena which remove neutrons from the incident beam, including absorption, thickness of the material (in transmission direction) becomes an important parameter. Samples which are too thin will have a weak Bragg edge signal which is flattened by the noise, while samples which are too thick will be dominated by absorption. There is, therefore, an optimum thickness, i.e., thickness which will provide the minimum uncertainty for the definition of the Bragg edge position, for each material.

The uncertainty of Bragg edge position depends on the edge height and its uncertainty (related to the scatter of the data). The optimal sample thickness  $z_{opt}$  for a Bragg edge imaging experiment can therefore be calculated from the contribution of neutron cross sections to the jump in transmission before and after the edge using Eq. (4.1) (Santisteban et al., 2001):

$$z_{opt} = \frac{1}{n\sigma_{hkl}} \ln \left( \frac{3}{2} \frac{\sigma_{hkl}}{\sigma_0} + \left[ \left( \frac{3}{2} \frac{\sigma_{hkl}}{\sigma_0} \right)^2 + \frac{\sigma_{hkl}}{\sigma_0} + 1 \right]^{1/2} \right) \quad (4.1)$$

where  $\sigma_{hkl}$  is the Bragg or elastic coherent cross section at the Bragg edge wavelength position of the corresponding  $\{hkl\}$  planes,  $\sigma_0$  is all of the attenuation contributions other than elastic coherent scattering for the  $\{hkl\}$ , and  $n$  is the number of unit cells per unit volume (Santisteban et al., 2001).  $\sigma_{hkl}$  and  $\sigma_0$  can be calculated using the *nxs* software (Boin, 2012). Table 4.1 provides the optimal sample thicknesses of common engineering metals.

It has to be noted that for titanium, the  $\sigma_0$ , which is dominated by absorption, is much larger than the Bragg cross section  $\sigma_{hkl}$ . For this reason, titanium does not exhibit intense Bragg edges in its transmission spectra, as can be seen in Fig. 4.4. This makes titanium a challenging material to be studied with Bragg edge imaging. This is an important observation since titanium produces well-defined Bragg diffraction peaks and would otherwise be expected to be suitable for neutron transmission experiments.

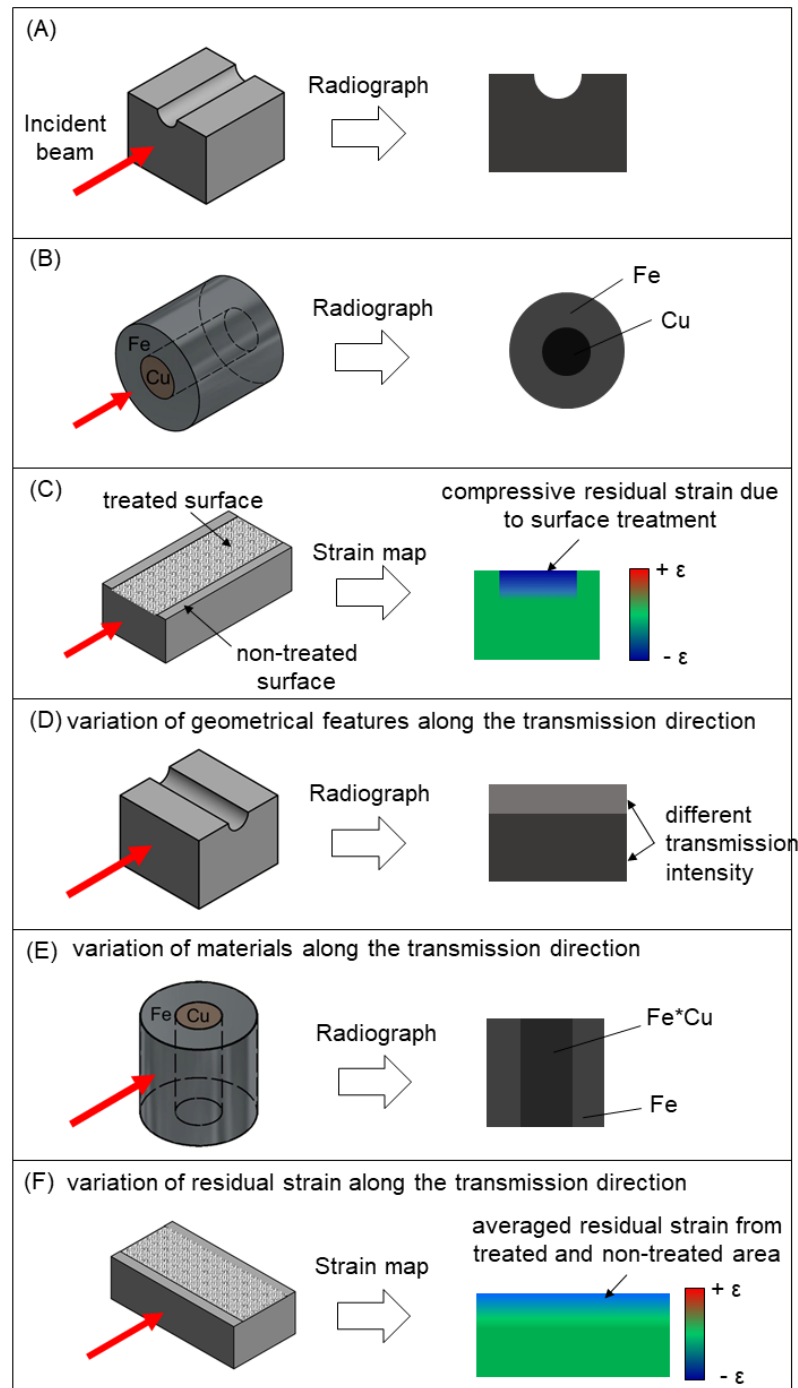


Fig. 4.2 Consideration of the sample geometry for neutron transmission experiment. Samples with homogeneous features (a)-(c) in the incident beam direction work best for transmission experiment; variation in (d) geometrical, (e) material, and (f) material parameter (e.g., strain) along the beam direction present challenges in the data analysis, and might cause important information to be lost in the averaging.

## 42 Experimental Method and Data Analysis for Bragg edge Neutron Transmission Imaging

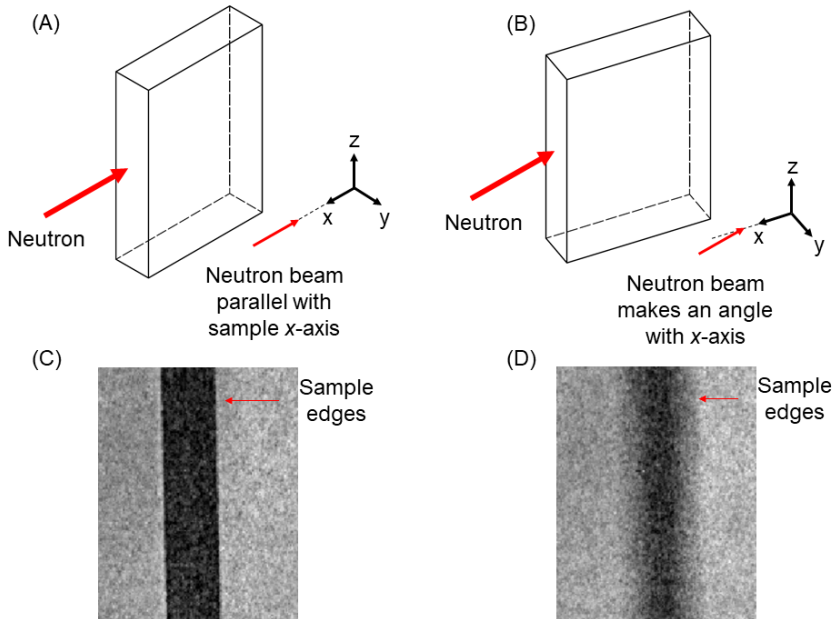


Fig. 4.3 Sample alignment in a neutron transmission experimental setup. Setup with (a) incident neutron beam parallel and (b) making an angle with the  $x$ -axis of the sample; (c) Radiographic image from (a), shows sharp edges; (d) Radiographic image from (b) shows blurry edges.

Table 4.1 Optimum sample thickness of different materials for the analysis of the first Bragg edge in transmission imaging experiment, calculated using Eq. (4.1)

Material	$\sigma_0$ (barns)	$\sigma_{hkl}$ (barns)	Optimal thickness (cm)
$\alpha$ -iron	13.08	29.23	1.59
Aluminium	3.77	5.49	18.95
Copper	38.35	27.82	1.74
Nickel	63.37	50.59	0.95
Titanium	40.82	2.60	5.02

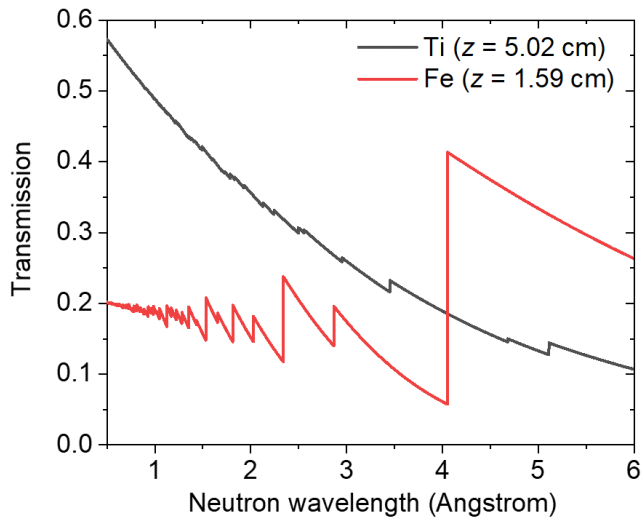


Fig. 4.4 Calculated transmission spectrum of titanium (grey curve) with optimal sample thickness in transmission direction of 5.02 cm. The spectrum does not exhibit intense Bragg edges. Calculated transmission spectrum of iron with optimal sample thickness is plotted for comparison.

#### 4.1.4 Geometrical blurring

There are three parameters which determine the geometrical image unsharpness or geometrical blurring,  $d_b$ , due to beam divergence: i) size of the pinhole,  $D$ ; ii) distance from the pinhole to the detector,  $L$ , and; iii) distance from the sample to the detector,  $l$ . With the collimation ratio  $L/D$ , the geometrical blurring is calculated as:

$$d_b = \frac{l}{(L/D)} \quad (4.2)$$

The relation between  $d_b$  and the three determining parameters is shown in Fig. 4.5(a), where beam divergence causes unsharpness on the recorded image. Based on Eq. (4.2), the sharpness can be improved by increasing  $L$ , decreasing  $l$ , or decreasing  $D$  (or the combination of the three). Since the distance between the pinhole and the detector is fixed in many beamlines, improving the sharpness is usually carried out by decreasing the sample-to-detector distance, Fig. 4.5(b), or by decreasing the size of the pinhole, Fig. 4.5(c). In the case where the sample has a significant thickness in the beam propagation direction, the  $l$  should be measured from the sample edge which is on the far side of the detector in order to account for the worst geometrical blurring.

#### 44 Experimental Method and Data Analysis for Bragg edge Neutron Transmission Imaging

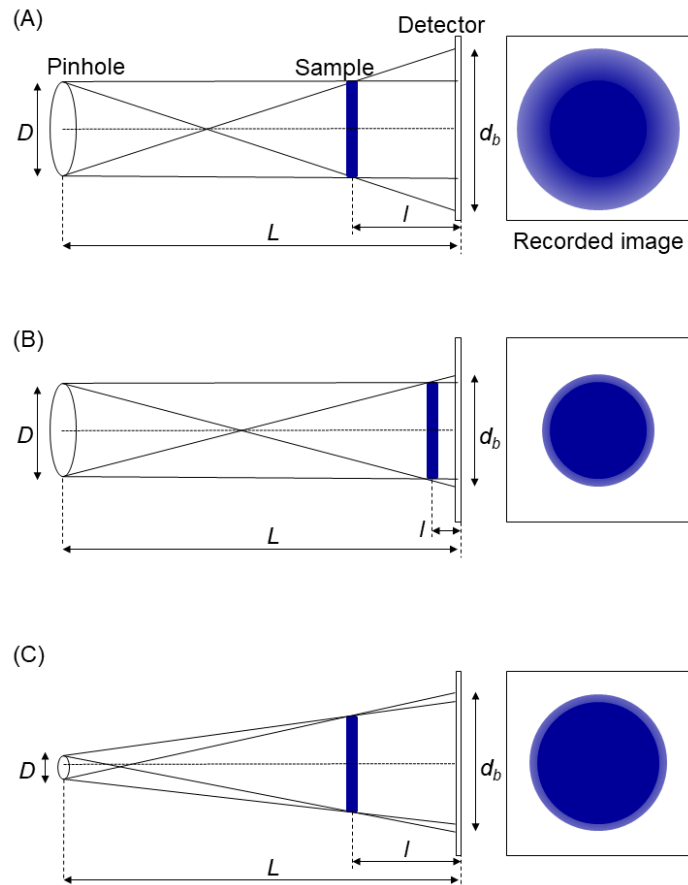


Fig. 4.5 (a) Illustration of geometrical image unsharpness or blurring due to the beam divergence. Since the  $L$  is fixed, image sharpness can be improved by (b) decreasing the sample-to-detector distance  $l$  or (c) decreasing the size of the pinhole  $D$ . The magnification,  $M$ , is given by  $M = L/(L - l)$ , and is exaggerated in the illustration.

Improvement of the geometrical blurring through the decrease of pinhole size comes at the expense of beam flux reduction. This leads to a longer counting time needed to achieve a statistical quality equivalent to that measured with bigger pinhole.

#### 4.1.5 Sample interface effect

A combination of more than one pixel of the transmission detector, i.e., a macro-pixel, is often required to obtain sufficient statistics for Bragg edge imaging, as will be described in more detail in **Section 4.3.3**. These macro-pixels average the counts from each of the sub-pixels and integrate the spectrum onto the centroid of the macro-pixel box. Therefore, careful interpretation needs to be carried out for data taken from the edge of the sample, where the macro-pixel averages the interface, e.g., between the sample edge and air, or between one sample material and the other.

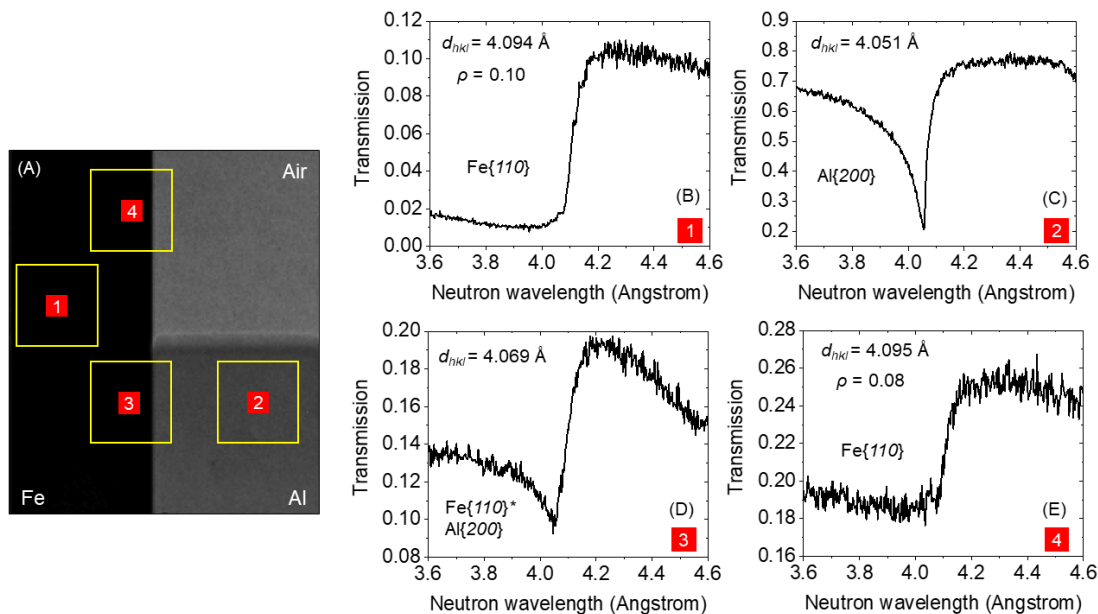


Fig. 4.6 The effect of the interface between sample and other materials to the Bragg edge spectra. (a) Interface between an iron (Fe) sample, aluminium (Al) spacer and air, macro-pixel for analysis shown by yellow boxes; (b) Fe {110} edge from macro-pixel 1; (c) Al {200} edge from macro-pixel 2; (d) Convolution of Fe {110} and Al {200} edges from macro-pixel 3; (e) Fe {110} edge with reduced Bragg edge height from macro-pixel 4.

To give an example, an iron (Fe) plate with thickness in the transmission direction  $z = 40 \text{ mm}$  was held by aluminium (Al) spacers ( $z = 50 \text{ mm}$ ). The material parameter (i.e., lattice spacing, phase, etc) of the Fe sample is homogeneous across the sample. The interface between the Fe sample and the Al spacer, and between the Fe sample and air are shown in

## **46 Experimental Method and Data Analysis for Bragg edge Neutron Transmission Imaging**

---

Fig. 4.6(a). In this case, the data were analysed using macro-pixels with a dimension of 30 × 30 pixels, shown by the yellow boxes in Fig. 4.6(a). The analysis for each macro-pixel is as follows:

1. Macro-pixel number 1 analysed the middle section of the Fe sample, where the macro-pixel fully comprised the Fe, and gave the Fe {110} Bragg edge position of  $\lambda = 4.094 \text{ \AA}$  and a Bragg edge height of  $\rho = 0.10$ , Fig. 4.6(b).
2. Macro-pixel number 2 fully comprised the Al spacer, with the spectrum includes Al {200} with  $\lambda = 4.051 \text{ \AA}$ , Fig. 4.6(c).
3. Macro-pixel number 3 and 4 were positioned so that the centroid analyses the edge section of the Fe sample. Macro-pixel number 3 comprises around 75% of Fe and 25% of Al, which caused the Fe {110} Bragg edge to be convoluted by the Al {200} Bragg edge, Fig. 4.6(d). This convolution can be easily misinterpreted as a change in Fe {110} lattice spacing, giving  $\lambda = 4.069 \text{ \AA}$ , a change equivalent to a pseudo-strain of  $6000 \mu\epsilon$  with respect to macro-pixel number 1. It is worth noting that the convolution problem of Bragg peak in diffraction-type measurement has been solved by performing a full-profile or multi-peak analysis of the data.
4. Macro-pixel number 4 comprises around 75% of Fe and 25% of air, which cause an overall increase of transmission but a decrease in Bragg edge height [ $\rho = 0.08$ , Fig. 4.6(e)]. This effect needs to be distinguished from real material parameters which affect Bragg edge height, e.g., phase fraction, Debye-Waller factor, etc. Nevertheless, the Bragg edge position is preserved, i.e., does not introduce a pseudo-strain. This is contrast to the partially-filled gauge volume in neutron diffraction measurement, which introduces geometrical pseudo-strain.

The interface effects mentioned above need to be considered while designing neutron imaging experiments, even though the macro-pixel size is chosen later at the analysis stage.. An experimental setup should avoid two materials with overlapping Bragg edge positions to be placed too close to each other in the field-of-view. Meanwhile, the Bragg edge height information can only be retrieved away from the sample edges.

## 4.2 Data analysis of neutron transmission imaging

### 4.2.1 Data structure of TOF neutron transmission imaging experiment

Time-of-flight neutron transmission imaging experiments produce a  $z$ -axis stack of 2-dimensional images in  $xy$ -plane, Fig. 4.7(a). The 2D image represents the variation of transmitted intensity read by the detector, where the darker area refers to low transmission and the lighter area means high transmission. Each image in the stack is captured using a different neutron energy range, and hence exhibits different neutron attenuation i.e., different transmission. Plotting the  $z$ -axis profile of a pixel or a group of pixels on a sample image will produce a transmission spectrum as a function of wavelength or time-of-flight, i.e., transmission spectrum, Fig. 4.7(b).

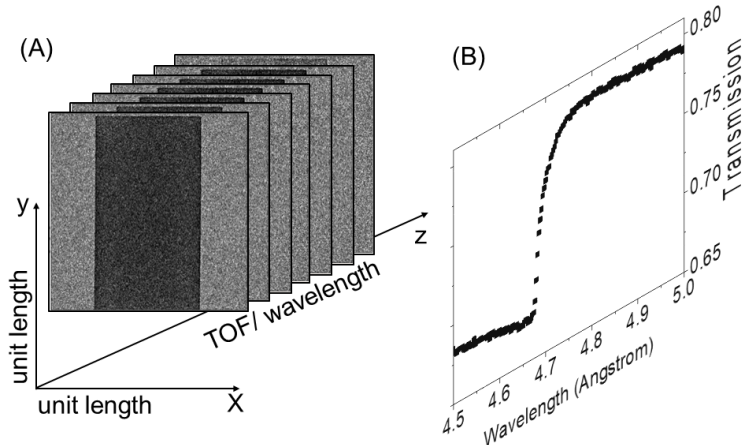


Fig. 4.7 (a) Data structure of the time-of-flight (TOF) neutron transmission imaging experiment, where data is saved as a  $z$ -axis stack of 2-dimensional image in  $xy$ -plane; (b) Plot of  $z$ -axis profile, showing transmission as a function of wavelength.

The amount of data collected depends on the number of pixels in the  $xy$ -plane, and the number of time- or wavelength-bins that can be recorded by the detector. For example, the micro-channel plate (MCP) detector with Medipix2/Timepix chip at the IMAT beamline, ISIS, produces up to around 3100 time-stamped images with a resolution of  $512 \times 512$  pixels at one exposure, which means a  $3100 \times 512 \times 512 \approx$  three-quarter billion space-time pixels can be taken in a single exposure.

### 4.2.2 Bragg edge fitting and parameters

Coherent elastic (or Bragg) scattering dominates the scattering of neutrons by most of the engineering materials within the thermal neutron energy range. Therefore, Bragg edge

## **48 Experimental Method and Data Analysis for Bragg edge Neutron Transmission Imaging**

---

transmission spectrum can be described by taking the integral of all the diffraction events which remove the intensity from the incident beam (Steuwer et al., 2001; Santisteban et al., 2001). For this reason, a good understanding of Bragg diffraction profile is important as a precursor to accurately describing the Bragg edge transmission profile.

Bragg diffraction peak profiles at pulsed sources display asymmetry which commonly described as a symmetric function (e.g. Gaussian) convoluted with a decaying exponential. The leading edge of the peak (short TOF/ low wavelength side) has Gaussian behaviour, of which its width mainly reflects the material contribution to the peak broadening, for example due to the presence of micro-strain (spread of  $d$ -spacing in the grains within the gauge volume convoluted in a single peak) or the effect of the crystalline size. Meanwhile, the trailing edge of the peak is determined by the moderator exponential decay and therefore is the instrumental contribution to the peak broadening. The instrumental broadening highly dependent of the type of the moderator being used on the instrument (see **Section 2.1.3**)

Since the Bragg edge transmission profile, as mentioned previously, is principally the integral of the Bragg diffraction peak, the Bragg edge broadening caused by material and instrumental contribution should be equivalent to diffraction peak broadening. As mentioned by Santisteban et al. (2001), one of the simplest models for diffraction peak shape is that proposed by Kropff et al. (1982), which consists of a Gaussian of deviation  $\sigma(\lambda)$  convoluted with a decaying exponential starting at a time  $t(\lambda)$  and decaying with a time constant  $\tau(\lambda)$ . Integrating the mentioned function and replacing the TOF,  $t$ , with  $\lambda$  (directly interchangeable assuming the flight path is known) resulting in an easy-to-fit, three-parameter function:

$$B(\lambda) = \frac{1}{2} \left[ \operatorname{erfc} \left( -\frac{\lambda - \lambda_{hkl}}{2^{1/2}\sigma} \right) - \exp \left( -\frac{\lambda - \lambda_{hkl}}{\tau} + \frac{\sigma^2}{2\tau^2} \right) \operatorname{erfc} \left( -\frac{\lambda - \lambda_{hkl}}{2^{1/2}\sigma} + \frac{\sigma}{\tau} \right) \right] \quad (4.3)$$

where  $\lambda_{hkl}$  is the position of the Bragg edge for the corresponding  $hkl$ ,  $\sigma$  is Gaussian broadening which is a property of the sample/ material (e.g., micro-strain, crystalline size), and  $\tau$  is a decay constant, which is a characteristic property of the moderator (resolution function) being used by the neutron instrument.

The transmission near the Bragg edge is approximated by linear functions within a narrow wavelength interval including the edge, and is given by:

$$\begin{aligned} Tr(\lambda) = & \exp[-(a_0 + b_0\lambda)] (\exp[-(a_{hkl} + b_{hkl}\lambda)]) \\ & + \{1 - \exp[-(a_{hkl} + b_{hkl}\lambda)]\} B(\lambda_{hkl,\sigma,\tau,\lambda}) \end{aligned} \quad (4.4)$$

where parameters  $a_0$  and  $b_0$  define the transmission on the far-right (high-wavelength) side of the edge while parameters  $a_{hkl}$  and  $b_{hkl}$  describe the jump in the transmission values. A step-by-step Bragg edge fitting routine using equation Eq. (4.4) is described by Santisteban et al. 2001.

Fig. 4.8 shows the Eq. (4.4) fits the experimental data very well, taking 110-Fe Bragg edge as an example. The plot on the bottom indicates the difference function. The inset shows a peak function obtained by differentiation of the Bragg edge, where the peak showing the characteristic asymmetry of Bragg diffraction peak from a pulsed neutron source.

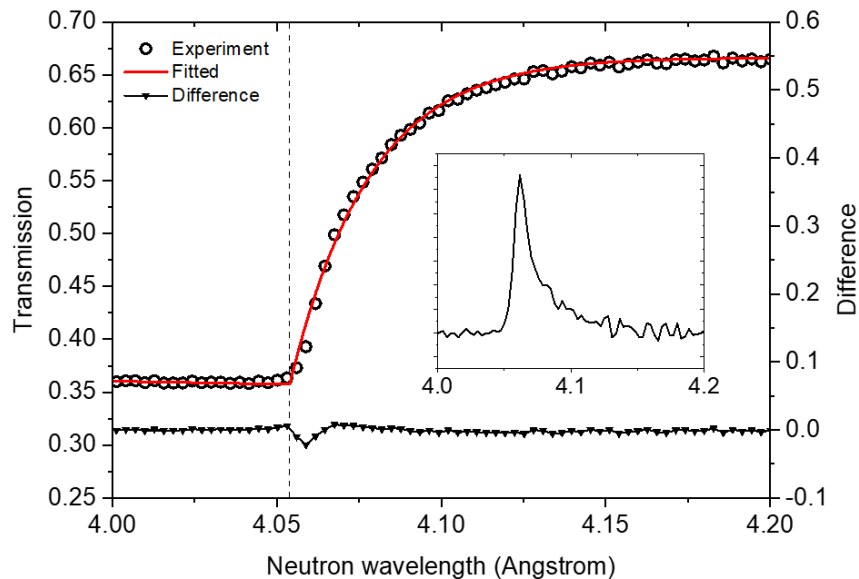


Fig. 4.8 Example of Bragg edge fitting using Eq. (4.4) on {110}-iron Bragg edge. The inset shows a peak function obtained by differentiation of the Bragg edge, with the peak showing characteristic asymmetry of Bragg diffraction peak profile from a pulsed source.

Another analytical function to describe the Bragg edge is described by Tremsin et al. 2009:

$$Tr(\lambda) = C_1 + C_2 \left[ \operatorname{erfc} \left( \frac{\lambda_{hkl} - \lambda}{2^{1/2} \sigma} \right) - \exp \left( \frac{\lambda_{hkl} - \lambda}{\tau} + \frac{\sigma^2}{2\tau^2} \right) \times \operatorname{erfc} \left( \frac{\lambda_{hkl} - \lambda}{2^{1/2} \sigma} + \frac{\sigma}{2^{1/2} \tau} \right) \right] \quad (4.5)$$

where  $C_1$  is the transmission before the edge and  $C_2$  is half of the Bragg edge height. Additional parameters of  $K_1$  and  $K_2$  have been included to Eq. (4.5) to accommodate the slope in the transmission signal before and after the Bragg edge. The equation becomes:

$$Tr(\lambda) = C_1 + K_1(\lambda - \lambda_{hkl}) + (C_2 + (K_2 - K_1)(\lambda - \lambda_{hkl})) \times \frac{1}{2} \left( \operatorname{erfc} \left( \frac{\lambda_{hkl} - \lambda}{2^{1/2}\sigma} \right) - \exp \left( \frac{\lambda_{hkl} - \lambda}{\tau} + \frac{\sigma^2}{2\tau^2} \right) \right) \operatorname{erfc} \left( \frac{\lambda_{hkl} - \lambda}{2^{1/2}\sigma} + \frac{\sigma}{\tau} \right) \quad (4.6)$$

where  $C_2$  in this case is the full Bragg edge height, while the other parameters such as  $\tau$  and  $\sigma$  have the same definition as the previous equations. The full assessment of the Bragg edge fitting functions described here is presented in **Section 7.2**.

Other Bragg edge fitting functions which are used by the neutron imaging community are:

1. Analytical function based on the Beer-Lambert-Bouguer law and implemented in the RITS code (Sato et al., 2011).
2. Analytical function mentioned in Steuwer et al. (2001) and implemented in iBeatles code (Bilheux, 2018).

### 4.2.3 Bragg edge parameter map reconstruction

In the previous section, Bragg edge fitting and parameterisation has been presented, which is useful to describe material parameters, e.g., lattice spacing, crystallographic orientation, and phase, in a selected location of a sample. The point of Bragg edge imaging, however, is to describe these parameters for a large area of a sample. In theory, the most obvious way to do it is to reconstruct Bragg edge parameter maps by performing pixel-by-pixel fitting across the field-of-view of the detector, as previously shown in Fig. 3.9. Considering a high spatial resolution neutron detector such as a micro-channel plate (MCP) detector has a quarter-million pixels, a software tool is needed to perform the pixel-by-pixel fitting and parameter map reconstruction.

In practice, however, it is not always possible to carry out a pixel-by-pixel analysis. Taking the MCP detector again as an example, within a reasonable measurement time at a pulsed neutron source, there are not enough neutron counts in a single  $55 \mu\text{m} \times 55 \mu\text{m}$  pixel to provide sufficiently good statistics for data analysis. Fig. 4.9(a) shows the transmission spectrum from a single pixel of the MCP detector, measured from  $\alpha$ -iron (Fe) with a thickness of 20 mm in the transmission direction for 4 hours with an 80 mm pinhole on the IMAT

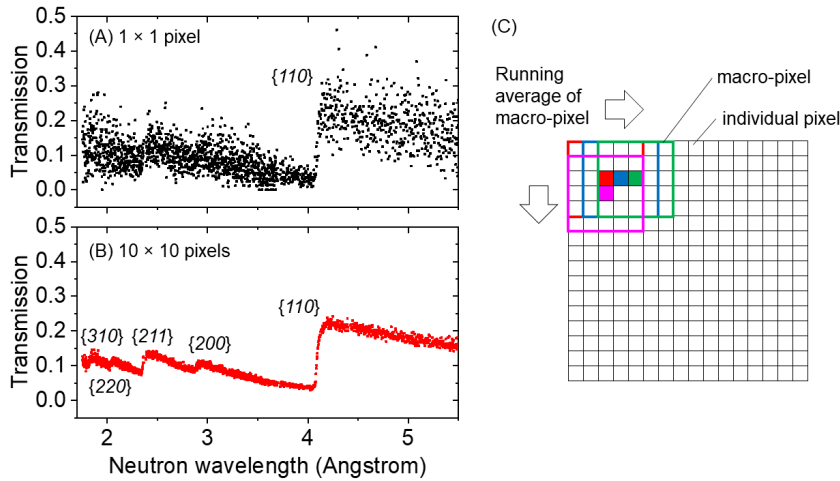


Fig. 4.9 Transmission spectrum from (a) 1 pixel and (b)  $10 \times 10$  macro-pixel, measured from  $\alpha$ -iron (Fe) sample with 20 mm thickness in transmission direction; (c) Illustration of Bragg edge map reconstruction using macro-pixel running average.

beamline. The spectrum is noisy with the Fe  $\{110\}$  the only resolvable Bragg edge. To improve the statistics, counts from a group of pixels are combined, a so-called macro-pixel. For the current version of MCP detector, the size of macro-pixel typically ranges from  $5 \times 5$  to  $50 \times 50$  pixels, with the spectrum assigned to the centroid of the macro-pixel. The running average of the macro-pixel with step size of 1 pixel ( $55 \mu\text{m}$ ) is then applied across the image to reconstruct the Bragg edge parameter map. The macro-pixel and the running average reconstruction is illustrated in Fig. 4.9(c). Meanwhile Fig. 4.9(b) shows the transmission spectrum from a  $10 \times 10$  macro-pixel (around  $0.5 \times 0.5$  mm), measured from the same Fe sample, where statistics are much improved with five resolvable Bragg edges.

In the case where the Bragg edge height parameter is of interest, there is an option to perform time-binning (instead of pixel-binning mentioned above), i.e., combined adjacent time-bins into single data points across the spectrum. While the time-binning reduce the wavelength resolution of the signal, it improves the statistics while preserving the spatial resolution.

#### 4.2.4 Bragg edge parameter mapping software tool

As mentioned in the previous section, a software tool is needed to perform a Bragg edge parameter map reconstruction. The general algorithm for the software tools to reconstruct a raw neutron transmission data into a Bragg edge parameter map is shown in Fig. 4.10. Raw data from sample and flat field measurement, in the form of image stacks, are prepared. A flat field or open beam measurement is a neutron exposure where no sample is mounted,

and is used to normalise the sample data and to account for detector and neutron beam inhomogeneities. A list of  $z$ -axis profiles, i.e., neutron counts (or intensity) as a function of wavelength, is extracted from the sample and flat field image stack, by applying the running average of macro-pixel across the image. Normalisation using Eq. (3.10) is then performed to obtain a list of transmission spectra. Bragg edge fitting is carried out for each of the transmission spectra. Finally, the fitted parameters are assigned accordingly onto an  $xy$ -plane to produce 2D maps of Bragg edge parameters.

There are several software tools currently available to perform Bragg edge mapping, with the main difference being the analytical function used to fit the Bragg edge. The currently available Bragg edge mapping software are as follows:

1. BEATRIX (Triestino Minniti, Personal Communication, June 2017) is a ROOT based code which uses Eq. (4.4) and Eq. (4.3) to fit the Bragg edges. It works well for lattice spacing (hence strain) determination in aluminium (Ramadhan et al., 2019), Bragg edge broadening analysis for the investigation of plasticity in steel (Reid et al., 2018), and Bragg edge height analysis for phase mapping (Vitucci et al., 2018a).
2. TPX\_Edgefit (Anton Tremsin, Personal Communication, 1 October 2016) is a C++ based code which utilises the 5-parameter non-linear fitting function described in Eq. 4.5. Despite using a function with less parameters, it has been proven to be reliable for mapping strain in dissimilar metal welds (Tremsin et al., 2016b) and weakly-textured aluminium silicon-carbide (AlSiC) metal matrix composite (Ramadhan et al., 2018). The strain maps presented in this work are mainly produced by the TPX\_Edgefit software, and to a lesser extent, the BEATRIX software.
3. iBeatles (Bilheux, 2018) is a Python-based code which uses a phenomenological function described by Steuwer et al. (2001). Similar to Eq. (4.3), the phenomenological function models Bragg edges with four parameters: position, height, width, and asymmetry. Gian Song et al. (2017) also mentioned a Bragg edge model that accounts for the distribution of crystallographic orientation and crystalline size in the publication; however the model has yet to be embedded in the iBeatles software.
4. RITS (Sato et al., 2011) is a single-edge fit and Rietveld-type Bragg edge analysis software. RITS considers the effect of incident neutron pulse shape, variation of the lattice spacing, crystallographic orientation distribution, and extinction inside one crystal. It then simulates a neutron transmission spectrum and fits the spectrum to an experimental spectrum by adjusting the parameter, pixel-by-pixel across the entire image. It has been demonstrated that the code has successfully provides a quantitative

visualisation of crystallographic texture and microstructure inside an  $\alpha$ -iron plate (Sato et al., 2011).

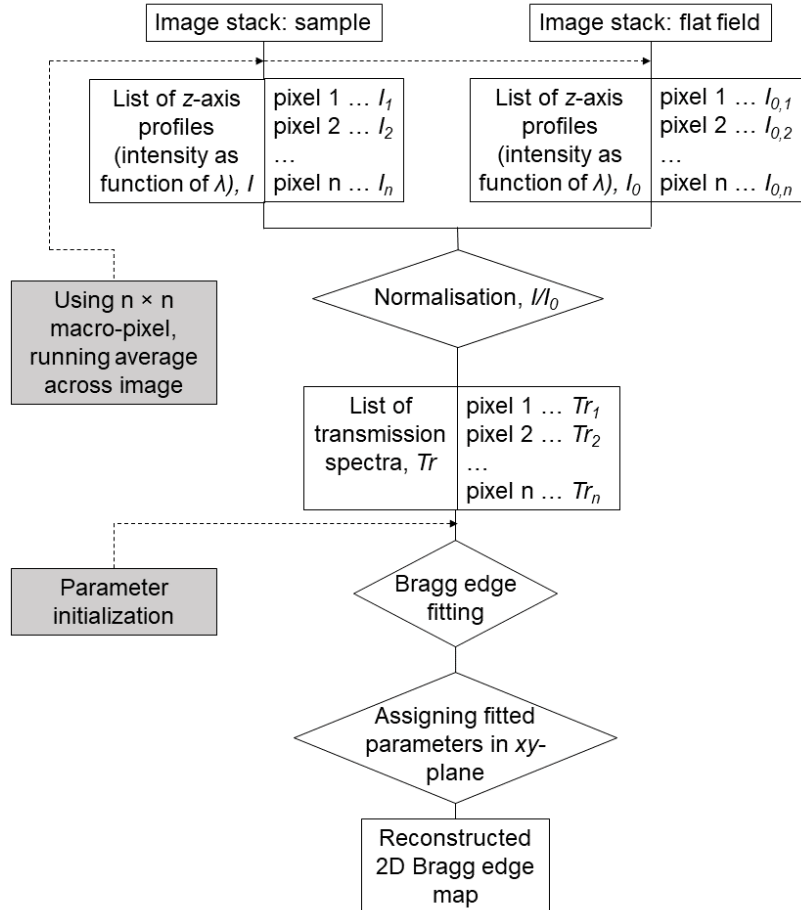


Fig. 4.10 Typical algorithm of Bragg edge parameter mapping.



# **Chapter 5**

## **Time-of-flight Neutron Imaging Beamline: IMAT at ISIS, UK**

This chapter provides a comprehensive description of a time-of-flight neutron imaging instruments: the IMAT beamline at the ISIS neutron source, Didcot, UK. Firstly, a brief overview of the IMAT instrument including the background, historical development and the principal design parameters will be presented. The detailed instrumentation of the beamline is then described, starting from the source all the way to the sample area. An emphasis will be given on the neutron imaging detectors on the beamline. Finally, the Bragg edge imaging software currently available on IMAT will be discussed. This chapter will provide an overview of the instrumentation of a neutron imaging instrument on a pulsed source, and will help future beamline users in understanding instrument parameters and how they will affect the experiments.

### **5.1 Overview of the IMAT beamline**

The proof-of-concept and development of time-of-flight (TOF) neutron imaging on pulsed sources have been carried out in the last decade, showing the potential benefit of the technique and making it a useful tool for material science and engineering studies (Kockelmann et al., 2007; Strobl, 2009; Strobl et al., 2011; Shinohara et al., 2016). Since the late 1990s, time-of-flight Bragg edge transmission performed in a radiography-type measurement setup has been developed at ISIS. A transmission detector with an array of  $10 \times 10$  pixels, with pixel size of 2 mm, was implemented on ENGIN-X, located at target station 1 (TS-1) in the late 1990s. The setup successfully provided a precise determination of Bragg edge position, lattice parameter and strain, as well as indication of texture (Steuwer et al., 2001; Santisteban et al.,

2002a, 2006b). While the setup demonstrated the potential of Bragg edge mapping, the beamline was not optimised for imaging and the detector spatial resolution was limited to 2 mm. On the other hand, the development of micro-channel based neutron detectors allows time-of-flight neutron imaging with high spatial resolution (Tremsin et al., 2009). This, and the growing importance of TOF imaging technique pushed forward the development of an imaging beamline at the ISIS neutron source, UK.

IMAT was proposed back in 2007 as the first dedicated imaging beamline at ISIS, with the capability to perform experiments in either imaging or spatially resolved diffraction mode, interchangeably. The project was started in 2011 with the first opening of the beam shutter in 2015. The engineering commissioning was carried out and overlapped with scientific commissioning between 2015 to 2018. In the beginning of 2016, the first time-of-flight imaging data from IMAT were acquired. IMAT started its user program in March 2018. While the main construction of the beamline is completed, developments are still being carried out especially on the imaging and diffraction detector. Currently, there are two time-of-flight imaging camera systems available (i.e., MCP and GP2 detector) and two white beam/ optical camera system ("Messina cameras") available on IMAT. Several other imaging camera systems are envisaged for the future (Kockelmann et al., 2018). Meanwhile, there are two, 90-degree prototype diffraction detectors currently installed. The full 90-degree detector modules along with the radial collimators will be installed in summer 2020 and will be ready for users in 2021. A project plan to install more diffraction detectors at forward and back-scattering angles is envisaged, with the design and simulation work currently being carried out.

IMAT is a multi-purpose neutron instrument which was designed to perform both spatially resolved diffraction and imaging measurements which include 2D and 3D (tomography) imaging. Therefore, the instrument needs to follow certain attributes and design considerations (Kockelmann et al., 2013), some of which are similar to engineering diffractometer designs at pulsed sources (Johnson and Daymond, 2003):

1. an ability of accurate atomic lattice spacing determination: the imaging and diffraction setup requires a long primary flight-path while the instrument's wavelength resolution ( $\Delta\lambda/\lambda$ ) needs to be sufficiently high for strain measurement via Bragg edge analysis.
2. an ability of measurement of multiple reflection planes, therefore the instrument needs to have a wide wavelength band.
3. an ability to modify the beam size: while the imaging mode requires a large beam (in the order of many  $\text{cm}^2$ ), the diffraction mode requires a small beam (in the order of  $\text{mm}^2$ ) for the definition of the gauge volume.

4. high beam flux, especially for imaging and in-situ diffraction applications, at the expense of wavelength resolution
5. a homogeneous beam profile at the sample position in space and time (wavelength), symmetric and flat across the imaging camera.
6. an ability to finely modify and accurately measure the orientation of the sample.
7. for imaging applications, an imaging detector with high spatial and temporal resolution.
8. for diffraction application, an ability of accurate gauge volume determination and simultaneous measurement of two orthogonal strain components: this can be achieved by placing diffraction detectors at 90-degrees at the left and right of the incoming beam, in conjunction with radial collimators.

To meet these objective characteristics, IMAT was build upon specific principal design parameters (Kockelmann et al., 2013). The characterisation of the instrument's parameters, especially for imaging, has been carried out in this work [see **Chapter 6**, also publication by the author in journal publication (Ramadhan et al., 2019)] and in other work (Minniti et al., 2018). Table 5.1. shows the IMAT design parameters, listed in (Kockelmann et al., 2018), with the validated parameters in this work highlighted. In order to understand the functioning of a time-of-flight imaging instrument for material science and engineering studies, the setup of the IMAT beamline is described in some detail in the following section.

## 5.2 IMAT instrumentation

### 5.2.1 General schematics

Fig. 5.1 shows the schematics of the ISIS pulsed neutron and muon source complete with the neutron and muon beamlines. Up to 2019, ISIS comprises 37 neutron and muon beamlines. IMAT, shown by the arrow, is located at the ISIS Target Station 2 (TS-2) beam port W5. While the front end of the instrument is located within the R80 experimental hall, the sample area is located in an extension to R80, owing to the length of the neutron guide require to deliver the desired resolution, Fig. 5.1. Fig. 5.2 shows a photograph of the IMAT extension building where the sample area is located.

Fig. 5.3 shows the schematic layout of the main IMAT beamline components. High energy protons hit the neutron target, producing high energy neutrons. The neutrons are slowed down in the moderator, producing neutrons in an energy range suitable for scattering

Table 5.1 IMAT instrument parameters for time-of-flight imaging as listed in (Kockelmann et al., 2018). The parameters written in blue are the ones validated in this work, presented and discussed in the following chapters.

This item has been removed due to third party copyright. The unabridged version of the thesis can be viewed at the Lanchester library, Coventry University

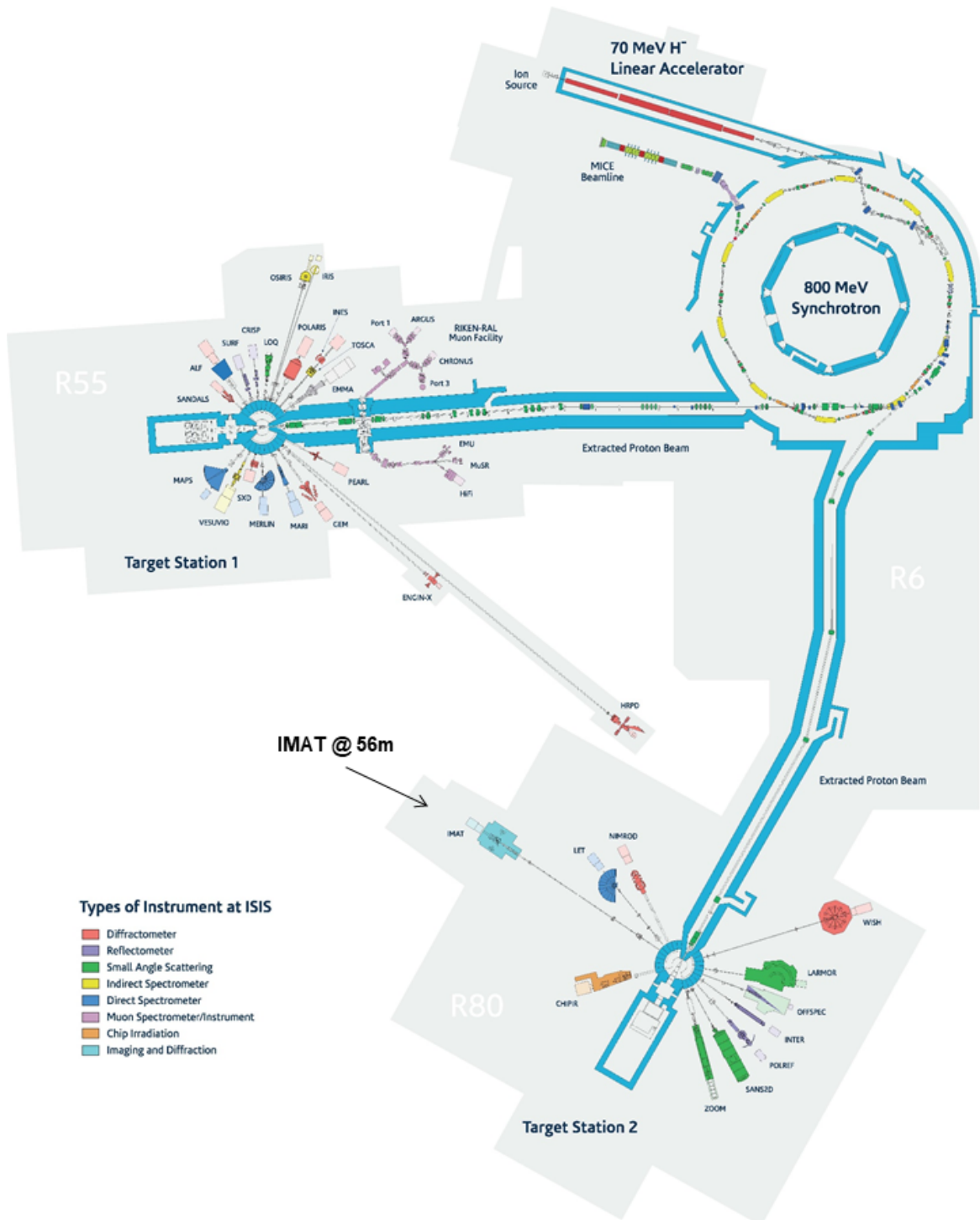


Fig. 5.1 Schematic of ISIS pulsed neutron source with the neutron and muon beamlines. The IMAT instrument is shown by the arrow.



Fig. 5.2 IMAT extension building to R80 experimental hall, where the sample area, sample preparation laboratory, active sample storage and chemistry laboratory are located.

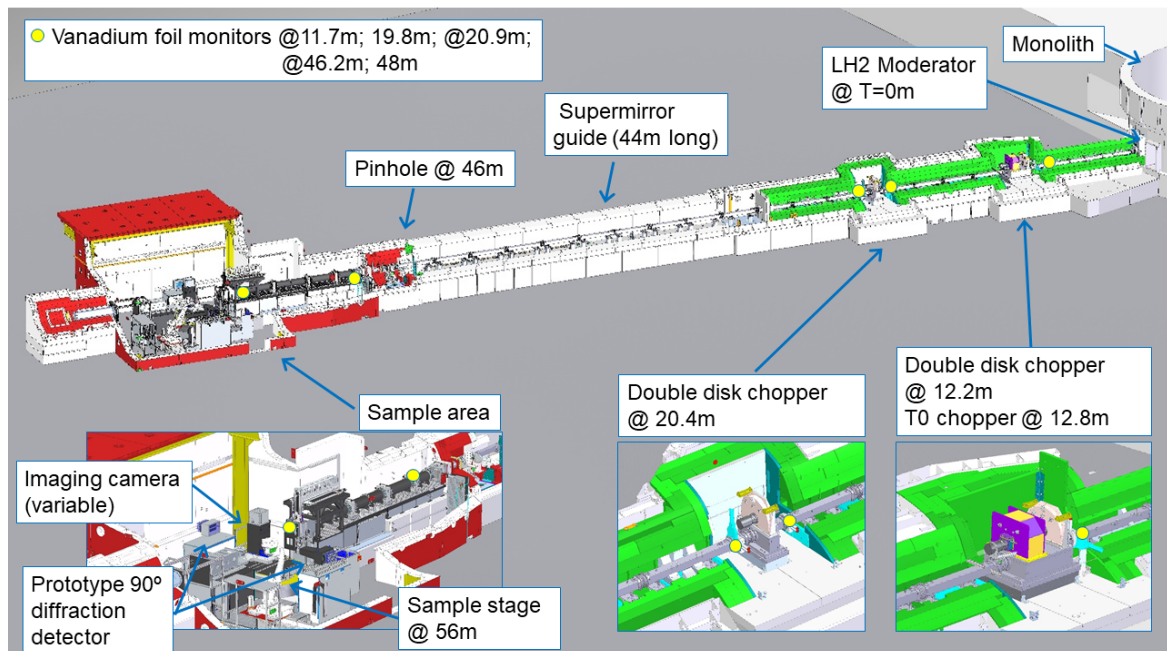


Fig. 5.3 Overall overview schematic of the IMAT beamline.

and imaging experiments. The neutrons are then transported to the sample area via an evacuated neutron supermirror guide with total length of 44 m. A series of choppers, 2 double disk choppers at 12.2 m and 20.4 m and a T<sub>0</sub> chopper at 12.8 m were placed in between the neutron guides to define the wavelength band of the neutrons and stop unwanted gamma radiation from the source. Before reaching the sample area, the neutron beam travels through the aperture or pinhole selector at 46 m, before being guided in evacuated tubes and shaped by a series of slits. The long flight path of 56 m from the face of the moderator to the centre position of the sample positioning system ensures a good time-of-flight resolution while retaining a large wavelength band. Neutrons traversing the sample are recorded by the imaging detector placed behind the sample in line with the beam propagation direction. Diffracted neutrons will be recorded by the diffraction detectors placed at different angles around the sample position (not shown in the Fig. 5.3). Instead, two prototype 90° diffraction detectors are indicated in the figure.

### 5.2.2 Source and moderator

The neutron generation at ISIS starts in the injector and the synchrotron. The process is illustrated in a schematic shown in Fig. 5.4. At the very start, an ion source produces H<sup>-</sup> ions (negatively charged hydrogen with a single proton and two electrons) via electric discharge. A Radio Frequency Quadrupole (RFQ) accelerators accelerates and separates the ions into bunches. These bunches are further accelerated in the linear accelerator (linac) to 70 MeV or equal to 37% of the speed of light. The ion bunches then enter the synchrotron, a ring of magnets with 163 m circumference. Upon entry, electrons are stripped from the ions using a thin graphene foil, leaving a beam of protons. The protons are then accelerated to 800 MeV, equal to 84% of the speed of light. The beam makes about 10,000 revolutions around the synchrotron before being ejected into the extracted proton beamline by fast kicker magnets. The acceleration and ejection process is repeated at a frequency of 50 Hz with a mean current of 200 μA.

80 percent of the pulses (40 Hz, 160 μA) is transported to the Target Station 1 (TS-1), while the rest (10 Hz, 40 μA) is transported to Target Station 2 (TS-2). In the target station, the proton beam hits the neutron target which is made of a series of thick tungsten plates clad with tantalum. Neutrons are then produced through a spallation process (**Section 2.1.2** and Fig. 2.2), before being slowed down for experimental use in the moderator. The IMAT is placed on the coupled 18 K liquid hydrogen moderator.

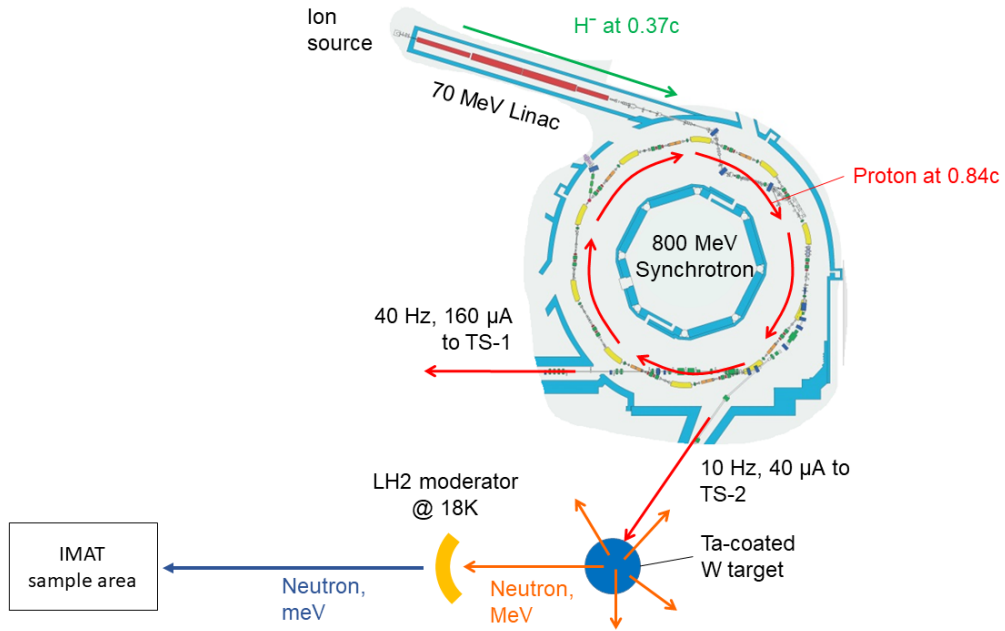


Fig. 5.4 Schematics of the neutron generation and moderation at ISIS.

### 5.2.3 Beam transport system

Fig. 5.5 shows the schematic overview of the system which transports the neutron beam from the moderator to the sample area. After the neutron beam is produced in the target assembly (tungsten target, moderators and reflectors), it is transported through a protective shutter and a shielding insert. These parts are enclosed in a heavily shielded area called the monolith. The shutter is a protective device, which on its lowest position fully blocks the neutron beam and allows safe access to the sample area. Multiple sections of 3 m supermirror guides, a total of 44 m, transports the neutrons to the sample area. The guide was manufactured and installed by Mirrortron. The guide ends at 45.7 m from the target and is followed by 9 m of vacuum flight tubes. The flight tubes, fabricated from aluminium alloys, include diagnostics and beam collimating equipment. The whole beam transport system is evacuated to avoid air scattering of the neutrons.

Four time-of-flight beam monitors are placed along the beam transport system for diagnostics purposes, made of 40  $\mu\text{m}$ -thick vanadium foil. Three monitors (M1 to M3) are positioned in between the choppers, Fig. 5.5, while the M4 monitor is positioned directly after the pinhole. A fifth M5 monitor is a remotely retractable monitor, made of 100  $\mu\text{m}$ -thick vanadium foil and is placed after the beam attenuator.

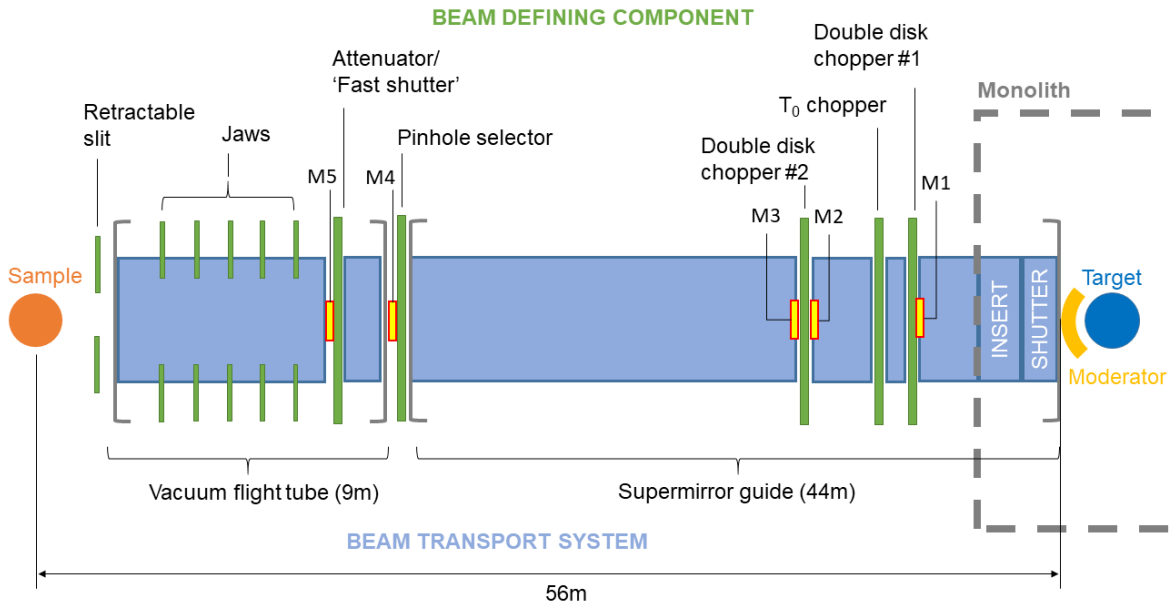


Fig. 5.5 Schematics of the beam transport system and the beam defining components.

#### 5.2.4 Beam defining components

There are several components applied along the beam transport system, illustrated in Fig 5.5, in order to define the neutron beam to the desired profile (i.e., energy, shape and intensity) for different experiments. IMAT has three choppers: two double disc choppers at 12.2 m, Fig. 5.6(a) and 20.4 m, Fig. 5.6(b), and a T-zero chopper at 12.7 m, Fig. 5.6(a), from the moderator to define the energy or wavelength profile of the beam. The double disc chopper has two 780 mm diameter aluminium alloy discs, each with a minimum of 10 mm layer of B4C ‘dough’ to attenuate the neutrons. Each disk has a slit to allow some neutrons to pass through, Fig. 5.6(c). Rotating at a defined frequency (typically 10 Hz), the choppers allow the definition of wider or narrower wavelength bands and also prevent frame-overlap of neutrons between successive time frames (Kockelmann et al., 2018). The T-zero chopper serves as a fast neutron and gamma filter.

IMAT has a pinhole selector wheel, Fig. 5.7(a) and (b), which is a rotating device which offers five circular apertures; currently installed  $D = 5, 10, 20, 40$ , and  $80$  mm diameter and one large square aperture of  $100 \times 100$  mm<sup>2</sup>. The pinhole produces a quasi-parallel neutron beam which governs beam divergence through the ratio  $L/D$ . Smaller pinholes produce smaller divergences at the expense of beam flux, described in more detail in Section 4.2.3.

The sample attenuator (or fast shutter) is a neutron absorbing blade made of a <sup>10</sup>B-coated aluminium sheet, installed on IMAT upstream from the sample position, and can be driven

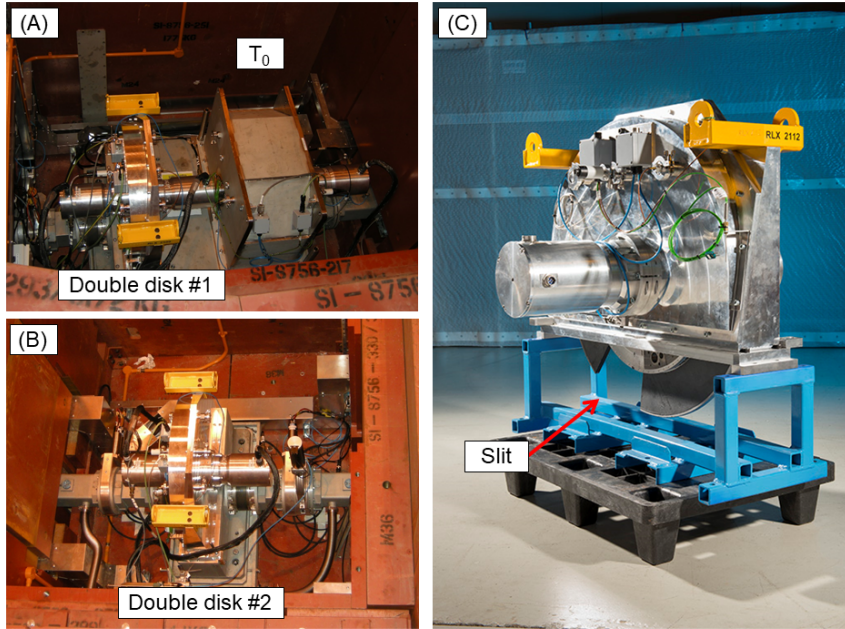


Fig. 5.6 Photograph of (a) chopper pit 1 containing the first double disk and the  $T_0$  chopper, and; (b) chopper pit 2 containing the second double disk chopper; (c) The photograph of a double disk chopper showing the slit.

into and out of the beam using a pneumatic actuator. The sample attenuator can be controlled both via the graphical user interface or script, and therefore used to minimise the sample and camera exposure to neutron (and therefore activation) when the shutter is open and the data is not being taken.

The beam size on IMAT can be varied between  $1 \times 1 \text{ mm}^2$  and  $200 \times 200 \text{ mm}^2$  using five collimating ‘jaws’, each made of four 10-mm-thick sintered boron carbide blades. When a very precise and well-defined beam size is needed, e.g., for determination of a gauge-volume in a diffraction experiment, a set of incident slits (3 mm thick  $^{10}\text{B}$  blades) retractable along the beam direction is available, Fig. 5.7(c). This can be used to define a small aperture between  $1 \times 1 \text{ mm}^2$  and  $50 \times 50 \text{ mm}^2$ .

### 5.2.5 Sample area

The IMAT sample positioning system (SPS), Fig. 5.8(a), is designed to accommodate a wide range of samples and experiments, and is used for sample alignment and sample rotation. The system was designed and manufactured by STFC Daresbury Laboratory. It has seven axes for sample movements:

1. A large rotation,  $\Theta_1$ , with a range of  $360^\circ$ .

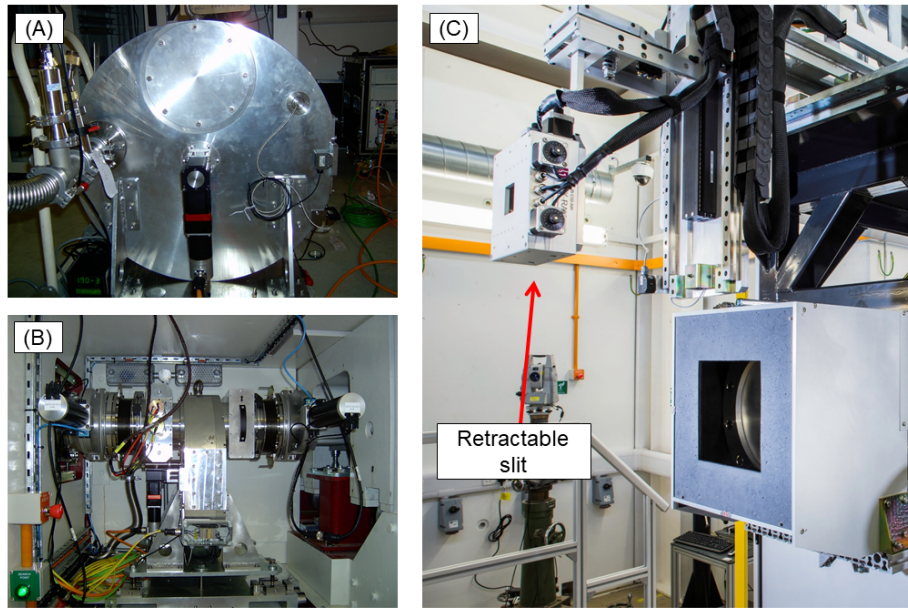


Fig. 5.7 Photograph of the pinhole selector wheel (a) off the beamline, showing the cross section, and (b) installed on the beamline; (c) Retractable slit in front of the vacuum flight tubes.

2. Three linear stages, ‘X’, ‘Y’ and ‘Z’, with a range of 1 m.
3. Two orthogonal tilts,  $\theta_1$  and  $\theta_2$  with a range of  $10^\circ$ .
4. A tomography rotation stage,  $\Theta_2$  with a range of  $360^\circ$

The x, y, and z direction of the SPS are in the beam direction, transverse direction, and vertical direction, respectively, consistent with the IMAT coordinate system. The SPS is designed to lift and accurately position 1.5 tonnes loads, while the smaller tomography rotation stage can handle samples of up to 50 kg. A laser pointer beam along the incident neutron beam direction and one theodolite are available to aid sample alignment.

A robotic camera positioning system (CPS) is available on IMAT, Fig. 5.8(b). The CPS is a 7 axis robotic manipulator arm designed to lift, accurately position and hold different neutron detectors. The system allows easy mounting and dismounting of different detector systems. Fig. 5.8(c) shows the main components inside the IMAT sample area, including the imaging detector and the prototype 90° diffraction detector.

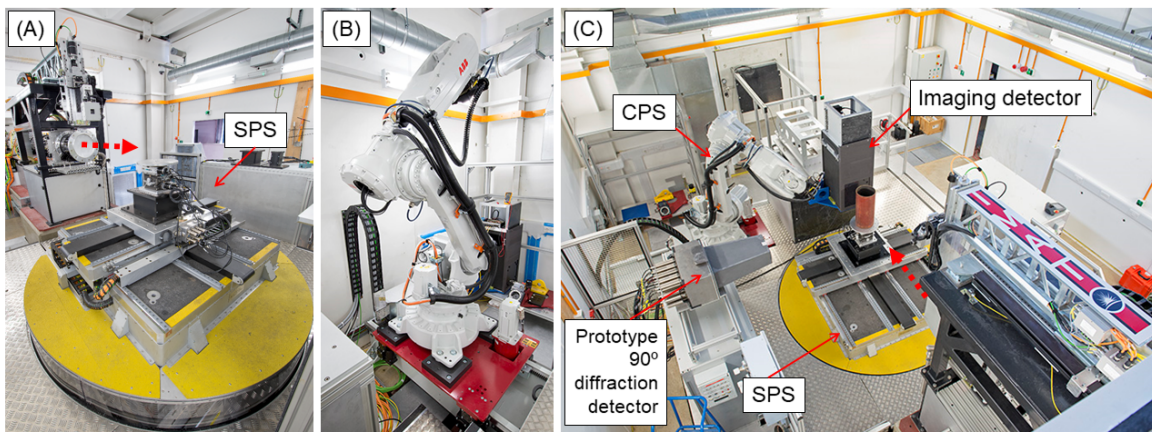


Fig. 5.8 Photograph of (a) the sample positioning system (SPS); (b) camera positioning system (CPS), and; (c) the sample area of IMAT, showing the imaging detector and the prototype 90° diffraction detector. The neutron beam direction is shown by the red-dotted arrow.

### 5.2.6 IMAT infrastructure

As a general user instrument, IMAT provides an infrastructure to ensure a safe and efficient operation for experiments. The experimental area (including part of flight tubes, SPS and detectors) are enclosed in a shielded 'blockhouse', with a power-operated roof to allow easy access for lifting heavy equipment or samples using a 2-ton crane. Most operations on IMAT can be performed from outside the blockhouse via a central control station called NDXIMAT in the IMAT cabin. Infrastructure for sample environment such as for operation of furnace and loading rigs are available. Also available are a sample preparation laboratory and a lockable room for storing large objects, valuable samples and radio-activated samples and equipment. A more detailed information about IMAT infrastructure are available (Kockelmann et al., 2018).

## 5.3 IMAT imaging detectors

### 5.3.1 MCP detector

The microchannel plate (MCP) detector on IMAT uses MCP containing 10%  $^{10}\text{B}_2\text{O}_3$  and 3%  $\text{Gd}_2\text{O}_3$  in a glass matrix. The doping materials work as a converter from neutrons to energetic charged particles (e.g., alpha and  $^7\text{Li}$  for  $^{10}\text{B}$ ). These charged particles impact onto the inner surfaces of the MCP pores and create an electron avalanche within a pore which is subsequently detected by the readout component.

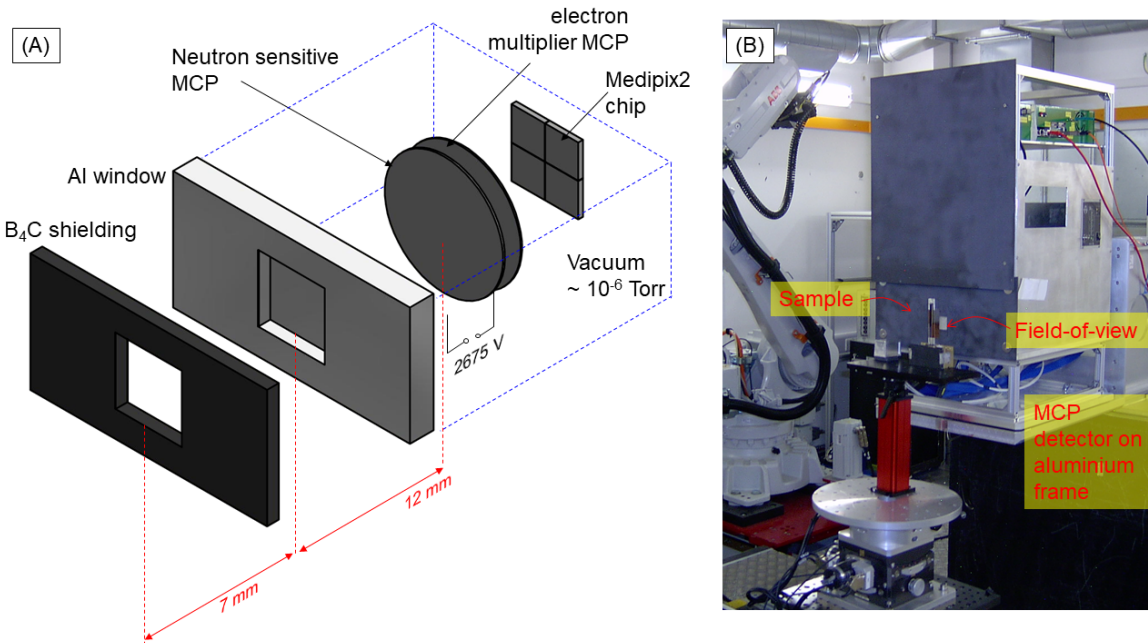


Fig. 5.9 (a) Exploded view of the main components of the MCP detector on IMAT; (b) Photograph of the MCP detector on an aluminium frame, showing the field-of-view and the sample in front of the detector.

The microchannel plate (MCP) detector on IMAT was developed by the University of California at Berkeley. The main components of the MCP detector, with a schematic shown in Fig. 5.9(a), comprises a stack of microchannel plates placed at  $\approx 0.8$  mm distance from the array of Medipix2/Timepix ASIC readout. The microchannel plates have a diameter of 50 mm, a thickness of 0.6 mm with  $\approx 10$   $\mu\text{m}$  pores packed with 12  $\mu\text{m}$  pitch. The plate on the incident beam side is doped and serves as a neutron-to-electron converter, while the plate on the detector side is not doped and acts as an electron amplifier via potential difference, with a total of 2675 V applied across the two MCPs. The electrons are then detected by a  $2 \times 2$  array of Timepix chips. Each chip has  $256 \times 256$  pixels with 55  $\mu\text{m}$  pixel size and a gap between chips of  $\approx 150$   $\mu\text{m}$  (Vitucci et al., 2018b), which provides a total active area of  $\approx 28 \times 28$   $\text{mm}^2$ . The MCP and readout assembly are placed in a vacuum enclosure operating at  $\approx 10^{-6}$  Torr pressures. In front of the neutron-sensitive MCP is an aluminium window, providing a total distance from the front of the window to the active area of 12 mm, Fig. 5.9(a). The window has a recess of 2 mm, and, to protect the electronics, a 5-mm-thick B<sub>4</sub>C shielding is attached around the aluminium window with a gap of around 2 mm. This results in a minimum sample-to-detector distance of 19 mm, thus limits the achievable spatial resolution and thus needs to be considered while designing experiments. The MCP detector,

vacuum pump and the data processing unit sit on an aluminium frame, Fig. 5.9(b), designed to work compatibly with the robotic camera positioning system.

While the Medipix2/Timepix chip has two other data acquisition modes, i.e., event counting mode and event centroiding mode, time-of-flight imaging uses the event timing mode, in which the arrival time of an individual neutron signal relative to the trigger signal is measured. The timing information is stored in each Timepix pixel before being transferred to the data processing unit. The data readout from all of the pixels takes place at the end of every ‘shutter period’, an arbitrary and adjustable data acquisition period within the 0.1 second pulsed source time frame. One frame can comprise multiple shutter periods. There are a maximum of 3100 time bins within a single frame, with the smallest time bin of 10 ns. Only one event, however, can be stored in each pixel for a given shutter period. Therefore, subsequent events in the same pixel are rejected until the data are transferred at the end of the shutter period. Under high flux condition, this ‘overlap’ effect can decrease the counting efficiency of the detector at the end of each shutter period and could severely distort the time-of-flight spectrum. This problem, however, can be solved by applying an overlap correction with a method proposed by Tremsin et al. (2014). Reducing the flux and shortening the length of the individual shutter period can also reduce the overlap effect. Other effects related to the current version of MCP detector available at IMAT has been characterised (Watanabe et al., 2017). All of the Bragg edge imaging measurements reported in this text, including measurements on BL22-RADEN beamline in J-PARC, Japan, uses this version of the MCP detector.

The main limitations of the current version of the MCP detector are the readout and the size of the field-of-view. These problems will be solved in the future with the implementation of the next generation of MCP detector with tiled MCP and Medipix3/Timepix2 chips, currently being developed. As mentioned above, readout at the end of every shutter period in the current MCP detector version causes saturation and decreases the efficiency of the detector, especially under high flux conditions. The next generation chip will allow ‘sparsified readout’, where data stored in the individual pixel is being readout each time an event occurs, therefore minimising the possibility of data rejection. The active area will also be increased by tiling readout chips side-by-side, producing an active area in  $28 \times N \text{ mm}^2$  configuration. The next generation chip will also allow greater number of time bins of up to 10,000.

### 5.3.2 GP2 detector

GP2 is a time-of-flight position sensitive neutron detector which utilises gadolinium as a neutron conversion material, combined with a second generation of mass spectrometry sensor

called PImMS2. The detector is developed in-house at ISIS in collaboration with Oxford University (Pooley et al., 2017).

The main component of the GP2 detector is a PImMS CMOS sensor, a monolithic sensor (i.e., not an array of sensors) with  $324 \times 324$  pixels, each with a pixel size of  $70 \times 70 \mu\text{m}$ , providing an active area of  $22.7 \text{ mm} \times 22.7 \text{ mm}$ . The sensor operates in event mode, and therefore every recorded neutron is assigned a position based on the pixel location and a unique time stamp. Each pixel has four 12-b SRAM memory registers which can record up to four neutrons per frame. A maximum of 4096 time slices can be recorded with a minimum time bin of 12.5 ns.

In order to make the PImMS sensor sensitive to neutrons, a thin film of gadolinium was sputtered onto the sensor surface, with film thickness of  $4 \mu\text{m}$ . The gadolinium acts as the neutron-to-electron converter. The electrons are then registered by the pixel in the detector. Due to its memory register capability, the sensor can operate as a 1, 2, 3, or 4 register detector, with higher register reducing the overlap effect but requiring longer readout time. Despite needing improvement in detection efficiency, currently around 8.5%, the GP2 detector has a compact design, allowing the camera to be placed close to a sample or a sample environment. This is useful where a small sample-to-detector distance is required.

### 5.3.3 Messina camera boxes

The Messina camera is an imaging system working in the event counting mode without time-resolving capability. However, it has a high spatial resolution and significantly larger active area compared to TOF cameras. Therefore the Messina camera is more suitable for white beam radiography and tomography. There are two optical boxes on IMAT: Messina-1 with CCD camera and Messina-2 with CMOS camera.

Largely sharing similar design with CCD-based camera system at various neutron facilities around the world, the Messina cameras are built upon a light-tight box, made of black-anodized aluminium (Finocchiaro et al., 2013). An interchangeable scintillator screen, typically  ${}^6\text{LiFZnS}$ -based with varying thickness from 20 to  $450 \mu\text{m}$ , is placed in the front side of the box facing the incident beam. The size of the scintillator is adapted field-of-view that range from  $60 \times 60$  to  $210 \times 210 \text{ mm}$ . The scintillator converts the neutrons to visible light with wavelengths in the range of 450-520 nm. A glass mirror, placed at  $45^\circ$  from the scintillator, reflects the light towards a focusing lens. The lens project the scintillator area onto the chip of the CCD or CMOS, located at the top of the box, thus dictate the field-of-view. The effective pixel size of the detector is in the range of  $29\text{-}103 \mu\text{m}$  for the Messina-1 and  $13\text{-}114 \mu\text{m}$  for the Messina-2. The schematic and the photograph of the Messina camera box is shown in Fig. 5.10.

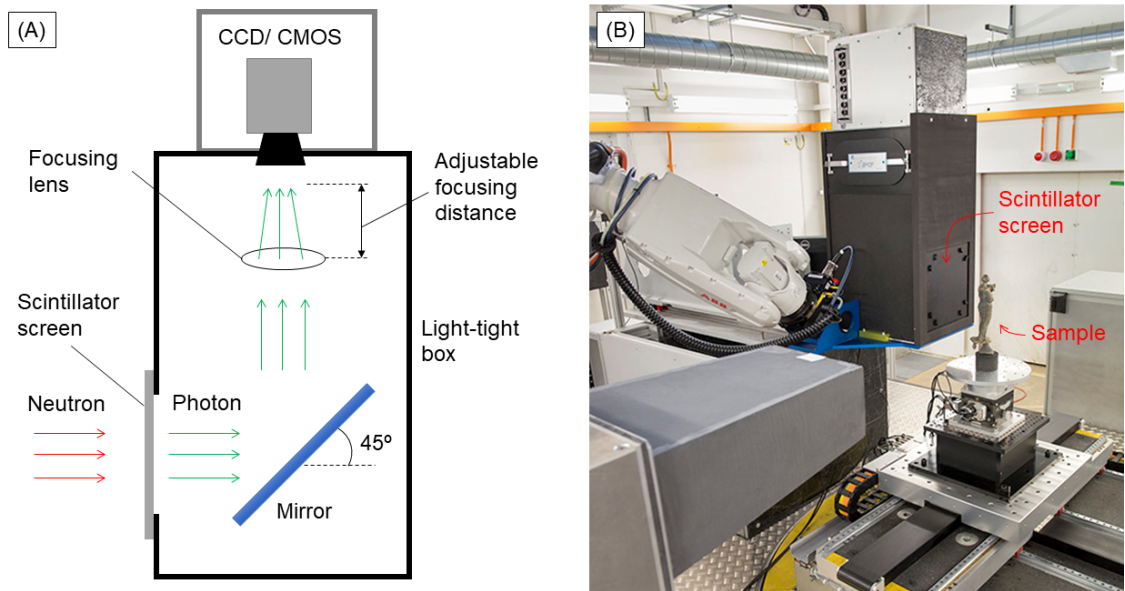


Fig. 5.10 (a) Schematics of the main components of the Messina camera on IMAT; (b) Photograph of the messina camera assembly, showing the light-tight box, scintillator screen and a sample in front of the detector.

Continuous development of imaging detectors on IMAT is being carried out, with emphasis on the improvement of detector active area and detection efficiency. A list of envisaged future IMAT camera systems is provided by Kockelmann et al. (2018).

## 5.4 IMAT GUI and analysis tools

It is important to note that the development of these software was not carried out by the author. However, the author was involved in testing and validation of some of the software, providing feedback to the developer to improved different aspects of the tool.

### 5.4.1 IMAT GUI

Most of the control and monitoring of the IMAT instrument components including choppers, pinhole selector, beam monitors, sample attenuator, jaws, and sample environment are carried out in the NDXIMAT machine using the IBEX instrument control graphical user interface. Fig. 5.11 shows a screen shot of the IBEX GUI. IBEX also controls the ISIS DAE-2 data acquisition system, which manages the ISIS trigger signal and records the monitor counts as a function of TOF, as well as reads out from the IMAT diffraction detectors in the future.

The control of components can also be achieved via command line and python scripts which enables scripting of most instrument control options and automates the instrument operation.

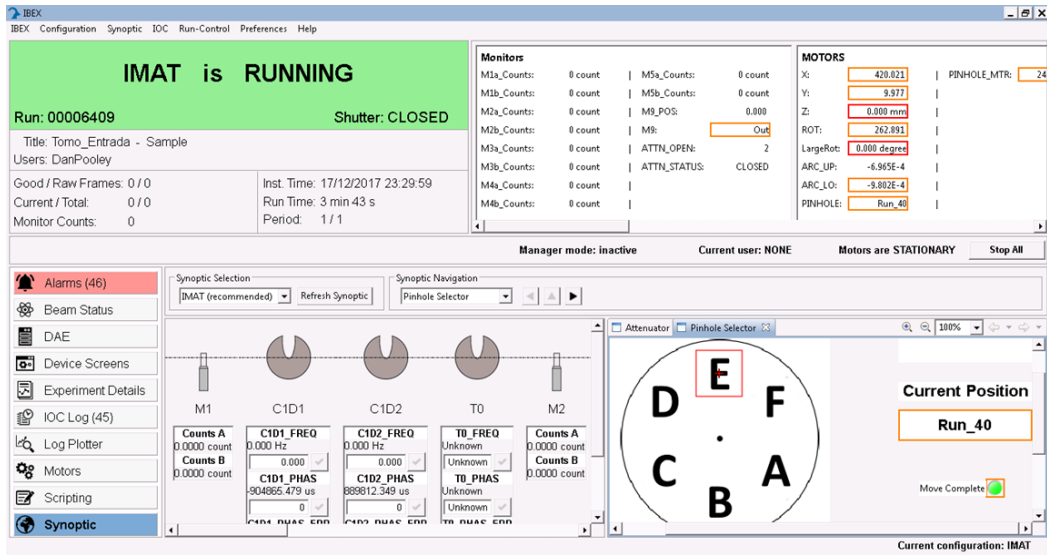


Fig. 5.11 IBEX Graphical User Interface to control IMAT instruments and cameras.

Each imaging detector on IMAT is set-up on a dedicated camera PC. Each camera systems use their own camera GUI to enable stand-alone operation: PIXELMAN for MCP and Messina GUI for the Messina camera. In the current operation, single images are saved in TIF or FITS format, while stacks of FITS are used for the MCP and event lists are used for the GP2.

### 5.4.2 Image-J

Image-J (Schneider et al., 2012) is a Java-based open source image processing software. It is proven to be a powerful tool for analysing multidimensional images such as a stack of radiographies recorded by different neutron wavelengths produced by the MCP detector. It allows different single image and image stack operation, for example: plotting the value of an individual or a group of pixels in the  $z$ -direction (i.e., transmission spectra as a function of wavelength), integrating the stacks in the  $z$ -direction into one image, performing mathematical operation on an image and between two images, performing spatial measurements, and many more. Image-J is used on IMAT at various stages of the analysis from data reduction to post data processing. An Image-J plugin, Neutron Imaging ISIS (Burca et al., 2016), with the included capability of performing scaling, overlap correction, and displaying TOF spectra for a region of interest, is also available to easily inspect the TOF spectra during or after the measurement. The interface of the plugin is shown in Fig. 5.12

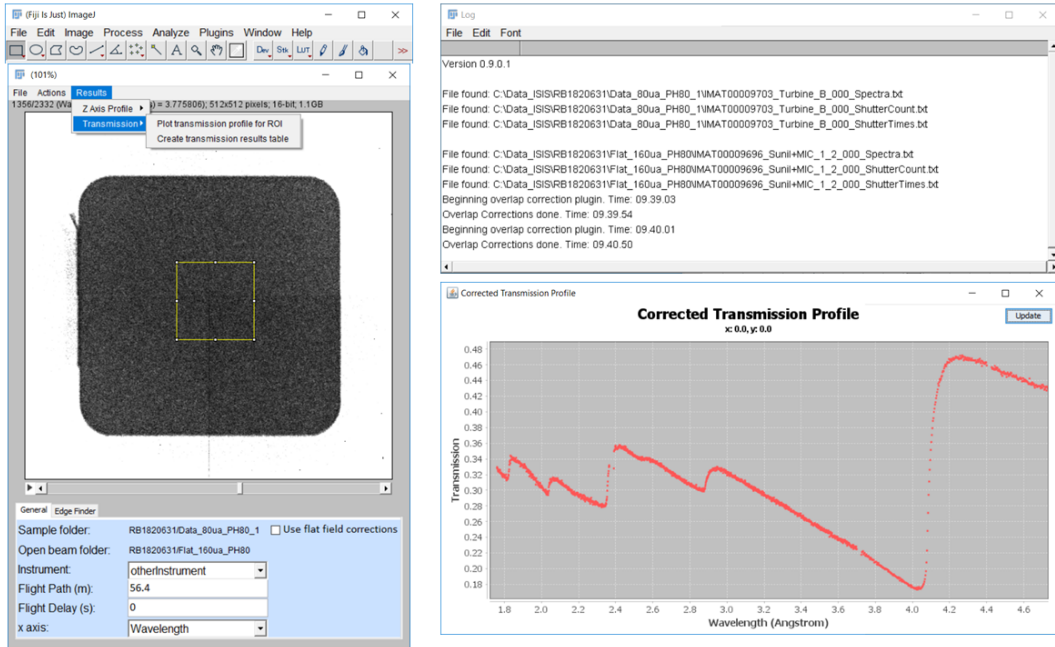


Fig. 5.12 The interface of the Neutron Imaging ISIS plugin on ImageJ. The radiograph shown on the left corresponds to a 40  $\mu$ s time slice at 53.8 ms (3.7758 Å). The Bragg edge spectrum of  $\alpha$ -iron is shown on the right, averaged for the yellow-box selection.

### 5.4.3 TPX\_Edgefit

TPX-edgefit is a code based on C++ to automate the process of pixel-by-pixel Bragg edge fitting and Bragg edge parameter map reconstruction (Anton Tremsin, personal communication, 1 October 2016). It uses the 5-parameter function, Eq. (4.5), to perform a single Bragg edge fitting. The input parameters for the fitting and reconstruction are prepared in a text-based parameter file. The input includes:

1. Parameter initialisation for the 5 Bragg edge parameters, i.e.,  $\lambda$ ,  $\tau$ ,  $\sigma$ , C1, and C2
2. Number of parameters to be fitted. Option is available to fix all of the parameters apart from  $\lambda$
3. Shift to trigger relative to the  $T_0$  in the acquired data
4. Flight-path of the instrument
5. Size of the macro-pixel
6. Wavelength range of the selected Bragg edge

7. Location of the data containing the sample. The software will automatically generate the sample intensity spectrum,  $I$ , pixel-by-pixel
8. Spectrum of the flat/ open beam,  $I_0$  for normalisation ( $Tr = I/I_0$ )
9. FITS file containing the intensity variation of the beam across the field-of-view

There are two ways of determining the intensity spectrum of the flat/ open beam measurement used by the software. The first one is to use a separate file containing the  $I_0$ , which is manually built by the user. This can be built using the neutron counts from the open beam data set. The second one is to determine the coordinate of an open beam region in the sample data set. Using the second method, the software will generate a file containing the  $I_0$  from the corresponding region, and use it for normalisation. Note that the software uses the same  $I_0$  to normalise different  $I$  across the field-of-view. The outputs of the software are the 5 parameter maps in FITS format.

Other tools are needed in conjunction with TPX\_Edgefit software, e.g., overlap correction code, data fitting software for parameter initialisation, text editor for manually building the open beam spectra, and image processing software for post data analysis. TPX\_Edgefit is a portable code and can be run in any analysis machine. A manual of TPX\_Edgefit software is provided in [Appendix A](#).

#### 5.4.4 BEATRIX

BEATRIX is a Bragg edge imaging software based on the ROOT programming language (Triestino Minniti, personal communication, 1 May 2018). Similar to TPX\_Edgefit, BEATRIX automates the pixel-by-pixel Bragg edge fitting for a large number (millions) of pixels. Most of the input parameters for the fitting and reconstruction are also similar. However, there are a few principal differences between BEATRIX and TPX\_Edgefit:

1. BEATRIX is developed using object-oriented C++ programming language and parallel processing, therefore is optimised to handle large, megapixel-sized data sets.
2. BEATRIX uses the 3-step function, Eq. (4.4) to perform the single Bragg edge fitting. There are, therefore, three wavelength regions which need to be decided before the fitting: i) region to the far right of the Bragg edge (higher wavelength); 2) region to the far left (lower wavelength), and; iii) the region where the Bragg edge is positioned.
3. A range of values can be given for parameter initialisation. This results in a more reliable fitting convergence.

4. There are two ways of the BEATRIX software in building the  $I_0$  spectra for normalisation: i) extracting the spectra pixel-by-pixel from the flat/ open beam data set; ii) extracting a single spectrum from a selected region in the flat/ open beam data. While the first option is theoretically the correct way to do a pixel-by-pixel analysis (each  $I$  is normalised with an equivalent  $I_0$ , i.e., from the same position within the field-of-view using the same macro-pixel size), it produces transmission spectra with poorer statistics for each pixel/ macro-pixel. Using the second option, the  $I_0$  spectrum can be generated from a larger region, thus better statistics.
5. BEATRIX provides a chi-square map to evaluate the goodness of fit across the field-of-view. This helps improving the accuracy of the result.
6. The output from the software can be opened with a GUI-based browser (TBrowser) which enables interactive manipulation of C++ objects. While this enables the users to display, manipulate and store the final result and produce high-quality graphical images, the output format makes the post-processing and extracting values from the reconstructed parameter maps quite difficult. Nevertheless, the software also produces an output in ASCII file, therefore allowing the extraction of parameter values from each pixel of the reconstructed map.

Another advantage of BEATRIX is that the code already includes algorithms for data pre-treatment, e.g., scaling and overlap correction, and therefore BEATRIX can be used on its own to produce the Bragg edge map. Since BEATRIX was developed in-house, there are scope to develop the tool further, e.g., expanding the capability from 2D maps to 3D maps of scalar Bragg edge parameter. Currently, the software is available on LINUX. The implementation of the code into the ISIS cluster is envisaged for the future.

# Chapter 6

## Characterisation of the IMAT Beamline

This chapter provides experimental validation of the IMAT design parameters, which are listed in **Section 5.1**. Some of the main instrument parameters, i.e., flight path and wavelength resolution of IMAT, and the effective spatial resolution of the imaging system with the MCP camera were all investigated in this project. These numbers are vital for designing experiments on the beamline, and therefore are useful for future users. Other IMAT parameters including beam flux and beam profile were presented elsewhere (Minniti et al., 2018).

### 6.1 IMAT flight path

#### 6.1.1 Theoretical background

As mentioned in the previous chapter, neutrons leave the surface of the moderator and are transported to the instrument via a 44 m long supermirror guide and collimated by a pinhole at 46 m position from the moderator. From the pinhole, neutrons travel through a 9 m flight tube and arrive at a neutron detector, in this case the MCP camera, held in position by a robot arm at around 10 m, usually at some distance downstream of the nominal sample position which has a neutron flight path of 56 m.

The position, ad hence the flight path of the MCP detector is variable, and can be different for different experiments. Therefore, a procedure is required to calibrate the flight path effectively. One of the ways to calibrate this parameter is by measuring Bragg edges or Bragg dips of a known material and fitting them against transmissions from calculated data sets. Recalling Eq. (2.1) and re-writing it in terms of flight path  $L_f$  (m), time-of-flight  $t$  (s), and time offset of source trigger received by data processing electronics  $\Delta t_0$  (s), yields:

$$\lambda = \frac{h(t + \Delta t_0)}{m_n L_f} \quad (6.1)$$

With  $h$  and  $m$  constants, Bragg edge positions of the calibration sample in  $\lambda$  calculated and Bragg edge positions in time-of-flight measured,  $L_f$  and  $\Delta t_0$  can be obtained.

### 6.1.2 Experimental and data analysis

In order to accurately determine the flight path of the instrument, appropriate calibration samples need to be prepared. For a flight path calibration using Bragg edges, ideally a calibration sample needs to have well-separated Bragg edges, with edge positions that are unaffected by crystallographic texture and internal strain. In the current work, calibration powder samples were used, assumed to have randomised crystallite orientation distribution and minimal internal strains.

Four powder materials: cerium oxide ( $\text{CeO}_2$ ), beryllium (Be),  $\alpha$ -iron (Fe) and aluminium (Al) powders were prepared. The  $\text{CeO}_2$  powder (Sigma Aldrich 211575 99.9% trace metal basis,  $< 5 \mu\text{m}$  powder) is commonly used as a standard to give a good approximation of instrument resolution since it has negligible intrinsic sample broadening. A sintered Be sample was selected since it can produce well-separated and well-defined Bragg edges in a relatively short measurement time. The Fe powder (Goodfellow FE006020 99.0% purity, particle size  $< 60 \mu\text{m}$ ) was used due to its high coherent cross section and its body-centred cubic (b.c.c.) structure producing well separated Bragg edges. The inclusion of Al powders (MBFiberglass IR350, 99.5% purity) was to represent a common engineering materials, and a sample with weak coherent cross-section. The  $hkl$  lists, lattice spacings, and structure factors of the powders were obtained from *nxsPlotter* (Boin, 2012) and are included in Table 6.1. Each powder was contained in thin-walled ( $\approx 1 \text{ mm}$ ) aluminium containers, and placed 30 mm in front of the MCP detector (Fig. 6.1).  $\text{CeO}_2$ , Fe and Al powders were measured for about 5 hours, while the Be sample was measured for about 30 minutes. A pinhole of  $D = 40 \text{ mm}$  ( $L/D \approx 250$ ) was used for these measurements.

For each sample, the measured transmissions were plotted as a function of time-of-flight. Then, the most intense Bragg edges, as shown in Table 6.1, were indexed. The Bragg edges were individually fitted using Eq. (4.4) and Eq. (4.3). The measured Bragg edge positions were plotted against calculated Bragg edge positions in  $\lambda$  provided in Table 6.1. The gradient and the intercept of the function were used to determine the flight path  $L_f$  and time offset  $\Delta t_0$ . Referring to Eq. (6.1),  $L_f$  and  $\Delta t_0$  are calculated as follows:

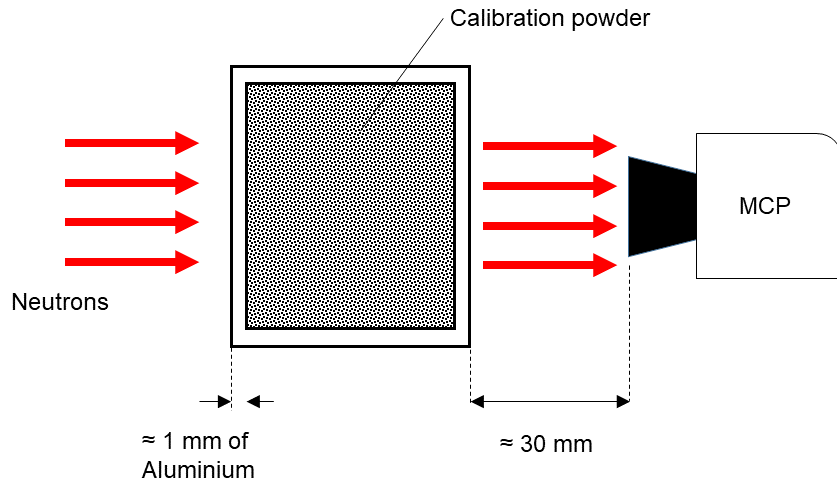


Fig. 6.1 Experimental setup of calibration experiment.

$$L_f = \frac{h}{m_n(\text{gradient})} \quad (6.2)$$

$$\Delta T_0 = \frac{\text{intercept}}{\text{gradient}} \quad (6.3)$$

### 6.1.3 Results

Fig. 6.2(a) shows the example of a transmission spectrum measured from a calibration powder sample, in this case  $\text{CeO}_2$ , with the corresponding lattice planes  $\{hkl\}$  of the most intense Bragg edges labelled. The fitted time-of-flight Bragg edge positions for different  $\{hkl\}$  are plotted against calculated  $d$ -spacings (and hence wavelengths  $\lambda$ ), shown in Fig. 6.2(b). The flight path  $L_f$  and  $\Delta T_0$  are obtained from the linear regression of calibration points: using Eq. (6.2) and (6.3), respectively, yielding:  $L = 56.37 \pm 0.01 \text{ m}$  and  $\Delta T_0 = 5.60 \times 10^{-5} \pm 1.06 \times 10^{-5} \text{ s}$ . Calibration results from the other calibration samples are provided in Table 6.2. It can be observed that flight paths calibrated using the different powders agree with each other within the measurement error. Since the powder samples were measured in different beam cycles, and following repositioning of the MCP detector with the camera positioning system, the consistency of the results reflects a very good reproducibility

Table 6.1 Lattice parameters  $\lambda_{hkl}$  and structure factors  $F$  of the calibration samples used in the experiment, with the most intense Bragg edges indexed. The values are calculated using the *nxsPlotter* software (Boin, 2012). The product of  $j * (\lambda_{hkl}^2 |F|^2)$ , where  $j$  is multiplicity, represents the Bragg edge height, with the values normalised to the most intense Bragg edges.

Materials	Lattice parameter ( $\text{\AA}$ )	$\{hkl\}$	$\lambda_{hkl}$ ( $\text{\AA}$ )	$j$	$j * (\lambda_{hkl}^2  F ^2)$
Cerium oxide	5.411* (Kuemmerle and Heger, 1999; Harwood, 1949; Whitfield et al., 1966; Varez et al., 2007); 5.412 (WoŁcyrz and Kepinski, 1992; Itoh et al., 2015); 5.409 (Stecura and Campbell, 1961); <b>5.4097 ± 0.0007 (current work)</b>	111	6.250	8	191.3
		200	5.410	6	179.6
		220	3.826	12	1000.0
		400	2.706	6	189.2
		422	2.210	24	382.9
		440	1.914	12	109.2
		620	1.712	24	133.3
Beryllium	$a = 2.286, c = 3.584^*$ (Yang and Coppens, 1978)	642	1.446	48	111.6
		100	3.960	6	1000.0
		002	3.584	2	269.5
		102	2.658	12	838.8
		110	2.286	6	296.4
		112	1.928	12	392.5
Iron	2.886* (Kochanovska, 1949; Jette and Foote, 1935; Straumanis and Kim, 1969); 2.867 (Owen and Yates, 1933; Gorton et al., 1965); 2.859 (Basinski et al., 1955); <b>2.8675 ± 0.00016 (current work)</b>	110	4.054	12	1000
		200	2.866	6	240.9
		211	2.340	24	619.5
		220	2.026	12	223.9
		310	1.812	24	345.5
		321	1.532	48	459.3
		330	1.352	12	83.1
Aluminium	4.049* (Owen and Yates, 1933; Swanson and Fuyat, 1953; Bourbia et al., 2010); 4.050 (Cooper, 1962; Figgins et al., 1956; Hull, 1917); 4.039 (Wilson, 2002); <b>4.0506 ± 0.0008 (current work)</b>	431	1.124	48	198.6
		111	4.676	8	1000
		200	4.050	6	550.6
		220	2.864	12	504.6
		311	2.442	24	686.9
		222	2.338	8	205.4
		331	1.858	24	333.8

\*used for input parameter in the *nxsPlotter* software

Table 6.2 Results of calibration measurement using CeO<sub>2</sub>, Be, Al and Fe powder

Calibration sample	<i>Gradient</i>	<i>Intercept</i>	Flight path $L_f$ (m)	$\Delta T_0 (\times 10^{-5} \text{ s})$
CeO <sub>2</sub>	70.18	0.00393	$56.37 \pm 0.01$	$5.60 \pm 1.06$
Be	70.22	0.00009	$56.34 \pm 0.05$	$0.13 \pm 3.49$
Al	70.20	0.00210	$56.35 \pm 0.03$	$2.99 \pm 2.11$
Fe	70.21	0.00273	$56.34 \pm 0.02$	$3.89 \pm 1.24$

of the detector position. The result shows the suitability of the calibration method to give an accurate flight path in any given experimental setup.

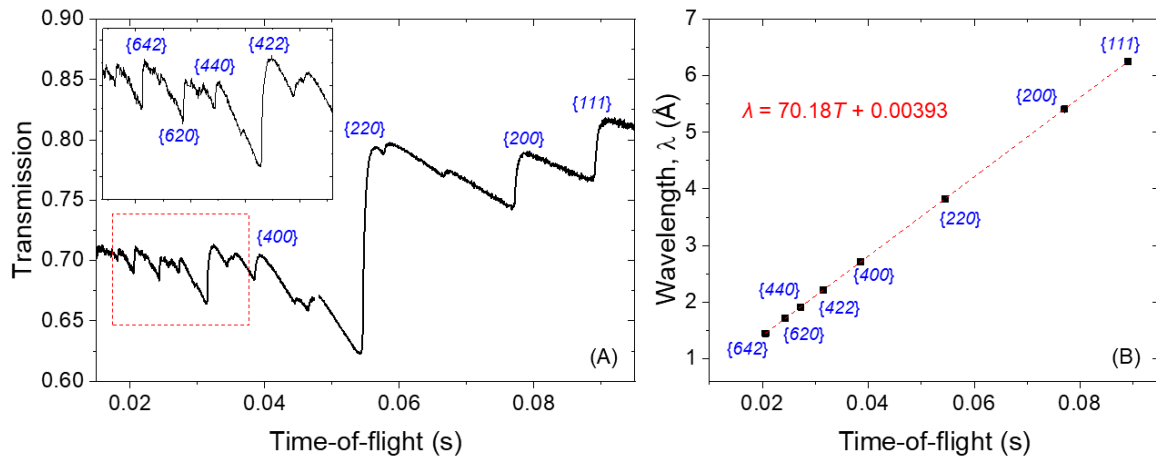


Fig. 6.2 Example of transmission spectrum from a calibration sample, in this case CeO<sub>2</sub>, and the corresponding calibration points. The gradient and intercept of the function shown by the dashed red line are used to determine the flight path  $L_f$  and time offset  $\Delta T_0$ .

## 6.2 IMAT wavelength resolution

### 6.2.1 Background

Wavelength (or spectral) resolution indicates the ability of an instrument to accurately determine the time-of-flight of neutrons with different energy. For strain measurement applications, wavelength resolution gives a measure of performance of an instrument, since the lattice spacing measurement is carried out through time-of-flight determination. The major contributor to the instrument's wavelength resolution is the moderator. As previously mentioned in **Section 2.1.3** and shown in Fig. 2.4, there is a time distribution for each

neutron energy (hence wavelength) leaving the moderator due to the thermalisation process and moderator geometry. This broadens the neutron pulse, and is reflected in the width of the Bragg peaks in a neutron diffraction instrument.

On an imaging instrument, e.g., IMAT, pulse broadening is translated to the width of the Bragg edges. In this work, the parameter  $\tau$  in Eq. 4.3 which is related to the time constant of the exponentially decaying ‘storage’ term of the moderator was chosen as a sample-independent quality to represent the instrument broadening. Monte Carlo simulations reported earlier for IMAT (Kockelmann et al., 2013; Burca et al., 2013) are also presented here as comparisons.

### 6.2.2 Experimental and data analysis

Experimental setup and types of material of calibration samples for wavelength resolution measurements are identical with those described in **Section 6.1.2**. The inclusion of different types of material ( $\text{CeO}_2$ , Be, Al, and Fe) was to ensure that the measured resolution function is sample-independent. Transmission spectra were obtained from each powder sample. Eq. (4.4) was then used to fit the most intense Bragg edges indexed in Table 6.1, and the fitted parameter  $\tau$  was used to describe the pulse width and resolution function of the IMAT instrument.

### 6.2.3 Results

This section reports the experimental evaluation of the IMAT wavelength resolution, and provides calibration values as a guide for Bragg edge analysis on the instrument. Fig. 6.3(a) presents the pulse width of IMAT as a function of neutron wavelength. The data points are the decay constant parameter  $\tau$  from Eq. 4.4 for the different Bragg edges of the calibration powders, with  $\{hkl\}$  values as indexed in Table 6.1. The size of the detection area, i.e., the number of pixels from which the Bragg edges were extracted was  $478 \times 478$  for  $\text{CeO}_2$ ,  $346 \times 346$  for Be,  $337 \times 337$  for Al, and  $274 \times 274$  for Fe. A sigmoidal logistic function [described in Eq. (6.4), where  $\tau$  is in  $\mu\text{m}$  and  $\lambda$  is in  $\text{\AA}$ ] is used to simultaneously fit the Fe and ( $\text{CeO}_2$ ) data points (ones with lowest uncertainties) as shown by the red curve in Fig. 6.3(a).

$$\tau = \frac{418}{1 + 155.1 \exp(-2.46\lambda)} \quad (6.4)$$

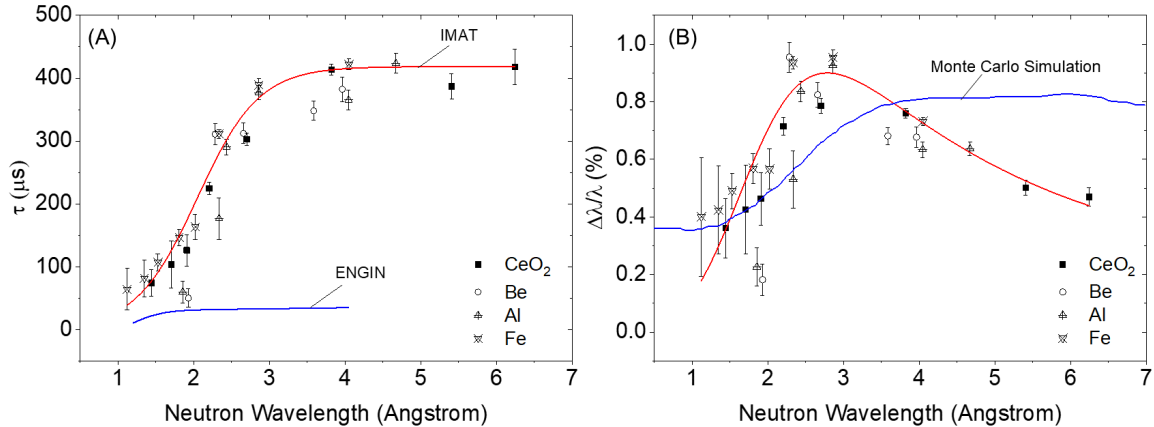


Fig. 6.3 (a) IMAT decay constant  $\tau$  as a function of neutron wavelength, representing the instrument's pulse width, determined from different calibration powders. The red curve is the sigmoidal fit described by Eq. (6.4). Comparison with ENGIN (Santisteban et al., 2001) emphasises the characteristics of the 'broad pulse' coupled moderator for IMAT compared to the 'sharp pulse' decoupled moderator for ENGIN-X; (b) Resolution function of IMAT beamline. Red curve is sigmoidal fit of the Al and Fe data points, while the blue curve is Monte Carlo simulation of IMAT (Kockelmann et al., 2013)

Fig. 6.3(b) presents the resolution function ( $\Delta\lambda/\lambda$ ) of the instrument, which is obtained by dividing the parameter  $\tau$  by the corresponding TOF position for each Bragg edge. The red curve shows the sigmoidal fit to the Fe and CeO<sub>2</sub> data points. The fit shows that the worst resolution of  $\approx 0.9\%t$  is observed at a wavelength of  $\approx 2.6 \text{ \AA}$ .

## 6.3 Spatial resolution of IMAT with MCP camera

### 6.3.1 Background

Spatial resolution can be defined as the smallest resolvable object from an image. This gives the measure of the detail of the image, where higher spatial resolution (smaller nominal value) means more detail. In neutron imaging, the spatial resolution of the system is not only determined by the physical pixel size of the sensor, but also the geometrical blurring  $d_b$ . The geometrical blurring is governed by the size of the pinhole  $D$ , the distance between the pinhole and the detector  $L$ , and the distance from the sample to the detector  $l$ . More details about this are described in Section 4.2.3.

The determination of the spatial resolution in neutron imaging can be carried out by measuring the modulation transfer function (MTF) of a sharp edge and by applying a 10%

contrast cut-off, i.e., the minimum intensity difference between two points to be categorised as a spatially resolved pixel (Treimer, 2009). While the determination of the achievable spatial resolutions on IMAT has been described by Minniti et al (Minniti et al., 2018) using an optical camera-based system and for white beam imaging, this section focuses on the spatial resolution on IMAT for Bragg edge imaging using the energy-resolving MCP camera with a physical pixel size of  $55\text{ }\mu\text{m}$ .

### 6.3.2 Experimental and data analysis

Measurement of the spatial resolution was carried out by measuring a "Siemens Star". The Siemens Star was used in conjugation with a sample (Fig. 6.4) to provide data for the determination of the spatial resolution of a reconstructed Bragg edge map, with results presented in **Section 7.4.2**. This sample set was measured at different distances  $l$  from the detector to study the effect of geometrical blurring on the spatial resolution. The quarter-Siemens Star used was a thin, neutron-absorbing pattern, made of  $7\text{ }\mu\text{m}$  thick gadolinium deposited on a silicon substrate (Pooley et al., 2017), with well-defined spokes to measure spatial resolution. It was attached to the back of a  $10\text{ mm} \times 10\text{ mm} \times 50\text{ mm}$  Fe rod. Using a pinhole of  $D = 80\text{ mm}$  ( $L/D = 125$ ), different sample-to-detector distances  $l$  were applied to produce different geometrical blurring values  $d_b$ . Since the thickness of the foil in the transmission direction is negligible, it does not contribute to the  $l$  value. The sample-to-detector distances were  $l = 25\text{ mm}$ ,  $75\text{ mm}$  and  $225\text{ mm}$ , to produce  $d_b$  values of  $0.2\text{ mm}$ ,  $0.6\text{ mm}$  and  $1.8\text{ mm}$ , respectively, according to Eq. (4.2). Each measurement was performed for two hours.

The white beam radiographs (averaged over the whole wavelength range) of each measurement with different  $d_b$  values were taken. From the radiographs, a line profile of neutron intensity was drawn on the edge of the Siemens Star, and a modulation transfer function (MTF) was derived [Nikolay Kardjilov, private communication, 1 June 2016]. A 10% contrast cut-off was applied to define the highest achievable spatial frequency, and the inverse of this yields the maximum achievable spatial resolution.

### 6.3.3 Results

Fig. 6.5(a), (b), and (c) show the white beam radiographs of the quarter Siemens Star attached to an Fe rod, taken with  $l = 25\text{ mm}$ ,  $75\text{ mm}$  and  $225\text{ mm}$  (thus  $d_b = 0.2\text{ mm}$ ,  $0.6\text{ mm}$  and  $1.8\text{ mm}$ ), respectively. Fig. 6.5 shows visually the effect of geometrical blurring to the spatial resolution of the image, where smaller geometrical blurring yields higher spatial resolution, i.e., a sharper image.

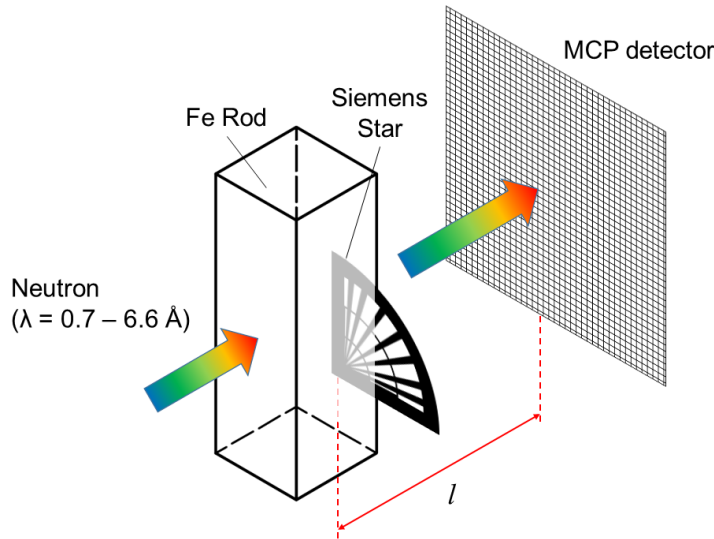


Fig. 6.4 Experimental setup of spatial resolution measurement. The distances  $l$  between the Siemens Star (attached to the back of the Fe rod) to the detector were  $l = 25 \text{ mm}$ ,  $75 \text{ mm}$  and  $225 \text{ mm}$ .

The red dashed box in Fig. 6.5 shows the location where the line profiles of neutron intensity (averaged over  $\approx 100$  pixels) were drawn. An example of the edge spread function (ESF) and the MTF analysis for the radiograph with  $d_b = 0.2 \text{ mm}$  is shown in Fig. 6.6. The 10% contrast cut-off of the MTF gave a spatial frequency of 5.6 line-pairs/mm which corresponds to a spatial resolution of  $89 \mu\text{m}$ . Analysing the MTF for the radiographs with two other  $d_b$  values of  $0.6 \text{ mm}$  and  $1.8 \text{ mm}$  yields spatial resolution values of  $240 \mu\text{m}$  and  $767 \mu\text{m}$ , respectively. The relation between the  $d_b$  values and the spatial resolution is shown in Fig. 6.7.

## 6.4 Discussion

Experiments mentioned in the previous sections are useful not only to provide the parameter values of the IMAT beamline, but also to serve as a guideline on how to perform calibration measurements in the future, either on IMAT or on other time-of-flight imaging beamlines.

$\text{CeO}_2$  powder sample provided a flight path calibration values with the smallest error. This can be attributed to the quality of the transmission spectrum, i.e., the number of well-defined Bragg edges, measured from the  $\text{CeO}_2$  powder. The largest uncertainty of  $\Delta L = 0.05 \text{ m}$  is shown by the calibration value measured from Be powder. This is equivalent to an uncertainty of lattice spacing determination  $\Delta d = 0.00062 \text{ \AA}$  which is equivalent to  $\approx 900 \mu\text{\AA}$ . Despite

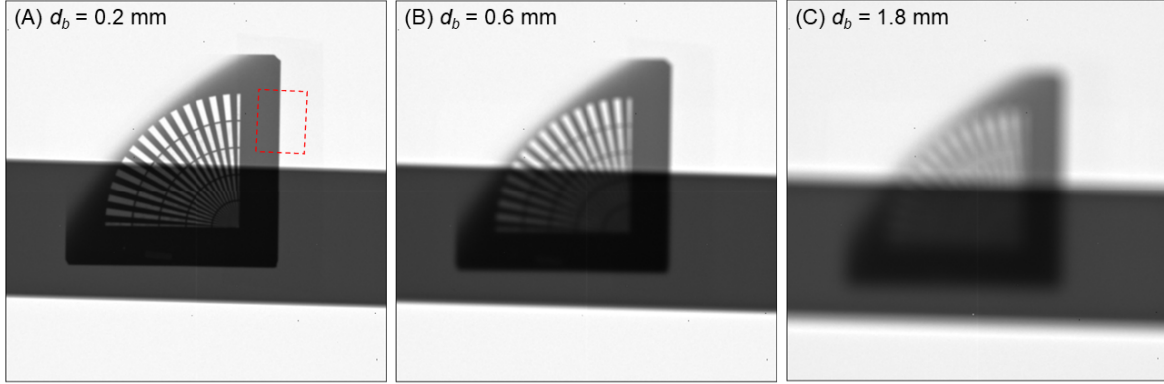


Fig. 6.5 Radiographs of Siemens Star attached to an Fe rod (rotated 90° counter-clockwise), taken with (a)  $l = 25$  mm ( $d_b = 0.2$  mm); (b)  $l = 75$  mm ( $d_b = 0.6$  mm); (c)  $l = 225$  mm ( $d_b = 1.8$  mm). The closer the  $l$  (the smaller the  $d_b$ ), the higher the spatial resolution, i.e., the sharper the image. The red dashed box represents the location from where the MTF analysis was performed.

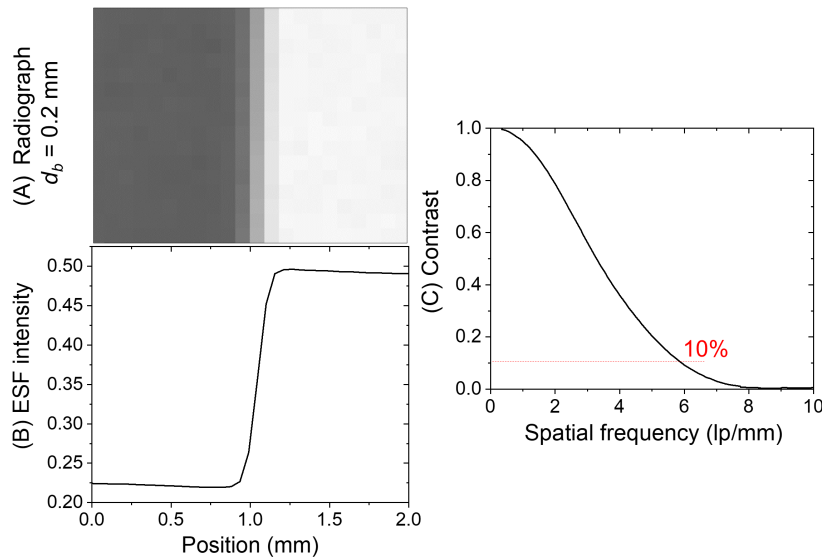


Fig. 6.6 (a) An example of the analysed sharp edge of the Siemens Star (radiograph taken with  $d_b = 0.2$  mm) with: (b) the corresponding ESF and; (c) MTF. 10% contrast cut-off applied to the MTF yields a spatial frequency of 5.6 line pairs/mm, equivalent to a spatial resolution of 89  $\mu\text{m}$ .

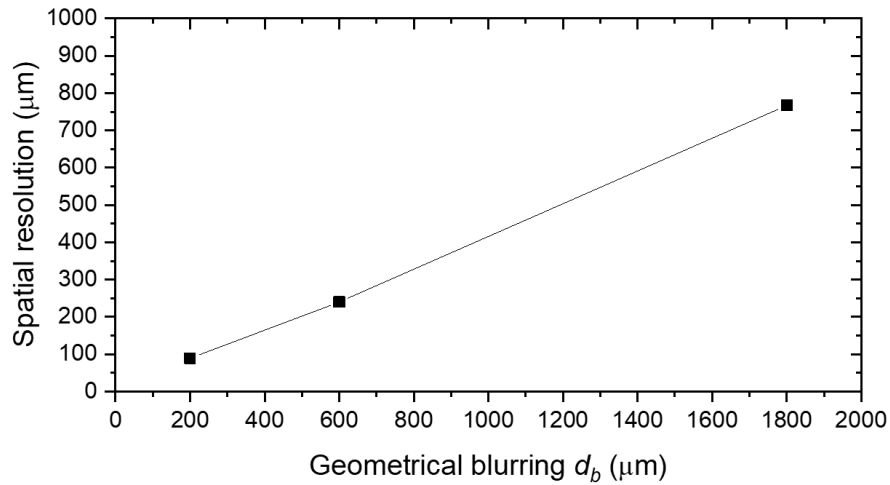


Fig. 6.7 The relation between geometrical blurring  $d_b$  and the spatial resolution.

the relatively larger uncertainty, Be powders allow flight path calibration in a relatively short measurement time. This is especially useful for strain imaging experiments where the main interest is the relative  $d$ -spacing values, rather than the absolute ones. The MCP camera at IMAT is held by a robot arm, and the default position along the beam is usually unchanged from one experiment to another. However, the camera position is variable and can, for example, be moved close to a sample on a stress rig in the focus of the diffraction detectors. The above procedures can be used for a relatively quick flight path calibration. For the default MCP position, the results summarised in Table 6.2, a flight path of around 56.40 m is well reproducible. It is a good practice, however, to have a calibration sample measured for each experiment.

In terms of uncertainty in determining the flight path of the instrument, the best resolution achieved in this work was the measurement of CeO<sub>2</sub> powder. The flight path measurement using CeO<sub>2</sub> powder produced uncertainty of 0.02 m, which is equivalent to around 180  $\mu\epsilon$ . This uncertainty, however, does not propagate to the determination of strain. This is because a single number is chosen for TOF to wavelength conversion across the field of view prior to the Bragg edge fitting, and therefore the strain uncertainty is solely depends on the uncertainty of the fitting. As will be discussed in **Section 7.5.2**, the uncertainty of the strain measurement is around 80-90  $\mu\epsilon$ . The uncertainty of the flight path calibration described in this work reflects the limitation of the method itself. The current method relies on the reliability of determining the position of multiple Bragg edges individually, which uncertainties of the individual Bragg edge fitting might propagate to the measured flight path.

There is a scope of alternative method of flight path calibration, which is analysis of Bragg dip/ resonance of single crystals at special orientations.

Meanwhile, to check the consistency of the flight path laterally, the data was analysed from different part of the detector as illustrated in Fig. 6.8(a), and the results are shown in Fig. 6.8(b). The results show that the flight-paths measured across the detector are consistent laterally, where the difference are within the uncertainty of the measurement. While the uncertainty itself is higher because of the lower statistics of the smaller analysed area, this can be improved by taking longer measurements, this result already shows that a single flight path value is, in most cases, sufficient to be taken for strain map analysis. In the future, it is still worth performing a dedicated measurement of spatial uncertainty of strain across the field of view with longer measurement time.

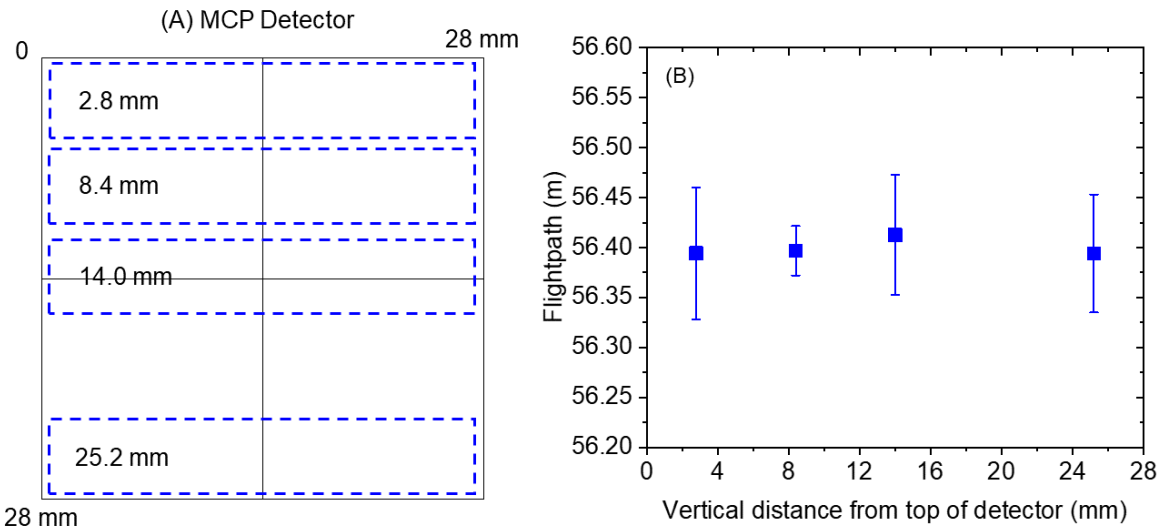


Fig. 6.8 (a) The blue boxes indicate the analysed regions, where the number inside the boxes show the distance of the region's centre line from the top of the detector; (b) Flight path measured at different locations across the detector, showing the consistency of the flight path calibration, laterally.

The determination of wavelength resolution carried out in this work with different calibration powders agrees well with previous measurements on IMAT (Minniti et al., 2018). Moreover, the  $\tau$  curve in Fig. 6.3(a) can be used as sample-independent constraints when performing Bragg edge fitting. Fig. 6.3(a) also demonstrates the effect of a different moderator on the wavelength resolution. Using a coupled liquid hydrogen moderator, IMAT has greater values by almost a factor of ten compared to ENGIN [blue curve in Fig. 6.3(a)]

which uses a decoupled liquid methane moderator. The same decoupled moderator is used by ENGIN-X. Consequently, IMAT produces broader Bragg edges compared to ENGIN-X, as will be shown in the next chapter. On the other hand, the use of the coupled moderator allows IMAT to have a much higher flux compared to ENGIN-X, supporting IMAT's main purpose as an imaging beamline.

Meanwhile, the instrument resolution function measured from calibration samples, fitted with the red curve in Fig. 6.3(b), agrees fairly well with and validates the level of spectral resolution that was obtained by modelling of the IMAT beamline using Monte Carlo simulations, shown by the blue curve. Differences in terms of the shape of the wavelength resolution between the measured and simulated curve can be influenced by a number of factors. The main factor would be the differences in the modelled and the actual in-service moderator. While the simulation was made for a coupled liquid hydrogen + solid methane moderator, IMAT is currently running on the coupled hydrogen moderator with the methane container empty. Nevertheless, this result shows that IMAT is performing close to the intended design parameter.

In the spatial resolution analysis, the values were analysed with reference to the geometrical blurring  $d_b$ , Fig. 6.7. While the  $d_b$  values in the current experiment were varied by changing the sample-to-detector distance  $l$  and keeping the  $L/D$  ratio fixed, it actually represents changes in any of the three variables given in Eq. (4.2). The relation shown in Fig. 6.7, therefore, can be used for any combination of pinhole size  $D$  and sample-to-distance ratio  $l$ , with the distance from the pinhole to the detector  $L$  on IMAT usually being 10 m but a second sample position at 5 m from the pinhole is envisaged. As can also be observed in Fig. 6.7, the nominal value of the spatial resolution is smaller than the geometrical blurring. This happened because the blurring is commonly calculated from the three times the standard deviation of the line spread function (LSF, a first derivative of ESF), as performed by Minniti et al. 2018. Therefore, it is effectively determined on a higher contrast criterion compared to the 10% contrast cut-off of the MTF which is used for spatial resolution determination. It is important to note that the presented spatial resolution values in Fig. 6.7 are valid for a radiographic image produced by MCP detector. For strain mapping, the spatial resolution of the reconstructed map is also affected by the size of the macro-pixel, and more detailed discussion will be presented in the next chapter.



# Chapter 7

## Development of the Residual Strain Mapping on IMAT

### 7.1 Overview

Bragg edges occur as a result of the back-scattering phenomenon, where a set of lattice planes ( $hkl$ ) with lattice spacing  $d_{hkl}$  are no longer contributing to the neutron coherent scattering at a set of critical wavelengths described by Bragg's law [Eq. (3.2)]. As for Bragg diffraction, crystallographic material parameters can be derived from these Bragg edge signals, for example the lattice spacing and crystallographic orientations. Using a TOF imaging camera, these parameters can be mapped across the sample with the caveat that the information is averaged through the sample thickness in the beam propagation direction.

Fig. 7.1(a) compares Bragg edges and Bragg peaks for an aluminium alloy 2024 (Al2024) powder. Bragg edges shown by blue symbols were obtained on IMAT by measuring the powder sample inside an aluminium foil container with a dimension of 35 mm in the transmission direction for 4 hours. The same powder was measured on ENGIN-X, ISIS, in both diffraction mode and transmission mode using the MCP detector, shown by the black line and red symbols in Fig. 7.1(a), respectively. The powder was measured using a gauge volume of  $2\text{ mm} \times 2\text{ mm} \times 2\text{ mm}$  for 0.5 hours in diffraction mode. For measurement in transmission mode, the powder was inserted into a container with a dimension of 50 mm in the transmission direction and measured for 6 hours. The transmission data from measurement on IMAT and ENGIN-X are averaged over the same detection area of  $160 \times 160$  pixels.

In Fig. 7.1(a), the transmission from IMAT and ENGIN-X and the normalised diffracted neutron counts are plotted as a function of  $d$ -spacing. As can be seen, the Bragg edges and

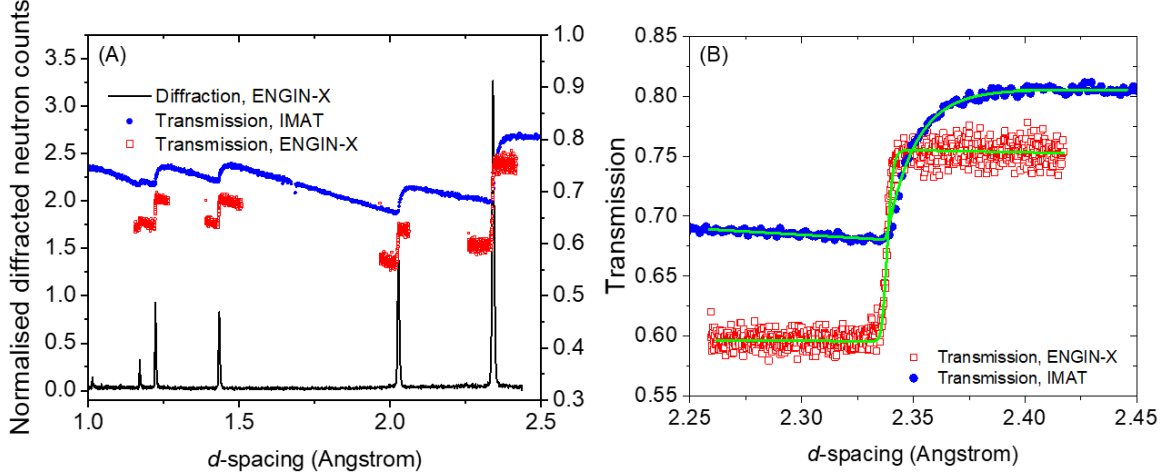


Fig. 7.1 (a) Bragg edges and Bragg diffraction peaks of Al2024 powder fall on top of each other, providing the lattice spacing information of the first five aluminium reflections measured. Bragg edges were measured on IMAT (blue symbols) and ENGIN-X (red symbols), having different shapes due to the different resolution functions of the two instruments. The diffraction pattern (black line) was measured on ENGIN-X; (b) a non-linear function given in Eq. (4.4) well describes the Bragg edges from the two instruments.

Bragg peaks occur at the same lattice spacing of the first five Al reflections measured. The difference in the transmission level between IMAT and ENGIN-X signals is caused by the sample thickness difference in the transmission direction i.e., the difference in transmission path-length: 35 mm on IMAT and 50 mm on ENGIN-X. The gaps in the transmission signal, which are more notable in the ENGIN-X signal, are related to the data readout setting of the detector. The ENGIN-X transmission spectrum has a higher statistical error, Fig. 7.1(a), despite being detected from the same detection area size as the spectrum from IMAT and integrated over a longer counting time (6 hours, compared to 4 hours on IMAT), demonstrating the higher beam flux at IMAT.

Precise determination of the lattice spacing from a Bragg edge may be achieved by using a non-linear fit, for example with functions given in Eq. (4.4), (4.5), or (4.6). Fig. 7.1(b) shows a non-linear least-square fit of the function in Eq. (4.4) to the Al {111} Bragg edges. Despite the different shapes of the edges from the two different instruments, Eq. (4.4) yields almost identical Al {111} lattice spacings of  $2.3378 \pm 0.0006 \text{ \AA}$  and  $2.3382 \pm 0.0001 \text{ \AA}$  for IMAT and ENGIN-X Bragg edges, respectively. The difference is smaller than the fitting error, and equivalent to  $\approx 171 \mu\epsilon$ . Fig. 7.1(b) also shows the broader IMAT Bragg edge compared to the much sharper ENGIN-X Bragg edge. This proves the findings presented

in Fig. 6.3(a), where IMAT shows larger pulse widths compared to ENGIN (on the same moderator as ENGIN-X), due to the use of different moderators.

As is the case with its Bragg diffraction counterpart, the accurate determination of the wavelength positions of Bragg edges is useful for applied strain, and especially residual strain measurement. The advantage of Bragg edge transmission is the ability to resolve the strain information spatially across the sample in a single exposure, averaged through the sample thickness in the beam propagation direction. The main steps of Bragg edge neutron transmission strain mapping are as follow:

1. Measurement of the sample and the flat field/ open beam (neutron exposure without sample) data. The flat field needs to be measured with the same setting, and should be counted at least as long as the sample measurement to get equivalent statistics.
2. Normalisation of sample data with flat field and generation of the transmission spectrum.
3. Selection of an individual Bragg edge to be analysed.
4. Determination of Bragg edge wavelength position  $\lambda_{hkl}$ , using the Bragg edge fitting function, across the whole field-of-view with a running average of the macro-pixel.
5. Calculation of lattice strain with respect to a stress-free reference value  $\lambda_{hkl_0}$ , according to Eq. (7.1), across the whole field-of-view. Since  $\sin \theta = 1$  ( $2\theta = 180^\circ$ ) during back-scattering,  $d_{hkl} = \lambda_{hkl}/2$ , and therefore the strain can be calculated directly using wavelength terms.

$$\varepsilon = \frac{\lambda_{hkl} - \lambda_{hkl_0}}{\lambda_{hkl_0}} \quad (7.1)$$

As outlined in **Section 3.2.2.**, there are different ways to determine the stress-free reference value  $\lambda_0$ : (i) Measuring a powder of the same material; (ii) Measuring a stress-free region of the sample, and; (iii) Measuring a stress-free cut section of the sample.

Bragg edge strain mapping has not reached a similar maturity level to neutron diffraction. Different aspects such as data analysis and the software to perform the mapping are still in the development process. Additionally, since the technique is performed in a new beamline, i.e., IMAT, validation of the results is important. This chapter reports the development of Bragg edge strain mapping on IMAT. Different Bragg edge fitting functions are assessed, highlighting the advantages of each and deciding which functions to be used for future data

analysis. A novel cross-correlation based data analysis is introduced as a parameter-free method to estimate Bragg edge shifts. Accuracy (the closeness of agreement to an actual value) and the uncertainty (dispersion of the measured value) of the measured strain are investigated. Strain resolution, which is the smallest strain that can be measured, is also demonstrated. Spatial resolution of the reconstructed strain map is determined, and the validation of the strain map is performed by comparing the result with neutron diffraction.

## 7.2 Assessment of Bragg edge fitting functions

Strain measurement for engineering purposes requires accuracy of the order of  $\delta(d)/d = 0.01\%$  or  $100 \mu\epsilon$ . This can be achieved by precisely determining the position of individual Bragg edges. In this work, either of the three Bragg edge models, i.e., Eq. (4.4), (4.5), or (4.6) is used to fit the measured data in a least-square refinement procedure, which procedures can be generally describe as follow:

1. Initial function curve is generated from a set of initial guess parameter values (usually including Bragg edge position  $\lambda$ , and Bragg edge width parameter  $\tau$  and  $\sigma$ ).
2. Iteration procedure is applied to adjust parameter values to make the curve closer to measured data points.
3. Stop the iteration when a minimum criteria is satisfied.

Assessment of the suitability of the three different Bragg edge fitting functions is carried out with the help of a data analysis software OriginPro (<https://www.originlab.com/origin>). The aforementioned models are implemented as user-defined functions. The software use Levenberg-Marquardt iterative procedure which combines the Gauss-Newton method and the steepest descent method, and has been proven to be robust and stable for Bragg edge fitting (Vogel, 2000). The algorithm minimise the reduced chi-square value,  $\chi^2_\nu$  (residual sum of squares, i.e., sum of the square of the deviation from each data point to the fit line, per degree of freedom). The code also output the uncertainty of the Bragg edge position, and therefore the uncertainty of the strain measurement can be determined.

The three Bragg edge functions are used to fit a data set from Al {111} Bragg edge (wavelength range of 4.60 - 4.90 Å) measured from the middle part of an aluminium silicon-carbide (AlSiC) metal matrix composite (MMC) plate. The MMC is made of an aluminium alloy matrix and pure silicon carbide particulates, therefore exhibited both aluminium and silicon carbide edges in the transmission spectra, Fig. 7.2(a). More detailed information on

the sample is provided in **Section 7.4.3**. The fitted Al {111} Bragg edge is highlighted by the red dashed box in Fig. 7.2(a).

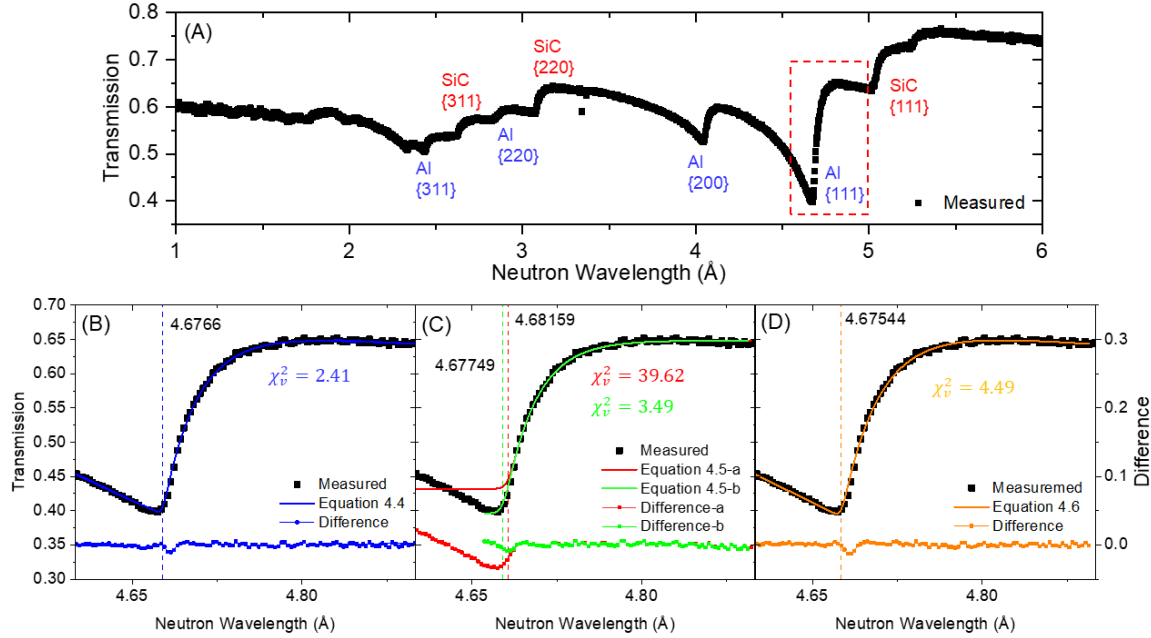


Fig. 7.2 Comparison between different Bragg edge fitting functions. (a) Transmission spectrum of AlSiC metal matrix composite, red dashed box highlight the Al {111}. The Bragg edge was fitted using (b) Eq. (4.4), blue line; (c) Eq. (4.5) with different wavelength range, red and green line, and; (d) Eq.(4.6), amber line.

The fitting process of Eq. (4.4) comprises three stages (Santisteban et al., 2001). Firstly, the data on the far-right (high-wavelength) side of the Bragg edge were fitted where the transmission is given by:

$$Tr(\lambda) = \exp [-(a_0 + b_0\lambda)] \quad (7.2)$$

Secondly, the data on the far-left (low-wavelength) side of the Bragg edge were fitted using parameters  $a_{hkl}$  and  $b_{hkl}$ , which describe the jump in transmission, while keeping the parameters  $a_0$  and  $b_0$  fixed. The transmission on the left side is given by:

$$Tr(\lambda) = \exp [-(a_0 + b_0\lambda)] \exp [-(a_{hkl} + b_{hkl}\lambda)] \quad (7.3)$$

Finally, Eq. (4.4) is used to fit the Bragg edge, keeping the parameters  $a_0$ ,  $b_0$ ,  $a_{hkl}$ , and  $b_{hkl}$  fixed.

The reduced chi-square value is typically used to represent the goodness of fit, where the reduced chi-square value of close to 1 indicates a good fit result. The Eq. (4.4) fitted the Al {111} edge well, Fig. 7.2(b) with  $\chi^2_v = 2.41$ .

Meanwhile the 5-parameter ( $\lambda_{hkl}$ ,  $\sigma$ ,  $\tau$ ,  $C_1$  and  $C_2$ ) model [Eq. (4.5)] does not have a parameter to describe the slope on the far-left and the far-right of the Bragg edge. Therefore, the accuracy of the function for Bragg edge position determination depends on the shape of the Bragg edges and/or the selection of the wavelength range of the Bragg edge. For example, when fitting the Al {111} Bragg edge with a wavelength range from 4.60 to 4.90 Å, the function did not properly replicate the far-left side of the Bragg edge, shown by the high residuals in the difference curve, Fig. 7.2(c). The fitting producing a high  $\chi^2_v$  value of 39.62. However, by narrowing the selection of the Bragg edge wavelength range from 4.66 to 4.90 Å, the slope in the far-left side can be avoided [green fitted curve and difference curve in Fig. 7.2(c)], and the fit produced  $\chi^2_v = 3.49$ .

Eq. (4.6) introduces two additional parameters  $K_1$  and  $K_2$  to the 5-parameter model, to describe the slope on the far-left and far-right side of the Bragg edge, respectively. Eq. (4.6) fitted the Al {111} Bragg edge well, shown by the orange curve in Fig. 7.2(d), with  $\chi^2_v = 4.49$ .

All three functions shows the ability to fit the Bragg edge data pretty well. The Eq. (4.4) and Eq. (4.5) with narrower wavelength range, however, have lower residuals compare to Eq. (4.6), especially in the inflection point of the Bragg edge. This is especially important for a reliable determination of the edge position. As mentioned in **Section 5.4**, the Eq. (4.4) and Eq. (4.5) are implemented in the IMAT analysis tool and are the functions to be taken forward for Bragg edge analysis, especially for strain measurement, and are used interchangeably throughout this work.

The above measured data has a good counting statistics, and the fitting procedures yield fitted Bragg edge position with uncertainty equivalent to 85-120  $\mu\epsilon$ . The relation between the fitting uncertainty and the instrumental resolution will be described later in **Section 7.5.2**.

### 7.3 Cross-correlation-based Bragg edge analysis

Sample anisotropy due to preferred orientation or crystallographic texture changes the shape and the heights of the Bragg edges (Santisteban et al., 2006b; Boin et al., 2011; Malamud et al., 2014). Fig. 7.3 shows the change of Al {111} Bragg edge shape due to crystallographic texture. The black curve was measured from a randomly-oriented powder sample and shows a regular Bragg edge shape. Meanwhile the red and the blue curves were measured from rolled Al2024 and Al1015 plates, respectively. The rolling process introduced texture to the

material, and consequently changes the shape of the Bragg edge. Some of the changes in shape, e.g., red curve in Fig. 7.3, can still be described by analytical functions (explained in previous subsection). However, some texture-affected Bragg edges, e.g., blue curve in Fig. 7.3, present a challenge to the analytical function in describing the shape and determining the position of the Bragg edge, since the function does not consider texture contributions in its parametrisation.

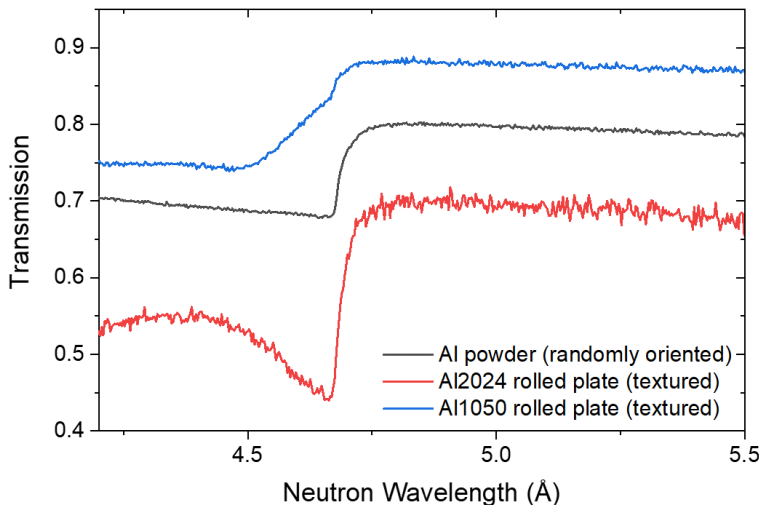


Fig. 7.3 Changes in Bragg edge shape due to crystallographic texture. The black curve is Al {111} Bragg edge measured from a randomly-oriented Al powder. The red and blue curves are Al {111} Bragg edges measured from rolled Al2024 and Al1015 plates, respectively. Different transmission values are due to the differences in the thickness of the samples in the transmission direction.

Rietveld-type analysis (Sato et al., 2011) and model-based fitting (Song et al., 2017) approaches have been attempted to solve this problem. In the absence of a fully validated analytical model for textured samples, a parameter-free cross-correlation-based analysis method has been developed and used in this work to estimate the shift of Bragg edges on both textured and non-textured samples. Cross-correlation measures the similarity between two signals as a function of the shift of one relative to the other. The steps of performing the analysis are described below.

Firstly a reference Bragg edge and the Bragg edge from the region of interest (ROI), having approximately the same shapes (i.e., having the similar preferred orientation), are selected, Fig. 7.4(a). A reference Bragg edge with similar shape is obtained by measuring the unstressed part of the same sample, or by measuring a stress-relaxed coupon sectioned from the sample. Then, the reference and region of interest Bragg edges are selected from a same wavelength range, i.e., both have the same number of data points, Fig 7.4(a). Secondly,

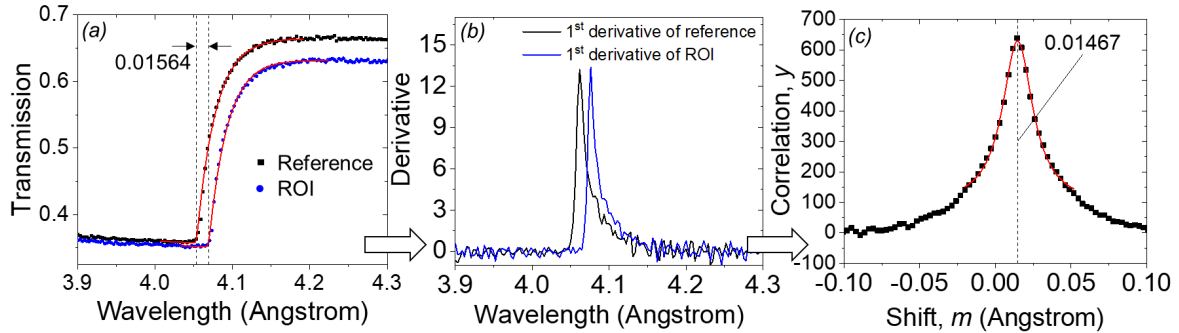


Fig. 7.4 Illustration of the steps of performing the cross-correlation based Bragg edge analysis. (a) Reference Bragg edge and Bragg edge from region of interest (ROI), having a similar shape. Measured shift using the edge analytical function approach between reference and ROI Bragg edge is 0.01564 Å; (b) The 1<sup>st</sup> derivative of reference and ROI Bragg edge; (c) Cross-correlation function of reference and ROI Bragg edge. The peak of the function represents the shift of the two Bragg edges, giving a value of 0.01467 Å.

since the edge-shaped transmission signal is not ideal for cross-correlation, i.e., causing the maximum correlation to be always in the middle with the shift of zero, the peak-shaped derivative of the signal is used. Numerical derivatives of both the reference Bragg edge and the Bragg edge from the region of interest are taken, Fig. 7.4(b), whilst it has to be noted that differentiation amplifies noise. Smoothing of the raw transmission data can be carefully carried out to help to mitigate the effects of noisy data, however over-smoothing (averaging over too many points) might add higher uncertainties to the final results of the cross-correlation.

The correlation coefficient  $y$ , as a function of the shift  $m$  of the two Bragg edge derivatives (reference and region of interest), is then calculated using Eq. (7.4).

$$y(m) = \sum_{\lambda_i, i=0}^{M-1} f(\lambda_i)g(\lambda_{i-m}) \quad (7.4)$$

where  $f(\lambda)$  and  $g(\lambda)$  are the two Bragg edge derivatives, and  $M$  is the region of the wavelength range. The correlation of the derivatives in Fig. 7.4(b) is shown in Fig. 7.4(c). The position of the maximum of the correlation function  $y(m)$  is assumed to provide the best estimate of the shift (i.e., difference in position) between the two Bragg edges. The correlation function can be obtained by peak fitting (in this case using a Voigt function) to determine the shift, while the fitting error can provide the shift uncertainty. Thus the shift between two Bragg edges is determined without requiring an analytical function. The cross-correlation

analysis in Fig. 7.4(c) yields an edge shift of  $0.01467 \text{ \AA}$ , which agrees well with the result using the analytical function approach, Fig. 7.4(a).

Another example is given by taking the textured Al [111] Bragg edge measured from Al1015 plate (shown by blue curve in Fig. 7.3) and manually shift the data by a known value, which in this case 10 time bins ( $10 \times 40 \text{ ms} = 400 \text{ ms}$ ) which equals to a shift of  $0.02806 \text{ \AA}$  for the corresponding setting on IMAT. The measured and the shifted data are shown by the red and blue data points in Fig. 7.5(a), respectively. Fitting the two curves with the Bragg edge model Eq. (4.4) produces a shift of  $0.03086 \text{ Angstrom}$ , which offset the real shift by  $2.80 \times 10^{-3} \text{ Angstrom}$  or equivalent to around  $600 \mu\epsilon$ . The difference is caused by the inconsistency of the Bragg edge model in fitting the data, shown by the difference curve in Fig. 7.5(a), resulting in the unreliable determination of Bragg edge position.

Meanwhile, first derivative of the textured Bragg edge profiles produced peak shaped curves which are still difficult to model analytically, shown by the inset in Fig. 7.5(a). However, using cross correlation method, the correlation curve are easily fitted by Voigt function, Fig. 7.5(b), and giving a shift of  $0.02876 \pm 5.7 \times 10^5$ . In this case, the cross correlation method produce shift with the accuracy within  $150 \mu\epsilon$ , which is in the ballpark of strain resolution of the instrument (more on that in **Section 7.5.2**).

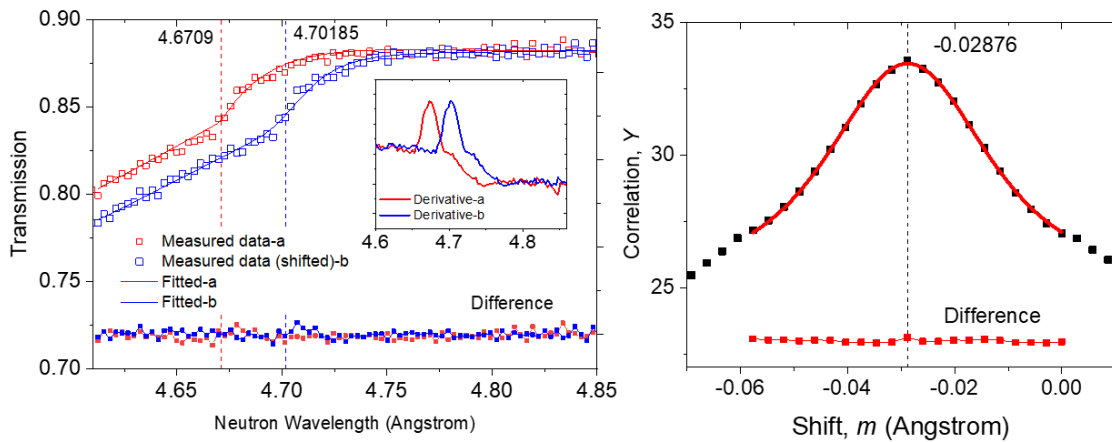


Fig. 7.5 Cross correlation analysis on textured Al Bragg edge. (a) Original (red data points) and shifted (blue data points) textured Al Bragg edge profile, fitted with Bragg edge function (solid curve). The inset show the first derivative of the Bragg edge profiles; (b) Correlation function of the first derivative of the Bragg edge profile, with the Voigt function fitted.

## 7.4 Commissioning experiments for Bragg edge strain mapping

A series of commissioning experiments were performed to characterise the Bragg edge imaging analysis on IMAT, in terms of accuracy and level of uncertainty of the result as well as the spatial resolution produced from the imaging. Transmission experiments at high temperature were performed to investigate the accuracy and resolution of the Bragg edge strain analysis performed on the instrument. Measurements of a sample at different distances from the detector were also performed to determine the achievable spatial resolution of the reconstructed strain map.

For all experiments, the flight path is approximately 56.37 m, which is the distance from the moderator to the MCP detector. The neutrons were collected in histogram mode (neutron counts as a function of the neutron time-of-flight). Choppers were set to a frequency of 10 Hz, providing a maximum wavelength range of 7 Å, with the maximum intensity recorded at around 2.6 Å. The wavelength band was divided into 2500-3000 bins, with a bin width of around 0.0014 Å (equivalent to 20 µs) for wavelengths  $< 3.3$  Å and bin width of around 0.0029 Å (40 µs) for wavelengths  $> 3.3$  Å. A narrower bin width at shorter wavelengths was applied considering the sharper pulse widths.

### 7.4.1 High temperature measurement

A neutron transmission experiment at elevated temperatures was performed on IMAT, where the thermal expansions of several samples were measured to provide data from stress-free changes in the lattice parameter of the materials. This could be then used to determine the level of uncertainty and the accuracy of the overall measurement system by comparing the measured values against documented thermal lattice strain data in the literature. CeO<sub>2</sub>, Fe and pure Al powders were used in the high-temperature experiment, representing measurements of ceramics and non-textured engineering metals. A rolled Al1050 plate (BS EN 573:3 1050A H14) with a nominal thickness of 6 mm was also measured to represent textured engineering alloys.

The CeO<sub>2</sub>, Fe, and Al powder samples were inserted into 15-mm-diameter vanadium cans of 0.15 mm wall thickness, while the textured Al plate was cut into a disc with 30 mm diameter, Fig. 7.6(a). These samples were then loaded into a “RAL5” furnace available at the ISIS facility which was installed in front of the MCP transmission detector, Fig. 7.6(b) and (c). The RAL5 furnace allows neutron transmission measurements at temperatures up to 1273 K by means of radiative heating with a vanadium foil element heater. A vacuum better

than  $10^{-3}$  mbar was applied to avoid oxidation of the samples, while the vanadium element and vanadium windows through heat shields and furnace vessel walls allowed neutrons to pass through with minimal Bragg diffraction. Two thermocouples, one at the bottom of the heating element and another attached to the sample, were fed into a proportional-integral-derivative (PID) temperature controller to record and regulate the sample temperature. Due to the installation of furnace on the beamline, the distance between the sample and the MCP detector was 170 mm.

Measurements were taken in-situ at a range of temperatures from room temperature up to 1143 K for Fe and CeO<sub>2</sub>, and up to 823 K for the Al samples. The temperature was held constant during each measurement within 2 K, with a measurement time of  $3 \times 0.5$  hours (1.5 hours in total) for the Fe and CeO<sub>2</sub> samples and  $4 \times 0.5$  hours (2 hours in total) for the Al samples. The 0.5 hour data blocks from each measurement were analysed individually and results showed good repeatability. The sum of the 0.5 hour blocks data from each measurement were taken to improve the statistics, and were used for the analysis in this paper. The experimental setup of the high-temperature measurements is illustrated in Fig. 7.7.

The uncertainty of the measured strain corresponds to the uncertainty in the determination of the Bragg edge position: this is similar to Bragg-peak analysis for strain measurement (Santisteban et al., 2006a). The strain was determined using Eq. 7.5 and the strain uncertainty was calculated following the error propagation expressed in Eq. 7.6.

$$\varepsilon = \frac{\lambda_T - \lambda_0}{\lambda_0} \quad (7.5)$$

$$\Delta\varepsilon = \sqrt{\frac{1}{\lambda_0^2}(\Delta\lambda_T)^2 + \frac{\lambda_T^2}{\lambda_0^2}(\Delta\lambda_0)^2} \quad (7.6)$$

where  $\lambda_0$  and  $\lambda_T$  are the fitted parameters of Eq. 4.4 describing the position of a Bragg edge at room temperature and at a particular temperature  $T$ , respectively; and  $\Delta\lambda_0$  and  $\Delta\lambda_T$  are the fitting uncertainties. Any  $T$  values can be used for uncertainty determination, in this case  $T = 573$  K. The Bragg edge being analysed was Fe {110}. The uncertainty of measurement as a function of time and macro-pixel size was analysed. The uncertainty of strain measurement on IMAT is reported in **Section 7.5.2**.

To assess the accuracy of the strain measurement, the thermal lattice expansions of the Fe, CeO<sub>2</sub>, and Al powders measured using neutron transmission were compared against literature data (Basinski et al., 1955; Stecura and Campbell, 1961; Wilson, 2002; Jette and Foote, 1935;

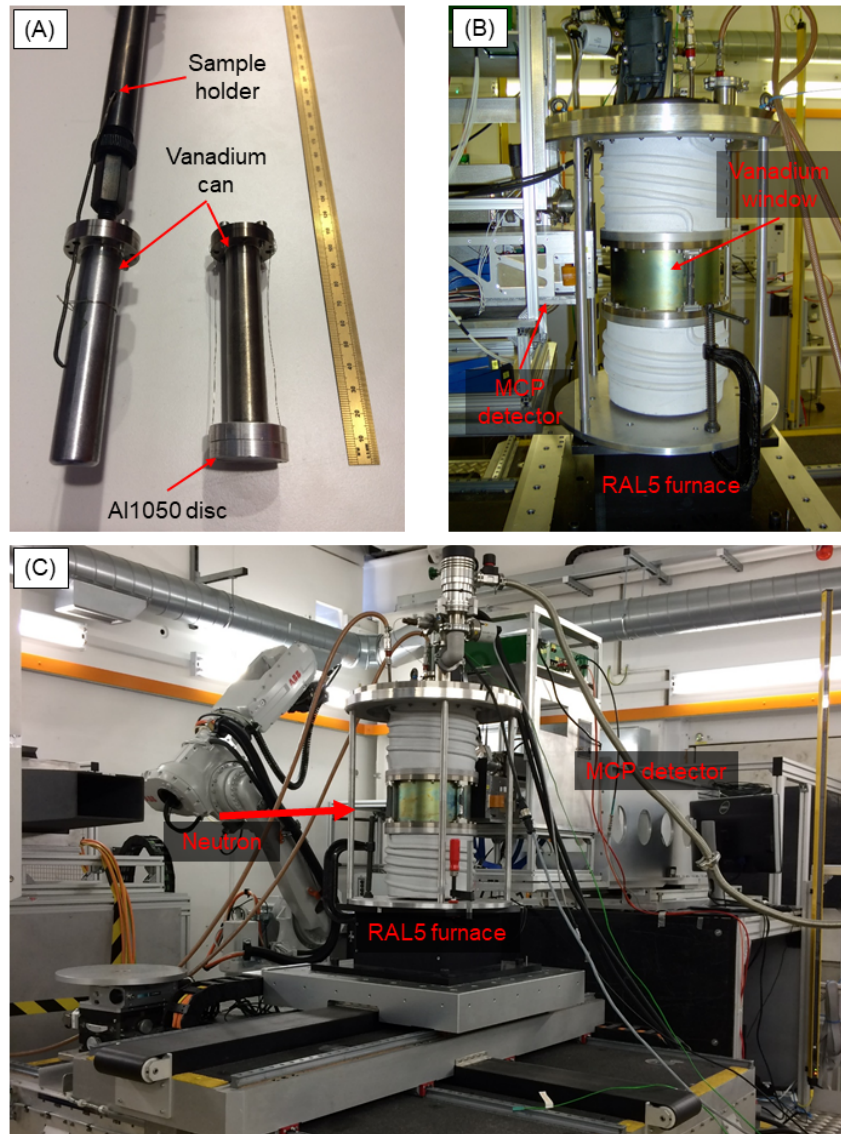


Fig. 7.6 Photographs of high temperature experiment: (a) Vanadium cans and the disc shaped Al1050 sample; (b) RAL5 furnace and MCP detector; (c) RAL5 furnace on IMAT.

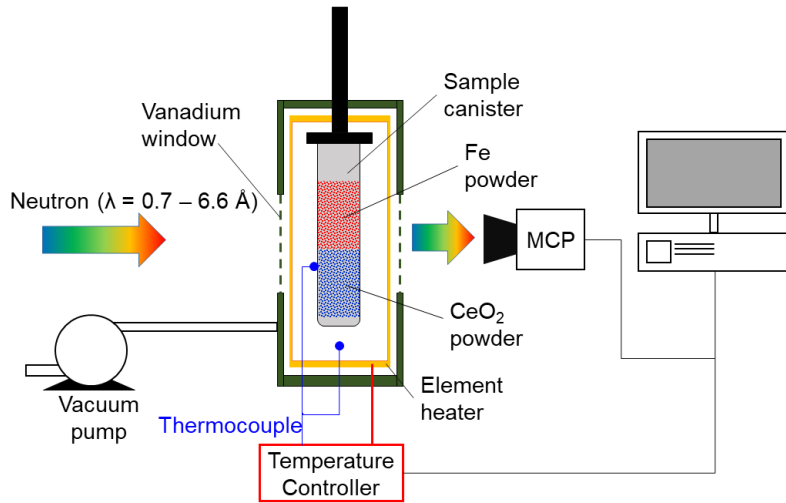


Fig. 7.7 Setup of high temperature experiment on IMAT, with simultaneous measurement of  $\text{CeO}_2$  and Fe powders.

Davey, 1925). In the current work, lattice parameters were determined by fitting Eq. 4.4 to Fe {110},  $\text{CeO}_2$  {220}, and Al {111} Bragg edges. The accuracy of strain measurement on IMAT is reported in **Section 7.5.3**.

To assess the accuracy of the cross-correlation method in determining changes in lattice spacings, the method was used to measure the thermal lattice strain  $\varepsilon_T$  on both textured and non-textured samples:

$$\varepsilon = \frac{\Delta a}{a_0} = \frac{a_T - a_0}{a_0} \quad (7.7)$$

where  $a_T$  is lattice parameter at temperature  $T$ , and  $a_0$  is the lattice parameter at room temperature. Bragg edge shift values obtained from the cross-correlation analysis are represented by  $\Delta a$ . Using cross-correlation, thermal strain was measured from texture-free powder samples using Fe {110} and  $\text{CeO}_2$  {220} Bragg edges; and from textured aluminium plate using the Al {111} Bragg edge. The results are compared against thermal strain analysed using non-linear fitting methods. The accuracy of the cross-correlation method is presented in **Section 7.5.4**.

#### 7.4.2 Spatial resolution measurement

Spatial resolution of a reconstructed strain map is mainly governed by two factors: 1) Geometrical blurring  $d_b$ , as explained in **Section 4.2.3** and investigated in **Section 6.3**, and;

2) macro-pixel size. As described in detail in **Section 4.3.3**, it is not possible to carry out a pixel-by-pixel analysis in reconstructing a Bragg edge map containing lattice spacing (hence strain) information due to limited counting statistics. For the current version of MCP detector, a macro-pixel with typical size ranging from  $5 \times 5$  to  $50 \times 50$  pixels is used, and a running average with step size of 1 pixel ( $55 \mu\text{m}$ ) is applied.

Measurement of the spatial resolution of a reconstructed Bragg edge map requires a sample to have both a Bragg edge spectrum and sharp edge features. These two requirements characteristics are contradictory: sufficient sample thickness is needed to produce a distinct Bragg edge spectrum in most materials, however a sample with considerable thickness (over a few hundred  $\mu\text{m}$  thick) introduces alignment issues and consequently will produce blurry edges. Therefore, measurements were made on a thin neutron-absorbing Siemens Star in conjunction with an Fe rod with 10 mm thickness along the transmission direction. The sample-to-detector distance  $l$  was varied in order to get data with geometrical blurring values of  $d_b = 0.2, 0.6$  and  $1.8$  mm. A detailed description about the sample setup is provided in **Section 6.3.2**. On the other hand, to measure the spatial resolution solely as a function of macro-pixel size, digital masks were applied to powder sample data. Fe and CeO<sub>2</sub> powder were used to investigate the dependence of the MTF analysis to the materials being analysed.

Bragg edge maps were reconstructed from the data using TPX\_EdgeFit with different macro-pixel sizes ranging from  $5 \times 5$  to  $50 \times 50$  pixels. The Bragg edge height [coefficient  $C_2$  in Eq. (4.5)] map was subjected to an MTF analysis with 10% cut-off using the edge of the Siemens Star covering the Fe rod sample. From the analysis, the spatial resolution of the macro-pixel method was determined and is reported in **Section 7.5.5**.

### 7.4.3 Strain validation measurement

In order to determine the accuracy of Bragg edge strain mapping on IMAT, it is necessary to compare the produced strain maps with a more established strain measurement technique, on a real engineering sample. Strain validation was carried out by performing Bragg edge strain mapping on a sample with well-known residual strain profile, and comparing the result with measurements from neutron diffraction.

Residual strain mapping was performed on an AlSiC<sub>p</sub> metal matrix composite (MMC). The material is an attractive option for engineering and structural applications (El-Gallab and Sklad, 1998). The composite sample was constituted of an Al2124 matrix and pure silicon carbide particulates at 20% weight fraction, and was fabricated by Aerospace Metal Composites, UK (now Materion AMC, UK). The production includes a heat treatment process comprising a solution heat treatment followed by cold water quenching, which is

expected to introduce a parabolic residual strain variation through the thickness of the plate. The sample dimensions are 35 mm × 35 mm × 15 mm.

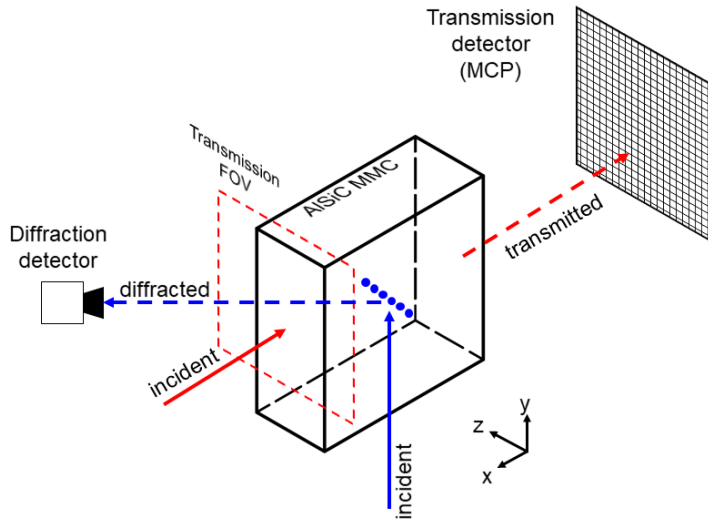


Fig. 7.8 Setup of neutron transmission (red lines and arrows) and neutron diffraction (blue dots and arrows) measurements on an AlSiC<sub>p</sub> metal matrix composite.

Neutron transmission data were collected on IMAT by placing the sample ≈ 29 mm in front of the MCP detector. The measurement time was four hours using a pinhole of 40 mm ( $L/D = 250$ ). The sample was aligned so the measured strain is averaged in the  $x$ -axis direction, where the coordinate system and the experimental setup are shown in Fig. 7.8. Neutron diffraction on the same sample was performed on ENGIN-X (Santisteban et al., 2006a) for comparison. A gauge volume of 2 mm × 2 mm × 10 mm was used, with 13 measurement points located along the  $z$ -axis, with 30 minutes measurement time per point. The gauge volume was elongated along the  $y$ -axis, since minimum strain variation was expected in this direction and the diffracting volume could thus be increased without compromising strain resolution. The sample was aligned to measure the  $x$ -axis strain, Fig. 7.8.

For both neutron transmission and diffraction, an Al powder which constitutes the composite matrix material was used for measurement of the strain-free lattice parameter  $d_0$ . The Al {111} Bragg edge was used for analysis to obtain the strain map from the transmission signal. The Bragg edge fitting method was used, and fitting was performed using the BEATRIX software with a macro-pixel size of 20 × 20. Neutron diffraction data were analysed by fitting the Al {111} Bragg-peak, using single peak fitting with double-

exponential TOF function convoluted with the Voigt function (Santisteban et al., 2006a). The results of the validation measurements are reported in **Section 7.5.6**.

## 7.5 Results

### 7.5.1 Transmission spectra at high temperature

Fig. 7.9 and 7.10 shows examples of neutron transmission spectra obtained from a non-textured sample (in this case Fe powder) and a textured sample (rolled Al plate) at different temperatures. Fig. 7.9 shows multiple Bragg edges from different sets of Fe  $\{hkl\}$  which shift to higher wavelengths with the increase of temperature, as a result of thermal expansion of the material. Moreover, it can be observed that the Bragg edge heights (the difference in transmission above and below the edge) decrease as the temperature increases. This observation relates to the thermal motion of atoms and will be further discussed in Chapter 8. It can also be observed that, beyond the Bragg cut-off at 4.05 Å, i.e., wavelength above the  $\{110\}$  Bragg edge for Fe, the transmission decreases as the temperature increases due to the increase in thermal diffuse scattering (TDS) while absorption does not change with temperature significantly apart from a change in density. As TDS increases and Bragg diffraction decreases with rising temperature, the change in transmission is less pronounced below the Bragg cut-off.

Fig. 7.10 shows transmission spectra through the whole thickness of the rolled Al plate, where spectra measured from room temperature to 573 K show irregular Bragg edge shapes, implying the presence of crystallographic texture. This is especially apparent for the  $\{111\}$  Bragg edge as shown in the inset of Fig. 7.10. At 623 K, however, the transmission spectrum changes drastically, where it resembles more closely data from a randomly-oriented sample. A spectrum from a completely non-textured sample, i.e., Al powder, is plotted for comparison. These changes are due to recrystallisation at higher temperature, and will be discussed further in Chapter 8.

### 7.5.2 Uncertainty and strain resolution

The uncertainty of a Bragg edge strain measurement is highly dependent on the statistical quality of the Bragg edge signal, and thus on the length of the measurement time and the size of the macro-pixel. Fig. 7.11. shows the  $\{110\}$  Bragg edges of the Fe powder, measured at room temperature for 1.5 hours. The figure illustrates the difference of statistical quality produced by different macro-pixel sizes.

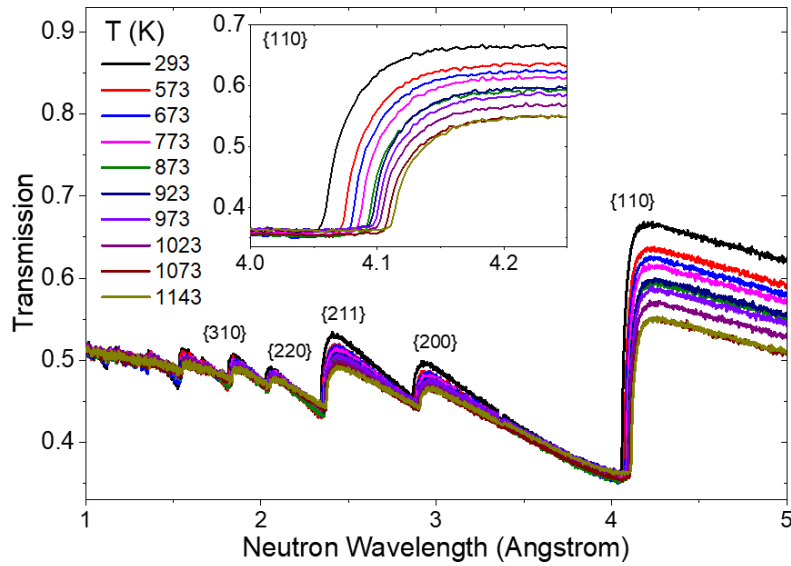


Fig. 7.9 Transmission spectra of Fe powder at different temperatures. The Bragg edges shift to higher wavelengths with increasing temperature because of thermal lattice expansion. The Bragg edge heights decrease with the increase of temperature because of the thermal motion of atoms. The typical detection area size for the spectra was  $\approx 256 \times 256$  pixel.

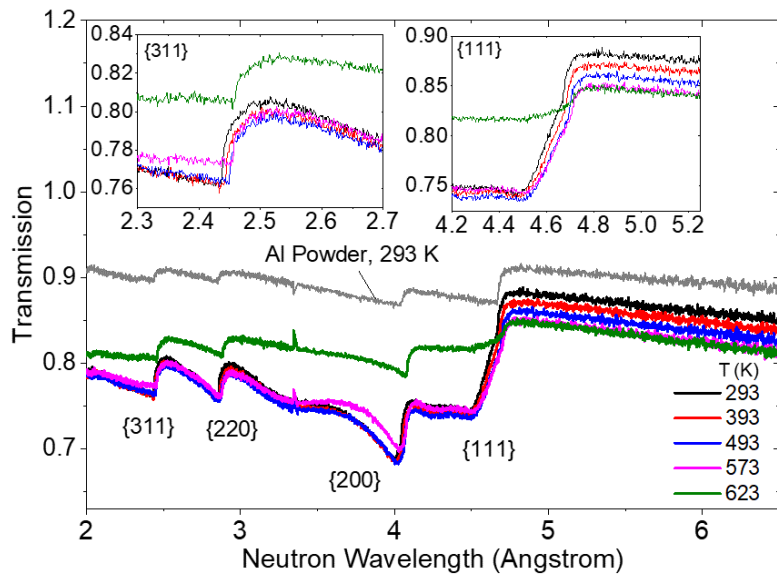


Fig. 7.10 Transmission spectra taken from the whole thickness section of the rolled aluminium plate (detection area size of  $\approx 200 \times 200$  pixels, sample thickness in transmission direction of 30 mm). At 623 K, the transmission spectra changes drastically, indicating recrystallisation. Spectra from non-textured Al powder are plotted for comparison, with higher transmission due to smaller sample thickness.

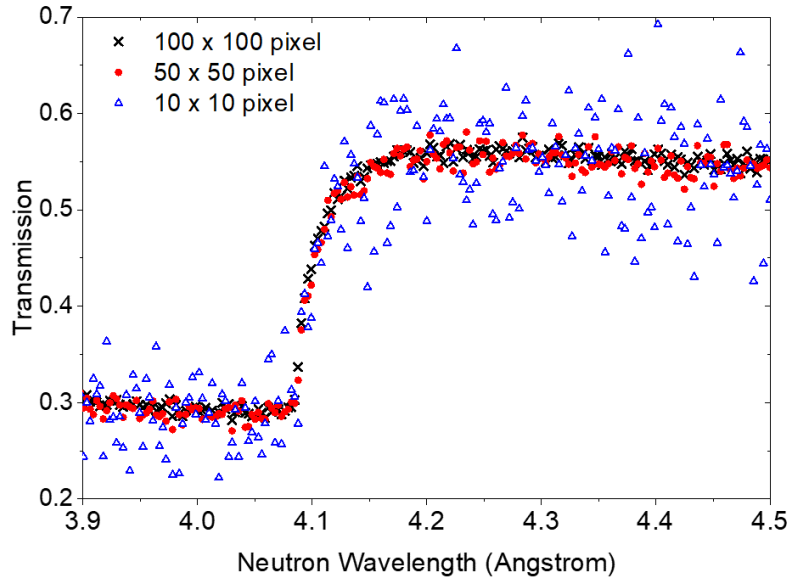


Fig. 7.11 Statistical quality of Fe {111} Bragg edges, measured using different macro-pixel sizes.

To investigate the uncertainty and the strain resolution, Fe {110} Bragg edges were analysed. The strain-affected Bragg edges were acquired from Fe powder data measured at  $T = 573\text{ K}$  for 1.5 hours (actual measurement time,  $t_{\text{act}}$ ). Bragg edges were obtained from different  $n \times n$  pixels (actual area,  $A_{\text{act}}$  ranging from  $4 \times 4$  to  $220 \times 220$  pixels) to obtain the uncertainty as a function of statistical quality. The reference Bragg edge was taken from Fe powder data measured at room temperature. When acquiring the reference Bragg edge, a large detection area size was selected in order to obtain good statistics. This reflects the actual experiment condition, where the reference or  $d_0$  sample is usually measured for a longer time to achieve the best statistics possible to minimise the strain uncertainty. The positions of the reference and the strain-affected Bragg edges,  $\lambda_0$  and  $\lambda_T$ , respectively, were determined by the analytical function described by Eq. (4.4), and were used to calculate the strain using Eq. (7.5). The fitting uncertainties  $\Delta\lambda_0$  and  $\Delta\lambda_T$  were then used to calculate the strain uncertainty using Eq. (7.6).

For experimental design, the interest is in the determination of the minimum achievable uncertainty and the time needed to achieve different levels of uncertainty. Therefore, the uncertainty as a function of statistical quality is represented in terms of macro-pixel size and effective measurement time  $t_{\text{eff}}$ . The four macro-pixel sizes of interest are  $10 \times 10$ ,  $20 \times 20$ ,  $50 \times 50$ , and  $100 \times 100$ , while  $t_{\text{eff}}$  is calculated using Eq. (7.8) below. The results are shown in Fig. 7.12.

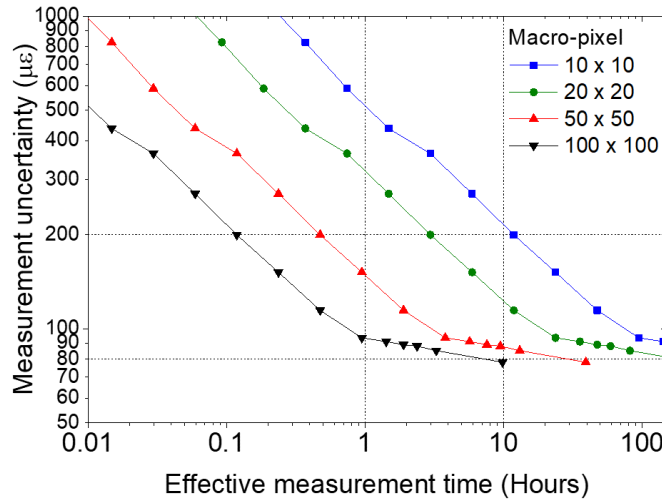


Fig. 7.12 Strain uncertainty analysed from the Fe {110} as a function of effective measurement time.

$$t_{eff} = \frac{A_{act} \times t_{act}}{\text{macro-pixel size}} \quad (7.8)$$

From Fig. 7.12, it can be observed that the curves flatten around the value of 80-90  $\mu\epsilon$ , indicating the upper limit of the strain resolution. Using a macro-pixel of  $20 \times 20$ , an uncertainty of 125  $\mu\epsilon$  can be achieved within 10 hours and an uncertainty of 200  $\mu\epsilon$  is achievable within 3 hours of measurement time. It is important to take note, however, that these numbers are valid for the given measurement conditions, i.e., specific to strain analysed from the most intense Fe {110} Bragg edges with a sample thickness of 15 mm and  $L/D$  of 250, the latter of which is giving an average neutron count rate of 1 neutron per second per 40  $\mu\text{m}$  TOF bin for a  $20 \times 20$  macro-pixel, with a detector efficiency of 40%. Different uncertainty plots, as displayed in Fig. 7.12, are expected for different Bragg edges and/or different sample geometries. An  $L/D$  of 250 provides a good compromise between spatial resolution and collection time for many IMAT experiments. The use of larger pinhole sizes (i.e., 80 mm or 100 mm) have already significantly reduced the measurement times on IMAT (by a factor of four or more) but with the penalty of lower spatial resolution due to larger geometrical blurring. Ultimately, the strain uncertainty can be improved by implementing a multiple Bragg edge refinement, which is the outlook for the future.

### 7.5.3 Accuracy of the lattice parameter & strain measurement

Lattice parameters obtained for Fe, CeO<sub>2</sub>, and Al powders at room temperature were compared against literature values. Using neutron transmission, the lattice parameter of Fe was measured to be  $2.8675 \pm 0.00016$  Å. This value agrees well with literature values listed in Table 6.1. The lattice parameters of CeO<sub>2</sub> and Al measured by neutron transmission are  $5.4097 \pm 0.0007$  Å and  $4.0506 \pm 0.0008$  Å, respectively. These values also agree well with literature values in Table 6.1. Agreement between the current work and literature values demonstrates the accuracy of neutron transmission for lattice parameter determination.

In order to give a measure of the accuracy of a strain measurement using neutron transmission, comparison between lattice parameter values of the Fe, CeO<sub>2</sub>, and Al powder at different temperatures from the current work are plotted against literature values, Fig. 7.13. It can be observed that, despite showing differences in the absolute lattice parameter values, particularly for Fe and Al, the present results agree very well with the literature for the relative changes of lattice parameter as function of temperature. This is shown by fitting a third-order polynomial to describe thermal expansion, to both the current measurement and literature values. The fitted coefficients are given in Fig. 7.13. For Fe and Al data, it can be observed that the expansion coefficients compare well with literature values, most of them within the fitting error, Fig. 7.13(a) and (c), respectively. Meanwhile for CeO<sub>2</sub> data, good agreement can be observed between the present results and literature values for all the fit parameters. Discrepancies in intercepts, i.e., absolute lattice parameters at room temperature, with results from Basinski et al. (1955) and Wilson (2002), Fig. 7.13(a) and (c) are conceivably due to the different amounts of impurities in the samples used. It can be noted that the two aforementioned literature comparisons were selected since both provide thermal expansions in a temperature range comparable with the current work. Meanwhile the good agreement between relative changes of lattice parameter as a function of temperature measured in the current work and in previous literature for all three samples is a confirmation of good accuracy and quantifies the strain uncertainties for the neutron transmission measurements on IMAT.

### 7.5.4 Accuracy of the cross-correlation data analysis

Fig. 7.14 shows thermal lattice strains [Eq. (7.7)] of Fe and CeO<sub>2</sub> powders analysed by analytical Bragg edge fitting and by the cross-correlation method. It can be observed that the results lay on a straight line with a slope of  $0.983 \pm 0.005$  and  $0.952 \pm 0.015$  for Fe and CeO<sub>2</sub> data, respectively, indicating that the cross-correlation method accurately reproduced the results from analytical Bragg edge fitting method for the non-textured samples. It can be

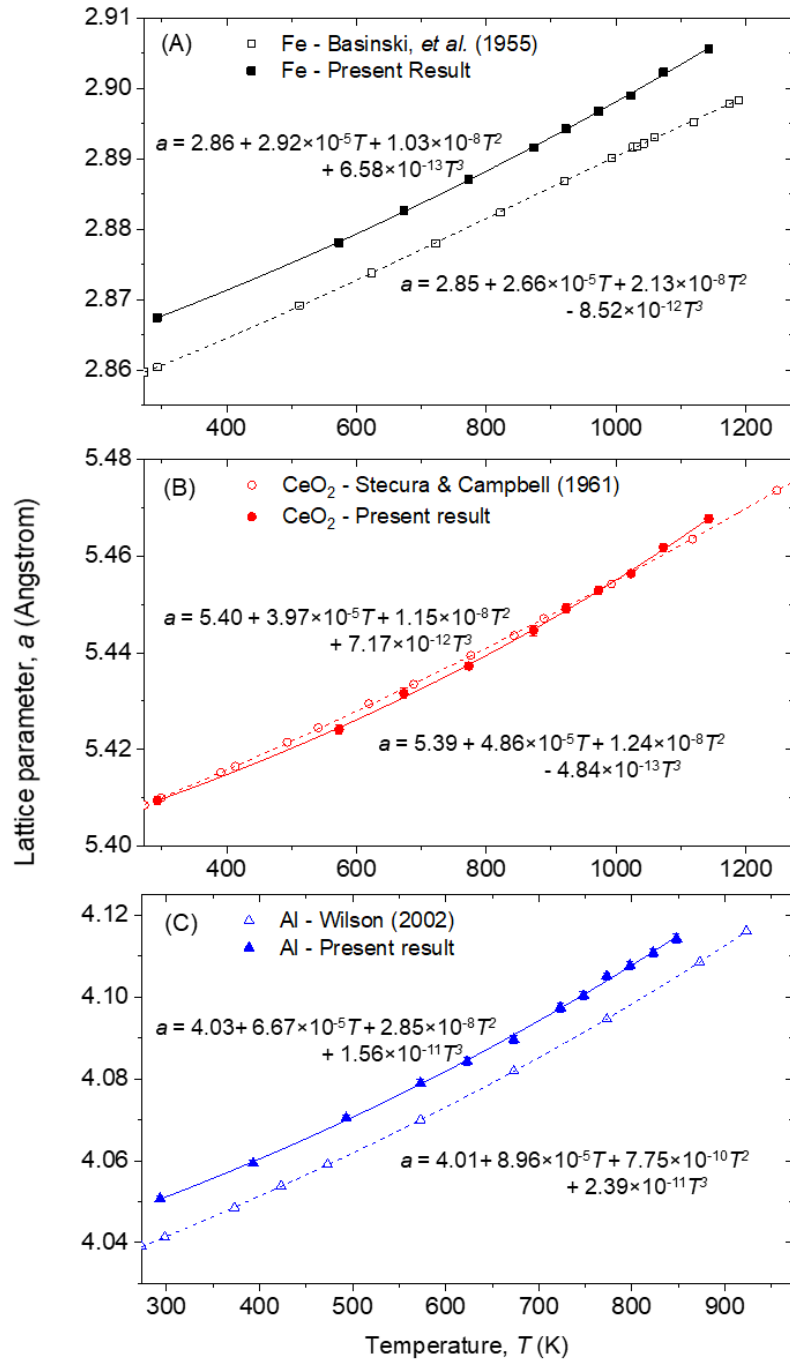


Fig. 7.13 Lattice parameters of (a) Fe, (b)  $\text{CeO}_2$ , and (c) Al powders as a function of temperature, measured in the current study by neutron transmission at IMAT (solid symbols), and compared with literature values (open symbols). Solid and dotted lines are third-order polynomial fits with the equation given on the graphs. The fitted Bragg edges were extracted from detection area size of  $256 \times 256$  pixels for Fe,  $230 \times 230$  pixels for  $\text{CeO}_2$ , and  $268 \times 268$  pixels for Al.

observed as well that the level of uncertainty that is achieved by cross-correlation is similar to that by Bragg edge fitting.

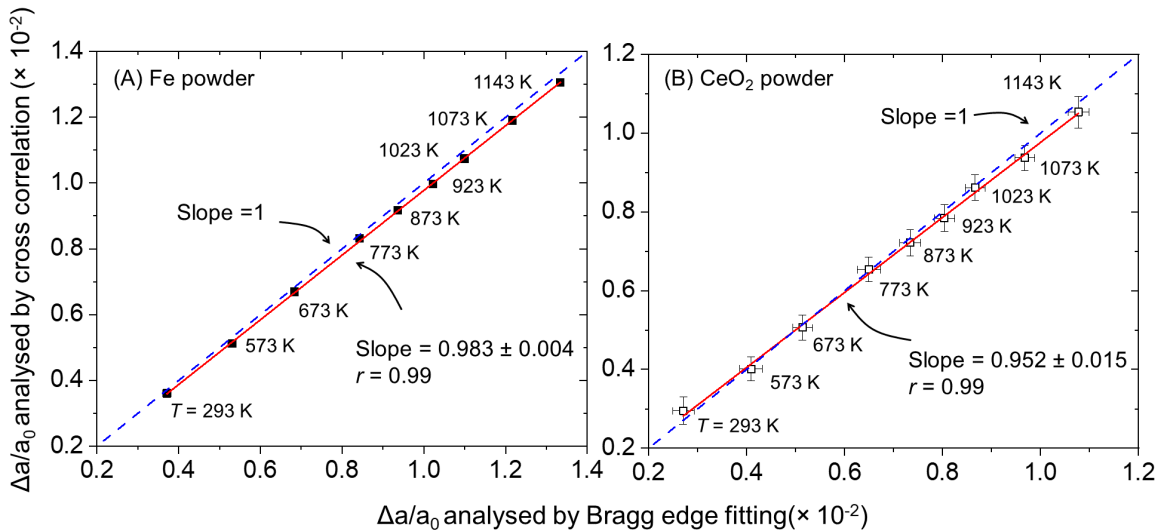


Fig. 7.14 Thermal lattice strains  $\Delta a/a_0$  of (a) Fe and (b)  $\text{CeO}_2$  analysed using cross-correlation and Bragg edge fitting methods. The red lines are the linear fit of the data points, while the blue dashed lines with slope of 1 are shown for comparison. The results indicate that cross-correlation successfully reproduces the Bragg edge fitting results for a non-textured sample. The Bragg edge spectra for both approaches were extracted from detection area sizes of  $256 \times 256$  pixels for Fe and  $230 \times 230$  pixels for  $\text{CeO}_2$ .

While it was shown that cross-correlation analysis works for non-textured samples, the main purpose was to demonstrate that this method works for measuring shifts of Bragg edges with irregular shapes in the presence of crystallographic texture. The analysis was performed for two Bragg edges of the same transmission spectrum taken from the textured Al11050 plate: Al {111} and Al {311}. From the spectra shown in the inset of Fig. 7.10, it can be seen that the Al {311} edge is a more regular, ‘powder-like’ Bragg edge compared to the Al {111} edge for which an almost linear increase of transmission is observed ahead of the Bragg edge itself. The shift of the two edges due to thermal expansion is the same as for the cubic unit cell of aluminium. Therefore, the more established edge function fit approach was applied to measure the shift of the Al {311} edges, and the results were used as the reference to benchmark the cross-correlation method for analysing the shift of Al {111} edges.

Fig. 7.15 shows that cross-correlation analysis on the irregular-shaped Al {111} Bragg edges produces thermal lattice strains that agree well with the reference, with differences being well within the uncertainty of the measurement. Meanwhile, thermal lattice strains from the Bragg edge fitting method on the textured {111} deviate significantly from the reference, although this is partly captured in the increased measurement uncertainty. This

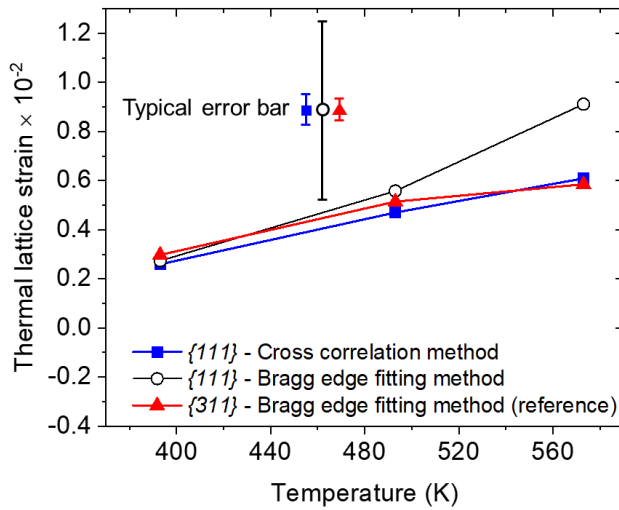


Fig. 7.15 Thermal lattice strain of the rolled aluminium plate, analysed from texture-affected Al {111} Bragg edge using the cross-correlation method and the Bragg edge function fitting method. The cross-correlation results agree well with the reference, i.e., thermal lattice strain analysed from ‘powder-like’ Al {311} Bragg edge using function fitting method, demonstrating the capability of cross-correlation for measuring strain on textured samples. All the Bragg edges were extracted from detection regions of  $268 \times 268$  pixels.

implies that the cross-correlation analysis better reproduces the strain measurement on a textured sample, and may be used in cases where the more conventional analytical Bragg edge function fitting approach is hampered by irregular-shaped Bragg edges.

### 7.5.5 Spatial resolution of the reconstructed map

Fig. 7.16 shows the example of the masking process of CeO<sub>2</sub> powder data for the spatial resolution measurement. CeO<sub>2</sub> powder data [Fig. 7.16(a)] was multiplied by the digital mask containing square features [Fig. 7.16(b)], resulting in a masked data [Fig. 7.16(c)]. Pixel-by-pixel Bragg edge fitting using different macro-pixel sizes was performed on the masked data [CeO<sub>2</sub> {220}], and spatial resolution was measured by performing an MTF analysis on the edge of the square features [Fig. 7.16(d)]. The same process was carried out for the Fe powder data [Fe {110}], and the results are presented in Fig. 7.17.

Fig. 7.17 shows a linear relation between macro-pixel size and spatial resolution, where the spatial resolution is approximately half of the macro-pixel size. Fig. 7.17 also shows that the spatial resolution analysis is independent of the type of the material: a Bragg edge maps reconstructed from Fe {110} and CeO<sub>2</sub> {220}, i.e. two Bragg edges with different height, produce almost identical spatial resolution values.

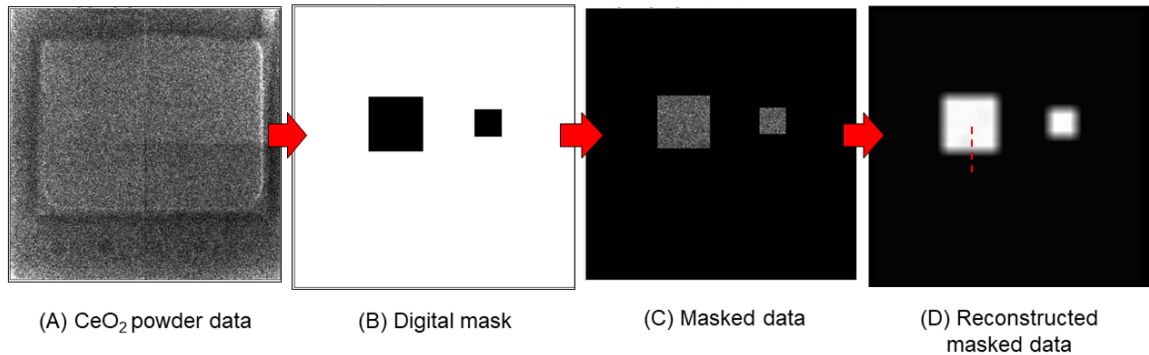


Fig. 7.16 Example of the masking process of  $\text{CeO}_2$  data, showing the (a)  $\text{CeO}_2$  powder data; (b) the applied digital masks; (c) the masked data, and; (d) the reconstructed map from the masked data. The dashed red line shows the edge used for MTF analysis.

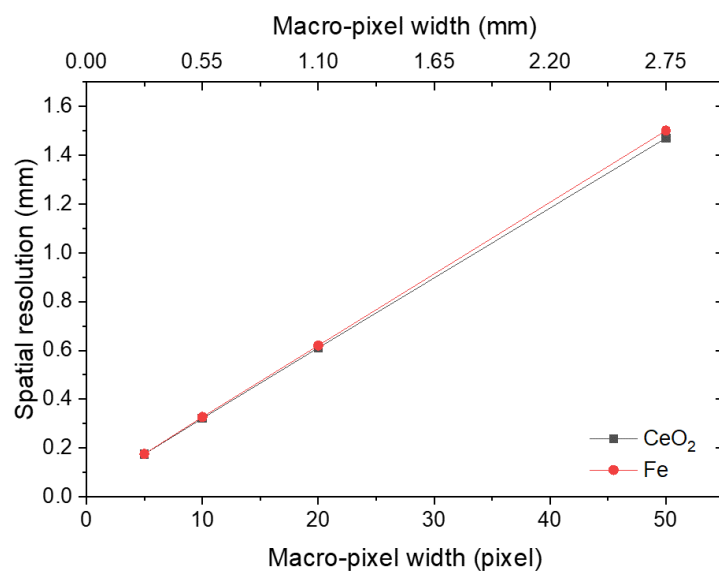


Fig. 7.17 Spatial resolution as a function of macro-pixel size, for Bragg edge maps reconstructed from Fe {110} and  $\text{CeO}_2$  {220}, producing identical result.

The effective spatial resolution of the reconstructed Bragg edge map is influenced by both the geometrical blurring and the macro-pixel size. To determine this effective spatial resolution, the MTFs with 10% contrast cut-off were calculated for Bragg edge height maps reconstructed using (i) different macro-pixel sizes, and (ii) for data with different geometrical blurring. Fig. 7.18(a) shows the reconstructed Bragg edge map (Fe rod covered by Siemens Star); the dashed red box shows the edge used for MTF analysis. Fig. 7.18(b) presents the examples of the map reconstructed using  $5 \times 5$ ,  $20 \times 20$ , and  $40 \times 40$  macro-pixels for data with  $d_b = 0.2$  mm, showing the Siemens Star edge over the map of the  $\{110\}$  Bragg edge of the Fe rod. The corresponding edge spread function (ESF) and modulation transfer function (MTF) are shown in Fig. 7.18(c) and Fig. 7.18(d), respectively, where 10% contrast cut-off is again used as criterion for spatial resolution.

The results are shown in Fig. 7.19. It can be observed that for  $d_b = 0.2$  mm, the relation between effective spatial resolution and macro-pixel size is almost linear. For  $d_b = 0.6$  mm, however, the improvement of spatial resolution due to the reduction of macro-pixel size becomes less significant, especially with the application of macro-pixels smaller than  $30 \times 30$  pixels. This is due to the geometrical blurring  $d_b$  limiting the maximum achievable spatial resolution, shown by the dashed line in Fig. 7.19. As indicated in Fig. 7.19, the trend is further observed for  $d_b = 1.8$  mm where reduction of the macro-pixel width by a factor of 10 (i.e., from 50 pixels to 5 pixels) only improved spatial resolution by around 40% (i.e., from 1.55 mm to 0.96 mm). The results show that the use of smaller macro-pixel sizes is desirable up to a point where geometrical blurring limits the achievable spatial resolution, and therefore needs to be considered when designing experiments. Fig. 7.19 also implies that the spatial resolution is better than the macro-pixel size, due to using a running-average with 55  $\mu\text{m}$  (1 MCP pixel) shift between each reconstructed point (Tremsin et al., 2018). This is equivalent to an ideal 55  $\mu\text{m}$  spatial resolution strain map blurred by a running Gaussian filter (Tremsin et al., 2016b).

### 7.5.6 Validation: Neutron transmission vs diffraction

The map of the  $x$ -axis residual strain of the AlSiC<sub>p</sub> metal matrix composite (MMC) sample is shown in Fig. 7.20(a). It can be observed that compressive residual strain can be found at both surfaces of the composite. The residual strain gradually changes to tensile strain towards the middle of the sample. A parabolic-shaped, symmetrical strain profile through the thickness of the plate can be clearly observed, while minimal strain variation along the  $z$ -axis direction can be seen. A line profile (averaged over line width of 180 pixels or approx. 10 mm) from the strain map, for the dashed line indicated in Fig. 7.20(a), shows that results from neutron transmission agree very well with results from neutron

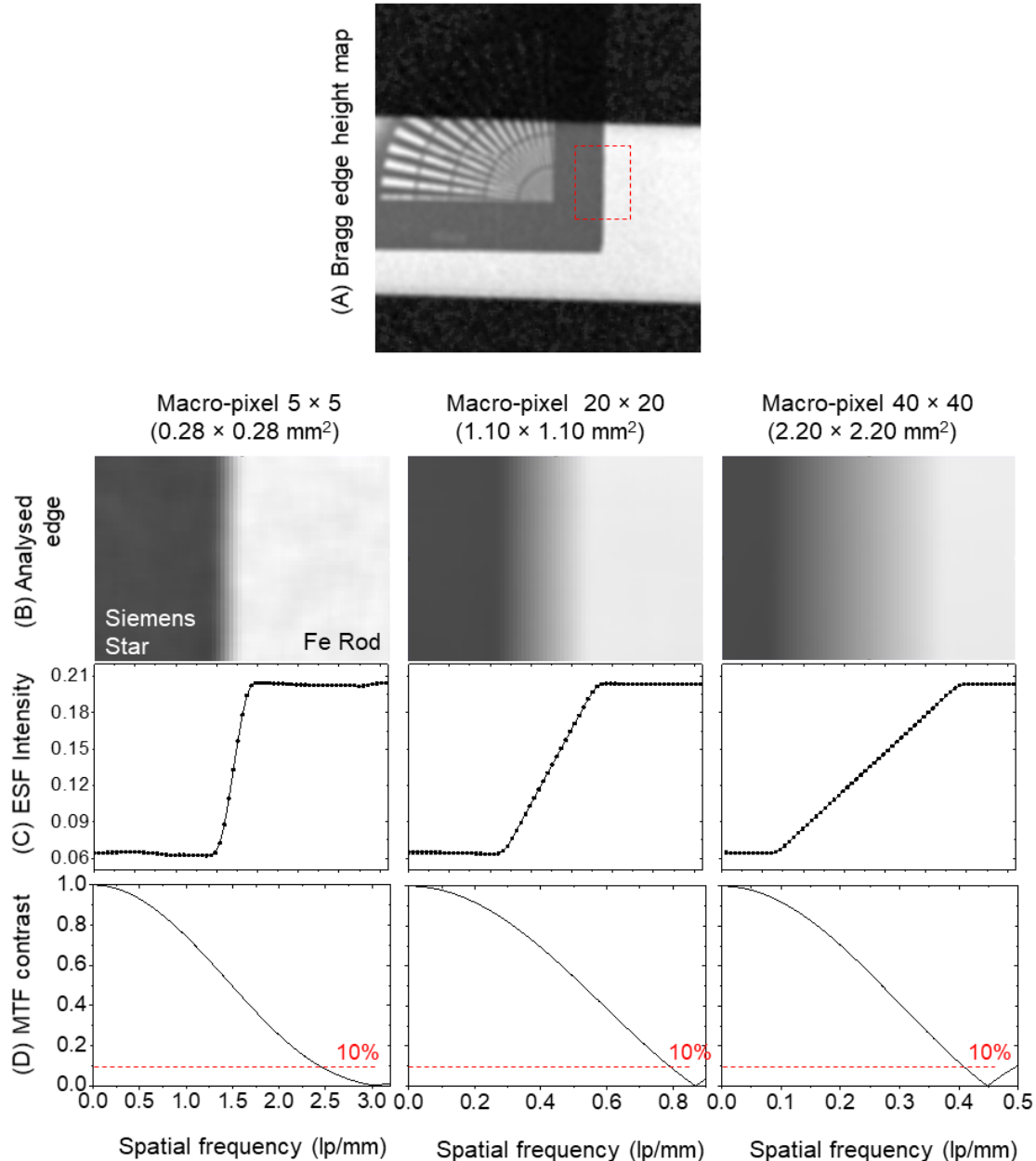


Fig. 7.18 (a) Bragg edge height maps of Siemens star edge behind the Fe rod, reconstructed from Fe  $\{110\}$ ; (b) the analysed edge reconstructed using macro-pixels of  $5 \times 5$ ,  $20 \times 20$  and  $40 \times 40$ , with corresponding ESF (c), and MTF (d). Red dashed box indicate the location from where the MTF analysis was performed. The reconstruction was performed using data measured with  $d_b = 0.2 \text{ mm}$ .

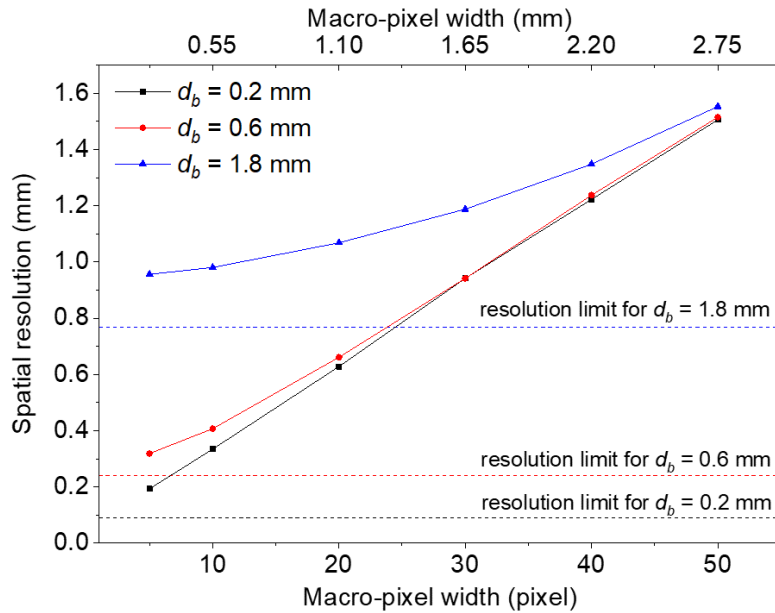


Fig. 7.19 Spatial resolution of a Bragg edge map as a function of macro-pixel size, reconstructed from data with different geometrical blurring values  $d_b$ .

diffraction, Fig. 7.20(b), with an average difference of less than  $270 \mu\epsilon$ . The discrepancies are reasonable due to the difference in the gauge volume from which the values were averaged in the two measurements. Considering the reliability of the diffraction result, this further shows the accuracy of the transmission measurement, as has been previously highlighted above through the high temperature experiment. The corresponding neutron transmission setup has a sample-to-detector distance of  $l = 64 \text{ mm}$  ( $29 \text{ mm} + 35 \text{ mm}$  of sample thickness in transmission direction) and  $L/D = 250$ , therefore has a geometrical blurring of  $d_b = 0.256 \text{ mm}$ . According to Fig. 7.19, this  $d_b$  value and a macro-pixel size of  $20 \times 20$  (used in the reconstruction) yields a the spatial resolution of the reconstructed map of around  $600 \mu\text{m}$ . This high-resolution 2D map was obtained within 4 hours of data collection. Obtaining a map with similar resolution with neutron diffraction would require hundreds of measurement points and would take much longer. This demonstrate one clear advantage of Bragg edge imaging.

## 7.6 Discussion

Through the experiments above, different aspects of neutron transmission strain mapping have been developed. Different data analysis methods have been assessed and the suitable ones have been identified. The three stage function and the 5-parameter function, described

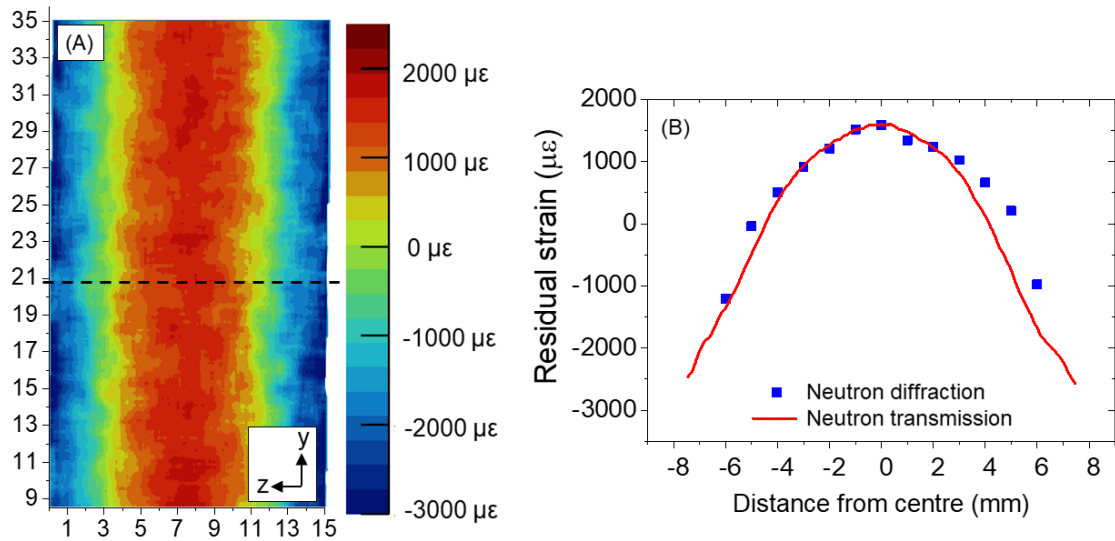


Fig. 7.20 (a) Residual strain map of AlSiC<sub>p</sub> metal matrix composite in *x*-direction produced by neutron transmission, showing compressive strains at both surfaces of the sample and tensile strains in the middle of the sample. Due to the limited size of the MCP detector field of view, only the top part of the sample was captured; (b) comparison between neutron transmission (red line) and neutron diffraction (blue symbols) results.

in Eq. (4.4) and Eq. (4.5), respectively, have been identified as the suitable Bragg edge analytical functions to determine the wavelength position of the Bragg edges. The two functions have been implemented in Bragg edge mapping software BEATRIX and TPX Edgefit, respectively, which are available on IMAT.

In the presence of crystallographic texture, where the shape of the Bragg edge changes to the point that the two analytical functions cannot be used, a cross-correlation based data analysis method can be performed to estimate the wavelength shifts (and thus strain) between the Bragg edges from the region of interest and the reference Bragg edge. In the presence of texture gradients, e.g. across the thickness of a rolled aluminium plate, thickness-specific reference Bragg edges have to be used to match the shape of the Bragg edge in the region of interest. Good statistical precision of the reference Bragg edge is desirable to minimise the uncertainty of the final result, in the same way it is needed for the conventional Bragg edge fitting method. While smoothing of the transmission signals prior to taking derivatives can help in overcoming the noise introduced by the differentiation, the current application of the technique is mainly for analysis of data with good statistical quality, which usually means averaging is required over a relatively large area of the sample. With the ongoing development of neutron instrumentation and detector technology, however, the statistical significance of neutron data is likely to improve, with scope to implement cross-correlation

for strain mapping. More work is needed to investigate how higher order differentiation can help dealing with noisy data in the cross correlation method, and whether Bragg edges with distinctly different shapes, e.g. due to averaging over significant strain gradients, can be treated with the correlation method.

With the two methods mentioned above, i.e., analytical function and cross correlation, data analysis for the majority of the cases can be carried out, reflecting that Bragg edge strain imaging on IMAT has become more mature, even though there is scope for development. The effort of improving Bragg edge analysis for strain mapping needs to be directed towards the development of multiple Bragg edge fitting. The fitting will involve more data across the whole transmission spectrum, thus taking the full benefit of the wide wavelength-range available at IMAT and other recently-developed neutron beamlines around the world. The involvement of more data also means a more accurate fitting for a given statistical quality, therefore measurement times can be reduced, and/or the macro-pixel sizes can be made smaller to improve the spatial resolution. Finally, a multiple Bragg edge fitting would likely need parameters to describe the preferred orientation distribution.

In terms of the characterisation of the Bragg edge strain imaging technique on the IMAT instrument, important parameters have been obtained through the commissioning experiments. Strain resolution of up to  $80 \mu\epsilon$  and spatial resolutions of up to  $200 \mu\text{m}$  can be produced within a reasonable measurement time, and therefore the technique and the instrument are suitable for the study of engineering samples.



# Chapter 8

## Bragg Edge Imaging for Crystallography

### 8.1 Overview

While the previous chapter described the development and application of Bragg edge strain imaging, there are more analyses opportunities that can be derived from the neutron transmission spectra. In general, neutron transmission spectra includes a wealth of information regarding the crystalline structure. A single crystal, oligocrystal or polycrystal samples exhibit different spectra profiles (Bragg edges or Bragg dip spectra). Parameters of Bragg edge spectrum (position, height/intensity, width and asymmetry) provides the information of crystal symmetry (phase transition, phase mapping), crystal lattice (lattice parameter, thermal expansion, crystal alignment), structure factor (Debye-Waller), and parameters of the microstructure (texture, microstrain, particle size, dislocation density) (Kockelmann et al., 2007; Steuwer et al., 2005; Sato, 2017) In this chapter, two analysis options of Bragg edges for crystallography, i.e., crystallographic texture mapping and Debye-Waller factor analysis will be described and discussed.

Crystallographic texture plays an important role in controlling material properties. Mapping of crystallographic texture across a sample is usually performed using electron back-scatter diffraction (EBSD) in a scanning electron microscope. While orientation distributions can be obtained through EBSD, the technique requires careful sample preparation and a relatively long scanning process, and only reveals the texture on the surface being measured. Texture analysis using neutron diffraction, such as on GEM at ISIS (Kockelmann et al., 2006), can provide information from the bulk sample volume. Time-of-flight neutron transmission offers the mapping of texture information through Bragg edge analysis.

Since the Bragg angle depends on the relative orientation between the neutron beam and the crystal, transmitted neutrons with a specific wavelength provide information of the number of crystallites having a selected orientation within the sample. Specifically, selecting

the neutron wavelength  $\lambda$  means imaging all the crystals having any of the  $(hkl)$  plane normals making the angle

$$\beta_{hkl} = \frac{\pi}{2} - \arcsin \frac{\lambda}{2d_{hkl}} \quad (8.1)$$

with the incident beam. According to Kockelmann et al. (2007), a factor  $R(\beta_{hkl})$  can be calculated to give the ratio of a number of crystallites of the textured material having the  $(hkl)$  normals making an angle of  $\beta_{hkl}$  with the incident beam, compared to the corresponding number for a perfectly random sample. The ratio is expressed in multiples of a random distribution (m.r.d.) with the function

$$R(\beta_{hkl}) = \frac{-\ln(I(\lambda)/I_{\text{base}}(\lambda))}{z f_{hkl} \lambda^2} \quad (8.2)$$

where  $I(\lambda)$  is attenuated neutron intensity after traversing a sample of thickness  $z$ ,  $I_{\text{base}}(\lambda)$  is base attenuation not affected by coherent scattering, and  $f_{hkl}$  is a materials parameter related to the structure factor (Kockelmann et al., 2007).

Another crystallographic parameter that can be derived from Bragg edge analysis is the temperature dependence of the Debye-Waller factor. The Debye-Waller parameter approximates the thermal motion of atoms around their crystallographic positions. The Debye-Waller factor  $e^{-2W}$  describes the effect of the thermal motion of atoms on the scattered intensity (Prakash et al., 1975). The exponent  $2W$  expresses numerically this motion and is directly related to the magnitude of average displacements of atoms in the crystal. When the thermal motion increases, the atoms deviate further from their original lattice position and thus the spread of  $d$ -spacing increases. As the  $d$ -spacing changes, the Bragg's Law, shown in Eq. (3.2), is less satisfied; coherent scattering is partially destroyed and Bragg edge heights decrease, Fig. 7.9, in the same way that Bragg peak intensities are depressed at higher temperatures.

Accordingly, it is difficult to separate the effects of the Debye-Waller factor from other effects such as magnetic scattering, extinction and crystallographic texture through single Bragg edge analysis. However, the temperature dependence of the Debye-Waller factor in a material can still be extracted, i.e., the other effects do not change with temperature. The same information has been obtained using different experimental methods such as X-ray diffraction (Haworth, 1960) and  $\gamma$ -ray resonant absorption (Debrunner and Morrison, 1965). However, neutron transmission offers the possibility to map the information across a sample. Previously, Haworth (1960), Prakash et al. (1975), and Kharoo et al. (1977) compared the

Debye-Waller factor dependencies on temperature in terms of the temperature parameter  $Y$ , which is defined by:

$$Y = \log_{10} e(\lambda / \sin \theta)^2 (2W_{T_0} - 2W_T) = (\lambda / \sin \theta)^2 \log_{10}(\rho_T / \rho_{T_0}) \quad (8.3)$$

where  $2W_T$  and  $2W_{T_0}$  are the Debye-Waller exponents for temperatures  $T$  and  $T_0$ , respectively. In Bragg edge transmission,  $\rho_T$  and  $\rho_{T_0}$  is the Bragg edge heights for temperatures  $T$  and  $T_0$ , respectively, and  $\sin \theta$  is equal to 1.

## 8.2 Experiments

To demonstrate the crystallographic texture mapping capabilities of IMAT, an example is provided by mapping the texture distribution of rolled Al2024-T351 plates, Fig. 8.1(a), with a dimension of 50 mm × 50 mm × 15 mm. Two measurements were performed with the rolling direction parallel and perpendicular to the neutron beam, Fig. 8.1(b) and 8.1(c), respectively. The texture is quantified by calculating the factor  $R$ , Eq. (8.2), for a wavelength of 4.68 Å, which corresponds to the position of the Al {111} Bragg edge. The base attenuation  $I_{\text{base}}$  is determined by using a radiograph collected above the Al {111} Bragg edge at 4.78 Å [see Kockelmann et al. (2007) for details]. Therefore, the  $R$ -factor map displays the number of crystals having the  $(111)$  normals aligned with the direction of the incident beam. The result of this study is presented in **Section 8.3.1**.

Meanwhile, to demonstrate the capability of Bragg edge imaging in visualising a process, i.e., recrystallisation, neutron transmission measurement on a rolled Al1050 plate at high temperature was conducted. Revisiting the high temperature experiment described in Chapter 7, a rolled aluminium plate was cut to a disc shape [Fig. 7.6(a)] and was measured at room and high temperature. The data taken below and above the recrystallisation temperature of aluminium were analysed, and the results are reported in **Section 8.3.2**.

As a proof of concept of using Bragg edge analysis for Debye-Waller factor determination, the temperature dependence of a Debye-Waller factor of  $\alpha$ -iron was quantified. The data were derived from the Fe powder data collected at different temperature as described in the high temperature experiment in Chapter 7. The temperature parameter  $Y$  was calculated using Eq. (8.3), where the Bragg edge height  $\rho$  is calculated using the first term in the right hand side of Eq. (4.4):

$$\rho = \exp[-(a_0 + b_0 \lambda_{hkl})] \{1 - \exp[-(a_{hkl} + b_{hkl} \lambda_{hkl})]\} \quad (8.4)$$

Room temperature was used as  $T_0$  in Eq. (8.3) in both the present work and literature studies, and the results are presented in **Section 8.3.3**.

## 8.3 Results

### 8.3.1 Crystallographic texture mapping

The  $R$ -factor maps for a wavelength of 4.68 Å are shown in Fig. 8.1(d) and 8.1(e) for the rolling direction parallel and perpendicular to the beam direction, respectively. It can be seen from Fig. 8.1(d) that the  $R$ -map exhibits a distinct pattern with  $R$ -values  $> 1$  at both surfaces of the plate and lower  $R$ -values  $< 1$  in the middle section. The result means that at the surfaces there is a larger number of crystallites having the  $(111)$  plane normals parallel to the beam direction (and to the rolling direction) while in the middle fewer  $(111)$  planes are found with such orientation. The inverse of this R-map, Fig. 8.1(e), is observed for the measurement direction rotated by an angle of 90°. Such symmetrical texture distributions through the thickness of the sample are indicative of a rolling process during manufacture, similarly shown by Sun et al. (2018) on rolled stainless-steel. According to Sun et al. (2018), verification of texture variation shown by neutron transmission using EBSD shows a strong texture band at the mid-thickness, where the  $(111)$  is the preferred orientation at the mid-thickness, Fig. 8.2.

Since the mapping was performed without macro-pixel averaging, the spatial resolution of the map is solely determined by the geometrical blurring. Considering a value of  $l = 79$  mm (29 mm of sample-to-detector distance + 50 mm of sample thickness in the transmission direction to calculate the worst geometrical blurring) and for an  $L/D$  ratio of 250, the geometrical blurring is  $d = 0.316$  mm. Interpolating from the values in Fig. 6.7 for  $d = 0.316$  mm yields a spatial resolution of around 130 µm. The spatial resolution is obviously higher for thinner samples in the transmission direction, with values as low as  $\approx 90$  µm shown in Fig. 6.7. The result demonstrates the ability of neutron transmission imaging to visualise texture distribution quickly and non-destructively.

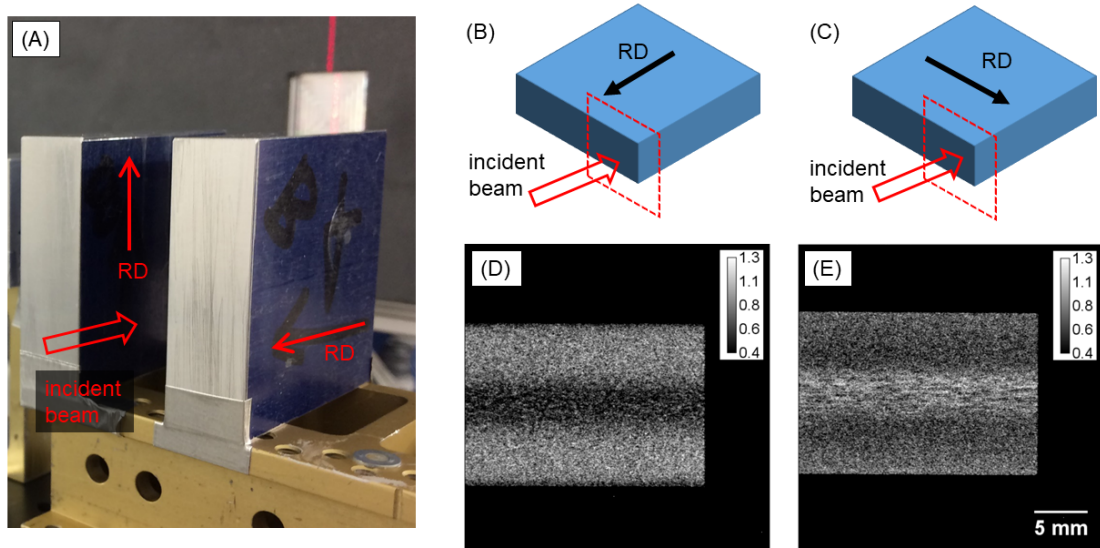


Fig. 8.1 (a) Photograph of Al2024-T351 plates, measured with neutron transmission with rolling direction RD (b) parallel and (c) perpendicular to the beam direction. The field of view is shown by the dashed box. Map of R-factor (m.r.d) for the Al {111} edge at  $\lambda = 4.68 \text{ \AA}$  ( $\beta = 0$ ) for measurement with RD (d) parallel and (e) perpendicular to the incident beam.

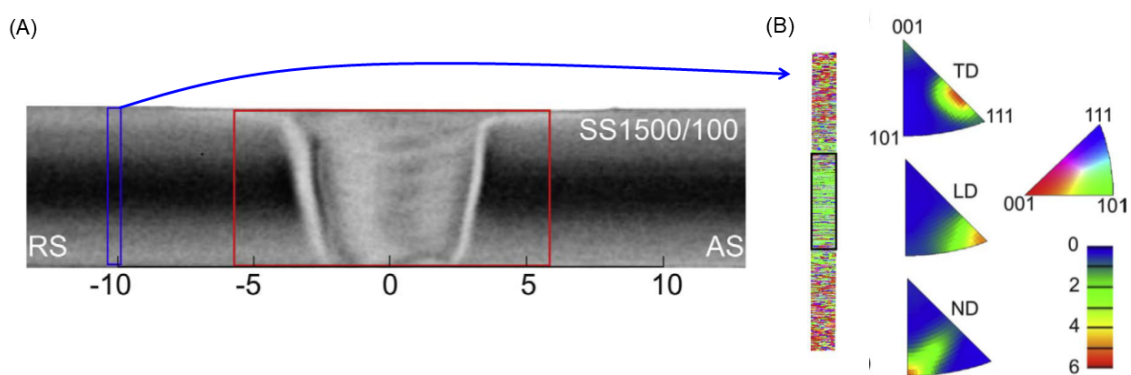


Fig. 8.2 Neutron transmission imaging and EBSD results for validation, from Sun et al. (2018). (a) TD-ND cross-section

### 8.3.2 Recrystallisation imaging

Fig. 8.3(a) shows the transmission spectra from a rolled aluminium plate at room and high temperature. It can be observed that there are no significant changes from room temperature to 573 K in terms of the shape of the transmission spectra, with Bragg edges indicating the presence of significant crystallographic texture. There are clear differences between transmission spectra taken from the surface (black curve) and the middle of the plate (red curve), Fig. 8.3(a), indicating texture variation from top to bottom. Increasing the temperature further by 50 K (from 573 K to 623 K), however, changes the spectra drastically. The Bragg edge height decreases at 623 K, and the spectra start to resemble those expected for randomly-oriented crystallites. Also, the differences between surface and middle sections of the sample are much less apparent at that temperature. This observation is caused by the recrystallisation of the aluminium. When recrystallisation occurs on deformed polycrystalline materials, the newly-developed grains are either randomly oriented or weakly textured (Humphreys and Hatherly, 2004), which explains the change in the shape of the transmission curves. It is also possible that grain growth has started to occur for Al1050 at 623 K, therefore large crystalline size might induce extinction effects which reduce the Bragg edge height (Sato et al., 2011). The recrystallisation temperature of commercially pure aluminium is 623 K (Hatch, 1984), which matches the temperature range where the abrupt changes in the transmission spectra were observed.

Texture variation in a sample can be made visible by energy-dispersive imaging. Radiographs taken at 4.5 Å, indicated by the vertical red dashed line in Fig. 8.3(a), showed a distinct texture distribution pattern produced by a rolling process, Fig. 8.3(b). This indicates a different number of crystallites at the surface and the middle section of the sample being preferentially aligned, with the  $(111)$  poles making an angle of  $\beta_{111} = 58.7^\circ$  with the incident neutron beam [Eq. 8.1]. Above the recrystallisation temperature, the texture variation between the surface and the middle section of the plate is less pronounced, indicating more randomly-oriented grains throughout the sample thickness. Radiographs taken at 4.68 Å, indicated by the vertical blue line in Fig. 8.3(a), were provided as comparison and do not show such variation of preferred orientation, Fig. 8.3(c). This wavelength corresponds to the Al  $\{111\}$  Bragg edge position.

### 8.3.3 Debye-Waller factor analysis

Fig. 8.4 shows the values of  $Y$  for Fe at different temperatures. In the present work, the values were obtained by fitting the Fe  $\{220\}$  Bragg edge, selected due to the minimum contribution of magnetic scattering to the transmission spectra at shorter wavelengths (Powers, 1938).

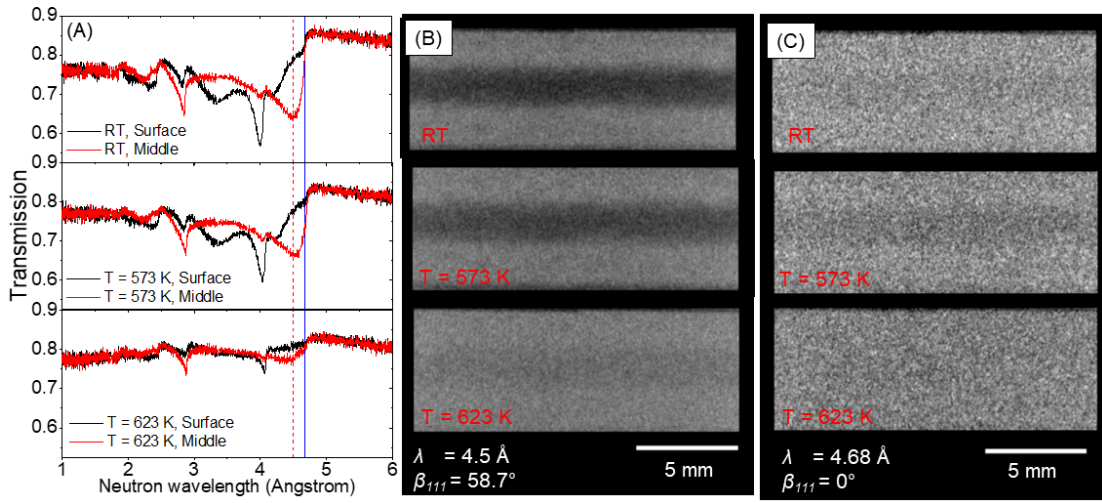


Fig. 8.3 (a) Transmission spectra of a rolled Al plate from the surface and the middle of the plate at room temperature (RT),  $T = 573 \text{ K}$  and  $T = 623 \text{ K}$ . Vertical solid blue line and dashed red line indicate the wavelengths for which radiographs were selected; (b) Radiographs of the plate taken using  $\lambda = 4.5 \text{ \AA}$  ( $\beta_{111}=58.7^\circ$ ) at RT and  $T = 573 \text{ K}$ , showing  $\{111\}$  planes preferentially aligned normal to the beam in the middle section of the sample. The texture variation diminished at  $T = 623 \text{ K}$  due to recrystallisation; (c) Radiographs taken at  $\lambda = 4.68 \text{ \AA}$  ( $\beta_{111}=0^\circ$ ) at RT,  $T = 573 \text{ K}$  and  $T = 623 \text{ K}$ , indicating a weak texture variation.

The present result is compared against previous experimental values from Debrunner & Morrison (1965) as mentioned in Prakash et al. (1975) and Kharoo et al. (1977), and from Haworth (1960) which used X-ray diffraction and similarly focused on the Fe  $\{220\}$  diffraction peak covering the temperature range of 286-1190 K. Theoretical values calculated by Prakash et al. (1975) and Kharoo et al. (1977) are also shown. The values from the present work agree well with the previous experimental values, considering the scatter in the results by Haworth. Meanwhile, both present and previous experimental values deviate from the theoretical calculations especially at higher temperatures, which is explained by the inclusion of several parameters in the model (Prakash et al., 1975). Nevertheless, the results show that the information on the temperature dependence of Debye-Waller factor can be derived from neutron transmission data.

## 8.4 Discussion

In this chapter, Bragg edge analysis at IMAT has been extended beyond strain mapping. While the analysis presented in **Section 8.3.1** can only provide the orientation of one crystallite plane with respect to the incident beam, neutron transmission imaging offers the ability to map the information across the sample. More importantly, it is a non-destructive technique

This item has been removed due to third party copyright. The unabridged version of the thesis can be viewed at the Lanchester library, Coventry University

Fig. 8.4 Temperature parameter  $Y$  of Fe at different temperatures through Bragg edge analysis, compared with literature values measured by  $\gamma$ -ray resonant absorption (Debrunner and Morrison, 1965) and X-ray diffraction (Haworth, 1960). Theoretical values from Prakash et al. (1975) and Kharoo et al. (1977) are shown for comparison as solid and dashed lines, respectively.

and, with the flux available at IMAT, therefore can be used to visualise a process such as phase change or recrystallisation, i.e., provide information about where and when the changes happen. More comprehensive quantification of the texture and grain size information can be performed either using Bragg edge modelling, which includes structural parameters (Song et al., 2017); Rietveld-type, full-pattern refinement (Sato et al., 2011); or Bragg dip transmission imaging (Sato et al., 2017; Malamud and Santisteban, 2016). There is scope to perform such quantitative analyses on IMAT by implementing these data analysis methods in the future.

Meanwhile, the proof of concept of Debye-Waller factor analysis using Bragg edge transmission spectra carried out in this work has not involved any mapping. This is due to the poor statistical quality of the high temperature experiment data, which makes them suitable only for bulk rather than spatially-resolved analysis. Additionally, the analysis describes the change in Debye-Waller factor as a function of temperature, described by the parameter  $Y$ , rather than the Debye-Waller factor itself. Again, a full-pattern refinement would be needed to separate and describe the different parameters of the crystallite, including texture, particle size, and Debye-Waller factor.

# **Chapter 9**

## **Energy-resolved Bragg Edge Imaging of Engineering Materials**

### **9.1 Overview**

In previous chapters, characterisation and validation experiments for Bragg edge imaging, both for strain mapping and crystallographic analysis have been presented. In this chapter, some case studies of Bragg edge imaging on engineering components at IMAT and other instruments are described. The main part of the application is the investigation of the laser shock peening (LSP) process on the generation of residual strain and texture changes of the components. The other application is the investigation of the residual strain generated by the cold-expansion process. Firstly, the overview of the laser shock peening and cold-expansion processes are presented. The materials and the experiments are then described, including the benchmark experiments used for comparison. Finally, the results are presented and the advantages and the limitations are discussed.

#### **9.1.1 Laser shock peening**

Laser shock peening is a surface treatment process which induces compressive residual stress near the treated surface and consequently improves the fatigue life of the component. The existence of locked-in compressive residual stress superimposes the applied stress when the component is externally loaded. In the case where a crack-opening tensile stress is applied, the compressive residual stress will lower the applied stress and therefore inhibit the crack growth and thus delay the initiation of fatigue cracks. The basic principle and the previous studies on the laser peening process using more conventional methods are briefly described

here, while comprehensive reviews on the historical development, the physics and impact of laser peening are available elsewhere (Fabbro et al., 1998; Gujba and Medraj, 2014).

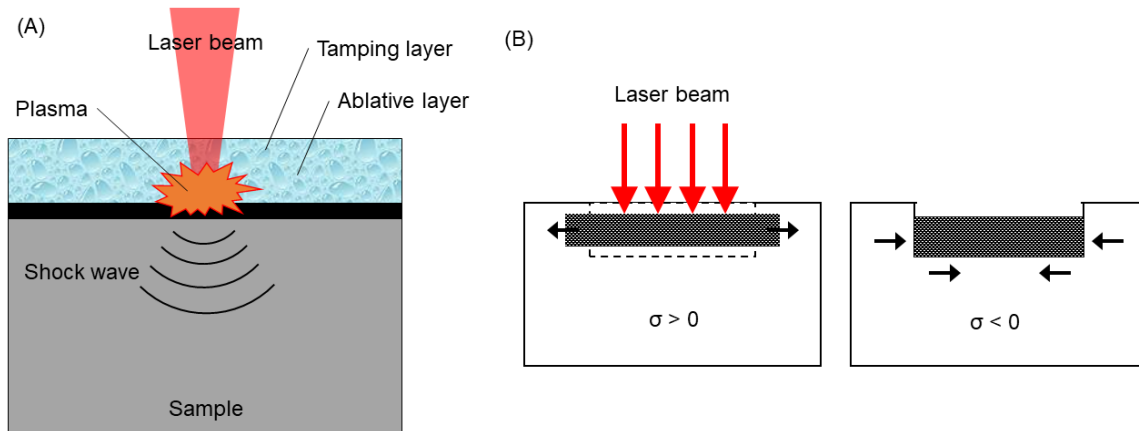


Fig. 9.1 (a) Schematic of the laser shock peening (LSP) process, adapted from Gujba and Medraj (2014); (b) Illustration of the residual stress generation by the LSP process.

In laser shock peening, the sample is prepared by applying an ablative (sacrificial) layer, and a tamping layer/ confining medium onto the surface which will be treated, Fig. 9.1(a). The ablative layer is used to absorb the laser energy and to create plasma on the surface. It also prevents melting and laser ablation of the treated surface and creates a high surface quality. Different materials have been used as an ablative layer, including aluminium, copper, lead, vinyl tape, zinc and black paint (Gujba and Medraj, 2014). Meanwhile, the tamping layer is used to restrict the plasma from expanding away off the surface and to increase the intensity of the shock wave into the sub-surface. Different tamping layer materials are water, quartz, glass, or silicon rubber (Gujba and Medraj, 2014).

Short pulses of a high intensity laser light are fired onto the surface of the component, vaporising the ablative layer and producing a local plasma. The confining material directs a shock wave into the material Fig. 9.1(a). The generation of the residual stresses in the sub-surface follows two steps: i) During and shortly after the short duration of laser-material interaction, the shock wave expand beyond the irradiated area and plastically deforms the affected surface ; ii) After the pulse duration, the elastically deformed surrounding material pushes back the deformed area, and thus creates compressive residual stress, Fig. 9.1(b), (Fabbro et al., 1998). The advantages of laser shock peening over conventional shot peening are well-documented: it produces higher depth of residual stress into the subsurface, higher stress magnitude, better uniformity, better surface finish, and the ability to peen more complex geometries such as notches and fillets (Gujba and Medraj, 2014).

There are extensive areas to be studied in the laser shock peening research, and therefore this work will only focus on the different measurement techniques available to study the residual strain profile (and in small portion, texture changes) generated by the process. Incremental hole drilling (IHD) is a semi-destructive residual stress measurement technique which involves drilling a small hole in the test specimen at incremental depth, and measuring the relaxed residual stress using a strain gauge glued to the surface of the specimen (Schajer and Whitehead, 2013). Incremental hole drilling has been widely used to study laser shock peened samples, including investigation of residual stress on thin aluminium sheets (Dorman et al., 2012; Toparli et al., 2017), on an aluminium samples with round edges (Coratella et al., 2015), on 316L steel (Kalainathan et al., 2012), and on Ti64 alloy (Yilbas et al., 2004).

Another widely used residual stress measurement technique for LSP study is the contour method. The contour method (Prime and Gonzales, 2000) is a full-field residual stress measurement technique which involves cutting through the cross-section of the specimen (usually with wire electrical discharge machining to minimise the introduction of new stresses), measuring the deformed surface profile due to the relaxed stress, and calculating the original residual stresses by determining the stress required to return the deformed surface shape to a flat plane using finite element analysis (Schajer and Ruud, 2013). The technique has been used to study residual stress generated by laser shock peening on aluminium samples with round edges (Coratella et al., 2015; Toparli et al., 2013), on Ti64 alloy aerofoil (Zabeen et al., 2013), and on a friction stir welded aluminium alloy joint (Hatamleh and DeWald, 2009). Other residual stress measurement techniques have also been used to study LSP samples, including X-ray diffraction and neutron diffraction (Dorman et al., 2012; Toparli and Fitzpatrick, 2011; Salimianrizi et al., 2016; Coratella et al., 2015).

The different stress measurement techniques have their own characteristics. Incremental hole drilling has a depth resolution of up to 20 µm (Grant et al., 2005), and therefore offers among the best depth-wise resolution for residual stress measurement. It can also measure stresses in two perpendicular directions in a single measurement. However, measurement of multiple points on a sample is limited by the minimum distance between drilled holes. The measurement of each point is also averaged over the area of the drilled hole. Additionally, there is a limitation of how deep the hole can be drilled, with a general agreement that the maximum hole depth is equal to half of the final hole diameter. This is due to the insensitivity of the strain gauge on the surface to the contribution of the subsequent depth increment (Grant et al., 2006). The rule normally gives a measurement depth of several hundred µm, which is in most cases is good enough for residual stress measurement due to LSP.

The contour method is a very powerful tool which can produce a 2D residual stress map in a single measurement. However, it is limited to only one stress direction per measurement.

More importantly, measuring stresses near the outer surface of the cut face region is difficult due to cutting-related issues with the EDM wire. Despite efforts to improve the contour method for studying LSP (Toparli et al., 2013), its application has proven to be challenging (Toparli and Fitzpatrick, 2016). Meanwhile, X-ray and neutron diffraction are useful to obtain residual stress profiles non-destructively. To produce a 2D stress map, however, requires multiple measurement points, and the achievable spatial resolution is limited by the gauge volume. Particularly for neutron diffraction, the smallest gauge volume available on many diffraction beamlines is typically 0.5 - 1 mm, which is not good enough for a near-surface residual stress measurements.

In this chapter, applications of Bragg edge imaging for studying LSP samples are presented. Although the technique can only produce through-thickness average strain information in one direction, the 2D mapping capability of Bragg edge imaging is very useful to provide information of both width and depth of the residual strain profile. On top of that, Bragg edge imaging is able to perform measurement on complex-shaped samples relatively straightforwardly. Additionally, the technique can also demonstrate the crystallographic texture changes due to the LSP process. The advantages and the limitations of Bragg edge imaging for this specific application will be further discussed.

### **9.1.2 Cold-expansion of fastener holes**

In engineering structures, fastener holes are a source of stress concentration and often become the site for crack initiation which can lead to fatigue failure. Cold-expansion is a well-known process to introduce compressive residual stress around fastener holes, which will retard the crack growth and therefore prolong the fatigue life of the structure. The process involves pulling an oversized mandrel through a pre-drilled hole, often with the help of a lubricated split-sleeve, and causing plastic deformation to the fastener hole. Material surrounding the hole, which deformed elastically during the process, pushed back and generates compressive residual stress around the hole. The process is illustrated in Fig. 9.2.

The improvement of the fatigue life depends on the residual stress profile generated from the cold-expansion process. Extensive works have been carried out to investigate the residual stress profile generated from the process, with X-ray diffraction (Cook and Holdway, 1993; Garcia-Granada et al., 1999; Stefanescu et al., 2002, 2004a,b), neutron diffraction (Edwards and Ozdemir, 1992; Stefanescu et al., 2004a) and Sachs boring method (Edwards and Ozdemir, 1992, 1993) used in previous studies. None of the studies mentioned above, however, provided a full residual stress distribution around the hole, leading to conflicting information about the location of the most compressive residual stress with respect to the split in the sleeve during the cold expansion (Granada, 1984).

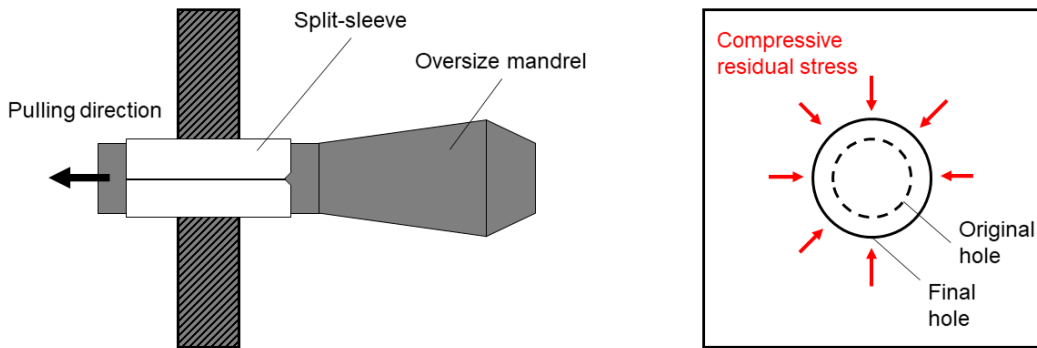


Fig. 9.2 Illustration of cold-expansion process: an oversized mandrel is pulled through a pre-drilled hole. Plastic deformation of the hole causes the elastically-deformed material surrounding the hole to be pushed back and creates compressive residual stress.

This chapter will present the application of Bragg edge imaging for strain mapping of cold-expanded holes. The technique can provide a full strain profile around the hole, therefore is useful to study the strain distribution and its relation to the split-sleeve position. Whilst the strain measured by the technique is the axial strain, it will be shown later that the strain can be correlated to the strain in the other two directions. The challenge presented by this type of sample will also be discussed.

## 9.2 Experiments

### 9.2.1 Materials, specimens and neutron transmission setup

This chapter reports multiple experiments using several different sets of samples. The experiments were performed using different instruments, settings and parameters (i.e., pinhole, counting time, sample-to-detector distance), considering the different sample geometry and the readiness level of the new IMAT beamline at the time of the experiment. The summary of the samples investigated in this study is given in Table 9.1. Note that for all of the experiments, the reference  $d_0$  values were taken from the regions of the sample which are far away from the affected areas (far-field  $d_0$ ). Most of the Bragg edge maps were reconstructed using the TPX-Edgefit software, considering the readiness level of the software on IMAT and the reliability of the 5-parameter Bragg edge fitting approach to analyse aluminium and iron Bragg edges.

The first set of samples are four laser shock peened aluminium sheets, labelled OU1 to OU4, made of aluminium alloy 2024-T351 ( $E = 73$  GPa and  $\nu = 0.3$ ) with dimensions of

Table 9.1 Summary of different sample sets prepared in the current work. All samples were measured on IMAT unless stated otherwise.

Set no.	Sample label & description
1	<b>OU1<sup>a</sup></b> - Al2024-T351 - Laser peened, 1 GW/cm <sup>2</sup> , 5.5 mm <sup>2</sup> spot, 2 layers (50%)
	<b>OU2</b> - Al2024-T351 - Laser peened, 3 GW/cm <sup>2</sup> , 5.5 mm <sup>2</sup> spot, 1 layer
	<b>OU3</b> - Al2024-T351 - Laser peened, 3 GW/cm <sup>2</sup> , 5.5 mm <sup>2</sup> spot, 2 layers (50%)
	<b>OU4</b> - Al2024-T351 - Laser peened, 3 GW/cm <sup>2</sup> , 3.5 mm <sup>2</sup> spot, 2 layers (50%)
2	<b>LSP1</b> - Al2024 - Laser peened, 3 GW/cm <sup>2</sup> , 5.5 mm <sup>2</sup> spot, 1 peen line
	<b>LSP2</b> - Al2024 - Laser peened, 3 GW/cm <sup>2</sup> , 5.5 mm <sup>2</sup> spot, 2 peen line
	<b>LSP3</b> - Al2024 - Laser peened, 3 GW/cm <sup>2</sup> , 5.5 mm <sup>2</sup> spot, 3 peen line
	<b>LSP4</b> - Al2024 - Laser peened, 3 GW/cm <sup>2</sup> , 5.5 mm <sup>2</sup> spot, 5 peen line
3	<b>SA1<sup>b</sup></b> - Al7050 - unpeened
	<b>SA2<sup>b</sup></b> - Al7050 - Laser peened, 11.1 GW/cm <sup>2</sup> , round spot, 2.5 spots/mm <sup>2</sup>
	<b>SA3<sup>b</sup></b> - Al7050 - Laser peened, 11.1 GW/cm <sup>2</sup> , round spot, 5 spots/mm <sup>2</sup>
	<b>SA4<sup>b</sup></b> - Al7050 - Laser peened, 11.1 GW/cm <sup>2</sup> , round spot, 10 spots/mm <sup>2</sup>
	<b>SA5<sup>b</sup></b> - Al7050 - Laser peened, 11.1 GW/cm <sup>2</sup> , round spot, 20 spots/mm <sup>2</sup>
4	<b>t1</b> - 12%Cr SS - convex corner, laser peened, 0.6 mm round spot, 5-6 GW/cm <sup>2</sup>
	<b>t2</b> - 12%Cr SS - concave corner, laser peened, 0.6 mm round spot, 5-6 GW/cm <sup>2</sup>
	<b>t3</b> - 12%Cr SS - grooved, laser peened, 0.8 mm round spot, 11-12 GW/cm <sup>2</sup>
5	<b>NP</b> - JIS SKD61 - unpeened
	<b>SP1; SP2; SP3</b> - JIS SKD61 - Shot peened, 0.33; 0.66; 1.33 s/mm
	<b>CP1; CP2; CP3</b> - JIS SKD61 - Cavitation peened, 20; 40; 80 s/mm
	<b>LP1; LP2; LP3</b> - JIS SKD61 - Laser peened, 10; 20; 40 pulse/mm <sup>2</sup>
6	<b>AD1<sup>c</sup></b> - 2624-T351 - Ø6.15 mm, drilled
	<b>CE1<sup>c</sup></b> - 2624-T351 - final hole Ø6.27 mm, 2% cold-worked
	<b>AD2</b> - 2024-T351 - final hole Ø12.7 mm, drilled
	<b>CE2L; CE2H</b> - 2024-T351 - final hole Ø12.7 mm, 3.16%; 4.16% cold-worked
	<b>CE3L; CE3H</b> - 7075-T651 - final hole Ø12.7 mm, 3.16%; 4.16% cold-worked

<sup>a</sup>measured on LARMOR, ISIS, UK; <sup>b</sup>measured on RADEN, J-PARC, Japan; <sup>c</sup>measured on ENGIN-X, ISIS, UK

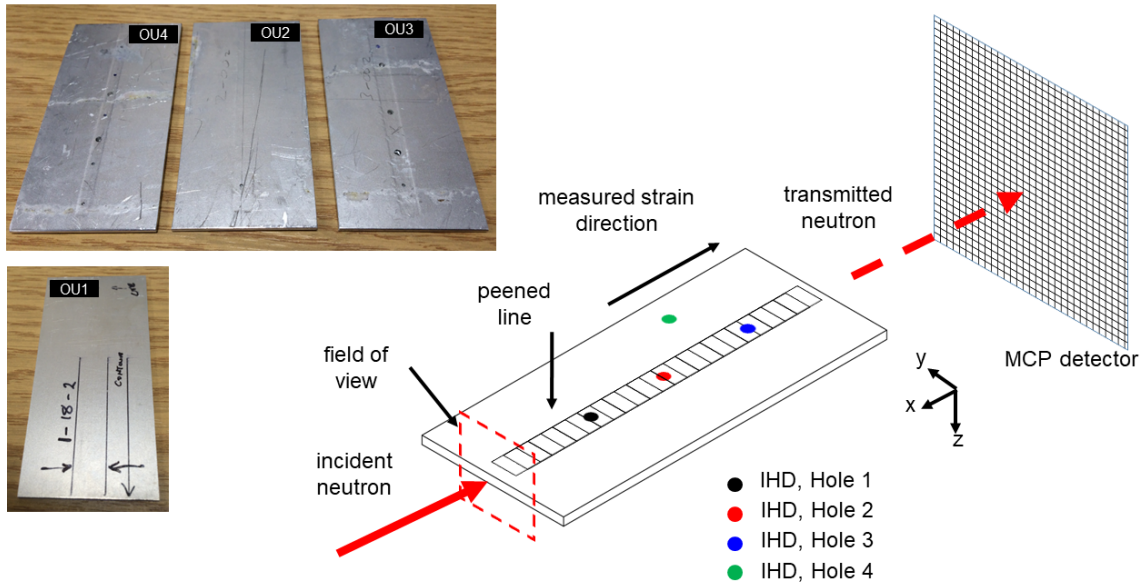


Fig. 9.3 Experimental setup of the neutron transmission for laser peened 2024-T351 aluminium alloy sheets with the sample aligned to measure strain in x-axis direction. Incremental hole drilling (IHD) measurement points are shown. The photographs of the samples are also shown.

85 mm × 38 mm × 1.8 mm. The thin aluminium sheets are representative of the laser shock peening application found in aircraft skin or web structure. The purpose of this experiment is to investigate the residual strain profile generated by different power density, spot size and peening layer parameters. An array of laser peen spots forming a line was applied along the length in the middle of each sheet, Fig. 9.3. The geometry of the peening was ideal to minimise the effect of through-the-thickness averaging of the neutron transmission. The samples OU1, OU2, and OU3 were peened with a spot size of 5 mm × 5 mm, while the sample OU4 was peened with 3.5 mm × 3.5 mm spot size. The power density used for sample OU1 was 1 GW/cm<sup>2</sup>, while that for sample OU2, OU3 and OU4 was 3 GW/cm<sup>2</sup>. Samples OU1, OU3, and OU4 were peened with two layers with 50% offset, i.e., the subsequent peen spot overlaps the previous by 50%, while sample OU2 was peened with one layer. The laser pulse duration of each spot was 18 ns. Sample OU1 was measured on the LARMOR beamline at ISIS, UK using MCP detector. LARMOR is located at ISIS target station 2 (TS-2) and installed on a 25 m flight path from the same coupled hydrogen moderator used by IMAT beamline. The rest of the samples from this set were measured on IMAT. All samples were aligned to measure strain in the x-axis direction, Fig. 9.3, parallel to the line of peen spots. On IMAT, the experiment used a pinhole of  $D = 40$  mm ( $L/D = 250$ ), a

sample-to-detector distance of  $l \approx 25$  mm, and a measurement time of 8 hours. The results from these measurements are reported in **Section 9.3.1**.

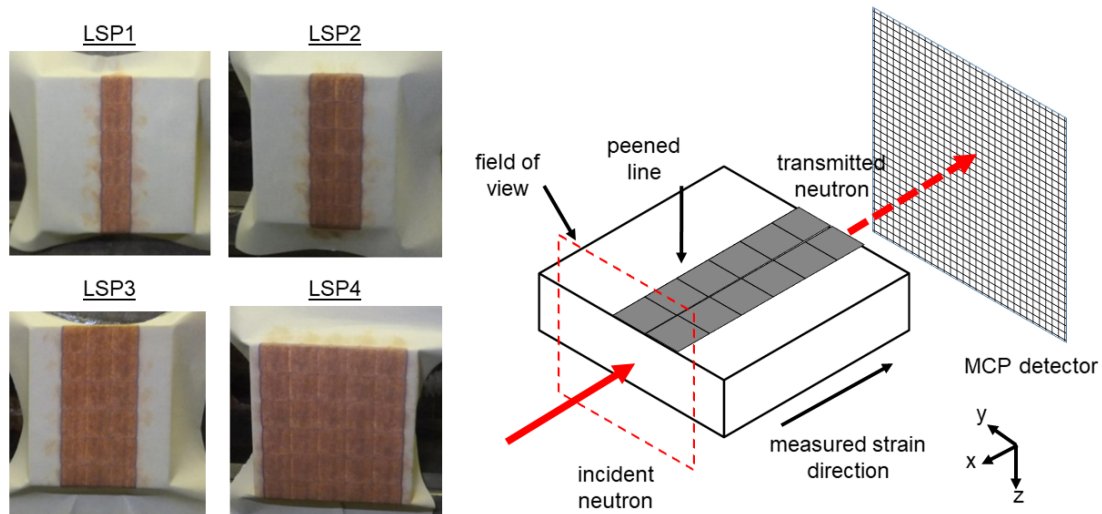


Fig. 9.4 Experimental setup of the neutron transmission for laser peened 2024 aluminium plates with sample aligned to measure strain in the  $x$ -axis direction. The photographs of the samples with the peening pattern are also shown.

The second set of samples are four laser shock peened aluminium plates, labelled LSP1 to LSP4, made of aluminium alloy 2024 with dimensions of  $35\text{ mm} \times 35\text{ mm} \times 6\text{ mm}$ . The plates were machined from cast 2024 aluminium alloy produced by ARCONIC, UK. The purpose of the experiment is to study the development of residual strain profile generated by an array of subsequent peen spots. The samples were treated with 5.5 mm peen spot size, a power density of  $3\text{ GW/cm}^2$ , and a pulse duration of 18 ns. The peening process was carried out by Metal Improvement Company (Curtiss-Wright Surface Technologies UK). Arrays of laser peen spots forming peen lines were applied along the length of the samples, with LSP1, LSP2, LSP3 and LSP 4 having one, two, three, and five peen lines, respectively, Fig. 9.4. As can be seen from the figure, there are no overlaps between the adjacent peen spots. All samples were aligned to measure strain in the  $x$ -axis direction, Fig. 9.4. The measurements were performed on IMAT using  $D = 80\text{ mm}$  ( $L/D = 125$ ),  $l \approx 25\text{ mm}$ , and a measurement time of 8 hours. The results from these measurements are reported in **Section 9.3.2**.

The third set of samples are five aluminium blocks, labelled SA1 to SA5, made of 7050 aluminium. The samples have a dimension of  $75\text{ mm} \times 17\text{ mm} \times 15\text{ mm}$ , and are offcuts from an actual wingtip device or 'winglet' of an aircraft. The purpose of this measurement is to study the residual strain and changes in the crystallographic texture on samples which are peened with high peening intensity and coverage. Samples SA2 to SA5 were peened on

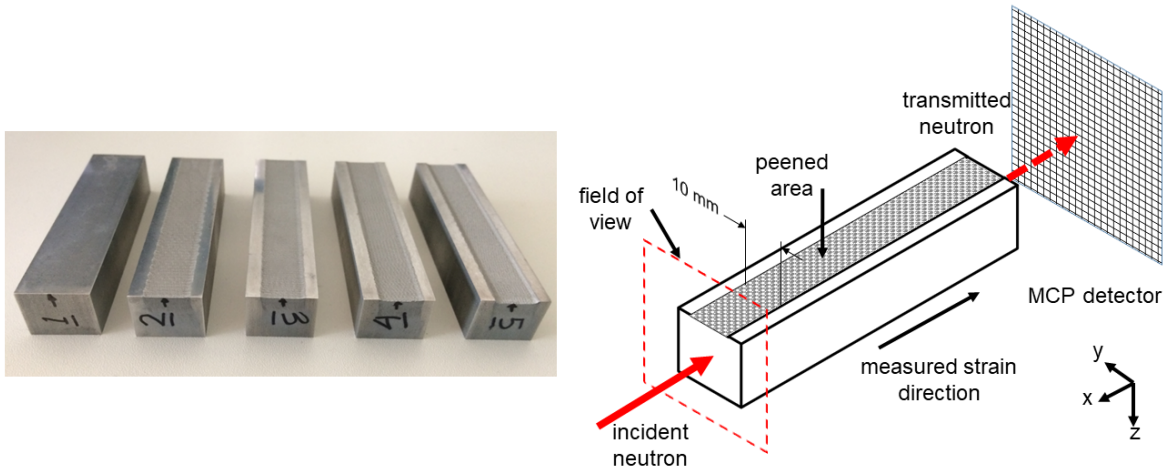


Fig. 9.5 Experimental setup of the neutron transmission for laser peened 7050 aluminium blocks with sample aligned to measure strain in x-axis direction. The photographs of the samples are also shown.

one side with the width of the peened area of 10 mm along the length of the sample, Fig. 9.5. The peening was carried out by CSIR National Laser Centre, South Africa, using a circular peen spot with diameter of  $\approx 1.45$  mm, power intensity of  $\approx 11.1$  GW/cm $^2$ , and pulse duration of  $\approx 5$  ns. The peening coverage for different samples was varied with the value of 2.5, 5, 10 and 20 spots per mm $^2$  for sample SA2, SA3, SA4, and SA5, respectively. Sample SA1 was not peened and is used as the reference. The measurements were performed on the BL22 'RADEN' beamline at the Materials and Life Science Experimental Facility (MLF) of J-PARC, Japan (Shinohara et al., 2016), using the MCP detector. The experiments on RADEN used an  $L/D$  ratio of 298, sample-to-detector distance of  $l \approx 20$  mm, and a measurement time of 4 hours. The results from these measurements are reported in **Section 9.3.3**.

The fourth sample set are three complex-shaped, laser shock peened coupons, labelled t1, t2, and t3. made of 12%Cr martensitic stainless steel commonly used in steam turbine blade applications. Samples t1 and t2 are square-shaped coupons having a width of around 20 mm and a thickness of 10 mm, with all four corners machined to have a convex and concave shape, respectively, Fig. 9.6(c) and (d). Laser shock peening was applied on two corners of sample t1 and t2, Fig. 9.6 (c) and (d), carried out by the CSIR National Laser Centre, South Africa. The peening was performed on an older peening system with peen spot size of 0.6 mm, peening coverage of 60 peen spot per mm $^2$ , and peening intensity of 5-6 GW/cm $^2$ . Sample t3 has a dimension of 20 mm  $\times$  20 mm  $\times$  15 mm. A half round groove with a radius of 2.5 mm was machined on the top surface of the sample, Fig. 9.6(e). Laser shock peening was applied to the top surface, including the half round groove and some part of the flat surface,

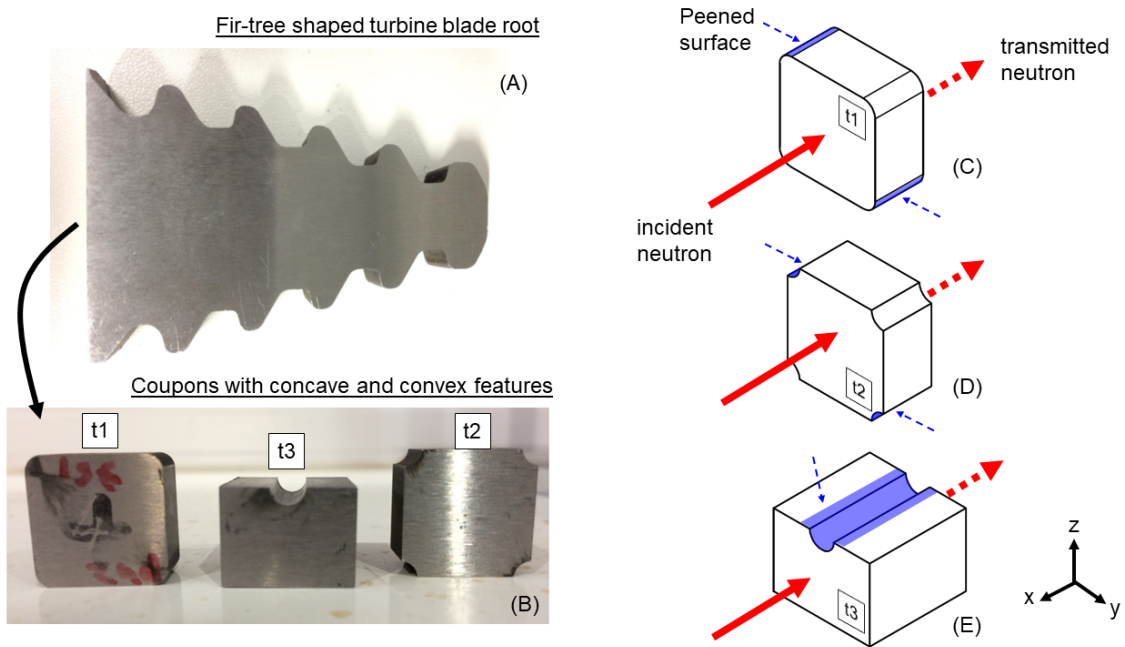


Fig. 9.6 (a) An offcut of a fir-tree shaped turbine blade root; (b) The photograph of the measured coupons; (c)-(e) Experimental setup of the neutron transmission for the complex-shaped laser shock peened steel coupons. The laser-peened surfaces are indicated by the blue dashed arrows and areas.

Fig. 9.6(e), using a newer peening system with peen spot size of 0.8 mm, peening coverage of 60 peen spot per  $\text{mm}^2$ , and peening intensity of 11-12  $\text{GW}/\text{cm}^2$ . The coupons were especially manufactured and peened to resemble the peening process on a fir-tree shaped turbine blade root containing convex and concave features, Fig. 9.6(a). The measurements were performed on IMAT using  $D = 80 \text{ mm}$  ( $L/D = 125$ ),  $l \approx 25 \text{ mm}$ , and measurement time of 4 hours. The samples are aligned to measure strains in  $x$ -axis direction, where the sample coordinates are indicated in Fig. 9.6(e). The results from these measurements are reported in **Section 9.3.4**.

The fifth sample set are a number of coupons made of alloy tool steel (JIS SKD61) which were peened with different peening techniques, i.e., shot peening, laser shock peening and cavitation shotless peening, at different peening parameter. Shot peening and cavitation shotless peening are similar to laser shock peening, but utilise different methods in creating plastic deformation on the surface of a component. Shot peening, which is considered the more conventional method, uses spherical media shot onto the surface which act as tiny peening hammers. Cavitation shotless peening uses a shock waves created by collapsing bubbles as a cavitating jet impinges the specimen surface submerged in water (Soyama et al., 2006). Each coupon has a dimension of  $15 \text{ mm} \times 15 \text{ mm} \times 6.1 \text{ mm}$ . A total of 10 coupons were measured, including three coupons for each peening technique (at low, medium, and

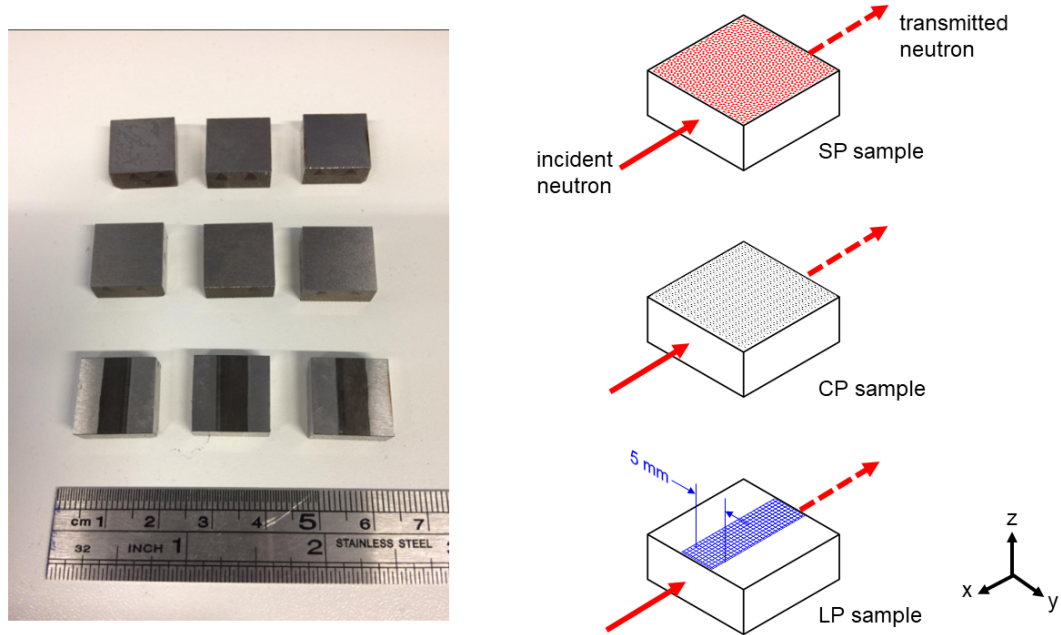


Fig. 9.7 Experimental setup of the neutron transmission for the peened steel coupons. The shot peened (SP) and the cavitation peened (CP) samples are peened on the entire surface of one side of the sample, while the laser peened (LP) sample is peened on an area with a width of 5 mm across the length of the sample in the  $x$ -axis direction.

high peening pulse density or processing time) and one un-peened coupon as a reference. The samples SP1, SP2, and SP3 were shot peened with processing time per unit length of 0.33, 0.66, and 1.33 s/mm, respectively, on one side of the sample, Fig. 9.7. The samples CP1, CP2, and CP3 were cavitation peened with processing time per unit length of 20, 40 and 80 s/mm, respectively, on one side of the sample, Fig. 9.7. The samples LP1, LP2 and LP3 were laser peened with a pulse density of 10, 20 and 40 pulse/ $\text{mm}^2$ , respectively. Laser peening was applied to one side of the sample with the width of 5 mm along the  $x$ -axis of the sample, Fig. 9.7. The peening intensity of the shot peening, laser shock peening and cavitation shot-less peening is equivalent to 0.22 mmA (arc height of Almen strip type 'A' of 0.2 mm). The measurements were performed at IMAT using  $D = 40\text{ mm}$  ( $L/D = 250$ ) and  $l \approx 25\text{ mm}$ . The peened samples were measured for 8 hours, while the non-peened sample was measured for 4 hours due to the limitation of the beam time. The results from this experiment are presented in **Section 9.3.5**.

The final sample set are a number of cold-expanded fastener holes made of different grades of aluminium alloys. Sample CE1, Fig. 9.8(a), is a 2624-T351 aluminium alloy ( $E = 73\text{ GPa}$ ,  $v = 0.33$ ) plate with a dimension of  $61\text{ mm} \times 61\text{ mm} \times 5\text{ mm}$ . A hole was drilled with an original hole diameter of 6.15 mm, and the hole was subjected to approximately

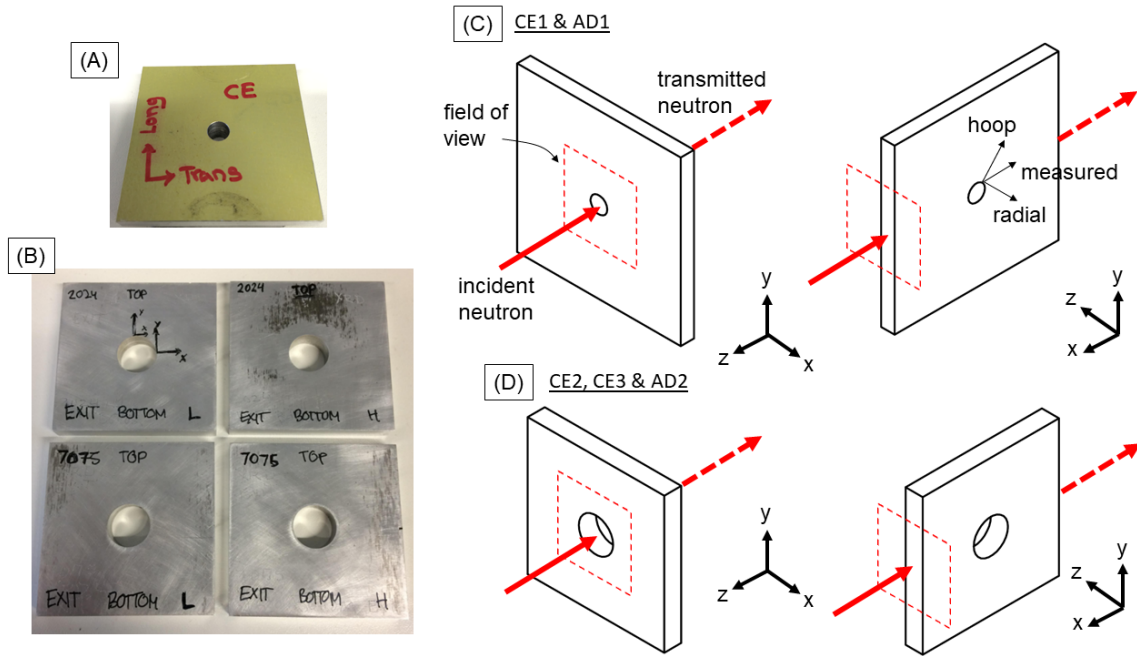


Fig. 9.8 Experimental setup of the neutron transmission for the cold expansion samples. Photograph of (a) CE1; (b) CE2 and CE3 samples; (c) CE1 and AD1 sample measured on ENGIN-X; (d) CE2, CE3 and AD2 samples measured on IMAT, all of the samples are aligned in both  $x$ -axis and  $y$ -axis direction.

2% cold work using a split-sleeve cold expansion system. The process resulted in a final hole diameter of 6.27 mm. A non-cold-expanded sample with identical geometry, sample AD1, was prepared for a reference. Sample CE2H and CE2L are 2024-T351 aluminium alloy plates with a dimension of 50.8 mm  $\times$  50.8 mm  $\times$  6 mm, with 4.16% and 3.16% cold-worked holes, respectively, and reamed to a final hole dimension of 12.7 mm. Two other samples with identical geometry, sample CE3H and CE3L, are made of 7075-T651 aluminium alloy with 4.16% and 3.16% cold-worked holes, respectively, Fig. 9.8(b). A non-cold-expanded sample with identical geometry, sample AD2, was prepared from 2024-T351 aluminium alloy. Samples CE1 and AD1 were measured using neutron transmission at the ENGIN-X beamline using the MCP detector. The samples were aligned to measure strain in both the  $x$ -axis and  $z$ -axis directions, Fig. 9.8(c), where the axes system is defined in the figure. The strain in the  $z$ -axis direction is the axial strain, while the strain in the  $x$ -axis direction is a mixture of hoop and radial strain depending on the position around the hole circumference, Fig. 9.8(c). The exposure time for ENGIN-X measurement was 7.5 hours. The rest of the samples were measured at IMAT, using  $D = 40$  mm ( $L/D = 250$ ),  $l \approx 25$  mm. The samples were aligned to measure strain in the  $z$ -axis direction with an exposure time of 10 hours, and in the  $x$ -axis direction with an exposure time of 2.5 hours, Fig. 9.8(d). Longer measurement

time was needed to determine the axial strain component from a small thickness of material contributing to the scattering. The results from the measurements are reported in **Section 9.3.6**.

### 9.2.2 Benchmark experiments

For benchmarking, measurements were made using the more established techniques, i.e., incremental hole drilling and neutron diffraction and the results were compared against some of the results obtained with neutron transmission. Incremental hole drilling (IHD) measurements were performed on the laser shock peened sample OU1. Before the measurements, the OU1 sample was adhesively bonded to a resin backing to prevent distortion during drilling. Three holes were drilled at different positions along the peened line, and one hole was drilled on the unpeened part of the sample, approximately 5 mm away from the middle of the peened line, as shown in Fig. 9.3. The final drilled hole diameter was measured to be between 1.85 and 1.95 mm. Strain relaxation was measured using a standard three-gauge rosette: two gauges separated by 90° to measure strain in the  $x$ - and  $y$ -axis directions, and one at 45°. All measurements were performed using an IHD measurement system developed by Stresscraft, UK, and according to the UK National Physical Laboratory Good Practice Guide (Grant et al., 2006). To interpret the data and convert the relaxed strains at various depths within the sample to the corresponding stresses, the integral method was applied (Grant et al., 2006) using the Stresscraft RS INT 5.1.2 software. The results are presented in **Section 9.3.1**.

The in-plane stresses in the  $x$ - and  $y$ -axis directions from IHD measurements were used to back-calculate the  $x$ -axis direction strain using Hooke's law, assuming stress in the  $z$ -axis direction is zero (plane stress). Then, the calculated  $x$ -axis direction strain was compared with the strain measured by neutron transmission. The IHD measurement was performed after the non-destructive neutron transmission measurement on the OU1 sample.

Neutron diffraction was performed on the cold-expanded hole samples at ENGIN-X, on samples CE1, CE2H and CE3H. All measurements were performed in two orientations to obtain strains from three orthogonal directions, i.e., directions parallel to the sample coordinate system axes, Fig. 9.9(a). For orientation 1, the detector bank 1 and bank 2 measured strain in the  $z$ - and the  $x$ -axis direction, respectively. Rotating the sample 90° around  $z$ -axis gave orientation 2, and the strain in the  $y$ -axis direction can be measured using detector bank 2, Fig. 9.9(a). Point-to-point neutron diffraction measurements were made using a gauge volume of  $2\text{ mm} \times 2\text{ mm} \times 2\text{ mm}$ . For sample CE1, measurements were performed at two different thickness locations:  $z = 1.5\text{ mm}$  and  $z = 3.5\text{ mm}$  from the sample entry face, Fig. 9.9(b). At each thickness, five measurements were performed at 3 o'clock position at 1.5, 3, 4.5, 6 and 7.5 mm away from the edge of the cold-expanded hole. For  $d_0$

reference, a stress-free reference sample was prepared by extracting a  $3\text{ mm} \times 3\text{ mm} \times 3\text{ mm}$  cube from the edge of the measured aluminium plate (i.e., away from the hole). The measurements were part of a different project (Syed et al., 2015), and were performed prior to the neutron transmission experiments. For sample CE2H and CE3H, measurements were made at 9, 12, and 3 o'clock position, at two different thickness locations:  $z = 1.65\text{ mm}$  and  $z = 4.35\text{ mm}$  from the sample entry face. At each position, a line scan containing 9 measurement points were made, Fig. 9.9(c), from 1.6 to 16 mm away from the edge of the cold-expanded hole.  $d_0$  measurements were made on the corners of samples CE2H and CE3H.

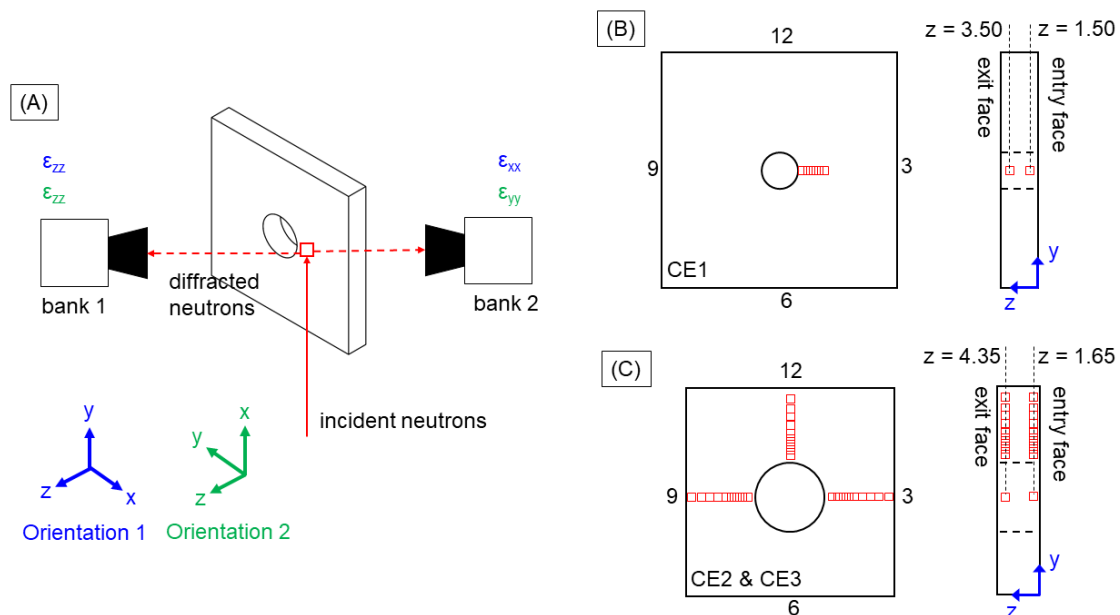


Fig. 9.9 (a) Experimental setup of the neutron diffraction for the cold expansion samples. The samples were aligned in two orientations to measure strains in  $x$ -,  $y$ -, and  $z$ -axis direction using two detector banks; (b) approximate measurement points of the CE1 sample; (c) approximate measurement points of the CE2H and CE3H samples.

From each measurement, multiple diffraction peaks were recorded. Pawley-type full pattern refinements were performed to determine the lattice parameters. Single peak fitting was also carried out using a convolution of double-exponential TOF and Voigt function to get plane-specific lattice spacings.  $d_0$  measurements were then used as reference from where the strains were derived. Strains from different thickness locations were averaged, and the results are presented in **Section 9.3.6**.

## 9.3 Results

### 9.3.1 Residual strain profiles for different peening parameters

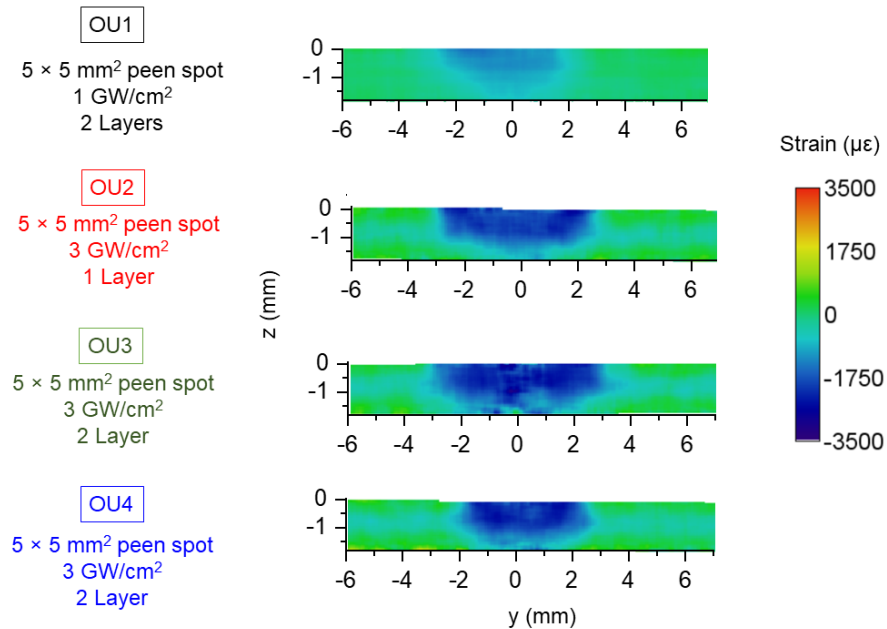


Fig. 9.10 Residual strain maps of laser shock peened Al2024-T351 thin plates, peened with different peening parameters. Compressive residual strain below the peened surfaces can be clearly observed, with the strains averaged through the neutron beam path in the *x*-axis direction.

Fig. 9.10 shows the 2D maps of *x*-axis direction residual strain of Al2024-T351 plates peened with different peening parameters. The strain maps were reconstructed from the Al {111} Bragg edge using a macro-pixel size of  $10 \times 10$  pixels. The compressive residual strains are shown below the peened surface, and the strain profile (shape and magnitude) clearly observed. To obtain more detailed information, line profiles of strain were extracted from the 2D maps, indicated by the dashed red line in Fig. 9.11. Line 1 plots the strain as a function of depth from the surface of the samples, Fig. 9.11(a). 2 layers of peening with  $1 \text{ GW/cm}^2$  power density (sample OU1) yielded residual strains of  $\approx 1300 \mu\epsilon$  at the surface of the sample, Fig. 9.11(a). Higher residual strain was produced by 1 layer of peening with  $3 \text{ GW/cm}^2$  power density (sample OU2), with a maximum compressive residual strain value of  $\approx 2000 \mu\epsilon$  at 0.5 mm from the surface, and  $\approx 1800 \mu\epsilon$  at the surface, Fig. 9.11(a). The highest residual strain was produced by 2 layers of peening with  $3 \text{ GW/cm}^2$  power density (sample OU3 and OU4), with maximum compressive residual strain of  $\approx 2250 \mu\epsilon$  at 0.5-0.6 mm from the surface, and  $\approx 2100 \mu\epsilon$  at the surface, Fig. 9.11(a). The typical strain

uncertainty of  $\pm 150 \mu\epsilon$ , originated from the Bragg edge fitting error, is also indicated in Fig. 9.11(a).

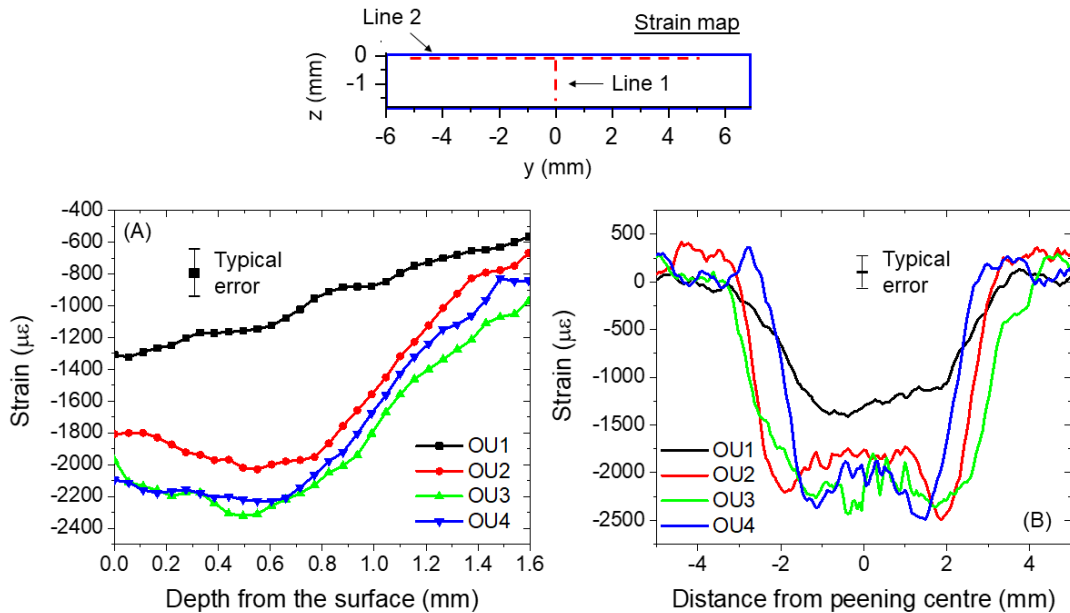


Fig. 9.11 Line profiles of strains extracted from the 2D strain map. (a) Strain profile as a function of depth from the sample surface, produced by Line 1; (b) Strain profile around the peened area, showing the effective peened area, produced by Line 2.

Line 2 plots the strain profile from 5 mm to the left to 5 mm to the right of the middle of the peen area, averaged for the first 0.5 mm depth from the surface. The plots are shown in Fig. 9.11(b), and are used to study the effective coverage area, i.e., the area of maximum compressive strain, of a single peen spot. For the OU1 sample with  $5 \times 5 \text{ mm}^2$  peen spot size and  $1 \text{ GW/cm}^2$  power density, the area of maximum compressive strain has a size of around 3.5 mm (from  $y \approx -1.5 \text{ mm}$  to  $y \approx 2 \text{ mm}$ ), black curve in Fig. 9.11(b). For OU2 and OU3 sample, using the same peen spot size as OU1 but triple the power density, the side length of the effective coverage area increased to around 4.5 mm, shown by the red and green curve in Fig. 9.11(b), respectively. The different peen layers between OU2 and OU3 do not seem to affect the side length of the effective coverage area. Finally, the peen spot size of  $3.5 \times 3.5 \text{ mm}^2$  of sample OU4 ( $3 \text{ GW/cm}^2$ ) produced the side length of the effective coverage area of around 3.3 mm, blue curve in Fig. 9.11(b).

Fig. 9.12 shows a comparison between neutron transmission (closed symbol) and incremental hole drilling (IHD) (open symbol) results for the OU1 sample. Three IHD measurements from the laser peened area, hole 1, 2 and 3, indicated in Fig. 9.3, were averaged and plotted. An IHD measurement from the unpeened area was also plotted. The

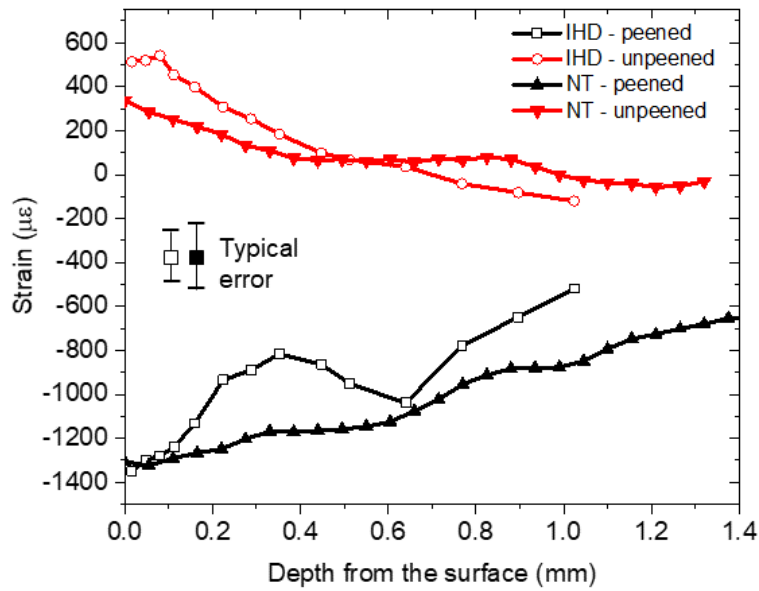


Fig. 9.12 Strain comparison between incremental hole drilling and neutron transmission results of OU1 sample, indicating reasonable agreement. The slight differences are due to the differences in averaging.

results are compared against the line profiles of strains extracted from the 2D neutron transmission strain map of OU1 sample, Fig. 9.12. From the figure, it can be observed that the neutron transmission (NT) results agree well with the IHD results, with the typical error of both measurement techniques indicated (typical error for IHD results are  $\pm 100 \mu\epsilon$ ). The differences between the two results, especially the results of the peened area, are due to the differences in averaging. Neutron transmission averages strains over the whole sample length, therefore it is insensitive to the strain variation which occurs between the centre and the edge of the peen spot (Dorman et al., 2012). Meanwhile, the IHD result averages strain from the areas where the holes were drilled, therefore it is more sensitive to the local strain variation. Nevertheless, the magnitude and trends of the IHD results are within the range of the neutron transmission residual strain profiles. Meanwhile, the tensile strain on the unpeened part of the sample, detected by both neutron transmission and IHD, is most likely the balancing strain to the compressive residual strain from the peening.

### 9.3.2 Mapping the residual strain in the developing LSP area

Fig. 9.13(a) shows the strain maps of the laser peened 2024 aluminium plates, reconstructed from the Al {111} Bragg edge using a macro-pixel size of  $30 \times 30$  pixels. Compressive residual strains can be observed below each of the peened surfaces, showing the strain profile

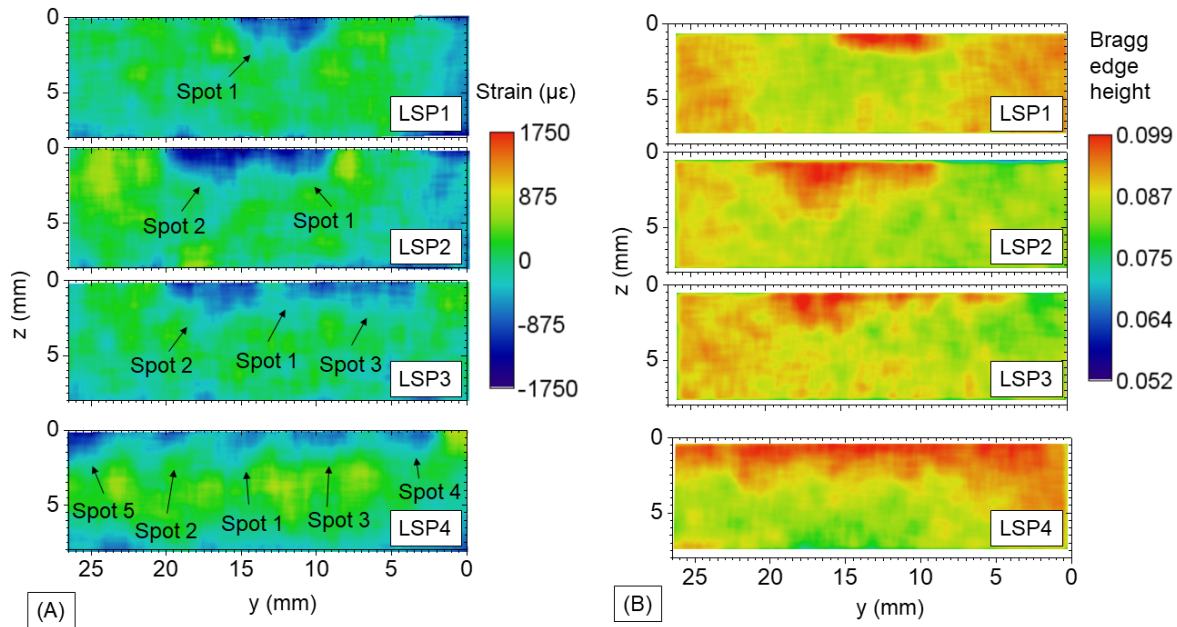


Fig. 9.13 (a) Residual strain and (b) Bragg edge height map of the laser shock peened Al2024 plates. Both parameters are averaged through the thickness of the sample in the  $x$ -axis direction.

development from a single spot to multiple spots covering a larger area. It can be observed especially for the strain maps of LSP3 and LSP4, there are areas of lower compressive residual strain in between two adjacent peen spots. Despite successfully mapping the strain profiles, however, the scatter of the strain value across the map is quite high. This is due to the poor statistical quality of the data from the measurements of aluminium with 35 mm thickness in the transmission direction. It also has to be noted that the compressive residual strains produced in these samples are much lower compared to those produced in the aluminium sheets discussed in the previous section, despite similar power density and pulse duration. The difference may be caused by different laser peening systems, ablative material and confining medium used during the process. These information is more difficult to be obtained considering the aluminium sheet samples were historical samples.

More interesting findings are the high Bragg edge height values below the peened surface, Fig. 9.13(b). The maps show the distribution of Bragg edge height, with the numbers being the fitted parameter  $C_2$  from Eq. (4.5). Note that the first few hundred  $\mu\text{m}$  of the map are omitted, Fig. 9.13(b), due to the sample interface effect, **Section 4.2.5**. Although high Bragg edge height values are also found in other parts of the sample, they are only consistently found below the peened surface. These high values below the peened surface can be attributed to the change in crystallographic texture due to the peening process. The base material of the

LSP1 - LSP4 samples is cast aluminium, hence the material is mostly expected to exhibit random crystallographic orientations. The laser peening process which involved treating the sample with one layer of a relatively large peening spot might realigned the crystals in a particular direction: in this case a significant number of crystals have realigned with their {111} perpendicular to the beam direction. This hypothesis needs to be investigated further using other texture mapping technique, e.g. using EBSD in a Scanning Electron Microscope (SEM).

### 9.3.3 Characterisation of the LSP process with high intensity and high coverage

Fig 9.14(a) shows the residual strain profiles of the Al7050 blocks, reconstructed from the Al {111} Bragg edges using a macro-pixel size of  $30 \times 30$  pixels. It can be seen that compressive residual strains is present below the peening surface of the sample SA2 to SA5, in contrast to the strain profile of the unpeened base material SA1. More detailed information were obtained by plotting line profiles of strain from each of the 2D maps, Fig. 9.15(a). Samples SA2 ( $2.5 \text{ spots/mm}^2$ ) and SA3 ( $5 \text{ spots/mm}^2$ ) have a compressive residual strain at the surface with the value of  $\approx 3000 \mu\epsilon$ , Fig. 9.15(a). Maximum compressive strain with a value of  $\approx 3500 \mu\epsilon$  can be found at a depth of 500 microns from the SA3 sample surface. Higher compressive residual strain can be found on the surface of samples with higher peening coverage, i.e.,  $\approx 3900$  and  $\approx 4200 \mu\epsilon$  for sample SA4 ( $10 \text{ spots/mm}^2$ ) and SA5 ( $20 \text{ spots/mm}^2$ ), respectively, Fig. 9.15(a).

Interesting observations were made by performing energy selective radiography on the samples. Taking a radiography with a neutron energy range of  $4.72 - 4.76 \text{ \AA}$  (near Al{111}), higher transmission intensities were detected below the peened surface, but to a much lesser degree for sample SA3, Fig. 9.14(b). The chosen wavelength range is indicated by the area between the dashed line in Fig. 9.15(b). The higher transmission indicates the change of crystallographic texture due to the laser peening. As can be seen in the transmission spectra taken from sample SA5, Fig. 9.15(b), the Bragg edge of the peened region (black curve) has a shape more similar to that of a randomly oriented material compared to the Bragg edge shape of the unpeened region (red curve). The hypothesis is that the high energy density and high coverage (multiple layer of peen spots) peening process increases the dislocation density, causing the dislocations to accumulate in the grain boundary and increase the misorientation between the grains. This randomises the orientations of the materials within the peened area, which are initially preferentially aligned. Again, this hypothesis can be further investigated with EBSD.

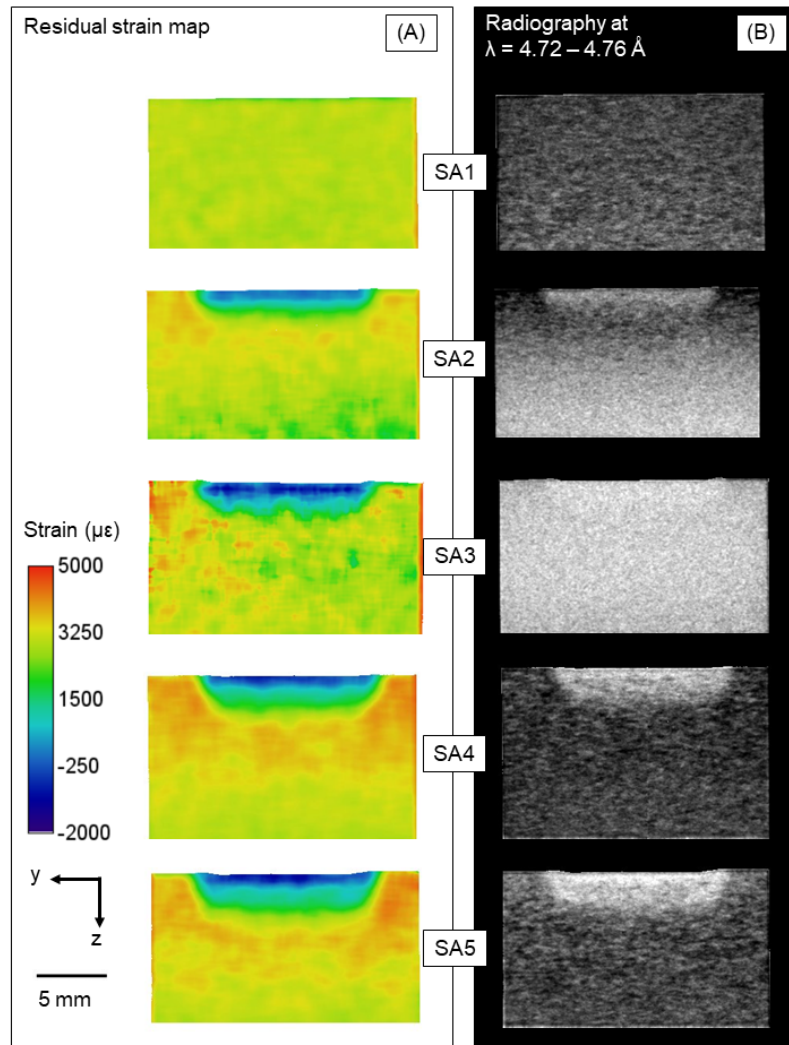


Fig. 9.14 (a) Residual strain map of the laser peened Al7050 blocks, reconstructed from Al {111} Bragg edges using a  $20 \times 20$  macro-pixel size, and averaged through the sample thickness in the  $x$ -axis direction. Compressive strain can be clearly observed below the peened surfaces; (b) Energy-resolved radiographies taken at the neutron wavelength range of  $4.72 - 4.76 \text{ \AA}$ , indicate higher transmissions below the peened surfaces. Both strains and transmissions are averaged through the thickness of the sample in the  $x$ -axis direction.

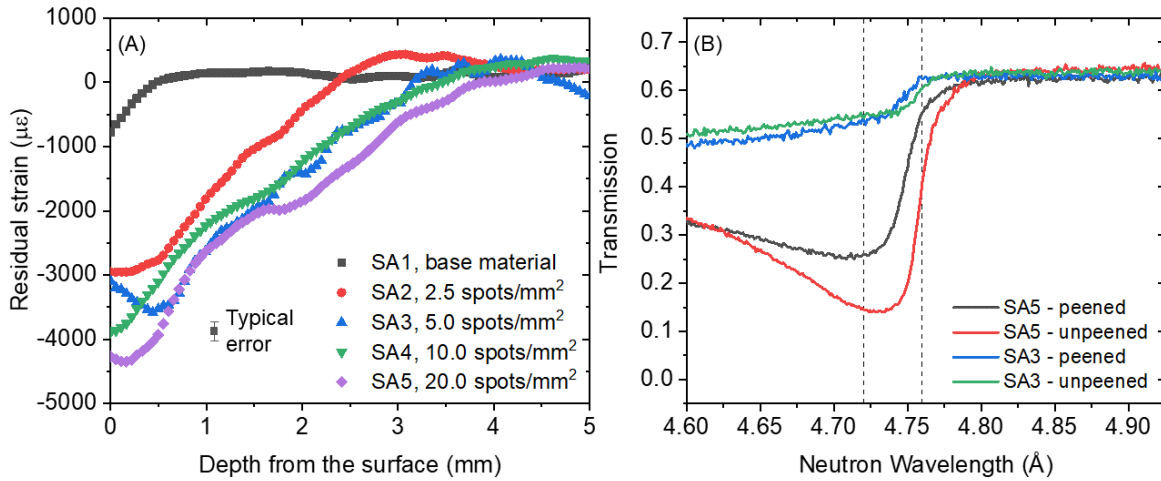


Fig. 9.15 (a) Line profiles of strains taken from the strain map of sample SA1 - SA5. The typical strain error is around  $\pm 150$ ; (b) The transmission spectra of samples SA3 and SA5. Al {111} Bragg edges of sample SA3 have noticeably different shapes compared to the other samples.

On the other hand, sample SA3 shows a distinct radiography: while the change in transmission can still be observed below the peened surface, the whole sample material has a significantly higher transmission compared to the other samples for the chosen wavelength range, Fig. 9.14(b). The transmission spectra from sample SA3 shows that the Al {111} Bragg edges have a different shape compared to those from other samples, e.g., sample SA5, Fig. 9.15(b). These findings indicate that sample SA3 has a different initial crystallographic texture compared to the other samples, most likely because the sample was taken from a different depth of the wing tip offcuts. Although sample SA3 produces weak Al {111} Bragg edges, which presents a challenge for the Bragg edge fitting analysis, a strain map can still be reconstructed and the strain information can be recovered, Fig. 9.14(a).

### 9.3.4 Residual strain mapping of LSP sample with complex geometries

Fig. 9.16(a)-(c) show the reconstructed strain maps of the complex-shaped, laser peened steel samples. Compressive residual strain can be observed below the concave and convex laser shock peened surfaces. Line profiles of strains are taken from the 2D strain map, indicated by the red dashed line in Fig. 9.16(a)-(c), are plotted to get more detailed information, Fig. 9.16(d)-(f). From Fig. 9.16(d) and (e), it can be seen that samples t1 and t2, which were peened with an older peening system, have compressive strain zones with a depth of around 500  $\mu\text{m}$  and a maximum compressive residual strain of  $\approx 1000 \mu\epsilon$  on the surface.

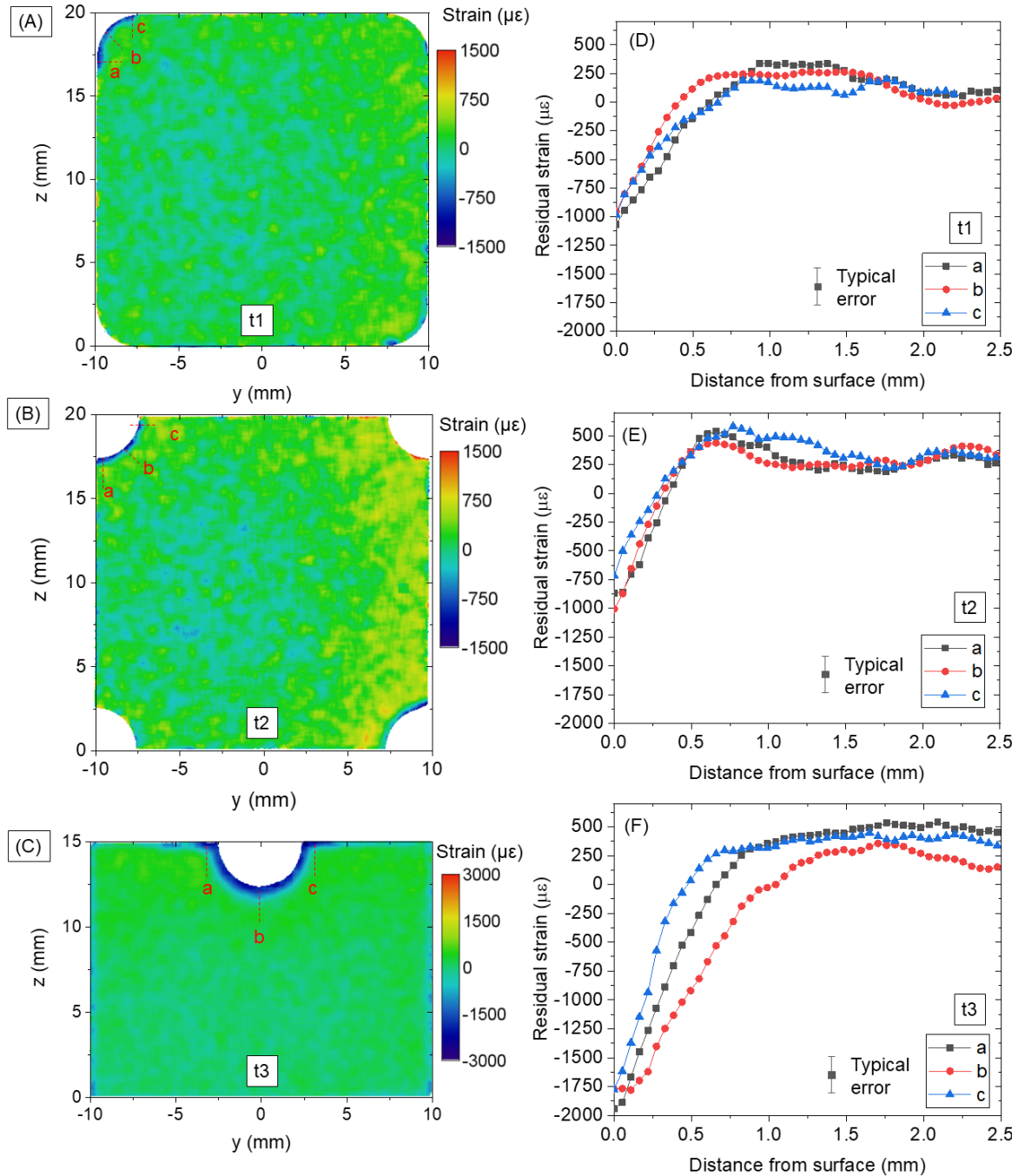


Fig. 9.16 Reconstructed strain maps of the complex-shaped, laser peened steel samples: (a) sample **t1**; (b) **t2**; and (c) **t3**. Compressive residual strain can be observed below the peened surfaces. The maps are reconstructed from Fe {110} Bragg edges using a  $10 \times 10$  macro-pixel size, and averaged through the sample thickness in the  $x$ -axis direction. Line profiles of strains taken from the 2D strain map for: (d) sample **t1**; (e) **t2**; and (f) **t3**. The typical strain error is  $\pm 160 \mu\epsilon$ .

Peened using a newer peening system, sample t3 has a compressive strain zone with a depth of around 400-1000  $\mu\text{m}$  and a maximum compressive residual strain of  $\approx 1800 \mu\epsilon$  on the surface, Fig. 9.16. There are no significant strain variations observed below the peened convex and concave surface of sample t1 and t2, respectively, as can be seen from the strain maps [Fig. 9.16(a) and (b)] as well as the line profiles of strains [Fig. 9.16(a) and (b)]. Meanwhile for sample t3, the strain below the peened concave surface (line b) shows deeper compressive residual strain compared to that below the peened flat surface (line a and c), Fig. 9.16(f).

This application further emphasises the advantage of Bragg edge neutron transmission for strain mapping over diffraction based methods. Neutron and X-ray diffraction will be limited by their size of gauge volume to measure a high strain gradient within the first few hundred microns. Partially-filled gauge volume will also be an issue for residual strain measurement at the sample surface. More importantly, it would require hundreds to thousands of measurement points in order to get the overall picture of residual strain profile on a complex-shaped feature or component. Despite only providing through-the-thickness average strain information in one direction, Bragg edge neutron transmission can quickly and straightforwardly determine the strain profile. This can help identify regions of interest in the sample, should a full stress measurement using any other method be required.

### 9.3.5 Comparison between shot, laser shock, and cavitation shot-less peening

Fig. 9.17 shows the reconstructed 2D strain maps and the line profiles of strains extracted from the corresponding 2D maps. The strain maps were reconstructed from Fe {110} Bragg edges using a macro-pixel size of  $3 \times 3$ , and averaged through the sample thickness in  $x$ -axis direction. The small size of macro-pixel was selected to capture the residual strain profile, which was expected to be present in the first few hundred microns from the sample surface. For the sample without peening (sample NP), Fig. 9.17(a), it can be observed that a compressive residual strain is present with a value of around  $2500 \mu\epsilon$  at the surface. The residual strains in the non-peened sample are most likely generated by the grinding process which was applied to the base material.

The shot peening process generated maximum compressive residual strain on the sample surfaces, with values of around 4900, 6000, and 6400  $\mu\epsilon$  for the low (SP1), medium (SP2) and high (SP3) processing time per unit length, respectively, Fig. 9.17(b). These values are higher compared to the residual strain generated by laser shock peening process with the equivalent peening density, with values of around 4000, 5100, and 5500  $\mu\epsilon$  for the low (LP1),

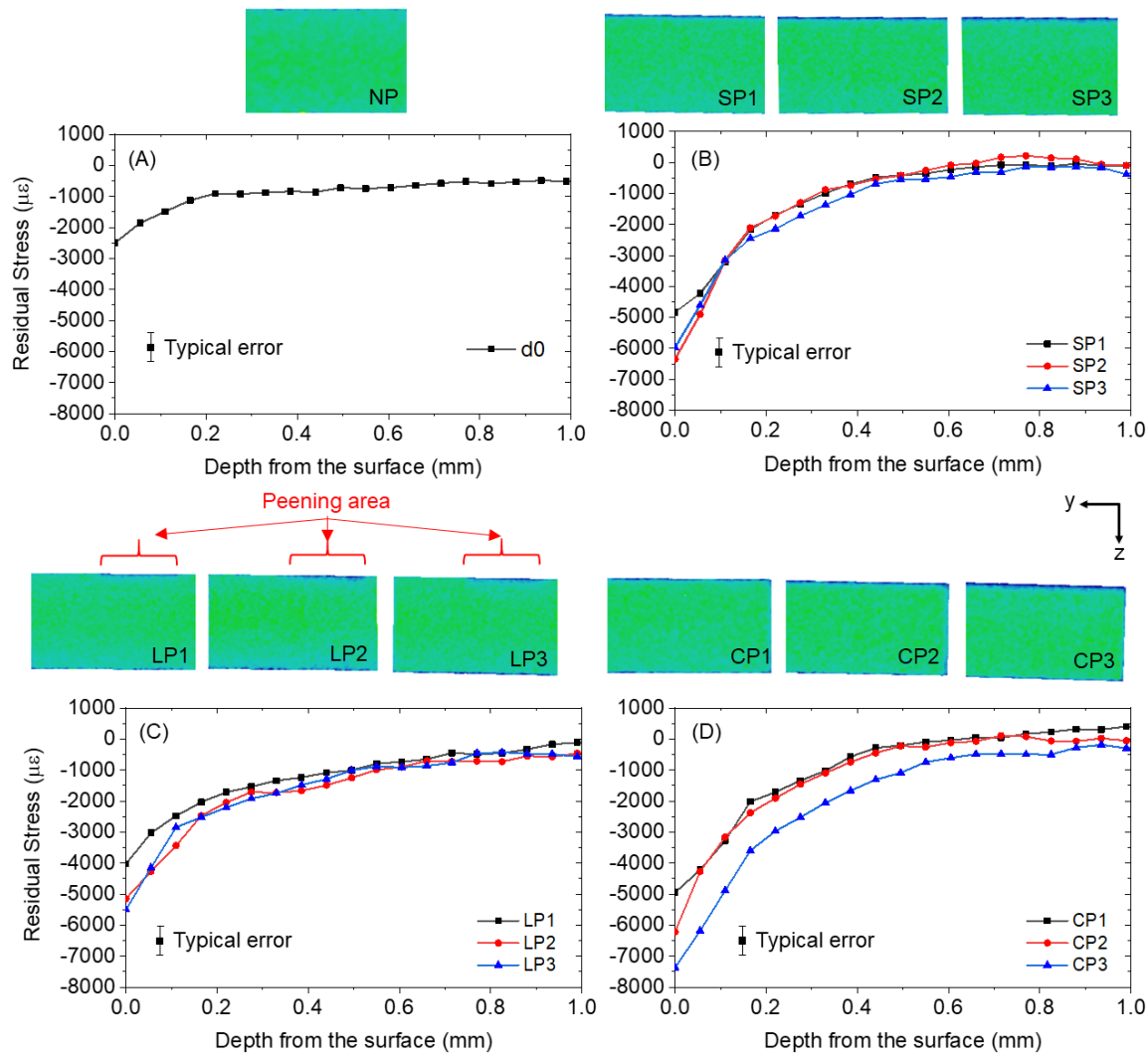


Fig. 9.17 Reconstructed strain maps and line profiles of strains of the 12%Cr steel coupons (a) without peening, peened with (b) shot peening, (c) laser shock peening, and (d) cavitation shotless peening. The strain maps were reconstructed from the Fe {110} Bragg edge using a macro-pixel size of  $3 \times 3$ , and averaged through the sample thickness in  $x$ -axis direction. The typical strain error is around  $\pm 400 \mu\epsilon$ .

medium (LP2) and high (LP3) pulse density, respectively, Fig. 9.17(b). Both techniques generated compressive residual strains with a depth of around 300-400  $\mu\text{m}$ . Cavitation shot-less peening generated the highest residual strain with values of around 5000, 6100, and 7500  $\mu\epsilon$  for the low (CP1), medium (CP2) and high (CP3) processing time per unit length, respectively, Fig. 9.17(c). Cavitation shot-less peening also generated a deeper compressive residual strain of up to around 600  $\mu\text{m}$  from the sample surface.

In this case, the spatial resolution of the Bragg edge neutron transmission strain mapping technique enables the measurement of residual strain at the depth of around 300-600  $\mu\text{m}$ , non-destructively. Based on the study performed in **Section 7.5.5**, the spatial resolutions of the reconstructed maps are around 100  $\mu\text{m}$ .

### 9.3.6 Residual strain mapping around cold-expanded holes

Fig. 9.18(a) and (b) show the comparison between residual strain fields for cold-expanded (sample CE1) and drilled (sample AD1) holes, respectively, in the  $z$ -axis (axial strain) and the  $x$ -axis (combined hoop and radial strain) directions. A significant difference is seen between the residual strain distributions around the cold-expanded hole and the drilled hole. Pronounced tensile residual strain, with a magnitude of up to around 3000  $\mu\epsilon$  was observed around the circumference of the cold-expanded hole, 9.18(a). Such high tensile residual strain was not found for the drilled holes, 9.18(b), where the residual strains around the circumference of the drilled hole were similar to those over the rest of the area of the sample. The tensile residual strain in the axial direction for the cold-expanded hole can be explained by the Poisson effect. As the mandrel used in the cold expansion process is removed, the elastic bulk of material surrounding the hole springs back and generates compressive strain in the vicinity of the hole in the hoop and radial directions [right part of Fig. 9.18(a)]. In the perpendicular axial direction, tensile strain is generated owing to the Poisson effect. This finding is consistent with neutron diffraction measurement results by Edwards and Ozdemir (1992) and neutron transmission results by Santisteban (2002a).

Strain asymmetry around the cold-expanded hole can also be observed in 9.18, where a significantly lower tensile residual strain can be observed at the 3 o'clock position. Line profile of axial residual strains (four lines, each 90° apart at 12, 3, 6, and 9 o'clock position) were extracted from the 2D axial strain map of CE1 sample to provide more detailed information about the strain asymmetry, Fig. 9.18(c). It can be observed from Fig. 9.18(c) that the strain profile taken from the 3 o'clock position has significantly lower tensile strain compared to those taken from the other positions. This residual strain asymmetry phenomenon is consistent with findings from finite-element simulation (Nigrelli and Pasta, 2008). The asymmetry of the strains around the cold-expanded hole is a result of the gap

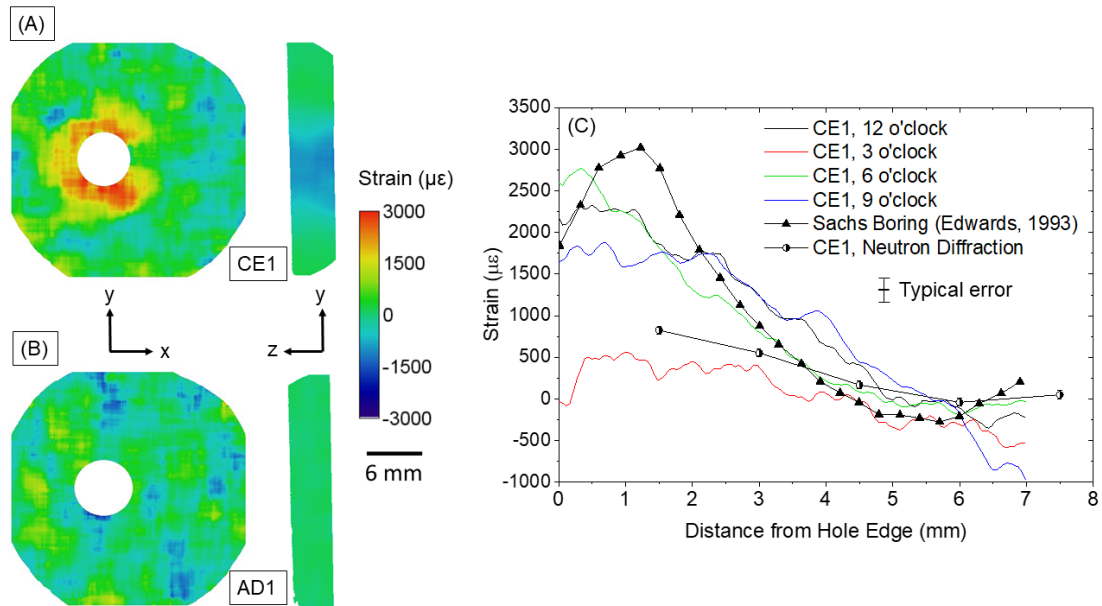


Fig. 9.18 Residual strain map of (a) cold-expanded and (b) conventionally drilled hole, showing the through-the-thickness averaged strain in  $z$ -axis (axial strain) and  $x$ -axis (combined hoop and radial strain) direction; (c) Line profiles of strains taken from the 2D axial strain map of CE1 sample, around the cold-expanded hole. The results are compared with measurements using the Sachs Boring method (Edwards and Ozdemir, 1993) and neutron diffraction.

in the split-sleeve used to facilitate the passage of the mandrel through the hole during the expansion process. During the expansion process, radial pressure is introduced by the oversized mandrel to the plate *via* the sleeve whereas on the opening of the sleeve, there is a lack of pressure on the plate. This leads to a low residual stress region in the sleeve opening area. Although the details of sleeve opening position was not available for the particular sample, the hypothesis is that the 3 o'clock position was the sleeve opening position and therefore exhibits lower strain values.

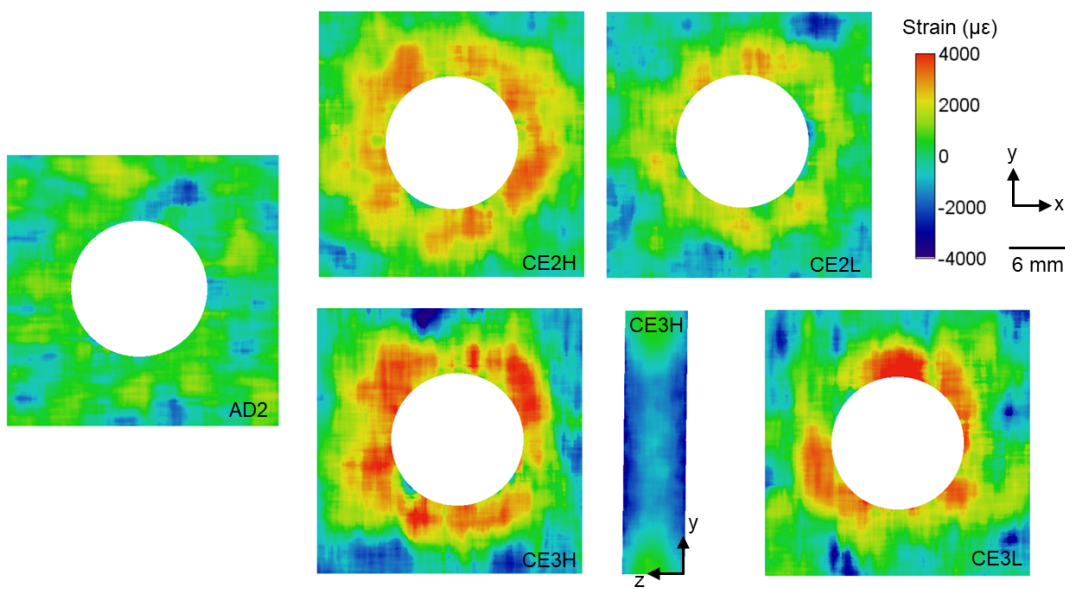


Fig. 9.19 Residual strain map of the drilled and cold-expanded holes on Al2024-T351 and Al7075-T651 plate. Tensile residual strain in the  $z$ -axis (axial strain) direction can be observed around the hole, while the drilled sample (AD2) has no significant residual strain around the hole. Residual strain of sample CE3H in the  $x$ -direction showed compressive residual strain.

Neutron diffraction measurements were performed on the CE1 sample, where the measurement points were on the 3 o'clock position, Fig. 9.9(b). The axial strains measured using neutron diffraction were then compared with those measured using neutron transmission and are plotted in Fig. 9.18(c). Also in Fig. 9.18(c) are residual strains from a cold-expanded hole measured using the Sachs boring method by Edwards and Ozdemir (1992). Their study reports hoop, radial, and axial residual stresses on a 4% cold-expanded hole in 7000-series aluminium alloy, and here axial strain was back-calculated using Hooke's Law. From Fig. 9.18(c), it can be seen that the neutron diffraction results are consistent with neutron transmission taken from the same position. Both results show low tensile residual strain below  $1000 \mu\epsilon$  close to the edge of the hole, and gradually approach zero strain as a function of

distance away from the hole. Meanwhile, axial residual strains measured using the Sachs boring method show high tensile strain close to the hole edge, and more closely resemble the neutron transmission results measured at the 6, 9, and 12 o'clock position.

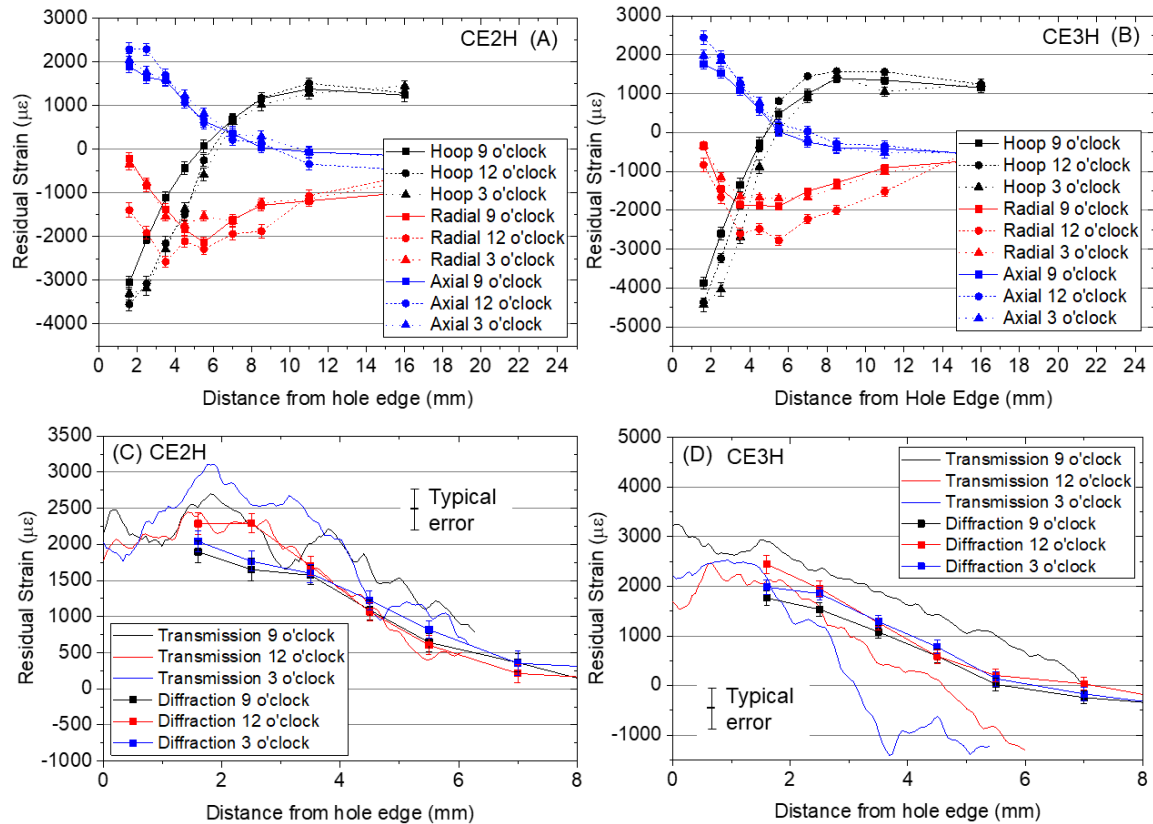


Fig. 9.20 Line profiles of residual strain of samples (a) CE2H and (b) CE3H measured using neutron diffraction on ENGIN-X. Comparison between axial strain measured using neutron diffraction and neutron transmission, of sample (c) CE2H and (d) CE3H, showing good agreement.

Fig 9.19 shows the residual strain maps of the drilled and cold-expanded holes on the Al2024-T351 and Al7075-T651 plates. The maps were reconstructed from the Al {111} Bragg edges, using a macro-pixel size of  $50 \times 50$ , and the strains are averaged through the sample thickness in the  $z$ -axis (axial strain) direction. One strain map of sample CE3H in the  $x$ -axis direction (combined hoop and radial strain) is also showed. The drilled hole on the Al7075-T651, sample AD2, showed no significant axial residual strain around the hole. Meanwhile, all of the cold-expanded samples show tensile axial residual strain. For the same material, the high cold-expanded samples (CE2H and CE3H) show higher tensile strain levels compared to low cold-expanded samples (CE2L and CE3L). Subjected to the equivalent degree of cold expansions, Al7075-T651 with higher yield strength compared to

Al2024-T351 sustained higher residual strain, Fig. 9.19. It can also be observed that there are variations of residual strain values around the cold-expanded hole. Overall, the scatter in the strain values within the axial strain maps is quite high. This is due to the small amount of aluminium material, which weakly diffract neutrons, producing data with a poor statistical quality. Meanwhile, the residual strain map in the  $x$ -axis direction measured from sample CE3H, as expected, shows compressive residual strain around the hole.

Fig. 9.20(a) and (b) show line profiles of residual strain of samples CE2H and CE3H, respectively, measured using neutron diffraction on the ENGIN-X. The trend of the line profiles for hoop, radial, and axial strains shows good agreement with previous studies (Cook and Holdway, 1993; Stefanescu et al., 2004a; Edwards and Ozdemir, 1993). There are no significant variations between line profiles of strain taken at the 9, 12, and 3 o'clock positions around the hole. Fig. 9.20(c) and (d) show line profiles of axial residual strain of sample CE2H and CE3H, respectively, measured using neutron diffraction and neutron transmission. The comparison between axial residual strain values measured using neutron transmission and neutron diffraction shows good agreement. There is a large scatter in the neutron transmission results, which are partially captured by the high error values of  $\pm 360 \mu\epsilon$ .

## 9.4 Discussion

Like any other strain measurement technique, Bragg edge neutron transmission strain mapping possesses a unique characteristics with its own advantages and limitations. Nevertheless, benefited by the development of this technique carried out in this work, neutron transmission has become a powerful addition into the engineer's toolbox for strain measurement.

As has been mentioned, neutron transmission works best on samples with minimum strain variation in the transmission direction, due to the through-the-thickness strain averaging nature of the technique. Also, due to the averaging, the strain mapping can only strictly measure one strain direction. The other strain directions can be obtained by rotating the sample, i.e.,  $90^\circ$ . However, it will average a completely different part of the sample (i.e., different gauge volume), and therefore information of stress is difficult to be recovered. Therefore, neutron transmission is more useful for parametric studies, e.g., optimum power density of peening process, optimum degree of cold-expansion, etc, rather than a detailed stress measurement.

Neutron transmission is useful for non-destructively measuring the strain profile on samples with high strain gradient, e.g., compressive residual strain field with a depth of 300-600  $\mu\text{m}$  from the laser peened surface. As demonstrated in this chapter (**Section 9.3.5**),

strain maps with spatial resolution of up to 100 µm have been produced. The technique is also useful for studying complex-shaped samples. Using neutron transmission, a full strain profile can be obtained relatively straightforwardly in a short period of time. This can be used to identify the region of interest where a more detailed stress measurement of all strain components, for example neutron diffraction, can be carried out. In the future, owing to the two 90° diffraction detectors to be installed, combined neutron transmission and neutron diffraction experiments can be performed simultaneously on the same beamline on IMAT.

Different types of aluminium alloys as well as steels have been tested to represent typical engineering materials used in aerospace and power generation applications. Aluminium presents a challenge due to its weak interaction with neutrons, which consequently requires a sample with relatively bigger length in transmission direction and/or longer counting time, as shown in the study of cold-expanded holes (**Section 9.3.6**). Additionally, aluminium samples, especially rolled plates, might have a strong crystallographic texture which might change the shape of the Bragg edges and complicate the Bragg edge fitting routines (e.g., sample SA3 in **Section 9.3.3**). Nevertheless, useful strain information was recovered successfully. Steel samples are more ideal due to its strong Bragg edge scattering. It has to be noted however, that the optimum sample thickness in the transmission direction is in the range of 10 to 20 mm.

In this chapter, the results from neutron transmission have consistently shown a good agreement with other more established residual strain measurement techniques, e.g., incremental hole drilling (**Section 9.3.1**) and neutron diffraction (**Section 9.3.6**). This further confirms the accuracy and quantifies the strain uncertainties of the neutron transmission experiment. There is a scope for the future to combine neutron transmission with other measurements, in order to extend the usability of neutron transmission. For example, in the case of the measurement of cold-expanded hole samples, there seems to be a correlation between the axial, hoop, and radial strains as a function of distance from the hole edge, as shown by the neutron diffraction result in Fig. 9.9(a) and (b). Using neutron diffraction data and a mathematical model, there is a possibility to extrapolate the hoop and radial strain from the axial strain maps produced by neutron transmission.

Based on the results presented in this chapter, neutron transmission has been proven as a unique and powerful method not only for residual strain mapping but also for capturing crystallographic texture changes due to manufacturing process, e.g., (**Section 9.3.2 and 9.3.3**). Therefore, future application of this technique for engineering studies should be encouraged.

# Chapter 10

## Conclusions

### 10.1 Conclusions

Exhaustive work in the development and validation of the Bragg edge imaging technique for strain mapping and crystallographic analysis applications, as well as the development of the IMAT imaging instrument has been carried out. Several key achievements and findings are as follows:

1. The instrumental parameters of the IMAT beamline, especially those which are important in determining the quality of Bragg edge imaging results have been characterised. At the current default position of the MCP detector, the flight path of the instrument, i.e., the distance from the surface of the moderator to the detector in its default position, is 56.4 m. This confirms the reproducibility of the camera placement, which position are determined through the camera positioning system. Should the position of the MCP detector need to be moved, e.g., due to installation of sample environment, the flight path calibration needs to be performed before the experiment, following experiments and data analysis steps described in **Section 6.2.2**. CeO<sub>2</sub> powder is proven to be a good calibration sample, while Be was also able to produce accurate calibration results in a significantly faster counting time. The IMAT resolution function has been experimentally validated, where the decay constant  $\tau$  was used to represent instrument's pulse width. The  $\tau$  value as a function of neutron wavelength  $\lambda$  is described in Eq. (6.4). The function describes the effect of the moderator, and therefore can be preserved as a reference for future experiments. Additionally, the function can be used as sample-independent constraint for the  $\tau$  parameter in Bragg edge fitting routines. Spatial resolution as a function of geometrical blurring  $d$  has been described, with the

spatial resolution shown to be equal to approximately 42% of the nominal geometrical blurring value.

2. Data analysis for Bragg edge imaging for strain mapping has been developed. Different Bragg edge analytical fitting functions have been evaluated and assessed. The 3-step parameter function, Eq. (4.4), is proven to be the most robust. Meanwhile the 5-parameter function, Eq. (4.5), has simpler fitting steps with fewer parameters, and works well to fit a regularly-shaped Bragg edge, i.e., with minimum slope around the Bragg edge. Both functions have been implemented in Bragg edge mapping software available on IMAT.
3. For the first time, a novel Bragg edge analysis based on cross-correlation was demonstrated in this work to provide an alternative measure of lattice parameter shifts for both non-textured and textured samples. For non-textured samples, strain values derived from Bragg edge fitting were successfully reproduced by the cross-correlation method. For Bragg edges from textured samples, where the analytical parameter-fitting approach often struggles to describe the Bragg edge shape, the cross-correlation method was shown to provide accurate results. The counting statistics of the neutron data still limit the implementation of the method in strain-mapping software tools, but, as neutron instrument and detector technologies improve, this will become feasible in the future.
4. The performance of the IMAT beamline in carrying out Bragg edge strain mapping has been evaluated. In this work, it has been proven that accurate strain mapping can be performed on IMAT. Typical measurements on IMAT with an MCP detector can provide a quarter of a million spatially resolved measurement points in a single exposure with counting times below 10 h. The detector has a single-pixel size of  $55 \times 55 \mu\text{m}$ . Pixel binning is often necessary to improve the counting statistics, but a strain map can be reconstructed with a spatial resolution in the range of  $100\text{-}600 \mu\text{m}$ . Such measurements provide strain uncertainties below  $200 \mu\epsilon$ , and uncertainties as low as  $\approx 80 \mu\epsilon$  have been obtained. These numbers show that IMAT is suitable for strain-mapping applications on engineering samples.
5. It has been demonstrated that Bragg edge neutron transmission has applications in several domains by offering the possibility to provide spatially resolved information on the local crystallographic structure. Extensive examples of mapping of residual strain inside engineering components have been successfully performed. The high spatial resolution of Bragg edge strain mapping was shown to be useful in measuring strain

profiles on samples with high strain gradient, and samples with complex geometry, despite its limitation due to strain averaging.

6. Bragg edge strain mapping results were validated using more established strain measurement techniques such as neutron diffraction and incremental hole drilling, showing good agreement.
7. It has been demonstrated that Bragg edge imaging has wider applications beyond strain mapping. Crystallographic texture distributions and evolution can be mapped using Bragg edge transmission with a scope of quantifying the texture parameters with a more comprehensive model. A proof of concept of measuring temperature dependence of structure parameters, such as the Debye–Waller factor, through Bragg edge analysis has been demonstrated, with results agreeing well with previous theoretical and experimental values.

## 10.2 Future work

While this work has positively contribution to the development of the Bragg edge imaging technique and of the IMAT beamline, there are a couple of areas where improvement can be made through future works, and are describes as follows:

1. Addition of a wider range of materials for strain mapping characterisation on IMAT. Presently, the study of the strain resolution and the spatial resolution of the strain map produced on IMAT were performed using Fe powders and Fe rod, respectively. Therefore, as mentioned previously in the text, the resolution values are valid specifically for the corresponding material and sample geometry. While the Fe samples provided good representation of engineering materials, further study with a wider spectrum of materials will provide a better representation of the beamline performance in carrying out strain mapping.
2. Implementation of multiple-edge analysis on IMAT. Currently, most of the Bragg edge analysis on IMAT, especially for strain mapping, are performed the single edge analysis which uses only a small portion of the recorded data. Using and implementing a multiple-edge analysis on IMAT, either using a currently available codes or building a new one, has the potential to improve the result, i.e., improve the uncertainty and the counting time. The implementation of multiple-edge analysis will also help in analysing data from highly-textured samples.



# References

- Abbey, B., Zhang, S. Y., Vorster, W., and Korsunsky, A. M. (2012). Reconstruction of axisymmetric strain distributions via neutron strain tomography. *Nuclear Instruments and Methods in Physics Research, Section B: Beam Interactions with Materials and Atoms*, 270(1):28–35.
- Abd El Bar, W., Mahmoud, I. I., Konber, H. A., and Mongy, T. (2015). Image reconstruction technique using projection data from neutron tomography system. *Alexandria Engineering Journal*, 54(4):1057–1066.
- Andersen, K. (2013). Reactor and spallation neutron sources. [http://www.oxfordneutronschool.org/2013/Lectures/Andersen-Neutron\\_Sources.pdf](http://www.oxfordneutronschool.org/2013/Lectures/Andersen-Neutron_Sources.pdf). Accessed: 2018-11-30.
- Andreani, C., Gorini, G., and Materna, T. (2009). Novel Neutron Imaging Techniques for Cultural Heritage Objects. In Bilheux, H. Z., McGreevy, R., and Anderson, I. S., editors, *Neutron Imaging and Applications: A Reference for the Imaging Community*, pages 229–252. Springer US, Boston, MA.
- Arai, M. and Crawford, K. (2009). Neutron Sources and Facilities. In Anderson, I. S., McGreevy, R. L., and Bilheux, H. Z., editors, *Neutron Imaging and Applications: A reference for the imaging community*, chapter 2, pages 13–31. Springer, New York.
- Banhart, J., Borbély, A., Dzieciol, K., Garcia-Moreno, F., Manke, I., Kardjilov, N., Kaysser-Pyzalla, A. R., Strobl, M., and Treimer, W. (2010). X-ray and neutron imaging – Complementary techniques for materials science and engineering. *International Journal of Materials Research*, 101(9):1069–1079.
- Basinski, Z., Hume-rothery, W., and Sutton, A. (1955). The lattice expansion of iron. *Proceedings of the Royal Society of London. Series A, Mathematical and Physical Sciences*, 229(1179):459–467.
- Bilheux, J. (2018). Bragg edge user interface (ibeatles). <https://jeanbilheux.pages.ornl.gov/project/ibeatles/>. Accessed: 2018-11-30.
- Boin, M. (2012). Nxs: A program library for neutron cross section calculations. *Journal of Applied Crystallography*, 45(3):603–607.
- Boin, M., Hilger, A., Kardjilov, N., Zhang, S. Y., Oliver, E. C., James, J. A., Randau, C., and Wimpory, R. C. (2011). Validation of Bragg edge experiments by Monte Carlo simulations for quantitative texture analysis. *Journal of Applied Crystallography*, 44(5):1040–1046.

- Bourbia, A., Draissia, M., Bedboudi, H., Boulkhessaim, S., and Debili, M. Y. (2010). X-ray and optical crystallographic parameters investigations of high frequency induction melted Al-( $\alpha$ -Al<sub>2</sub>O<sub>3</sub>) alloys. *Journal of X-Ray Science and Technology*, 18(2):201–219.
- Brokmeier, H.-G. and Bunge, H. J. (1988). Neutron Diffraction Texture. *Textures and Microstructures*, 10(1):1–8.
- Burca, G. (2012). *Combined Neutron Imaging and Diffraction: Instrumentation and Experimentation*. PhD thesis, The Open University, UK.
- Burca, G., Kelleher, J., Peacock, A. ., Hayes, M., and Deliry, P. (2016). An integrated tool for Bragg edge analysis at ISIS. In *NEUWAVE-8 Workshop, Abingdon UK*.
- Burca, G., Kockelmann, W., James, J. A., and Fitzpatrick, M. E. (2013). Modelling of an imaging beamline at the ISIS pulsed neutron source. *Journal of Instrumentation*, 8(10).
- Chen, Y. S., Peng, H., Hussey, D. S., Jacobson, D. L., Tran, D. T., Abdel-Basset, T., and Biernacki, M. (2007). Water distribution measurement for a PEMFC through neutron radiography. *Journal of Power Sources*, 170(2):376–386.
- Cook, R. and Holdway, P. (1993). Residual stresses induced by hole cold expansion. *Transactions on Engineering Sciences*, 2:91–100.
- Cooper, A. S. (1962). Precise lattice constants of germanium, aluminum, gallium arsenide, uranium, sulphur, quartz and sapphire. *Acta Crystallographica*, 15(6):578–582.
- Copley, J. (2001). *The fundamentals of neutron powder diffraction*. NIST recommended practice guide. U.S. Department of Commerce, Technology Administration, National Institute of Standards and Technology.
- Coratella, S., Sticchi, M., Toparli, M. B., Fitzpatrick, M. E., and Kashaev, N. (2015). Application of the eigenstrain approach to predict the residual stress distribution in laser shock peened AA7050-T7451 samples. *Surface and Coatings Technology*, 273(1):39–49.
- Coules, H. E., Cozzolino, L. D., Colegrove, P., Ganguly, S., Wen, S. W., and Pirling, T. (2013). Neutron Diffraction Analysis of Complete Residual Stress Tensors in Conventional and Rolled Gas Metal Arc Welds. *Experimental Mechanics*, 53(2):195–204.
- Crow, L. (2009). Neutron detectors for imaging. In *Neutron Imaging and Applications: A reference for the imaging community*, chapter 4, pages 47–63. Springer, New York.
- Davey, W. P. (1925). Precision measurements of the lattice constants of twelve common metals. *Physical Review*, 25(6):753–761.
- de Novion, C. H. (2003). The use of neutrons for materials characterization. In M.E. Fitzpatrick and A. Londini, editors, *Analysis of Residual Stress by Diffraction using Neutron and Synchrotron Radiation*, chapter 1, pages 5–27. Taylor & Francis, London.
- Debrunner, P. and Morrison, R. J. (1965). Determination of Recoilless Fractions from Mössbauer Scattering. *Review of Scientific Instruments*, 36(2):145–149.

- Deschler-Erb, E., Lehmann, E. H., Pernet, L., Vontobel, P., and Hartmann, S. (2004). The complementary use of neutrons and X-rays for the non-destructive investigation of archaeological objects from Swiss collections. *Archaeometry*, 46(4):647–661.
- Dorman, M., Toparli, M. B., Smyth, N., Cini, A., Fitzpatrick, M. E., and Irving, P. E. (2012). Effect of laser shock peening on residual stress and fatigue life of clad 2024 aluminium sheet containing scribe defects. *Materials Science and Engineering A*, 548:142–151.
- Edwards, L. and Ozdemir, A. (1992). Residual Stresses at Cold Expanded Fastener Holes. In Hutchings, M. T. and Krawitz, A. D., editors, *Measurement of Residual and Applied Stress Using Neutron Diffraction*, pages 545–554. Springer Science+Business Media, B.V.
- Edwards, L. and Ozdemir, A. (1993). Effect of residual stress on fatigue life of cold expanded fastener holes. *Transactions on Engineering Sciences*, 2:101–109.
- El-Gallab, M. and Sklad, M. (1998). Machining of Al/SiC particulate metal-matrix composites Part I: Tool performance. *Journal of Materials Processing Technology*, 83(1-3):151–158.
- Fabbro, R., Peyre, P., Berthe, L., and Scherpereel, X. (1998). Physics and applications of laser-shock processing. *Journal of Laser Applications*, 10(6):265.
- Fermi, E., Sturm, W. J., and Sachs, R. G. (1947). The transmission of slow neutrons through microcrystalline materials. *Physical Review*, 71(9):589–594.
- Festa, G., Caroppi, P. A., Filabozzi, A., Andreani, C., Arancio, M. L., Triolo, R., Celso, F. L., Benfante, V., and Imberti, S. (2008). Composition and corrosion phases of Etruscan Bronzes from Villanovan Age. *Measurement Science and Technology*, 19(3).
- Figgins, B. F., Jones, G. O., and Riley, D. P. (1956). The thermal expansion of aluminium at low temperatures as measured by an X-ray diffraction method. *Philosophical Magazine*, 1(8):747–758.
- Filges, D. and Goldenbaum, F. (2010). *Handbook of Spallation Research*. Wiley.
- Finocchiaro, V., Aliotta, F., Tresoldi, D., Ponterio, R. C., Vasi, C. S., and Salvato, G. (2013). The autofocusing system of the IMAT neutron camera. *Review of Scientific Instruments*, 84(9).
- Garcia-Granada, A., Lacarac, V., Smith, D., Pavier, M., Cook, R., and Holdway, P. (1999). 3D residual stress around cold expanded holes in a new creep resistant aluminium alloy. *Transactions on Engineering Sciences*, 25:103–116.
- Gopalakrishna, H. D., Narasimha Murthy, H. N., Krishna, M., Vinod, M. S., and Suresh, A. V. (2010). Cold expansion of holes and resulting fatigue life enhancement and residual stresses in Al 2024 T3 alloy - An experimental study. *Engineering Failure Analysis*, 17(2):361–368.
- Gorton, A. T., Bitsianes, G., and Joseph, T. L. (1965). Thermal expansion coefficients for iron and its oxides from X-ray diffraction measurements at elevated temperatures. *Transactions of the Metallurgical Society of AIME*, 233:1519–1525.

- Granada, J. R. (1984). Total Scattering Cross Section of Solids for Cold and Epithermal Neutrons. *Zeitschrift fur Naturforschung - Section A Journal of Physical Sciences*, 39(12):1160–1167.
- Grant, P., Lord, J., Whitehead, P., and Fry, A. T. (2005). The Application of Fine Increment Hole Drilling for Measuring Machining-Induced Residual Stresses. *Applied Mechanics and Materials*, 3-4:105–110.
- Grant, P. V., Lord, J. D., and Whitehead, P. (2006). The Measurement of Residual Stresses by the Incremental Hole Drilling Technique. Technical Report 2, National Physical Laboratory. [https://www.npl.co.uk/special-pages/guides/gpg53\\_drilling](https://www.npl.co.uk/special-pages/guides/gpg53_drilling).
- Gujba, A. K. and Medraj, M. (2014). Laser peening process and its impact on materials properties in comparison with shot peening and ultrasonic impact peening. *Materials*, 7(12):7925–7974.
- Hannon, A. C. (2010). Neutron Diffraction, Theory. In *Encyclopedia of Spectroscopy and Spectrometry*, pages 1779–1789. Academic Press.
- Harwood, M. G. (1949). Variation in density and colour of cerium oxide. *Nature*, 164(4175):787.
- Hatamleh, O. and DeWald, A. (2009). An investigation of the peening effects on the residual stresses in friction stir welded 2195 and 7075 aluminum alloy joints. *Journal of Materials Processing Technology*, 209(10):4822–4829.
- Hatch, J. E. (1984). Properties and Physical Metallurgy. *Aluminum, ASM International, Materials Park, Ohio*, pages 25–57.
- Haworth, C. W. (1960). Measurement of the Debye-Waller temperature factor for silver and alpha-iron. *Philosophical Magazine*, 5(60):1229–1234.
- Hendriks, J. N., Gregg, A. W. T., Wensrich, C. M., Tremsin, A. S., Shinohara, T., Meylan, M., Kisi, E. H., Luzin, V., and Kirsten, O. (2017). Bragg-edge elastic strain tomography for *in-situ* systems from energy-resolved neutron transmission imaging. *Physical Review Materials*, 1(5):053802.
- Herwig, K. W. (2009). Introduction to the Neutron. In Anderson, I. S., McGreevy, R. L., and Bilheux, H. Z., editors, *Neutron Imaging and Applications: A reference for the imaging community*, chapter 1, pages 3–12. Springer, New York.
- Hrabe, N., Gnupel-Herold, T., and Quinn, T. (2015). Fatigue properties of a titanium alloy (Ti-6Al-4V) fabricated via electron beam melting (EBM): Effects of internal defects and residual stress. *International Journal of Fatigue*.
- Hull, A. W. (1917). Crystal structures of common elements. *Physical Review*, 10:661–696.
- Humphreys, F. and Hatherly, M. (2004). Recrystallization Textures. In *Recrystallization and Related Annealing Phenomena*, pages 379–413. Elsevier.

- Hutchings, M. T. (1992). Neutron Diffraction Measurement of Residual Stress Fields: Overview and Points for Discussion. In Hutchings, M. T. and Krawitz, A. D., editors, *Measurement of Residual and Applied Stress Using Neutron Diffraction*, pages 3–18. Springer Science+Business Media, B.V.
- ISO/TS 21432:2005(en) (2005). Non-destructive testing — standard test method for determining residual stresses by neutron diffraction. Standard, International Organization for Standardization, Geneva, CH.
- Itoh, T., Mori, M., Inukai, M., Nitani, H., Yamamoto, T., Miyanaga, T., Igawa, N., Kitamura, N., Ishida, N., and Idemoto, Y. (2015). Effect of annealing on crystal and local structures of doped zirconia using experimental and computational methods. *Journal of Physical Chemistry C*, 119(16):8447–8458.
- Iwase, K., Sakuma, K., Kamiyama, T., and Kiyanagi, Y. (2009). Bragg-edge transmission imaging of strain and microstructure using a pulsed neutron source. *Nuclear Instruments and Methods in Physics Research, Section A: Accelerators, Spectrometers, Detectors and Associated Equipment*, 605(1-2):1–4.
- Iwase, K., Sato, H., Harjo, S., Kamiyama, T., Ito, T., Takata, S., Aizawa, K., and Kiyanagi, Y. (2012). In situ lattice strain mapping during tensile loading using the neutron transmission and diffraction methods. *Journal of Applied Crystallography*, 45(1):113–118.
- Jette, E. R. and Foote, F. (1935). Precision determination of lattice constants. *The Journal of Chemical Physics*, 3(10):605–616.
- Jeyakumar, M. and Christopher, T. (2013). Influence of residual stresses on failure pressure of cylindrical pressure vessels. *Chinese Journal of Aeronautics*, 26(6):1415–1421.
- Johnson, M. W. and Daymond, M. R. (2003). Neutron pulsed source instrumentation. In *Analysis of Residual Stress by Diffraction using Neutron and Synchrotron Radiation*, chapter 9, pages 146–169. Taylor & Francis, London.
- Kalainathan, S., Sathyajith, S., and Swaroop, S. (2012). Effect of laser shot peening without coating on the surface properties and corrosion behavior of 316L steel. *Optics and Lasers in Engineering*, 50(12):1740–1745.
- Kardjilov, N., Baechler, S., Bastürk, M., Dierick, M., Jolie, J., Lehmann, E., Materna, T., Schillinger, B., and Vontobel, P. (2003). New features in cold neutron radiography and tomography Part II: Applied energy-selective neutron radiography and tomography. *Nuclear Instruments and Methods in Physics Research, Section A: Accelerators, Spectrometers, Detectors and Associated Equipment*, 501(2-3):536–546.
- Kardjilov, N., Manke, I., Hilger, A., Strobl, M., and Banhart, J. (2011). Neutron imaging in materials science. *Materials Today*, 14(6):248–256.
- Kharoo, H. L., Gupta, O. P., and Hemkar, M. P. (1977). Temperature Dependence of Debye-Waller Factors in bcc Metals. I. *Journal of the Physical Society of Japan*, 43(6):2030–2035.
- Kochanovska, A. (1949). Investigation of thermal dilatation of cubic metals. *Physica*, 15(1-2):191–196.

- Kockelmann, W., Chapon, L. C., and Radaelli, P. G. (2006). Neutron texture analysis on GEM at ISIS. *Physica B: Condensed Matter*, 385-386 I:639–643.
- Kockelmann, W., Frei, G., Lehmann, E. H., Vontobel, P., and Santisteban, J. R. (2007). Energy-selective neutron transmission imaging at a pulsed source. *Nuclear Instruments and Methods in Physics Research, Section A: Accelerators, Spectrometers, Detectors and Associated Equipment*, 578(2):421–434.
- Kockelmann, W., Minniti, T., Pooley, D., Burca, G., Ramadhan, R., Akeroyd, F., Howells, G., Moreton-Smith, C., Keymer, D., Kelleher, J., Kabra, S., Lee, T., Ziesche, R., Reid, A., Vitucci, G., Gorini, G., Micieli, D., Agostino, R., Formoso, V., Aliotta, F., Ponterio, R., Trusso, S., Salvato, G., Vasi, C., Grazzi, F., Watanabe, K., Lee, J., Tremsin, A., McPhate, J., Nixon, D., Draper, N., Halcrow, W., and Nightingale, J. (2018). Time-of-Flight Neutron Imaging on IMAT@ISIS: A New User Facility for Materials Science. *Journal of Imaging*, 4(3):47.
- Kockelmann, W., Zhang, S. Y., Kelleher, J. F., Nightingale, J. B., Burca, G., and James, J. A. (2013). IMAT - A new imaging and diffraction instrument at ISIS. *Physics Procedia*, 43:100–110.
- Koerner, S., Lehmann, E., and Vontobel, P. (2000). Design and optimization of a CCD-neutron radiography detector. *Nuclear Instruments and Methods in Physics Research, Section A: Accelerators, Spectrometers, Detectors and Associated Equipment*, 454(1):158–164.
- Koetzle, T. F. and McIntyre, G. J. (2012). *Single-Crystal Neutron Diffraction*, pages 1–14. American Cancer Society.
- Kramer, D., Lehmann, E., Frei, G., Vontobel, P., Wokaun, A., and Scherer, G. G. (2005). An on-line study of fuel cell behavior by thermal neutrons. *Nuclear Instruments and Methods in Physics Research, Section A: Accelerators, Spectrometers, Detectors and Associated Equipment*, 542(1-3):52–60.
- Kropff, F., Granada, J. R., and Mayer, R. E. (1982). The bragg lineshapes in time-of-flight neutron powder spectroscopy. *Nuclear Instruments and Methods In Physics Research*, 198(2-3):515–521.
- Kuemmerle, E. A. and Heger, G. (1999). The structures of C-(Ce<sub>2</sub>O<sub>3+d</sub>), Ce<sub>7</sub>O<sub>12</sub> and Ce<sub>11</sub>O<sub>20</sub>. *Journal of Solid State Chemistry*, 147:485–500.
- Lehmann, E. H., Hartmann, S., and Speidel, M. O. (2010). Investigation of the content of ancient tibetan metallic buddha statues by means of neutron imaging methods. *Archaeometry*, 52(3):416–428.
- Lehmann, E. H., Vontobel, P., Deschler-Erb, E., and Soares, M. (2005). Non-invasive studies of objects from cultural heritage. *Nuclear Instruments and Methods in Physics Research, Section A: Accelerators, Spectrometers, Detectors and Associated Equipment*, 542(1-3):68–75.
- Liang, X. Z., Dodge, M. F., Kabra, S., Kelleher, J. F., Lee, T. L., and Dong, H. B. (2018). Effect of hydrogen charging on dislocation multiplication in pre-strained super duplex stainless steel. *Scripta Materialia*, 143:20–24.

- Lionheart, W. R. B. and Withers, P. J. (2015). Diffraction tomography of strain. *Inverse Problems*, 31(4):045005.
- Maawad, E., Sano, Y., Wagner, L., Brokmeier, H.-G., and Genzel, C. (2012). Investigation of laser shock peening effects on residual stress state and fatigue performance of titanium alloys. *Materials Science and Engineering: A*, 536:82–91.
- Makowska, M. G., Strobl, M., Lauridsen, E. M., Kabra, S., Kockelmann, W., Tremsin, A., Frandsen, H. L., and Theil Kuhn, L. (2016). In situ time-of-flight neutron imaging of NiO-YSZ anode support reduction under influence of stress. *Journal of Applied Crystallography*, 49(5):1674–1681.
- Malamud, F. and Santisteban, J. R. (2016). Full-pattern analysis of time-of-flight neutron transmission of mosaic crystals. *Journal of Applied Crystallography*, 49:348–365.
- Malamud, F., Santisteban, J. R., Vicente Alvarez, M. A., Bolmaro, R., Kelleher, J., Kabra, S., and Kockelmann, W. (2014). Texture analysis with a time-of-flight neutron strain scanner. *Journal of Applied Crystallography*, 47(4):1337–1354.
- Manke, I., Hartnig, C., Grünerbel, M., Kaczerowski, J., Lehnert, W., Kardjilov, N., Hilger, A., Banhart, J., Treimer, W., and Strobl, M. (2007). Quasi-in situ neutron tomography on polymer electrolyte membrane fuel cell stacks. *Applied Physics Letters*, 90(18):2005–2008.
- Minniti, T., Kockelmann, W., Burca, G., Kelleher, J., Kabra, S., Zhang, S., Pooley, D., Schooneveld, E., Mutamba, Q., Sykora, J., Rhodes, N., Pouzols, F., Nightingale, J., Aliotta, F., Bonaccorsi, L., Ponterio, R., Salvato, G., Trusso, S., Vasi, C., Tremsin, A., and Gorini, G. (2016). Materials analysis opportunities on the new neutron imaging facility IMAT@ISIS. *Journal of Instrumentation*, 11(03):C03014–C03014.
- Minniti, T., Watanabe, K., Burca, G., Pooley, D. E., and Kockelmann, W. (2018). Characterization of the new neutron imaging and materials science facility imat. *Nuclear Instruments and Methods in Physics Research Section A: Accelerators, Spectrometers, Detectors and Associated Equipment*, 888:184 – 195.
- Nakanishi, T. M. (2009). Neutron Imaging Applied to Plant Physiology. In Bilheux, H. Z., McGreevy, R., and Anderson, I. S., editors, *Neutron Imaging and Applications: A Reference for the Imaging Community*, pages 305–317. Springer US, Boston, MA.
- Nam, Y.-S., Jeong, Y.-I., Shin, B.-C., and Byun, J.-H. (2015). Enhancing surface layer properties of an aircraft aluminum alloy by shot peening using response surface methodology. *Materials & Design*, 83:566–576.
- Nigrelli, V. and Pasta, S. (2008). Finite-element simulation of residual stress induced by split-sleeve cold-expansion process of holes. *Journal of Materials Processing Technology*, 205(1-3):290–296.
- Oswald, S. E., Menon, M., Carminati, A., Vontobel, P., Lehmann, E., and Schulin, R. (2008). Quantitative Imaging of Infiltration, Root Growth, and Root Water Uptake via Neutron Radiography. *Vadose Zone Journal*, 7(3):1035.
- Owen, E. and Yates, E. (1933). Precision measurements of crystal parameters. *Philosophical Magazine*, 7:1933.

- Penumadu, D. (2009). Material Science and Engineering with Neutron Imaging. In Bilheux, H. Z., McGreevy, R., and Anderson, I. S., editors, *Neutron Imaging and Applications: A Reference for the Imaging Community*, pages 209–227. Springer US, Boston, MA.
- Pooley, D. E., Lee, J. W., Brouard, M., John, J. J., Kockelmann, W., Rhodes, N. J., Schoon-eveld, E. M., Sedgwick, I., Turchetta, R., and Vallance, C. (2017). Development of the 'GP2' Detector: Modification of the PImMS CMOS Sensor for Energy-Resolved Neutron Radiography. *IEEE Transactions on Nuclear Science*, 64(12):2970–2981.
- Powers, P. N. (1938). The magnetic scattering of neutrons. *Physical Review*, 54(10):827–838.
- Prakash, J., Pathak, L., and Hemkar, M. P. (1975). Debye-Waller Factors of a-Iron and Sodium. *Australia Journal of Physics*, 28:63–68.
- Priesmeyer, H. (2003). The use of neutron transmission for materials analysis. In Fitzpatrick, M. E. and Londini, A., editors, *Analysis of Residual Stress by Diffraction using Neutron and Synchrotron Radiation*, chapter 11, pages 190–206. Taylor & Francis, London.
- Prime, M. B. and Gonzales, A. R. (2000). the Contour Method: Simple 2-D Mapping of Residual Stresses. *Sixth International Conference on Residual StressesSixth International Conference on Residual Stresses, July 10-12,, 836(January 2000):617–624.*
- Pynn, R. (2009). Neutron scattering - a non-destructive microscope for seeing inside matter. In Rinaldi, R. and Liang, L., editors, *Neutron Applications in Earth, Energy and Environmental Sciences*, pages 1–29. Springer.
- Ramadhan, R. S., Kockelmann, W., Minniti, T., Chen, B., Parfitt, D., Fitzpatrick, M. E., and Tremsin, A. S. (2019). Characterization and application of Bragg-edge transmission imaging for strain measurement and crystallographic analysis on the IMAT beamline. *Journal of Applied Crystallography*, 52(2):351–368.
- Ramadhan, R. S., Syed, A. K., Tremsin, A. S., Kockelmann, W., Dalgliesh, R., Chen, B., Parfitt, D., and Fitzpatrick, M. E. (2018). Mapping residual strain induced by cold working and by laser shock peening using neutron transmission spectroscopy. *Materials & Design*, 143:56–64.
- Reid, A., Martinez, I., Marshall, M., Minniti, T., Kabra, S., Kockelmann, W., Connolley, T., and Mostafavi, M. (2018). Mapping of axial plastic zone for roller bearing overloads using neutron transmission imaging. *Materials and Design*, 156(June):103–112.
- Richards, W. J., Barrett, J. R., Springgate, M. E., and Shields, K. C. (2004). Neutron radiography inspection of investment castings. *Applied Radiation and Isotopes*, 61(4):675–682.
- Russell, G. J. (1990). Spallation Physics - An Overview. *International Collaboration on Advanced Neutron Sources KEK. Tsukuba*, pages 291–299.
- Salimianrizi, A., Foroozeh, E., Badrossamay, M., and Farrokhpour, H. (2016). Effect of Laser Shock Peening on surface properties and residual stress of Al6061-T6. *Optics and Lasers in Engineering*, 77:112–117.

- Santisteban, J. R., Daymond, M. R., James, J. A., and Edwards, L. (2006a). ENGIN-X: A third-generation neutron strain scanner. *Journal of Applied Crystallography*, 39(6):812–825.
- Santisteban, J. R., Edwards, L., Fitzpatrick, M. E., Steuwer, A., Withers, P. J., Daymond, M. R., Johnson, M. W., Rhodes, N., and Schooneveld, E. M. (2002a). Strain imaging by Bragg edge neutron transmission. *Nuclear Instruments and Methods in Physics Research, Section A: Accelerators, Spectrometers, Detectors and Associated Equipment*, 481(1-3):765–768.
- Santisteban, J. R., Edwards, L., Fitzpatrick, M. E., Steuwer, A., and Withers, P. J. (2002b). Engineering applications of Bragg-edge neutron transmission. *Applied Physics A: Materials Science and Processing*, 74(SUPPL.II):1433–1437.
- Santisteban, J. R., Edwards, L., and Stelmukh, V. (2006b). Characterization of textured materials by TOF transmission. *Physica B: Condensed Matter*, 385-386 I:636–638.
- Santisteban, J. R., Edwards, L., Steuwer, A., and Withers, P. J. (2001). Time-of-flight neutron transmission diffraction. *Journal of Applied Crystallography*, 34(3):289–297.
- Sato, H. (2017). Deriving Quantitative Crystallographic Information from the Wavelength-Resolved Neutron Transmission Analysis Performed in Imaging Mode. *Journal of Imaging*, 4(2):7.
- Sato, H., Kamiyama, T., and Kiyanagi, Y. (2011). A Rietveld-Type Analysis Code for Pulsed Neutron Bragg-Edge Transmission Imaging and Quantitative Evaluation of Texture and Microstructure of a Welded alpha-Iron Plate. *Materials Transactions*, 52(6):1294–1302.
- Sato, H., Shiota, Y., Morooka, S., Todaka, Y., Adachi, N., Sadamatsu, S., Oikawa, K., Harada, M., Zhang, S., Su, Y., Kamiyama, T., Ohnuma, M., Furusaka, M., Shinohara, T., and Kiyanagi, Y. (2017). Inverse pole figure mapping of bulk crystalline grains in a polycrystalline steel plate by pulsed neutron Bragg-dip transmission imaging. *Journal of Applied Crystallography*, 50(6):1601–1610.
- Sato, H., Shiota, Y., Shinohara, T., Kamiyama, T., Ohnuma, M., Furusaka, M., and Kiyanagi, Y. (2015). Development of the Tensor CT Algorithm for Strain Tomography Using Bragg-edge Neutron Transmission. *Physics Procedia*, 69(October 2014):349–357.
- Schajer, G. S. and Ruud, C. O. (2013). Overview of Residual Stresses and Their Measurement. In *Practical Residual Stress Measurement Methods*, chapter 1, page 2. John Wiley & Sons.
- Schajer, G. S. and Whitehead, P. S. (2013). Hole Drilling and Ring Coring. In Schajer, G. S., editor, *Practical Residual Stress Measurement Methods*, chapter 2, page 29. John Wiley & Sons, 1 edition.
- Schillinger, B., Beaudet, A., Fedrigo, A., Grazzi, F., Kullmer, O., Laaß, M., Makowska, M., Werneburg, I., and Zanolli, C. (2018). Neutron Imaging in Cultural Heritage Research at the FRM II Reactor of the Heinz Maier-Leibnitz Center. *Journal of Imaging*, 4(1).
- Schillinger, B., Brunner, J., and Calzada, E. (2006). A study of oil lubrication in a rotating engine using stroboscopic neutron imaging. *Physica B: Condensed Matter*, 385-386:921–923.

- Schneider, C. A., Rasband, W. S., and Eliceiri, K. W. (2012). NIH Image to ImageJ: 25 years of image analysis. *Nature Methods*, 9:671.
- Shinohara, T., Kai, T., Oikawa, K., Segawa, M., Harada, M., Nakatani, T., Ooi, M., Aizawa, K., Sato, H., Kamiyama, T., Yokota, H., Sera, T., Mochiki, K., and Kiyanagi, Y. (2016). Final design of the Energy-Resolved Neutron Imaging System “RADEN” at J-PARC. *Journal of Physics: Conference Series*, 746:012007.
- Song, G., Lin, J., Bilheux, J., Xie, Q., Santodonato, L., Molaison, J., Skorpenske, H., M. Dos Santos, A., Tulk, C., An, K., Stoica, A., Kirka, M., Dehoff, R., Tremsin, A., Bunn, J., Sochalski-Kolbus, L., and Bilheux, H. (2017). Characterization of Crystallographic Structures Using Bragg-Edge Neutron Imaging at the Spallation Neutron Source. *Journal of Imaging*, 3(4):65.
- Soyama, H., Odhiambo, D., and Saito, K. (2006). Cavitation Shotless Peening for Improvement of Fatigue Strength. *Shot Peening*, pages 435–440.
- Sprauel, J. (2003). Study of second- and third-order stresses. In Fitzpatrick, M. E. and Londini, A., editors, *Analysis of Residual Stress by Diffraction using Neutron and Synchrotron Radiation*, chapter 5, pages 78–96. Taylor & Francis, London.
- Stecura, S. and Campbell, W. J. (1961). Thermal expansion and phase inversion of rare-earth oxides. Technical report, U.S. Dep. of the Interior, Bureau of Mines, Washington.
- Stefanescu, D., Edwards, L., and Fitzpatrick, M. E. (2002). X-Ray Diffraction Measurement of the Residual Stresses Surrounding a Cold Expanded Hole. *Materials Science Forum*, 404-407:185–190.
- Stefanescu, D., Santisteban, J. R., Edwards, L., and Fitzpatrick, M. E. (2004a). Residual stress measurement and fatigue crack growth prediction after cold expansion of cracked fastener holes. *Journal of Aerospace Engineering*, 17(3):91–97.
- Stefanescu, D., Steuwer, a., Owen, R. a., Nadri, B., Edwards, L., Fitzpatrick, M. E., and Withers, P. J. (2004b). Elastic strains around cracked cold-expanded fastener holes measured using the synchrotron X-ray diffraction technique. *The Journal of Strain Analysis for Engineering Design*, 39(5):459–469.
- Steuwer, A., Santisteban, J. R., Withers, P. J., Edwards, L., and Fitzpatrick, M. E. (2003). In situ determination of stresses from time-of-flight neutron transmission spectra. *Journal of Applied Crystallography*, 36(5):1159–1168.
- Steuwer, A., Withers, P. J., Santisteban, J. R., and Edwards, L. (2005). Using pulsed neutron transmission for crystalline phase imaging and analysis. *Journal of Applied Physics*, 97(7):1–8.
- Steuwer, A., Withers, P. J., Santisteban, J. R., Edwards, L., Bruno, G., Fitzpatrick, M. E., Daymond, M. R., Johnson, M. W., and Wang, D. (2001). Bragg Edge Determination for Accurate Lattice Parameter and Elastic Strain Measurement. *Physica Status Solidi (A) Applied Research*, 185(2):221–230.

- Straumanis, M. E. and Kim, D. C. (1969). Lattice constants, thermal expansion coefficients, densities and perfection of structure of pure iron and of iron loaded with hydrogen. *Ziet fuer Metallkunde*, 60(4):272–277.
- Strobl, M. (2009). Future prospects of imaging at spallation neutron sources. *Nuclear Instruments and Methods in Physics Research, Section A: Accelerators, Spectrometers, Detectors and Associated Equipment*, 604(3):646–652.
- Strobl, M., Kardjilov, N., Hilger, A., Penumadu, D., and Manke, I. (2011). Advanced neutron imaging methods with a potential to benefit from pulsed sources. *Nuclear Instruments and Methods in Physics Research, Section A: Accelerators, Spectrometers, Detectors and Associated Equipment*, 651(1):57–61.
- Strobl, M., Manke, I., Kardjilov, N., Hilger, A., Dawson, M., and Banhart, J. (2009). Advances in neutron radiography and tomography. *Journal of Physics D: Applied Physics*, 42(24).
- Strobl, M., Woracek, R., Kardjilov, N., Hilger, A., Wimpory, R., Tremsin, A., Wilpert, T., Schulz, C., Manke, I., and Penumadu, D. (2012). Time-of-flight neutron imaging for spatially resolved strain investigations based on Bragg edge transmission at a reactor source. *Nuclear Instruments and Methods in Physics Research, Section A: Accelerators, Spectrometers, Detectors and Associated Equipment*, 680:27–34.
- Sun, T., Tremsin, A. S., Roy, M. J., Hofmann, M., Prangnell, P. B., and Withers, P. J. (2018). Investigation of residual stress distribution and texture evolution in AA7050 stationary shoulder friction stir welded joints. *Materials Science and Engineering A*, 712(October 2017):531–538.
- Swanson, H. E. and Fuyat, R. K. (1953). Standard X-ray diffraction powder patterns II. *National Bureau of Standards*, 539:1–65.
- Syed, A. K., Fitzpatrick, M. E., Moffatt, J. E., Doucet, J., and Durazo-Cardenas, I. (2015). Effect of impact damage on fatigue performance of structures reinforced with GLARE bonded crack retarders. *International Journal of Fatigue*, 80:231–237.
- Toparli, M. B. and Fitzpatrick, M. E. (2011). Residual stresses induced by laser peening of thin aluminium plates. *Materials Science Forum*, 681:504–509.
- Toparli, M. B. and Fitzpatrick, M. E. (2016). Development and Application of the Contour Method to Determine the Residual Stresses in Thin Laser-Peened Aluminium Alloy Plates. *Experimental Mechanics*, 56(2):323–330.
- Toparli, M. B., Fitzpatrick, M. E., and Gungor, S. (2013). Improvement of the Contour Method for Measurement of Near-Surface Residual Stresses from Laser Peening. *Experimental Mechanics*, 53(9):1705–1718.
- Toparli, M. B., Smyth, N., and Fitzpatrick, M. E. (2017). Effect of Treatment Area on Residual Stress and Fatigue in Laser Peened Aluminum Sheets. *Metallurgical and Materials Transactions A*, 48(4):1519–1523.

- Treimer, W. (2009). Neutron Tomography. In Anderson, I. S., Mc Greevy, R. L., and Bilheux, H. Z., editors, *Neutron Imaging and Applications: A reference for the imaging community*, chapter 6, pages 81–108. Springer, New York.
- Tremsin, A., Kockelmann, W., Kelleher, J., Paradowska, A., Ramadhan, R., and Fitzpatrick, M. (2018). Energy-Resolved Neutron Imaging for Reconstruction of Strain Introduced by Cold Working. *Journal of Imaging*, 4(3):48.
- Tremsin, A., Yau, T. Y., and Kockelmann, W. (2016a). Non-destructive Examination of Loads in Regular and Self-locking Spiralock ® Threads through Energy- resolved Neutron Imaging. *Strain*, 52:548–558.
- Tremsin, A. S., Ganguly, S., Meco, S. M., Pardal, G. R., Shinohara, T., and Feller, W. B. (2016b). Investigation of dissimilar metal welds by energy-resolved neutron imaging. *Journal of Applied Crystallography*, 49(4):1130–1140.
- Tremsin, A. S., McPhate, J. B., Kockelmann, W. A., Vallerga, J. V., Siegmund, O. H. W., and Feller, W. B. (2009). Energy-Resolving neutron transmission radiography at the isis pulsed spallation source with a high-resolution neutron counting detector. *IEEE Transactions on Nuclear Science*, 56(5):2931–2937.
- Tremsin, A. S., McPhate, J. B., Vallerga, J. V., Siegmund, O. H., Bruce Feller, W., Lehmann, E., Kaestner, A., Boillat, P., Panzner, T., and Filges, U. (2012). Neutron radiography with sub-15  $\mu\text{m}$  resolution through event centroiding. *Nuclear Instruments and Methods in Physics Research, Section A: Accelerators, Spectrometers, Detectors and Associated Equipment*, 688:32–40.
- Tremsin, A. S., McPhate, J. B., Vallerga, J. V., Siegmund, O. H. W., Kockelmann, W., Steuwer, A., and Feller, W. B. (2011). High-resolution neutron counting sensor in strain mapping through transmission Bragg edge diffraction. *IEEE Sensors Journal*, 11(12):3433–3436.
- Tremsin, a. S., Vallerga, J. V., McPhate, J. B., and Siegmund, O. H. W. (2014). Optimization of Timepix count rate capabilities for the applications with a periodic input signal. *Journal of Instrumentation*, 9(05):C05026–C05026.
- Tremsin, A. S., Vallerga, J. V., McPhate, J. B., Siegmund, O. H. W., and Raffanti, R. (2013). High resolution photon counting with MCP-timepix quad parallel readout operating at > 1 KHz frame rates. *IEEE Transactions on Nuclear Science*, 60(2):578–585.
- Van Langh, R., James, J., Burca, G., Kockelmann, W., Zhang, S. Y., Lehmann, E., Estermann, M., and Pappot, A. (2011). New insights into alloy compositions: Studying Renaissance bronze statuettes by combined neutron imaging and neutron diffraction techniques. *Journal of Analytical Atomic Spectrometry*.
- Varez, A., Garcia-Gonzalez, E., Jolly, J., and Sanz, J. (2007). Structural characterization of Ce<sub>1-x</sub>Zr<sub>x</sub>O<sub>2</sub>(0 < x < 1) samples prepared at 1650 °C by solid state reaction. A combined TEM and XRD study. *Journal of the European Ceramic Society*, 27(13-15):3677–3682.
- Vitucci, G., Minniti, T., Di Martino, D., Musa, M., Gori, L., Micieli, D., Kockelmann, W., Watanabe, K., Tremsin, A. S., and Gorini, G. (2018a). Energy-resolved neutron tomography of an unconventional cultured pearl at a pulsed spallation source using a microchannel plate camera. *Microchemical Journal*, 137:473–479.

- Vitucci, G., Minniti, T., Tremsin, A. S., Kockelmann, W., and Gorini, G. (2018b). Investigation of image distortion due to MCP electronic readout misalignment and correction via customized GUI application. *Journal of Instrumentation*, 13(04):C04028—C04028.
- Vogel, S. (2000). *A Rietveld-Approach for the Analysis of Neutron Time-of-Flight Transmission Data*. PhD thesis, Christian-Albrechts-Universität zu Kiel.
- Watanabe, K., Minniti, T., Kockelmann, W., Dalglish, R., Burca, G., and Tremsin, A. S. (2017). Characterization of a neutron sensitive MCP/Timepix detector for quantitative image analysis at a pulsed neutron source. *Nuclear Instruments and Methods in Physics Research Section A: Accelerators, Spectrometers, Detectors and Associated Equipment*, 861(January):55–63.
- Watkin, K. L., Bilheux, H. Z., and Ankner, J. F. (2009). Probing the Potential of Neutron Imaging for Biomedical and Biological Applications. In Bilheux, H. Z., McGreevy, R., and Anderson, I. S., editors, *Neutron Imaging and Applications: A Reference for the Imaging Community*, pages 253–264. Springer US, Boston, MA.
- Whitfield, H. J., Roman, D., and Palmer, A. R. (1966). X-ray study of the system ThO<sub>2</sub>CeO<sub>2</sub>Ce<sub>2</sub>O<sub>3</sub>. *Journal of Inorganic and Nuclear Chemistry*, 28(12):2817–2825.
- Wilson, A. J. C. (2002). The thermal expansion of aluminium from 0 to 650 C. *Proceedings of the Physical Society*, 53(3):235–244.
- Winholtz, R. (2003). Characterization of macrostresses. In Fitzpatrick, M. and Londini, A., editors, *Analysis of Residual Stress by Diffraction using Neutron and Synchrotron Radiation*, chapter 4, pages 60–77. Taylor & Francis, London.
- WoŁcyrz, M. and Kepinski, L. (1992). Rietveld refinement of the structure of CeOCl formed in Pd/CeO<sub>2</sub> catalyst: Notes on the existence of a stabilized tetragonal phase of La<sub>2</sub>O<sub>3</sub> in LaPdO system. *Journal of Solid State Chemistry*, 99(2):409–413.
- Woracek, R., Penumadu, D., Kardjilov, N., Hilger, A., Boin, M., Banhart, J., and Manke, I. (2015). Neutron Bragg Edge Tomography for Phase Mapping. *Physics Procedia*, 69(October 2014):227–236.
- Woracek, R., Penumadu, D., Kardjilov, N., Hilger, A., Strobl, M., Wimpory, R. C., Manke, I., and Banhart, J. (2011). Neutron Bragg-edge-imaging for strain mapping under in situ tensile loading. *Journal of Applied Physics*, 109(9):2–6.
- Woracek, R., Santisteban, J., Fedrigo, A., and Strobl, M. (2018). Diffraction in neutron imaging—A review. *Nuclear Instruments and Methods in Physics Research, Section A: Accelerators, Spectrometers, Detectors and Associated Equipment*, 878(August 2017):141–158.
- Yang, Y. W. and Coppens, P. (1978). The electron density and bonding in beryllium metal as studied by Fourier methods. *Acta Crystallographica Section A*, 34(1):61–65.
- Yilbas, B. S., Gondal, M. A., Arif, A. M. F., and Shuja, S. Z. (2004). Laser shock processing of Ti-6Al-4V alloy. *Proceedings of the Institution of Mechanical Engineers, Part B: Journal of Engineering Manufacture*, 218(5):473–482.

- Zabeen, S., Preuss, M., and Withers, P. J. (2013). Residual stresses caused by head-on and 45° foreign object damage for a laser shock peened Ti–6Al–4V alloy aerofoil. *Materials Science and Engineering: A*, 560:518–527.

# Appendix A

## TPX\_EdgeFit Manual for Bragg Edge Strain Mapping

### A.1 Overview

TPX\_EdgeFit is a software to automate pixel-by-pixel Bragg edge fitting and Bragg edge parameter reconstruction to create 2D maps of Bragg edge parameters (Anton Tremsin, personal communication, 1 October 2016). The software, along with overlap correction codes is available on IMAT. The general algorithm used by the software is shown in Fig. 4.10.

The preparation that needs to be performed prior to starting the data analysis are as follows

1. **Preparing the data set.** While it is possible to have only the sample data set to carry out the data analysis, accurate strain mapping ideally needs a sample data set and a flat/ open beam data set.
2. **Preparing the software file.** To perform the overlap correction, the folder \Overlap containing files *TPX\_CubeRead.exe* and *cfitsio.dll* is required. To perform the Bragg edge mapping, the folder \BraggEdgeMap containing files *TPX\_Edgefit.exe*, *ParamFile.txt* and *cfitsio.dll* is required.
3. **Preparing the data analysis folder.** It is recommended to create a new folder for each data analysis run. All three files contained in the \BraggEdgeMap is copied into this new data analysis folder. The output of the software will be automatically saved in this analysis folder.

## A.2 Data Analysis

### A.2.1 Overlap correction

Overlap correction (Tremsin et al., 2014) is needed to recover the time-of-flight (TOF) spectrum affected by overlap effect, produced by MCP detector. An overlap effect is a distortion of transmission spectrum due to a drop in the detector efficiency at the end of a shutter period. MCP detector pixel can only be occupied by one neutron event for a given shutter period. Therefore, subsequent events in the same pixel are rejected until the data are transferred at the end of the shutter period, decreasing the counting efficiency of the detector especially under high flux condition. Overlap correction is needed for both sample and open beam data set. The step to run the overlap correction code are as follows:

1. Open Command Prompt *cmd.exe* on Windows
2. Drag and drop the *TPX\_CubeRead.exe* into the Command Prompt
3. On Command Prompt window, hit space bar on keyboard
4. Drag and drop the first FITS file from the sample or open beam data folder into the Command Prompt
5. Hit Enter on keyboard
6. The corrected data will be saved in the folder containing the sample or the open beam data set, in a folder named \Corrected. It is recommended to rename the folder containing the corrected data set to avoid confusion further down the data analysis.

### A.2.2 Data scaling

In order to obtain a correct transmission spectra  $Tr = I/I_0$ , the incident intensity  $I_0$  and the transmitted intensity  $I$  need to have equivalent counting time. This is often not the case in the experiment, i.e., either the sample or the flat data set has longer counting time relative to the other. Therefore, data scaling is needed. There are two ways to get the scale factor,  $SF$ .

**Option 1.** Using the shutter count value:

1. On each of the data set folder, open the file named ending with *\_ShutterCount*.
2. The file contains two columns, the first column is the index of the shutters (started from 0), and the second column is the neutron counts from the corresponding shutters.

3. The scale factor can then be calculated by comparing the shutter counts (either averaged across the whole shutters or choosing a specific shutter period) from the sample data set and the flat data set,  $SF = \frac{\text{flat shutter count}}{\text{sample shutter count}}$

**Option 2.** Using the open beam intensity of the data set. An open beam region, i.e., region in the detector field-of-view without any sample in front of the detector, on the sample data set is required for this method.

1. Load the sample and the flat data set onto ImageJ
2. Get the intensity form the open beam region of the sample data set: Select the open beam region on the sample data set, Fig. A.1(a), then select from the menu Image > Stack > Plot Z-axis Profile > List.
3. Get the intensity from the equivalent region of the flat data set, Fig. A.1(b). To copy the selection into the flat data set, select from the menu Edit > Selection > Restore Selection. The rest of the steps are the same with point 2,
4. The scale factor can then be calculated by comparing the average intensity from the sample and the flat, (either across the whole wavelength spectrum or from specific shutter period).  $SF = \frac{\text{flat intensity}}{\text{sample intensity}}$

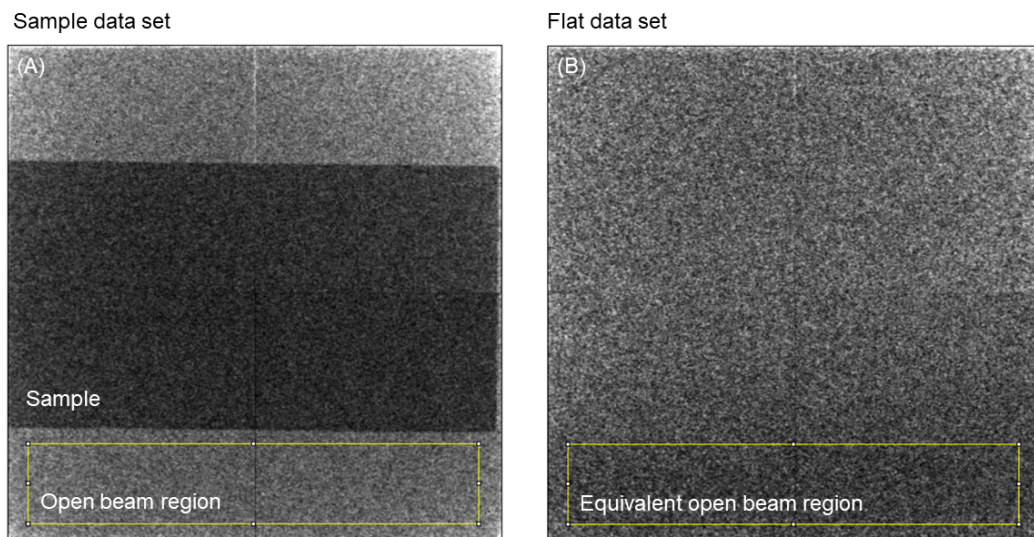


Fig. A.1 Open beam region on sample and flat data set.

Including the scale factor in the transmission calculation yields:

$$Tr = \frac{I}{I_0} \times SF \quad (\text{A.1})$$

To apply the scaling factor to either the sample or the flat data set, and to save the scaled dataset, the steps are as follows:

1. On the ImageJ menu, select Process > Math > Multiply, then insert the scaling factor
2. To save the scaled data set, select from the menu File > Save As > Image Sequence. Select FITS as the format, insert the name, put 0 as Start At, and put 5 as the number of Digits. Untick the 'Use slice labels as file names' option. Save the image sequence in a separate folder.

It is worth noting that scaling down a data set is preferable to avoid amplifying the error.

### A.2.3 Transmission spectra

Building the transmission spectra is useful to get the idea of the data being analysed and to observe and select which Bragg edge to bring forward for analysis.

1. Create an spreadsheet file with the first column providing the index of each neutron TOF/ wavelength. For analysis using TPX\_Edgefit, it is very important to note that the index must start from 0.
2. Time-of-flight of the data set can be obtained from the first column of the file named ending with \_Spectra in the data set folder.
3. Neutron wavelength of the data set can be calculated with the knowledge of the instrument flightpath, using Eq. (6.1).
4. Transmission spectrum  $Tr$  can be calculated using Eq. (A.1). The transmitted intensity  $I$  can be obtained by selecting a region of interest from the sample, then select from the menu Image > Stack > Plot Z-axis Profile > List. The size of the region of interest should be the same as the size of the macro-pixel (see **Section 4.2.3**) which will be used in the reconstruction. The incident intensity  $I_0$  can be obtained by selecting region of interest from the flat data set and plotting the Z-axis profile. The region of interest from the flat data set does not have to be the equivalent of that from sample data set, and the size can be made larger to improve the statistics.

5. The example of the spreadsheet containing transmission spectra is shown in Fig. A.2

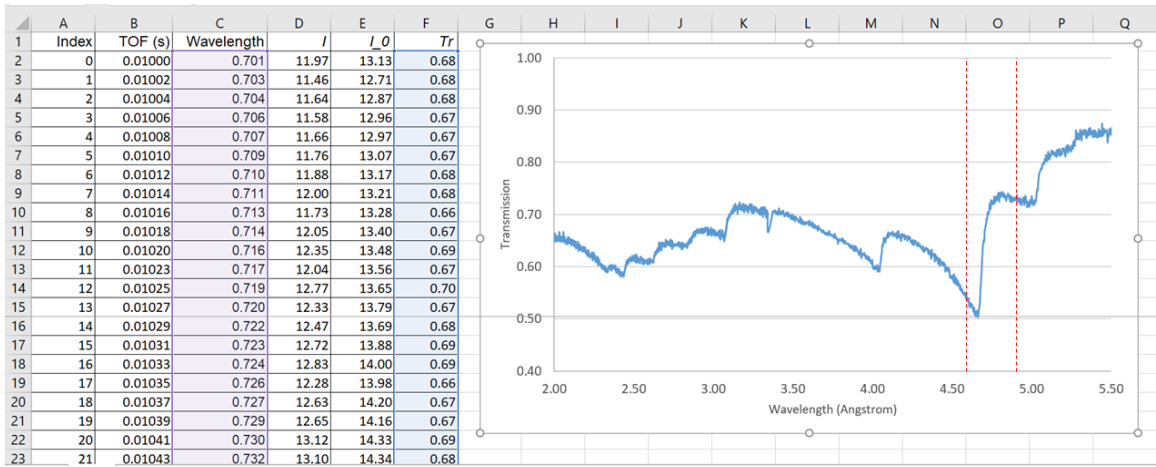


Fig. A.2 Example of spreadsheet containing transmission spectrum.

#### A.2.4 Parameter initialisation

Parameter initialisation is needed to do the pixel-by-pixel Bragg edge fitting and Bragg edge parameter map reconstruction. The parameter initialisation can be performed by fitting a selected edge using analytical function described by Eq. (4.5), which is also used by the TPX\_Edgefit software. This can be performed using a pre-prepared excel spreadsheet available on IMAT.

1. Select a Bragg edge, and determine the range of wavelength from which the Bragg edge fitting will be performed, e.g., from 4.6 to 4.85 Å, Fig. A.2.
2. Open the file EdgeFit.xls, and copy the Index, TOF, wavelength and measured transmission,  $Tr$ , into the first four columns, Fig. A.3.
3. Column 7 is the transmission spectrum calculated using analytical function Eq. (4.5), based on the Bragg edge parameter values in the cell highlighted yellow in Fig. A.3.
4. Perform the least square fitting with Data > Solver menu by minimising the cell labelled 'Sum error' (highlighted green in Fig. A.3), which is the sum squared difference between the measured and calculated transmission spectrum, by changing the Bragg edge parameters in the cells labelled 'Lambda\_edge', 'Sigma', 'Tau', 'C1', and 'C2' (highlighted yellow in Fig. A.3).

5. The red data points in the graph of Fig. A.3 are the measured transmission  $Tr$ , while the green curve is the analytical function.
6. The initial Bragg edge parameter is now defined.

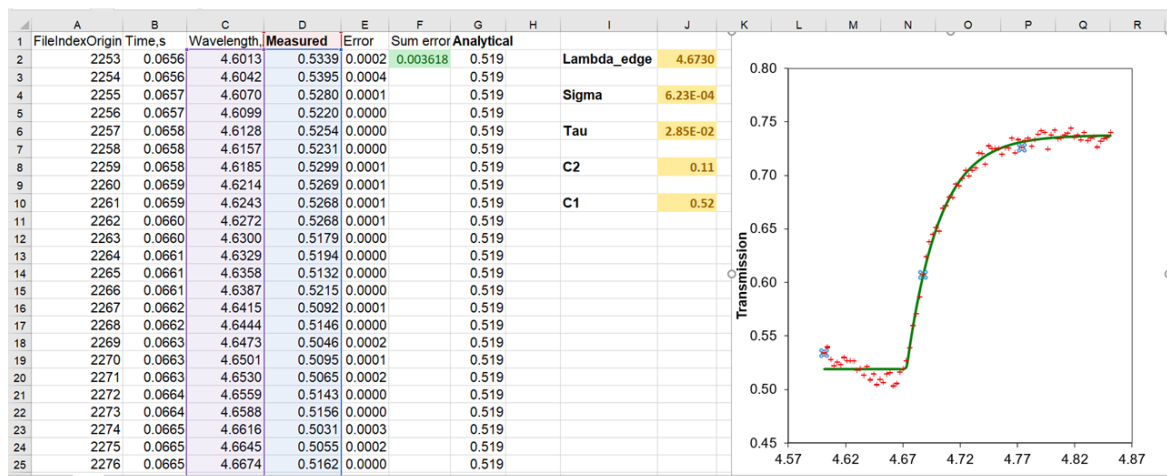


Fig. A.3 Pre-prepared EdgeFit spreadsheet for Bragg edge parameter initialisation.

### A.2.5 Prepare flat files for normalisation

As mentioned in the text, TPX\_EdgeFit build a list of transmission spectra by getting the transmitted intensities  $I$  pixel-by-pixel and normalising them by a single spectrum of incident intensity  $I_0$ . The input for the software to readout the transmitted intensities will be determined in the 'ParamFile' (described in the next section), meanwhile there are two ways to input the incident intensity: 1) extracting  $I_0$  from the open beam region of the sample data, with area defined in ParamFile, or; 2) manually create a  $I_0$  spectrum in a separate file. Using the former would negate the need of a separate flat data set.

Using the later option, the steps to prepare the file are as follows:

1. Open an Excel spreadsheet file and fill the first 9 columns as shown in Fig. A.4, or use the template spreadsheet file Flat.txt available on IMAT.
2. Fill the first and second column with the neutron TOF (in microsecond) and wavelength (Angstrom), respectively. The TOF and wavelength range must match the selected range determined in the step 1 of **Section A.2.4**.
3. Fill the third column with the counts from incident intensity  $I_0$ . This can be the same as the  $I_0$  determined in step 4 of **Section A.2.3**.

4. Fill the fourth column with an arbitrary small number, for example 0.01% of the  $I_0$ .
5. Save the spreadsheet as .txt file, e.g., Flat.txt. The  $I_0$  spectrum in this file will be called in the ParamFile.

	A	B	C	D	E	F	G	H	I	J
1	Time,us	Wavelength,A	Counts	Sigma	Rectangle: x=0	y=0	width=512	height=512		
2	66296.3	4.65014473	84.21	0.00842						
3	66337.3	4.65302055	83.875	0.00839						
4	66378.2	4.65588935	83.824	0.00838						
5	66419.2	4.65876516	83.778	0.00838						
6	66460.2	4.66164098	83.621	0.00836						
7	66501.1	4.66450978	83.421	0.00834						
8	66542.1	4.6673856	83.251	0.00833						
9	66583	4.6702544	83.196	0.00832						
10	66624	4.67313021	83.049	0.0083						
11	66665	4.67600603	82.87	0.00829						
12	66705.9	4.67887483	82.929	0.00829						
13	66746.9	4.68175065	82.958	0.0083						
14	66787.8	4.68461945	83.242	0.00832						
15	66828.8	4.68749526	83.182	0.00832						
16	66869.8	4.69037108	83.351	0.00834						
17	66910.7	4.69323988	83.124	0.00831						
18	66951.7	4.6961157	83.095	0.00831						
19	66992.6	4.6989845	82.968	0.0083						

Fig. A.4 Example of spreadsheet file containing  $I_0$  spectrum for transmission spectra normalisation.

A second normalisation of the transmission spectrum is needed to take into account the variation of neutron intensity across the image due to the spatial inhomogeneity of the neutron beam and the variation of efficiency across the detector. To do the normalisation, an image containing the intensity variation is prepared by collapsing the neutron counts at different wavelengths into a single image:

1. Load the flat data set into ImageJ
2. Collapse the image stack into a single image by selecting from the menu Image > Stacks > Z Project, select the entire image slice and select 'Average Intensity' as Projection type.
3. Save the images as .FITS file, e.g., Flat.fits

### A.2.6 Prepare the 'ParamFile'

ParamFile.txt is the parameter setting file where the initial parameterisation, size of the macro-pixel for reconstruction, and path to the data set, among other things, is inputted. Line-by-line description of the file, referring to Fig. A.5, is as follows (the line which are not described can be kept fixed without changing the result).

```

----- Fit parameters -----
(1)... 4.668479276    - Lambda0
(2)... 3.99E-04        - Sigma (width)
(3)... 2.30E-02        - Tau (asymmetry)
(4)... 0.113543167     - Edge height
(5)... 0.533195155     - Edge pedestal
-----Open Beam Area from the same image-----
(6)... 420             - X
(7)... 22              - Y
(8)... 77              - Width
(9)... 474             - Height
-----0.0e-3 - SHIFT_T //shift of trigger in milliseconds relative to T0 in the dta acquired
(11)... 56.4            // the flight path in meters
-----3 - Number of parameters to fit FIT_ONLY_THREE_OR_FIVE_PARAM
(15)... -8351.36        - Tmin (us), The time of the min time bin in the edge used for the calculations
(16)... -8812.18        - Tmax (us), The time of the max time bin in the edge used for the calculations
(17)... 2270            - FileIndMin //The min index of the file to be used in reconstruction of the edge
(18)... 2357            - FileIndMax //The max index of the file to be used in reconstruction of the edge
(19)... 0               - AREA_INTEREST_LEFT //pixels, where the left border for calculation are is
(20)... 511             - AREA_INTEREST_RIGHT //pixels, where the right border for calculation are is
(21)... 0               - AREA_INTEREST_TOP //pixels, where the top border for calculation are is
(22)... 511             - AREA_INTEREST_BOT //pixels, where the bottom border for calculation are is
(23)... -51.2            - SPCTR_BIN (us), the time bin to be used for building the spectra
-----C:\Data_ISIS\MMC-Powder-IMAT\Exx\Scaled_IMAT_exx\Scaled_
(25)... C:\Data_ISIS\Raden-IMAT-ENGINX\Strainmap\IMAT\IMAT-EXX\Flat.txt
(26)... C:\Data_ISIS\Raden-IMAT-ENGINX\Strainmap\IMAT\IMAT-EXX\Flat.fits

```

Fig. A.5 ParamFile, the input parameter file for the TPX\_EdgeFit software.

1. **Line 1 to 5:** The initial parameter input for  $\lambda_{hkl}$ ,  $\sigma$ ,  $\tau$ ,  $C_2$ , and  $C_1$ , respectively.
2. **Line 6 to 8:** The  $x$ - and  $y$  coordinate, the width and the height, respectively, of the open beam region of the sample data for transmission spectrum normalisation (as mentioned in **Section A.2.5**).
3. **Line 10:** The shift between the trigger signal relative to the  $T_0$  in the data acquired (in milliseconds). This is required if a delay box is used in conjunction with the MCP detector.
4. **Line 11:** Flight path of the neutron beamline, in meter.
5. **Line 12 and 13:** The  $x \times y$  size, respectively, of the macro-pixel, in pixel, to be used for Bragg edge map reconstruction.
6. **Line 14:** The number of parameters to be fitted in the fitting and reconstruction. The maximum number of 5 will fit all the aforementioned parameters. Inserting a number of 4 will keep the  $\tau$  parameter fixed. Inserting a number of 3 will keep the  $\tau$  and the  $\sigma$  parameter fixed.
7. **Line 17 and 18** The starting and the ending file index, respectively, from which the analysed Bragg edge is selected. Can be referred to the 'FileIndexOriginal' column in Fig. A.3.

8. **Line 19 to 20** The starting and the ending pixel, from left to right (relative to the image loaded onto ImageJ), from where the calculation is performed. Value 0 and 511 for Line 21 and 22, respectively, will produce a calculation of the full width of the image.
9. **Line 21 to 22** The starting and the ending pixel, from bottom to top (relative to the image loaded onto ImageJ), from where the calculation is performed. Value 0 and 511 for Line 21 and 22, respectively, will produce a calculation of the full height of the image.
10. **Line 24** File path of the sample data set, up to the image file name minus the index.
11. **Line 25** File path of the .txt file used for normalisation (refer to **Section A.2.5**). If an open beam region of the sample data is used for the normalisation, put NONE on the Line 25.
12. **Line 26** File path of the .FITS file used for spatial variation normalisation (refer to **Section A.2.5**). If no normalisation is required, leave the line blank.

### A.2.7 Run the TPX\_EdgeFit Software

After preparing the ParamFile, and all the files required, the calculation can be performed by double-clicking the TPX\_EdgeFit.exe. A command prompt window will appear showing the pixel-by-pixel fitting and the progress status.

### A.2.8 Output of the data analysis

The program will produce six .FITS files containing each Bragg edge parameters:

1. **Coeff0** →  $\lambda_{hkl}$  which is the Bragg edge position
2. **Coeff1** →  $\sigma$
3. **Coeff2** →  $\tau$
4. **Coeff3** → C2, which corresponds to a half of the edge height
5. **Coeff4** → C1

An additional parameter map **Coeff5** shows the inflection point of the Bragg edges. This parameter, however, is currently not being used for analysis. The program also produced error map for each parameter. The error values, however, is often unrealistically huge and is

not representative of the uncertainty of the result. A separate Bragg edge fitting using the corresponding analytical function Eq. (4.5) is often performed to obtain a typical uncertainty of the result.

## A.3 Post-processing

### A.3.1 Create and apply mask

In order to highlight the region of interest of the analysed data set, a mask can be created and applied to the Bragg edge parameter map.

To create a mask from the original sample image, the steps are as follows

1. Load the sample data set to ImageJ. To make the selection process easier, collapse the image stack into one image using the menu **Image > Stacks > Z Project**.
2. Make a selection using any of the available selector tool, e.g., the yellow box on Fig. A.6(a).
3. Create a mask from the selection using the menu **Edit > Selection > Create Mask**. This will create a new image with zeros and 255s (for 8-bit image), Fig. A.6(b).
4. Convert the mask value to zeros and ones by performing math operation using the menu **Process > Math > Divide > Value: 255**.
5. Save the mask image as .FITS file.

The steps to apply the masks are as follows, example given for applying the mask to Bragg edge position map Coeff0.

1. Load the Coeff0 and the mask file to ImageJ
2. Perform image calculation using the menu **Process > Image Calculator**. Multiply the Coeff0 image with the mask image.
3. A new masked Coeff0 image will be produced, Fig. A.6(d).

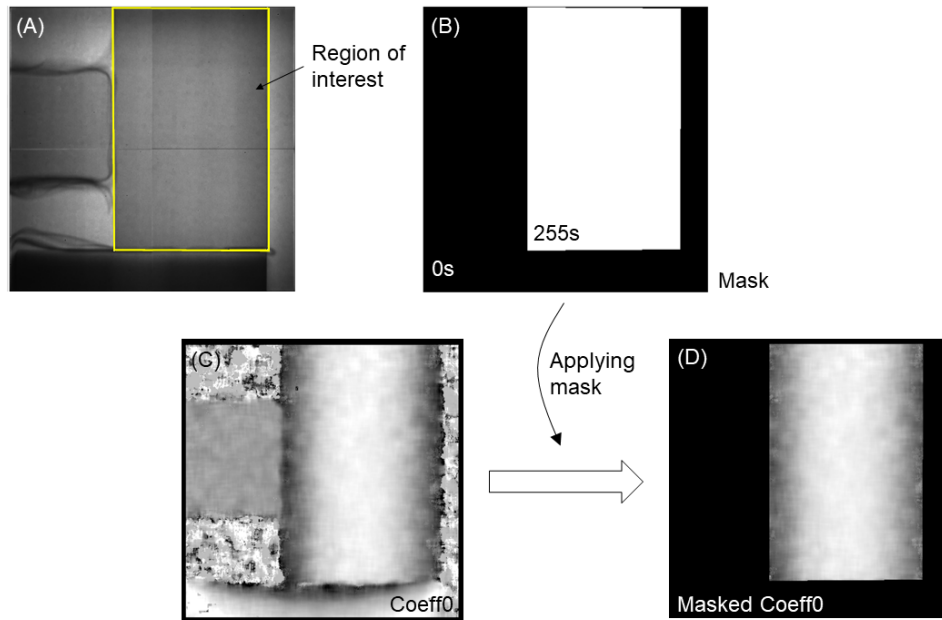


Fig. A.6 Creating and applying mask to highlight the region of interest.

### A.3.2 Calculate strain

The strain, in  $\mu\epsilon$ , can be calculated from the Bragg edge position using Eq. (7.1), which can be rewritten as:

$$\epsilon = \left( \frac{\lambda_{hkl}}{\lambda_0} - 1 \right) \times 10^6 \quad (\text{A.2})$$

Therefore, to obtain strain map from the Bragg edge position map Coeff0, the steps are as follows:

1. Divide the Coeff0 image by  $\lambda_0$  value using the menu Process > Math > Divide.
2. Subtract the resulting image by 1 using the menu Process > Math > Subtract.
3. To get the strain in  $\mu\epsilon$ , multiply the resulting image by 1 million using the menu Process > Math > Multiply
4. The result yield the strain map in  $\mu\epsilon$ . To adjust the display range, use the menu Image > Adjust > Brightness and Contrast > Set, then input the minimum and maximum displayed value.

### A.3.3 Scale, colour profile and calibration bar

To set the scale of the Image with the real physical dimension of the sample, the steps are as follows:

1. Select the menu Analyse > Set Scale
2. Insert the distance in pixels of 1, corresponds to a known distance of 0.055 (physical dimension of the Medipix2/Timepix chip), pixel aspect ratio of 1, and unit of length of mm.
3. Tick the Global option to apply the scale to all opened images.
4. Each pixel is now has the dimension of 55  $\mu\text{m}$ .
5. To display the scale bar, select the menu Analyze > Tool > Scale Bar. Adjust the settings accordingly.

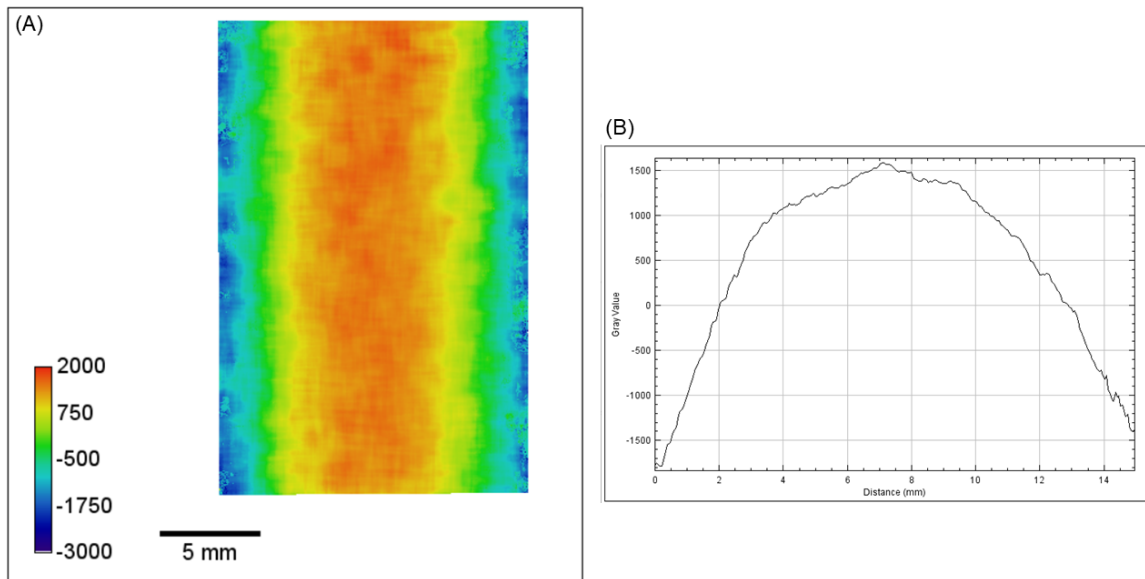


Fig. A.7 (A) An example of reconstructed strain map, and; (B) line profile of strain.

To enhance the contrast of the strain map and to aid visualisation, colour profile can be applied to the strain map using the menu Image > Lookup Tables. There are several built-in colour palettes to chose from. To manually create, edit and save a colour palette, use the menu Image > Color > Edit LUT.

To add a calibration bar, use the menu Analyse > Tool > Calibration Bar, and adjust the settings accordingly. The example of strain map with calibration bar and scale bar is shown in Fig. A.7(a).

#### A.3.4 Plot line profile of strain

To get more detailed information from the strain map, line profile of strain can be extracted from the map using the steps as follows:

1. Select the straight line tool from the toolbar menu. The thickness of the line can be adjusted by double-clicking the line tool button.
2. Draw a line from which the strain profile will be extracted.
3. Display the profile using the menu Analyse > Plot Profile. The example of the result is shown in Fig. A.7(b).



## Appendix B

# BEATRIX Manual for Bragg Edge Strain Mapping

### B.1 Overview

BEATRIX is another Bragg edge mapping software to automate the pixel-by-pixel Bragg edge fitting and parameter reconstruction (Triestino Minniti, personal communication 1 May 2018). It is developed in-house on IMAT and uses object-oriented C++ programming language and making use of the ROOT framework libraries for data analysis. The current version of the software is only available for user on the IMAT-Linux PC, with a possibility of accessing the program via a remote-desktop setup. The main difference of BEATRIX compared to TPX\_EdgeFit software is that the former used the 3-steps analytical function shown in Eq. (4.4) to fit the Bragg edge.

The preparation that is needed prior to starting the data analysis are as follows:

1. **Copying the data set.** The sample and flat data set need to be copied to the local drive of the IMAT-Linux PC.
2. **Creating mask image.** The mask image is one of the input during the data analysis, and therefore needs to be prepared beforehand. The steps to create a mask image is described in [Section A.3.1](#).

### B.2 Data Analysis

The BEATRIX code already integrates overlap correction and data scaling and therefore does not require separate analysis. However, getting the transmission spectra and performing a

Bragg edge fitting using a separate program is useful to get the feeling about the data and to obtain the initial guess value for the Bragg edge parameter. The transmission spectrum from the data can be generated by following the steps mentioned in **Section A.2.3**.

Meanwhile, for parameter initialisation, the pre-prepare spreadsheet available on IMAT, EdgeFit.xls, can be used. Despite the difference in the Bragg edge analytical function used by the spreadsheet [Eq. (4.5)] and the BEATRIX software, the important  $\lambda_{hkl}$ ,  $\sigma$ , and  $\tau$  parameters are still comparable. Alternatively, the fitting using Eq. (4.4) can be performed with data analysis program such as Python, Matlab or Origin using a user-defined function.

## B.2.1 Accessing BEATRIX software

The BEATRIX software on the IMAT-Linux PC can be found in directory Home > Application > BEATRIX. Inside the folder are seven object files, a setting file, and an executable to run the program. User is advised to copy all of these files into a separate folder for each data analysis.

## B.2.2 Preparing the ‘Global\_Settings’ file

The Global\_Settings.txt is the file containing all the input needed for the data analysis and reconstruction. Line-by-line description of the file, referring to Fig. B.1, is as follows (the line which are not described can be kept fixed without changing the result):

1. **Line 4.** The region of interest for which the data analysis is performed. Defined by four numbers which represent the coordinates of minimum and maximum  $x$ -axis and minimum and maximum  $y$ -axis, respectively.
2. **Line 5.** Instrument flight path in meter.
3. **Line 8.** The option on whether or not the software will run the pixel-by-pixel fitting. Insert 1 to perform the fitting, and insert 0 otherwise.
4. **Line 9.** Two numbers that define the normalisation. The first number define the  $I_0$  used for normalisation. Value 1 use a standard pixel-by-pixel normalisation where unique  $I_0$  is taken for each pixel, while value 2 use an average  $I_0$  from a larger area from the Flat data set. The second number define the scale factor, where value 1 use an open beam area from the sample data set while value 0 will use the shutter counts file from the sample and open beam data set.
5. **Line 10.** Number of CPU processors to use for calculation, a value between 1 to 8.

6. **Line 11.** An open beam area from the sample data set to be used in the calculation of scale factor, if the value 1 is inserted in the second number of line 9.
7. **Line 12** The  $x$ - and  $y$ -position of specific pixel on the image to check the signal. Up to 4 pixels on different positions can be checked.
8. **Line 13.** The size of the macro-pixel (in pixel) to be used for the running average analysis of the Bragg edge map reconstruction. Only odd numbers should be inserted since the average value of the macro-pixel will be assigned to a pixel in the centroid.
9. **Line 14.** The value of  $d_0$  in Angstrom that is used for the strain map calculation.
10. **Line 15.** The initial guess value and the range (minimum and maximum value) of the  $\lambda_{hkl}$  parameter, respectively.
11. **Line 16.** The initial guess value and the range (minimum and maximum value) of the  $\sigma$  parameter, respectively.
12. **Line 17.** The initial guess value and the range (minimum and maximum value) of the  $\tau$  parameter, respectively.
13. **Line 18.** Three numbers to define whether or not the  $\lambda$ ,  $\sigma$  and  $\tau$  parameter will be fixed during the calculation. Insert value 1 to fit any of the parameters, or 0 otherwise.
14. **Line 19.** The lambda range (minimum and maximum, respectively) of the region on the far-left (lower wavelength) of the Bragg edge to be fitted.
15. **Line 20.** The lambda range (minimum and maximum, respectively) of the region on the far-right (higher wavelength) of the Bragg edge to be fitted.
16. **Line 21.** The lambda range (minimum and maximum, respectively) of Bragg edge to be fitted.
17. **Line 23.** File path of the mask image.
18. **Line 25 and 26.** File path and base name of the sample data set, respectively.
19. **Line 28 and 29.** File path and base name of the open beam data set, respectively.
20. **Line 31 and 32.** Path of the folder and the base name (with the name format file-name.root) for the output of the program.

This item has been removed due to third party copyright. The unabridged version of the thesis can be viewed at the Lanchester library, Coventry University

Fig. B.1 Global\_settings file of the BEATRIX software.

This item has been removed due to third party copyright. The unabridged version of the thesis can be viewed at the Lanchester library, Coventry University

Fig. B.2 Output of the BEATRIX software opened with GUI-based TBrowser.

### B.2.3 Run the data analysis

To run the data analysis, open the file containing the executable file on Terminal, then type `\BEATRIX` and hit enter.

## B.3 Post processing

The calculation performed by the software produces one .root file and maps of  $\lambda$ ,  $\tau$ ,  $\sigma$  and strain along with the corresponding error map in ASCII file. A chi-square map is also produced to check the ‘goodness-of-fit’ across the reconstructed Bragg edge map. Those ASCII files can be used to check the numerical value of specific pixels on the parameter map.

The .root file contains objects that can be opened and manipulated with a GUI-based browser (TBrowser). To open the .root file on TBrowser, double click the output file file-name.root. A new command window will come up. Type in TBrowser, and hit enter. The TBrowser window will open, as shown in Fig. B.2, and objects including the strain map can be observed.



# Appendix C

## Publications

Journal papers and conference proceeding resulted from this work is included in this appendix:

### ***Journal papers:***

1. Ramadhan, R. S., Kockelmann, W., Minniti, T., Chen, B., Parfitt, D., Fitzpatrick, M. E., & Tremsin, A. S. (2019). Characterization and application of Bragg-edge transmission imaging for strain measurement and crystallographic analysis on the IMAT beamline. *Journal of Applied Crystallography*, 52(2), 351–368.  
doi:10.1107/S1600576719001730.
2. Ramadhan, R. S., Syed, A. K., Tremsin, A. S., Kockelmann, W., Dalgliesh, R., Chen, B., ... Fitzpatrick, M. E. (2018). Mapping residual strain induced by cold working and by laser shock peening using neutron transmission spectroscopy. *Materials & Design*, 143, 56–64.  
doi:10.1016/j.matdes.2018.01.054.
3. Kockelmann, W., Minniti, T., Pooley, D., Burca, G., Ramadhan, R., Akeroyd, F., ... Nightingale, J. (2018). Time-of-Flight Neutron Imaging on IMAT@ISIS: A New User Facility for Materials Science. *Journal of Imaging*, 4(3), 47.  
doi:10.3390/jimaging4030047.
4. Tremsin, A., Kockelmann, W., Kelleher, J., Paradowska, A., Ramadhan, R., & Fitzpatrick, M. (2018). Energy-Resolved Neutron Imaging for Reconstruction of Strain Introduced by Cold Working. *Journal of Imaging*, 4(3), 48.  
doi:10.3390/jimaging4030048.

*Conference proceedings:*

1. Ramadhan, R. S., Kockelmann, W., Tremsin, A. S., & Fitzpatrick, M. E. (2018). Neutron Transmission Strain Measurements on IMAT: Residual Strain Mapping in an AlSiCp Metal Matrix Composite. *Materials Research Proceedings*, 4, 149–154.  
doi: 10.21741/9781945291678-23.
2. Kockelmann, W., Minniti, T., Ramadhan, R.S., Ziesce, R., Pooley, D.E., Capelli, S., Glaser, D., & Tremsin, A.S. (2019). Wavelength resolved neutron imaging on IMAT. *Materials Research Forum*, in print.